AN ABSTRACT OF THE DISSERTATION OF

Larry W. O'Neill for the degree of Doctor of Philosophy in Oceanography presented on August 16, 2007.

Title: Surface Wind Modification Near Mid-Latitude Ocean Fronts: Observational and Dynamical Analysis

Abstract approved:

Dudley B. Chelton

Interactions between surface winds and meanders in mid-latitude sea surface temperature (SST) fronts with horizontal length scales of 100-1000 km are investigated from satellite observations and numerical simulations. Observations from the SeaWinds scatterometer on the QuikSCAT satellite show that the magnitude, direction, curl, and divergence of the surface wind stress and 10-m winds are well correlated with small-scale SST structures associated with large-scale ocean currents. Detailed analysis of the response of the surface winds to SST fronts from these satellite observations exposed shortcomings in previous conceptual hypotheses governing the relationships between surface winds and SST. To gain understanding of the physical mechanisms

needed to explain the satellite wind observations, we performed a numerical experiment simulating the atmospheric flow over meandering SST fronts. Based on these results, a new conceptual model is constructed to explain the dynamical response of the surface winds consistent with the satellite observations and numerical simulation analysis.

Of particular importance was the finding that the wind stress curl and divergence fields observed from QuikSCAT are linearly related to the crosswind and downwind components of the SST gradient, respectively. This relationship was generally thought to result from modification of the vertical turbulent mixing of momentum within the atmospheric boundary layer (ABL). We show that this mechanism is overly simplistic; nearly all of the terms in the momentum budget are needed to explain these observed statistical relationships, consistent with recent work. SST-induced surface wind changes are a manifestation of more complicated changes to the vertical structure of the dynamic forces within the ABL.

Among the most significant of several new findings presented here concerns the influence of SST on the meridional wind field. Since winds are generally westerly at mid-latitudes, SST-induced changes in meridional wind cause changes in the surface wind direction that significantly influence the wind stress curl and divergence fields through modification of streamline curvature and diffluence. From numerical and analytical results, these meridional wind perturbations are shown to result from a baroclinic Ekman adjustment mechanism modified by horizontal advection.

Surface Wind Modification Near Mid-Latitude Ocean Fronts: Observational and Dynamical Analysis

by
Larry W. O'Neill

A DISSERTATION

submitted to

Oregon State University

in partial fulfillment of
the requirements for the
degree of

Doctor of Philosophy

Presented August 16, 2007
Commencement June 2008

Doctor of Philosophy dissertation of Larry W. O'Neill presented on August 16, 2007.

APPROVED:

Major Professor, representing Oceanography

Dean of the College of Oceanic and Atmospheric Sciences

Dean of the Graduate School

I understand that my dissertation will become part of the permanent collection of Oregon State University libraries. My signature below authorizes release of my dissertation to any reader upon request.

Larry W. O'Neill, Author

ACKNOWLEDGMENTS

I first would like to extend my deepest thanks to my advisor, Dudley Chelton, for his professional and personal support and for his photographic advice throughout my time here and for being a good advisor. I greatly thank my co-advisor Steve Esbensen, who has helped me immensely with understanding of air-sea interaction and for his countless hours of help. I also thank the members of my committee Michael Freilich, Eric Maloney, and Roger Samelson for their enthusiastic guidance and help.

To my wonderful close family, Garry, Larry, Greg, Betsy, and Christine for their love and support.

To Kristel Fesler, who has been a great study partner and for her loving support of me.

My office mates, past and present for providing a great, distracting work environment: Eric Beals, Antonio Fetter, Craig Risien, Renellys Perez, John Lyman, and Dylan Righi.

And finally, to all my friends who have made Corvallis a true home to me. Thank you all.

CONTRIBUTION OF AUTHORS

I wish to acknowledge the following individuals for their contributions to this research. Michael Schlax has provided data files for the satellite wind and SST fields used during my first year here and provided several computational subroutines. Throughout the course of this research, Michael Freilich, Michael Schlax, and Barry Vanhoff have provided valuable advice and technical assistance in the analysis of several datasets used in this research. I also thank Eric Beals for maintaining the technical computing resources needed to complete this research. Andrew Bennett, Antonio Fetter, Ralph Foster, Eric Maloney, Ricardo Matano, Roger Samelson, Eric Skyllingstad, Justin Small, Qingtao Song, and Nicolai Thum are thanked for helpful discussions throughout the course of this analysis.

TABLE OF CONTENTS

TABLE OF CONTENTS (Continued)

Page

TABLE OF CONTENTS (Continued)

Page

LIST OF FIGURES

LIST OF FIGURES (Continued)

LIST OF FIGURES (Continued)

Figure Page

LIST OF TABLES

Chapter 1

Introduction

The main theme of this dissertation is the study of the surface wind response to sea surface temperature (SST) fronts at mid-latitudes with spatial scales between 100 and 1000 km (hereafter referred to as "small-scale"[1]). The relationship between surface wind speed and SST occuring over these smaller spatial scales differs substantially from the relationship occurring over larger spatial scales. On larger scales, changes in atmospheric circulation patterns alter surface winds which change SST through modulation of surface heat fluxes and upper ocean mixing (e.g., Mantua et al. 1997; Okumura et al. 2001). Over small scales, however, SST significantly modifies the dynamic and thermodynamic structure of the marine atmospheric boundary layer (MABL). Changes in surface winds are a manifestation of the MABL modification

[1]These spatial scales are small in the sense that they correspond to the low range of horizontal length scales resolved by current operational microwave satellites used in this research and by global numerical weather prediction models.

caused by small-scale SST perturbations. The surface wind speed waxes and wanes depending on whether the surface winds are blowing towards progressively warmer or cooler water. The present work concentrates on characterizing the coupling between surface winds and SST from satellite observations of vector winds and SST. A second objective is to describe the dynamical mechanisms responsible for the small-scale surface wind modification by SST observed in these satellite wind and SST observations.

The ocean-atmosphere coupling investigated in this dissertation was motivated by earlier investigations over the eastern tropical Pacific by Chelton et al. (2001). There, satellite observations showed that the surface wind stress magnitude was closely correlated with perturbations in the SST front of the equatorial cold tongue, where wind stress was enhanced over warmer water and reduced over cooler water.

From this correlation, Chelton et al. (2001) hypothesized that the acceleration of surface winds across SST fronts from cooler to warmer water created a wind stress divergence associated with the downwind SST gradient. Similarly, winds blowing along SST fronts were hypothesized to generate a wind stress curl associated with the crosswind SST gradient. Statistical analysis of vector wind stress observations from the QuikSCAT scatterometer and SST observations from the TRMM microwave imager (TMI) confirmed these hypothesized dependencies and found that the wind stress curl and divergence fields were linearly related to the crosswind and downwind components of the SST gradient field, respectively. These relationships between the surface wind stress curl and divergence and the small-scale SST fields over mid-

latitudes have been a fundamental topic of my dissertation research.

The robust findings of the Chelton et al. (2001) analysis led us to investigate whether the ocean-atmosphere coupling observed over the eastern tropical Pacific also existed over large mid-latitude ocean currents with their plethora of meanders and associated small-scale SST perturbations.

Research Objective 1. *Does the coupling between the surface wind stress curl and divergence and the crosswind and downwind SST gradients observed over the eastern tropical Pacific also exist over mid-latitude ocean regions?*

Initially, the Southern Ocean was chosen owing to the rich array of stationary and propagating small-scale SST perturbations associated with the meandering Antarctic Circumpolar Current. In addition to providing ample numbers of statistically-independent observations, no wind-SST interaction studies had been conducted in the Southern Ocean over such broad scales.

At the beginning of this study, satellite microwave SST observations were not available at latitudes poleward of 38° to complement the global vector wind observations made by the SeaWinds scatterometer onboard the QuikSCAT satellite. Scatterometer and passive microwave measurements of ocean surface winds and SST are not affected by persistent, non-precipitating cloud cover endemic to mid-latitude ocean regions since the atmosphere is essentially transparent to microwave radiation at the 13.4 GHz frequency used. The best SST data available over the Southern Ocean at start of this analysis were the Reynolds SST analyses (Reynolds et al. 2002), which

use bias-adjusted infrared SST measurements available from the Advanced Very High Resolution Radiometer (AVHRR) on the NOAA series of polar-orbiting satellites. To reduce sampling limitations associated with infrared measurements in cloudy regions, the Reynolds SST analyses essentially degraded the spatial and temporal resolution of the satellite infrared SST measurements to enhance accuracy, therefore smoothing over much of the small-scale SST variability of interest here[2].

Using the first two years of QuikSCAT wind stress curl and divergence observations and global SST fields from the Reynolds SST analyses, it is shown in Chapter 2 that SST influences the wind stress curl and divergence fields over the entire Southern Ocean in much the same way as it does over the eastern tropical Pacific. The coarse spatial resolution of the Reynolds SST analyses, however, was a major limitation in that study because it did not resolve small-scale variability present in the QuikSCAT wind fields thought to be associated with real, non-resolved small-scale SST structure.

Research Objective 2. *How does the spatial resolution of the SST field affect the statistical coupling between the surface winds and SST in the satellite observations?*

It became possible to investigate this question following the launch of the Advanced Microwave Scanning Radiometer on the Earth Observing System – Aqua (AMSR–E) satellite in May 2002. Even before the launch of the AMSR-E and the start of its data record in early June 2002, it was clear that small-scale SST perturbations strongly affected the small-scale structures in the surface wind field. It

[2]Improved AVHRR-based SST analyses with much higher spatial and temporal resolution have recently become available for the period 1985-present (Reynolds et al. 2007, J. Climate)

also became clear that the spatial resolution of the Reynolds SST analyses severely underestimated the strength of the coupling between the surface winds and SST.

The first year of AMSR-E SST observations showed that the small-scale wind and SST perturbations were much more highly correlated than was previously apparent from use of the Reynolds SST analyses (Chapter 3). The coarseness of the Reynolds SST analyses was thus demonstrated to be a significant source of uncertainty in our original study from Chapter 2. The Reynolds SST fields were demonstrated to underestimate the SST gradients by a factor of 5 relative to the AMSR-E SST fields (Fig. 5 in Chapter 3).

Use of the accurate, high resolution satellite wind and SST fields exposed inconsistencies in the hypothesis regarding the response of the surface wind stress curl and divergence to the crosswind and downwind SST gradients (Chapter 3). Hypothesized dependencies of the curl and divergence to SST gradients were developed on the notion that SST fronts create cross-frontal gradients in wind speed. If cross-frontal changes in wind speed only were responsible for the curl and divergence responses to the crosswind and downwind SST gradients, the responses should be equal. The curl response to crosswind SST gradients, however, is consistently only about one-half to two-thirds the magnitude of the divergence response to downwind SST gradients as described in detail in Chapter 3. Similar differences in the divergence and curl responses to SST gradients had previously been noted by Chelton et al. (2001; 2004).

Research Objective 3. *What causes the wind stress curl response to crosswind SST*

gradients to be weaker than the wind stress divergence response to downwind SST gradients? What dynamical mechanisms are responsible for the effect of small-scale SST perturbations on the curl and divergence?

These questions are the subject of the analysis in Chapter 5, where the difference in the curl and divergence responses are investigated from satellite observations and numerical simulation using the Weather Research and Forecasting (WRF) mesoscale model over a portion of the Agulhas Return Current. The effects of SST on the surface wind direction are shown to be nearly as important as wind speed in generating curl and divergence perturbations near SST fronts.

To understand the dynamical mechanisms underlying the vorticity and divergence responses to SST gradients, simulations of the SST-induced responses of the ABL momentum balances in the WRF model were analyzed (Chapter 4). Significant progress was made in understanding the dynamics of the zonal and meridional momentum budgets in the WRF simulation, including investigation of the vertically-integrated ABL momentum budget, the vertical structure of the forcing terms, and the momentum budgets in the crosswind and downwind directions. This work extended the analysis by Thum (2006). The vertical structure of the individual terms in the momentum budget were shown to be important to describe the dynamics of the ABL response to SST. Additionally, the separate roles of turbulent friction and surface stress in the SST-induced surface wind response was distinguished.

The difference in responses of the zonal and meridional momentum budgets to

SST was of particular interest in Chapter 4 to understand the SST-induced changes in wind direction. This was important in determining the dynamics associated with the differences in the curl and divergence responses to SST gradients.

Research Objective 4. *Why is the response of the meridional wind component to SST different than the zonal wind response?*

It was found that SST-induced surface heating creates air temperature gradients within the ABL, modifying the vertical structure of the horizontal winds through baroclinic changes in ABL structure. The effect of this SST-generated thermal wind shear modification is further investigated analytically using the two-layer boundary layer model of Samelson et al. (2006) (Appendix A). It is shown that the modeled meridional winds are strongly affected by thermal wind shear generated by small-scale SST gradients.

In addition, a statistical coupled wind-SST response model is proposed for use in ocean general circulation models (OGCMs) employing the statistical relations between the vorticity and divergence and the crosswind and downwind SST gradients observed in satellite wind and SST fields (Appendix B). A method of retrieving the SST-induced vector wind components from the crosswind and downwind SST gradients is outlined that can be used to simulate the small-scale vector wind response to the evolving SST field in OGCMs forced by low-resolution wind stress fields, e.g., the wind fields from operational numerical weather prediction models or the even lower resolution reanalysis wind fields. Investigation of the feedback onto the ocean from

small-scale SST perturbations may thus proceed without sophisticated coupled ocean-atmosphere models but using an observationally-based wind response. Preliminary OGCM analysis suggests that small-scale wind structure significantly effects ocean circulation. This statistical model therefore may of interest to those using coarse spatial resolution winds from numerical weather prediction model analyses fields to force OGCMs.

OBSERVATIONS OF SST-INDUCED PERTURBATIONS OF THE WIND STRESS FIELD OVER THE SOUTHERN OCEAN ON SEASONAL TIMESCALES

Larry W. O'Neill, Dudley B. Chelton, and Steven K. Esbensen

Journal of Climate

45 Beacon Street

Boston, MA 02108-3693

Vol. 16, 15 July 2003

Chapter 2

Abstract

The surface wind stress response to SST over the latitude range 30°S−60°S in the Southern Ocean is described from the QuikSCAT scatterometer observations of wind stress and Reynolds analyses of sea surface temperature (SST) during the 2-yr period August 1999 to July 2001. While ocean-atmosphere coupling at mid-latitudes has previously been documented from several case studies, this is the first study to quantify this relation over the entire Southern Ocean. The spatial structures of the surface wind perturbations with wavelengths shorter than 10° latitude by 30° longitude are closely related to persistent spatial variations of the SST field on the same scales. The wind stress curl and divergence shown to be linearly related, respectively, to the crosswind and downwind components of the SST gradient. The curl response has a magnitude only about half that of the divergence response. This observed coupling is consistent with the hypothesis that SST modification of marine atmospheric boundary layer (MABL) stability affects vertical turbulent mixing of momentum, inducing

perturbations in the surface winds. The non-equivalence between the responses of the curl and divergence to the crosswind and downwind SST gradients suggests that secondary circulations in the MABL may also play an important role by producing significant perturbations in the surface wind field near SST fronts that are distinct from the vertical turbulent transfer of momentum. The importance of the wind stress curl in driving Ekman vertical velocity in the open ocean implies that the coupling between winds and SST may have important feedback effects on upper ocean processes near SST fronts.

2.1 Introduction

The response of the near-surface wind field to underlying sea surface temperature (SST) gradients has been investigated in the eastern tropical Pacific in several recent studies from analyses of satellite observations of SST and wind stress (Chelton et al. 2001; Liu et al. 2000; Hashizume et al. 2001; Polito et al. 2001). The broad spatial coverage and high temporal resolution of the satellite data sets has allowed a quantitative test of the coupling between SST and surface winds hypothesized by Wallace et al. (1989) from climatological SST and wind data. Chelton et al. (2001) showed that this coupling is most clearly manifested in the wind stress curl and divergence fields, which were found to be linearly related to the crosswind and downwind components of the underlying SST gradient field, respectively. SST-induced perturbations of the wind stress, wind stress curl and wind stress divergence were also shown to travel along with the surface SST signatures of the westward propagating tropical instability waves (TIWs), providing statistically quantitative evidence of the rapid response of the near-surface wind field to the underlying spatially and temporally varying SST field. The eastern tropical Pacific analysis of Chelton et al. (2001) is extended in this study to investigate ocean-atmosphere coupling in regions of persistently strong SST gradients in the Southern ocean.

Some issues pose challenges in extending the analysis of Chelton et al. (2001) to the Southern Ocean. First, the lack of high-quality SST data over the Southern Ocean is a fundamental limitation due to sparse in situ sampling and biases in the

satellite infrared SST. Second, the very energetic synoptic variability in the winds over the Southern Ocean tends to obscure the presence of the coupling between SST and surface winds. To address these concerns, the analysis presented here is based upon three-month averages of the analyzed SST fields (Reynolds and Smith 1994) and QuikSCAT observations of surface wind stress.

Past observational and modeling studies of the effects of SST on near-surface winds are summarized in section 2.2. The data analyzed here and the motivation for using 3-month average wind stress and SST fields are described in Section 3. The details of the analysis methods are discussed in section 2.4. The results are presented in section 2.5 and discussed in section 2.6.

2.2 Background

Observations in mid-latitudes clearly show that air flowing across SST fronts experiences changes in the air-sea heat flux and vertical turbulent mixing. In an early observational study, Sweet et al. (1981) found that surface winds intensified over the warmer water of the Gulf Stream, producing a visibly rougher ocean surface compared to the colder water closer to the coast. Throughout a series of aircraft flights, they reported turbulent flying conditions over the warmer water on the seaward side of the Gulf Stream and smooth conditions over the colder slope water. Smooth ocean waves on the cold water surface and whitecaps on the warm water surface exemplified the change in surface wind conditions associated with the SST front. From vertical

profiles of atmospheric virtual potential temperature θ^* in the lower 610 m of the atmosphere, they showed that $\partial\theta^*/\partial z$ was positive over the colder water and negative over the warmer water, indicating stable and unstable conditions, respectively. Since stability influences vertical turbulent mixing through buoyancy, Sweet et al. (1981) suggested that the observed changes in wind speed across the front were caused by increased downward turbulent mixing of momentum from aloft to the surface over the warmer water. It is noteworthy that Sweet et al. (1981) found evidence of rising air over the warmer water and subsiding air over the cooler water in temperature and moisture patterns, suggestive of secondary circulations associated with the SST front.

Jury and Walker (1988) observed the same coupling between SST and surface winds from aerial surveys of the marine atmospheric boundary layer (MABL) across the the Agulhas Current south of Africa. Surface winds increased by 7 m s^{-1} in association with a 6°C change in SST over a distance of 400 km. They also found that turbulent momentum transfers over the warmer water were more efficient than over the colder water, reducing the magnitude of the vertical wind shear between the 70 m and 300 m levels.

Rouault and Lutjeharms (2000) further investigated the role of the SST on the overlying atmosphere south of Africa by measuring SST and atmospheric profiles of temperature, moisture and wind from a ship survey across an SST front associated with the Agulhas Return Current. Over the colder water, they found lower wind speeds, increased atmospheric stability and reduced air-sea heat fluxes compared

to the warmer water. From coincident ERS-1 scatterometer wind data, they also showed that the surface wind speed over a persistent warm-core eddy shed from the Agulhas Return Current was much higher than the wind speed over the surrounding colder water. Ship-based observations indicated that this occurred where the air-sea temperature difference created an unstable MABL, allowing increased vertical turbulent transport of momentum.

Mid-latitude coupling between winds and SST has also been recently observed over the Kuroshio Extension by Nonaka and Xie (2002). Weekly averages of wind speed anomalies were found to be positively correlated with SST anomalies using wind speed measurements from a combination of QuikSCAT scatterometer data, satellite microwave imagers and moored buoys. They also showed clear evidence that the wind speed anomalies propagated westward in phase with SST anomalies associated with westward propagating meanders in the Kuroshio.

While observations have consistently found that the near-surface winds depend strongly on SST-induced stabilization of the MABL, Hsu (1984) proposed that another mechanism also contributes to SST-induced wind variations over SST fronts. He showed analytically that temperature contrasts associated with SST fronts can induce secondary circulations perpendicular to the front, causing an acceleration of the surface winds across the front. Wai and Stage (1989) drew similar conclusions from a 2-dimensional numerical model study of the northern edge of the Gulf Stream. In their model, secondary circulations developed over the SST front with rising air

and low surface pressure over the warmer water and descending air and high surface pressure over the colder water. The associated cross-frontal surface pressure gradient was balanced by the vertical turbulent stress divergence. This balance caused the smallest surface wind stress to occur over the cold water; the wind stress increased across the front and then decreased gradually over the warm water.

Warner et al. (1990) obtained very similar results from a 3-dimensional mesoscale model study of the Gulf Stream using realistic SST patterns. They found that the increased surface winds associated with cross-frontal secondary circulations enhance the surface heat fluxes, which further reinforces the secondary circulations. The Gulf Stream observations of Sweet et al. (1981) are consistent with the secondary circulations and the associated pressure distribution found in the Wai and Stage (1989) and Warner et al. (1990) models.

Satellite observations in the tropical Pacific have documented the relationship between SST and surface winds in much greater detail than has been possible from ship-based observations. As SST modification of surface winds has been studied more extensively in the tropical Pacific than at mid-latitudes, we highlight here some important conclusions from the tropical Pacific that we believe have relevance to air-sea interaction in mid-latitudes.

The near-surface wind response to SST gradients is especially clear in the tropics because of the relatively weak signals of synoptic variability near the equator. Wallace et al. (1989) noted a weakening of the surface winds directly over the equatorial cold

tongue in climatological average surface winds and SST. Cross-equatorial southerly winds increased over the warmer water north of the cold tongue with intensity dependent on the strength of the temperature contrast between the cold tongue and the warmer water to the north. Apparently unaware of the Gulf Stream observations by Sweet et al. (1981), Wallace et al. (1989) hypothesized independently that the principal mechanism for changing the surface winds is the modification of the vertical wind shear in the MABL through turbulent vertical momentum transport.

To investigate the relationship between the TIW-induced perturbations of SST and the surface winds hypothesized by Wallace et al. (1989), Hayes et al. (1989) analyzed time series of winds and SST measured from the Tropical Ocean-Atmosphere (TAO) mooring array along 110°W at 2°N, the equator, and 2°S. Although the TAO mooring locations do not adequately resolve the zonal component of the surface wind divergence, Hayes et al. (1989) showed that latitudinal variations of the meridional component of the surface wind divergence correlated well with TIW-induced perturbations of the SST gradient field.

In the first satellite-based study of surface wind response to SST variability, Xie et al. (1998) showed that ERS-1 satellite scatterometer estimates of the 10 m surface wind field clearly resolved the coupling between TIW-induced perturbations of SST and surface winds. With the four-fold improvement in sampling (Schlax et al. 2001) and the presence of the well-developed cold tongue associated with the La Niña conditions after May 1998, QuikSCAT scatterometer observations of wind stress and

Tropical Rainfall Measuring Mission (TRMM) Microwave Imager (TMI) observations of SST more vividly depicted these SST-induced perturbations of the surface wind field during the first five months of the QuikSCAT mission (Chelton et al. 2001; Liu et al. 2000; Hashizume et al. 2001). SST modification of the MABL is also evident in satellite measurements of clouds, columnar-integrated water vapor, and precipitation (Deser et al. 1993; Xie et al. 1998; Hashizume et al. 2001; Hashizume et al. 2002). Satellite and *in situ* buoy measurements show the effect of SST perturbations on the surface heat fluxes (Thum et al. 2002).

From ship-based observations along 2°N during September 1999, Hashizume et al. (2002) concluded that sea level pressure anomalies were too small to force the observed TIW-induced wind anomalies in the eastern tropical Pacific. Consistent with the hypothesis of Wallace et al. (1989), Hashizume et al. (2002) found that SST perturbations associated with the TIWs modulated the vertical wind shear through changes in MABL stability. During the TIW cold phase, they observed that strong temperature stratification suppressed vertical mixing. During the warm phase, the reduced MABL static stability allowed generation of vertical turbulent mixing that weakened the vertical wind shear. In response to increased SST during the warm phase, Hashizume et al. (2002) also found that the MABL warmed uniformly throughout, deepened significantly and became capped by clouds. Due to the change in inversion height across the SST front, a dipole pattern of temperature anomalies developed vertically, with a warm anomaly below 1 km and a cold anomaly at the base of the

inversion down to 1 km (the inversion height was above 1 km for the duration of the cruise). Thus, a positive hydrostatic pressure anomaly occurred near the top of the MABL that was compensated by the negative hydrostatic pressure contribution from the warm layer below. Hashizume et al. (2002) found that the cancellation was almost complete from their soundings, reducing the sea level pressure anomalies expected for a MABL of constant depth.

The effects of sea level pressure anomalies in the equatorial Pacific were first investigated by Lindzen and Nigam (1987) using a simple one-layer model of the MABL. They proposed that variations in the MABL height across the cold tongue would reduce the sea level pressure gradient relative to what would occur within an MABL of constant depth. They further speculated that horizontal convergence and divergence of mass within the boundary layer modulate the hydrostatic pressure by changing the thickness of the MABL, with the ultimate effect of reducing the sea level pressure anomalies relative to those expected from an MABL with a rigid, flat top. The convergent mass would eventually exit the MABL into the bases of overlying cumulus clouds once the MABL reached a steady state. Since this mechanism reduces the cross-isotherm sea level pressure gradient from what would occur if the top of the MABL were rigid, Lindzen and Nigam (1987) describe this as a "back pressure" effect.

Hashizume et al. (2002) provided an alternative interpretation of the "back pressure" effect consistent with their observations of the MABL over the eastern tropical Pacific. They reconciled their TIW observations with the Lindzen and Nigam (1987)

model by suggesting that the hydrostatic effects of temperature anomalies near the MABL top due to the deepening and shallowing mixed layer compensate the effects of the warm and cool anomalies in the lower parts of the layer. Hashizume et al. (2002) propose that this compensation, rather than the horizontal mass adjustment hypothesized by Lindzen and Nigam (1987), causes the sea level pressure over the warmer water to be smaller than expected from thermal heating considerations alone. This effect decreases the pressure gradient between the SST anomalies associated with the TIWs, suggesting that the turbulent transfer of momentum may be the dominant mechanism in SST-induced surface wind variations.

These various studies show that SST fronts significantly alter the entire MABL, not just the surface wind field. The hypothesized mechansims for changes in the surface wind field in the vicinity of SST fronts include vertical turbulent transport of momentum from aloft to the surface and pressure-induced secondary circulations. It is not possible to distinguish between these two mechanisms without direct observations of the full 3-dimensional wind field and density structure of the MABL, which is currently not available over the Southern Ocean. This study therefore documents only the effects that SST fronts have on the surface wind stress field.

2.3 Data description

The wind stress and SST data analyzed here span the 2-yr period from 1 August 1999–31 July 2001, which corresponds to the first two complete years of the

QuikSCAT scatterometer mission. For this analysis, we consider the Southern Ocean region between the latitudes 30°S and 60°S. The wind stress and SST data are described in detail in this section.

The SeaWinds scatterometer onboard the QuikSCAT satellite infers surface wind stress magnitude and direction from measurements of microwave radar backscatter received from a given location on the sea surface at multiple antenna look angles (Freilich et al. 1994). Scatterometer wind stress retrievals are calibrated to the neutral-stability wind at a height of 10-m above the sea surface. The vector wind stress $\boldsymbol{\tau}$ is obtained from the 10-m neutral-stability wind $\mathbf{v}_{10}^N$ by $\boldsymbol{\tau} = \rho C_d^N \mathbf{v}_{10}^N |\mathbf{v}_{10}^N|$, where ρ is the air density and C_d^N is the neutral stability drag coefficient (e.g., Large and Pond 1981). The QuikSCAT measurements have a 25-km resolution over a single 1600-km swath centered on the satellite ground track.

In this analysis, the QuikSCAT wind stress measurements have been smoothed and interpolated onto a 1° latitude by 1° longitude spatial grid at 7-day intervals using a locally weighted regression (loess) smoother (Schlax et al. 2001) with filter cutoff wavelengths of 2° latitude by 4° longitude and a filter cutoff period of 15 days. This filtering is similar to 1.2° latitude by 2.4° longitude by 9-day block averages. Except in raining conditions, the atmosphere is nearly transparent at microwave frequencies. The persistent cloud cover over the Southern Ocean therefore does not degrade the accuracy of the scatterometer estimates of surface wind stress in non-precipitating conditions.

The accuracy of the QuikSCAT scatterometer measurements of 10-m winds has been extensively investigated by M. Freilich (2002, personal communication). Briefly, the QuikSCAT measurement accuracy is best characterized in terms of random component errors of the 10-m neutral stability vector wind retrievals (Freilich and Dunbar 1999). The measurement errors have been found to be less than 1 m s^{-1} for each orthogonal component with no significant dependence on wind speed. The wind speed accuracy is thus about 1.5 m s^{-1} over the full range of wind speeds, and the directional uncertainty decreases rapidly with increasing wind speed. Additionally, there is no evidence of systematic SST-dependent measurement errors in the QuikSCAT data.

Radar backscatter from sea ice results in large apparent wind speed, which causes spurious values of the derivative wind stress fields near the Antarctic ice edge. Wind stress and SST poleward of the northernmost extent of the sea ice over the 2-yr period were therefore eliminated from the analysis presented here. The sea ice edge information was provided by M. Freilich based on brightness temperature measurements by the Special Sensor Microwave Imager (SSM/I) flown onboard the Defense Meteorological Satellite Program satellites. The maximum extent of the sea ice boundary excluded from the 2-yr analysis period is shown in gray in Fig. 2.1.

The analysis of ocean-atmosphere coupling in the eastern tropical Pacific by Chelton et al. (2001) utilized the Tropical Rainfall Measuring Mission (TRMM) Microwave Imager (TMI) for all-weather measurements of SST. Because of the low inclination of

the TRMM satellite orbit, the TMI measures SST only in the latitude range between 38°S and 38°N. Most of the Southern Ocean region of interest here lies south of 38°S. Satellite microwave measurements of SST will soon become available at these higher latitudes with the recent launch of an Advanced Microwave Scanning Radiometer (AMSR) on the EOS-Aqua satellite launched in April 2002 and a second AMSR on the Advanced Earth Observing Satellite-II (ADEOS-II) launched in December 2002. Since microwave measurements of SST are not yet available for the Southern Ocean, the present study uses SST fields produced by the National Oceanic and Atmospheric Administration (NOAA) based on the optimum interpolation technique described by Reynolds and Smith (1994).

The so-called Reynolds weekly average SST analyses blend all available in situ moored buoy and ship observations of SST with satellite infrared SST observations from the Advanced Very High Resolution Radiometer (AVHRR) on the NOAA series of polar orbiting satellites. The SST analyses first apply the blending technique described in Reynolds (1988) and Reynolds and Marsico (1993) using input fields of in situ and AVHRR SST data. The blending effectively uses satellite SST data to define the SST gradient field in regions with sparse in situ data. The final SST fields are then obtained by adjusting the gradient fields to the in situ SST observations to remove large-scale biases in the satellite data. This blending technique results in a degradation of the spatial resolution to roughly 6° latitude by 6° longitude (Reynolds and Smith, 1994).

In order to improve the resolution of the SST analyses, Reynolds and Smith (1994) used optimum interpolation (OI) to attempt to preserve the resolution capabilities of the satellite infrared SST. The OI technique described by Reynolds and Smith (1994) first uses the coarse resolution SST fields derived from the blending to provide a large-scale correction to the satellite SST retrievals. The SST estimates are obtained from the OI analysis of in situ and corrected satellite SST data on a 1° latitude by 1° longitude spatial grid. OI apparently allows improved spatial resolution of SST over the blended fields while retaining the benefit of bias reduction in the satellite measurements provided by the blending technique.

Two main problems affect the quality of the Reynolds SST analyses in the Southern Ocean. The first is sparse AVHRR sampling owing to persistent cloud coverage, where the annual mean cloud amount exceeds 75% over the Southern Ocean region of interest in this study (Rossow and Schiffer 1991; Hahn et al. 1995). The second is sparse in situ sampling because of the small number of standard shipping routes poleward of 30°S. The sparse sampling of both datasets raises serious concerns about the quality of the Reynolds SST analyses in the Southern Ocean region. In situ sampling is especially poor at the highest southern latitudes, where Antarctic resupply ships crossing the ACC during the austral summer provide nearly all of the yearly *in situ* SST measurements poleward of 50°S.

Reynolds and Marsico (1993) noted another problem affecting the blending technique in vast areas of the Southern Ocean. Differences between the AHVRR day and

night cloud detection algorithms cause a warm bias in the averages of the satellite SST retrievals. Greater confidence is instilled in the daytime cloud screen, which uses both visible and infrared satellite observations to identify clouds; the daytime cloud screen accepts 3 times more observations than the nighttime cloud screen, which is based only on infrared satellite observations. Reynolds and Marsico (1993) suggest that the resulting SST estimates are not representative of the average daily SST, but are biased towards the more numerous and warmer daytime temperatures, thus resulting in SST estimates that were too warm over much of the Southern Ocean.

In an attempt to reduce the bias in the satellite SSTs, Reynolds and Marsico (1993) include the assimilation of sea-ice data from the U.S. Meteorological Center to estimate the physical location of the sea-ice boundary. At the ice edge, they imposed an external boundary condition in the blending algorithm that set the SST to $-1.8°C$, which is the freezing temperature of seawater at a salinity of 32.86 psu. The inclusion of this ice edge temperature as a boundary condition in the blended analyses reduces the warm bias over large portions of the Southern Ocean. The assumption of an SST value of $-1.8°C$ at the ice edge is likely to be adequate during freezing conditions. However, during the melt season and in regions of low ice concentrations, this assumption may lead to an underestimation of the SST by several tenths of a degree Celsius, since freshwater stratifies the surface sea water, leading to a heating of only a very thin layer at the surface. Uncertainty in the precise location of the ice edge will also cause uncertainty in the SST.

Despite the limitations summarized above, the Reynolds SST analyses provide the best SST estimates presently available poleward of 38°S. In an attempt to assess the quality of these SST fields, the root mean squared (RMS) differences between weekly averaged TMI SST and the Reynolds weekly average SST analyses are shown in Fig. 2.1. The largest differences occur near the highest latitudes sampled by the TMI. Some of these differences may be attributable to errors in the TMI SST (Stammer et al. 2002); however, most are likely due to errors in the Reynolds SST analyses and from the spatial smoothing inherent in the Reynolds blending algorithm as summarized above. This is especially a concern in the Southern Ocean region of interest here, since the RMS difference exceeds 0.7°C poleward of 30°S where in situ SST data are sparse and the nearly ubiquitous cloud cover masks the infrared satellite SST retrievals. As discussed by Emery et al. (2001), there is a legitimate and pressing need for a comprehensive SST validation program, particularly in the region poleward of 30°S.

To mitigate the random errors that surely exist in the Reynolds SST analyses, the weekly analyses were averaged here in overlapping 3-month blocks at monthly intervals from 1 August 1999–31 July 2001 for the latitude band 30°S to 60°S. The overall average over this 2-yr period is contoured in Fig. 2.2a. Contours of the climatological average dynamic height relative to 1000 m depth from Levitus and Boyer (1994) are overlaid on the 2-yr average SST in Fig. 2.2b. Over the geographical region shown in this figure, the correlation between the 2-yr average SST and climatological

average dynamic height is 0.91. The close agreement between these two fields implies that isotherms in the Reynolds SST analyses closely correspond to streamlines of the large-scale mean surface flow of the Antarctic Circumpolar Current (ACC) as represented by the climatological average dynamic height. The average Reynolds SST analyses evidently resolve most of the features of the mean surface circulation. The large, steady meanders in the flow result from the interactions between the mean current and bathymetry and are relatively stationary (Chelton et al. 1990). Moreover, the 2-yr averaging period considered here is evidently representative of long-term climatological average conditions in the Southern Ocean.

To be consistent with the smoothed Reynolds SST fields analyzed here, the QuikSCAT wind stress fields were averaged in overlapping 3-month blocks at monthly intervals over the same 2-yr period from 1 August 1999–31 July 2001. The vector average wind stress field measured from QuikSCAT over the 2-yr period is overlaid on the 2-yr average Reynolds SST in Fig. 2.2c. The wind stress vectors are predominately westerly as expected within this latitude band in proximity to the Southern Hemisphere mid-latitude surface westerly wind maximum. It is significant to note that the winds blow obliquely across the meandering isotherms in many places throughout the Southern Ocean. This provides ample opportunity to investigate whether wind stress curl and divergence perturbations occur in association with the underlying SST gradient field as observed by Chelton et al. (2001) in the eastern tropical Pacific.

2.4 Methods

2.4.1 Geometric relation between the wind stress and SST gradient vectors

The total SST gradient vector can be decomposed into local crosswind and downwind components. In vector notation, the cross product $(\nabla T \times \hat{\boldsymbol{\tau}}) \cdot \hat{\boldsymbol{k}} = |\nabla T| \sin\theta$ represents the crosswind component, where T is the SST, $\hat{\boldsymbol{\tau}}$ is a unit vector in the direction of the wind stress, $\hat{\mathbf{k}}$ is a unit vector in the vertical direction, and θ is the counterclockwise angle between the vectors ∇T and $\hat{\boldsymbol{\tau}}$. The vector dot product $\nabla T \cdot \hat{\boldsymbol{\tau}} = |\nabla T| \cos\theta$ is the projection of ∇T onto $\hat{\boldsymbol{\tau}}$ and represents the downwind component of the SST gradient.

As summarized in section 2.2, previous observations have found that the wind stress magnitude changes across SST fronts in response to changes in surface forcing caused by spatial gradients in SST. A schematic of winds blowing obliquely across a hypothetical SST front is shown in Fig. 2.3. When the crosswind SST gradient is non-zero, the lateral (crosswind) gradient of wind stress that develops as the winds increase over the warmer water results in a non-zero wind stress curl. Likewise, when the downwind SST gradient is non-zero, the longitudinal (downwind) deceleration or acceleration of the wind stress across the front results in a non-zero convergence or divergence. The wind stress curl and divergence should therefore depend, respectively, on the magnitudes of the crosswind and downwind SST gradients.

At $\theta = 0°$, the wind blows across isotherms (parallel to the SST gradient) towards warmer water. The increased wind sress over the warmer water should result in a maximum in the divergence, while the curl should vanish. At $\theta = 180°$, there should be a maximum convergence and zero wind stress curl. Conversely, at $\theta = 90°$, the wind blows along isotherms (perpendicular to the SST gradient) with warmer water to the right of the wind and colder water to the left. In response, a maximum positive wind stress curl should develop, while the divergence should vanish. At $\theta = 270°$, there should be a maximum negative wind stress curl and zero divergence. These anticipated relations between the derivative wind stress fields and the SST gradient field are investigated quantitatively in Section 5.

2.4.2 Spatial filtering of the wind stress fields

Confirmation of the hypothesized relations between the derivative wind stress fields and the angle between the wind stress and the SST gradient requires the removal of other signals in the wind field that are unrelated to the SST field. At the high southern latitudes of interest in this study, energetic synoptic-scale weather disturbances and the large-scale transverse gradient of the mid-latitude mean westerly wind maximum dominate the wind stress curl field, masking perturbations that may exist in association with the SST gradients. The influence of transient synoptic-scale weather disturbances is mostly eliminated in the 3-month averages considered here. The influence of the large-scale background wind stress curl is evident in the 2-yr

average wind stress curl field shown in the top panel of Fig. 2.4. The westerly wind varies meridionally and is maximum along the approximate axis of the ACC. The decrease of the westerly winds equatorward and poleward of this westerly wind maximum result in positive and negative wind stress curl on the north and south sides of the maximum, respectively. Removal of the strong curl associated with the mean westerly winds by spatial high-pass filtering is necessary to isolate the SST-induced perturbations of the wind stress curl field that are of interest here.

The large-scale wind stress curl field obtained by applying a spatial low-pass filter to isolate variability with wavelengths longer than 10° latitude by 30° longitude is shown in the middle panel in Fig. 2.4. Although these filter cutoff wavelengths are roughly equivalent to those of simple 6° latitude by 18° longitude block averages, the 2-dimensional loess smoother used here has a more desirable filter transfer function (see Fig. 1 of Chelton and Schlax 2003). The precise choice of the filter cutoff wavelengths does not greatly influence the results of the analysis presented here.

Fig. 2.4 (bottom) shows the 2-yr average spatially high-pass filtered curl fields obtained by subtracting the 10° by 30° spatially smoothed curl field from the unfiltered curl field, thus retaining spatial variability with wavelengths shorter than 10° latitude by 30° longitude but longer than the 2° by 4° wavelengths of the original smoothed wind stress fields. It is apparent that the high-pass filtered curl field is most intense and spatially variable within a band centered along the axis of the ACC where SST gradients are strong (see the contours in Fig. 2.4). Away from the ACC, the magni-

tudes of the short-scale curl perturbations are small. Visually, the magnitudes of the short-scale wind stress curl signals are as strong as the large-scale curl shown in the middle panel of Fig. 2.4. The implications this has on the local ocean circulation are discussed in section 2.6.

The 2-yr average wind stress divergence and SST fields for the Southern Ocean are shown in the top panel in Fig. 2.5. Like the curl, the divergence exhibits patchy spatial variability within the band of strong SST gradients centered on the axis of the ACC. The middle panel shows the spatially low-pass filtered divergence field, which was obtained in the same way as the large-scale curl field in the middle panel of Fig. 2.4. In contrast with the curl field, the magnitude of the spatially low-pass filtered divergence is small everywhere, reflecting the inherent tendency for the wind stress field to be nearly non-divergent. Consequently, the spatially high-pass filtered wind stress divergence in the bottom panel of Fig. 2.5 differs little from the unfiltered wind stress divergence in the top panel.

The spatial high-pass filtering shown in the bottom panels of Figs. 2.4 and 2.5 for the 2-year average from 1 Aug 1999–31 Jul 2001 was applied to each of the overlapping 3-month average curl and divergence fields for the analyses in section 2.5. These spatially high-pass filtered curl and divergence fields are referred to hereafter as the perturbation wind stress curl and divergence.

The crosswind and downwind SST gradient fields were spatially high-pass filtered in the same manner as the wind stress curl and divergence fields. In vector nota-

tion, $(\nabla T \times \hat{\boldsymbol{\tau}})' \cdot \hat{\mathbf{k}}$ and $(\nabla T \cdot \hat{\boldsymbol{\tau}})'$ denote the spatially high-pass filtered crosswind and downwind SST gradients, respectively. These represent the contributions of the SST gradient field hypothesized to induce the perturbations in the wind stress curl and divergence fields under investigation in this study. Since the perturbation wind stress curl and divergence are expected to depend on the perturbation crosswind and downwind SST gradients, they should depend, respectively, on the sine and cosine of the perturbation angle defined by

$$\theta' = \tan^{-1}\left[\frac{(\nabla T \times \hat{\boldsymbol{\tau}})' \cdot \hat{\mathbf{k}}}{(\nabla T \cdot \hat{\boldsymbol{\tau}})'}\right]. \tag{2.1}$$

2.5 Results

The perturbation curl and divergence fields for the Southern Ocean were binned as functions of the perturbation angle θ' defined by Eqn. 2.1 for each of the 11 overlapping 3-month average fields over the 2-year period 1 Aug 1999–31 Jul 2001. The overall averages within each bin are shown as the points in Fig. 2.6. The error bars represent ± 1 standard deviation of the means within each bin computed from the 11 individual 3-month averages. As in the tropical study by Chelton et al. (2001), the Southern Ocean QuikSCAT perturbation curl and divergence fields agree remarkably well with the expected sine and cosine dependencies on θ'. The solid curves represent least-square fits of a sine and cosine to the overall binned averages. The perturbation curl is maximum when the wind vector is perpendicular to the SST gradient (parallel

to isotherms) and zero when the wind vector is parallel to the SST gradient (perpendicular to isotherms). Likewise, it is apparent that the perturbation divergence or convergence is approximately largest when the wind vector is oriented parallel to the SST gradient (perpendicular to isotherms) and approximately zero when the wind vector is oriented perpendicular to the SST gradient (parallel to isotherms).

An interesting feature of the perturbation divergence dependence on θ' is that the sinusoidal variation of the divergence is shifted slightly relative to a pure cosine. The wind stress divergence is maximum when the wind direction is 23° clockwise relative to the SST gradient. This is discussed further in section 2.6.

While the relationships shown in Fig. 2.6 clarify the dependencies of the perturbation curl and divergence fields on the perturbation angle θ', the magnitude of the curl and divergence responses to a given SST gradient cannot be inferred from these binned averages as a function of θ'. The perturbation curl and divergence binned as a function of the perturbation crosswind and downwind components of the SST gradient, respectively, are shown in Fig. 2.7. The perturbation curl and divergence exhibit linear, positive trends with the perturbation crosswind and downwind SST gradient, respectively, consistent with the hypothesis discussed in 2.4 and with the results found in the eastern tropical Pacific by Chelton et al. (2001). The solid line represents a linear least-squares fit to the binned averages. Probably coincidentally, the slope of the lines in Fig. 2.7, denoted here as the coupling coefficient α_C for the curl and α_D for the divergence, are quite close to those obtained between 3°N and

1°S in the eastern tropical Pacific by Chelton et al. (2001) (see Table 2.1). Notably, α_D is about double the value of α_C in both regions.

2.6 Discussion and conclusions

The coupling between SST and the lower atmosphere has been studied extensively in the eastern tropical Pacific (e.g., Wallace et al. 1989; Hayes et al. 1989; Xie et al. 1998; Liu et al. 2000; Chelton et al. 2001; Hashizume et al. 2001; Polito et al. 2001). Several case studies based on in situ observations (Sweet et al. 1981; Jury and Walker 1988; Rouault and Lutjeharms 2000) and on satellite scatterometer data (Rouault and Lutjeharms 2000) have documented a similar coupling in mid-latitudes. Nonaka and Xie (2002) have recently shown from QuikSCAT data that this air-sea interaction also exists over the Kuroshio Extension. The present study is the first to quantify this coupling statistically over the entire Southern Ocean, which encompasses nearly 25% of the world ocean. The emerging view that ocean-atmosphere coupling is a globally important phenomenon is only becoming fully appreciated with the availability of the multi-year data record of spatially and temporally dense observations of surface winds from the QuikSCAT scatterometer.

At the present time, the only SST fields available for investigation of SST perturbations of surface winds at latitudes higher than 38°S are the Reynolds SST analyses produced by NOAA (Reynolds and Smith 1994). As summarized in section 2.3, these SST fields are unquestionably the weakest part of the present analysis, although tem-

porally averaging the Reynolds SST analyses over 3-month periods for the analysis presented here addresses some of the concerns about their accuracies over the Southern Ocean. The high correlation between the 2-yr average SST field and the long-term average dynamic height field engenders confidence that the Reynolds SST analyses are adequate in sufficiently long term temporal averages. The existence of persistent meanders in the flow of the ACC and in the associated SST field thus allow an investigation of the effects of SST on the 2-yr mean wind stress fields observed by QuikSCAT.

The spatially high-pass filtered wind stress and SST fields used in this study isolate the short-scale perturbations of interest here with zonal and meridional wavelengths shorter than 10° of latitude by 30° of longitude and longer than 2° latitude by 4° longitude. The spatial variability in the spatially high-pass filtered derivative wind stress fields considered here is largest within a broad band centered along the axis of the ACC between 40°S and 50°S. The spatial structures of these perturbation derivative wind stress fields were shown to be remarkably closely related to the perturbations of the SST field throughout the Southern Ocean.

The surface observations analyzed here cannot elucidate the details of the boundary layer dynamics and thermodynamics of SST modification of low-level winds. However, the observed coupling is consistent with the hypothesis of Sweet et al. (1981) and Wallace et al. (1989) that SST modification of the MABL produces changes in stability that cause variations in the surface winds through vertical turbulent transfer

of momentum to the surface.

The magnitudes of small-scale variability in the wind stress curl field are qualitatively seen from the bottom and middle panels of Fig. 2.4 to be comparable to the magnitudes of the background large-scale curl field itself. To quantify the effects that this has on the upper ocean, histograms of the wind stress curl-induced Ekman pumping velocity were calculated separately from the spatially high-pass filtered and spatially low-pass filtered 2-yr average curl fields (Fig. 2.8). Though shifted to have zero mean value, the dynamic range of values of the Ekman pumping velocity calculated from the perturbation curl field is nearly the same as that of the background large-scale curl field. The perturbation curl field associated with the persistent perturbation crosswind temperature gradients therefore produces a local ocean response comparable to that associated with the large-scale wind forcing. This suggests a coupling whereby SST gradients drive an atmospheric response that feeds back on the SST through Ekman pumping. Modeling studies are needed to determine whether this feedback tends to reinforce or reduce the SST gradient that is responsible for the perturbations of the wind stress curl field. The steady short-scale variability of the Ekman pumping field may also have locally significant biological consequences that merit detailed investigation.

It was noted in section 2.5 that the magnitude of the coupling between the perturbation wind stress curl field and the underlying SST field is somewhat weaker than that of the perturbation wind stress divergence (see Table 2.1). This was also found

to be the case in the eastern tropical Pacific (Chelton et al. 2001). The difference between the magnitudes of the coupling coefficients α_C and α_D suggests that a different combination of mechanisms could be responsible for the perturbation divergence response to downwind SST gradients than for the perturbation curl response to crosswind SST gradients. Without knowledge of the full 3-dimensional wind and density fields in the MABL, we can only speculate about the mechanisms responsible for the different coupling coefficients.

One possible explanation for the stronger response of the wind stress divergence to the downwind SST gradient compared with the wind stress curl response to the crosswind SST gradient is the finite time scale of boundary layer adjustment to the surface SST boundary condition. For flow across an SST front, a parcel of air experiences a continually changing SST boundary condition. Convective and turbulent fluxes are therefore not able to reach their equilibrium values. As suggested by Chelton et al. (2001), this would result in divergence or convergence that is stronger than would be the case for an equilibrated boundary layer structure. In the case of flow along an SST front, the weak downwind SST gradient may allow sufficient time for equilibration adjustment of the boundary layer, thus resulting in a wind stress curl that is weaker than would be the case for a non-equilibrated boundary layer. Thum et al. (2002) found strong evidence that a disequilibrium boundary layer is responsible for a spatial shift between the surface heat fluxes and perturbation SSTs associated with TIWs in the eastern tropical Pacific.

Because scatterometers measure the wind stress relative to the moving sea surface (Cornillon and Park 2001; Kelly et al. 2001), ocean surface currents could also contribute to some of the apparent difference between the response of the perturbation wind stress divergence and curl fields to underlying perturbations in the SST field. Without coincident surface current observations, the effects that surface ocean currents have on the wind stress field cannot be directly quantified. Surface ocean currents in the Southern Ocean can easily be as strong as 0.5 m s^{-1}, which is a sizable fraction of the typical perturbation surface wind speed of ~2-3 m s^{-1} in this region. The high correlation between the dynamic height and the SST fields implies that the surface ocean currents would most significantly affect the wind stress curl, which is strongest when the wind blows parallel to isotherms (i.e., parallel to the flow). Ocean currents would thus reduce the wind stress curl response to the crosswind SST gradients as observed from QuikSCAT, leading to smaller values of α_C.

The observational and modeling studies summarized in section 2.2 suggest a third possible mechanism for the difference between α_C and α_D. The increase of winds at the ocean surface is likely attributable to a mixture of the vertical turbulent transfer of momentum and the effects of secondary circulations across SST fronts. The turbulent transfer mechanism should produce equal responses in the curl and divergence fields to crosswind and downwind SST gradients. In contrast, secondary circulations would have little or no effect on the wind stress curl since the surface winds associated with the secondary circulations would be oriented in the cross-frontal direction. This

efficaciously augments the effects of the SST gradient on the wind stress divergence relative to the wind stress curl. Surface air blowing obliquely across an SST front would accelerate more across the front than along it, leading to a larger wind stress divergence than wind stress curl for a given downwind SST gradient, thus explaining at least part of the larger values of α_D compared with α_C.

We again note the existence of what we believe is a significant clockwise rotation of about 23° between the binned values of the perturbation divergence and the perturbation angle θ' in the top panel of Fig. 2.6. Chelton et al. (2001) found no evidence of such a rotation over the eastern equatorial Pacific. It is noteworthy that there is no evidence of a systematic phase shift between the binned values of the perturbation curl and the expected sine dependence on θ' (see the bottom panel of Fig. 2.6). The physical reason for the rotation in the divergence over the Southern Ocean is not yet clear. As shown in Fig. 2.9, it is linked to a negative, linear relation between the perturbation wind stress divergence and the perturbation crosswind SST gradient. It is conceivable that the crosswind SST gradient sets up a cross-frontal pressure gradient that causes a cross-frontal acceleration of the wind stress over the front. This contribution to the divergence could also arise from secondary circulations forcing an increase in cross-frontal winds as air flows along isotherms that perhaps influences the divergence more than the curl, thus resulting in the 23° rotation in the top panel of Fig. 2.6. Further observational, analytical, and modeling studies are needed to fully understand this observation.

We close by reemphasizing our concern about the accuracies of the Reynolds SST fields. From a preliminary analysis of SST data from the AMSR on the EOS-Aqua satellite, the SST gradients within a broad band centered on the ACC are significantly underestimated in the Reynolds SST fields. The actual coupling between SST and the overlying wind stress field is therefore stronger than has been deduced here from the QuikSCAT winds and the Reynolds SST analyses. This bias will be quantified in future work as the AMSR data record continues to accumulate.

Acknowledgments. We thank Michael Freilich for the QuikSCAT data and the ice field information and Michael Schlax for producing the smoothed QuikSCAT and Reynolds SST fields used in this study and for many helpful discussions throughout the course of this study. We also thank Michael Freilich for providing detailed helpful comments on this manuscript. The research presented in this paper was supported by NASA grant NAS5-32965 for funding of Ocean Vector Winds Science Team activities and grant NA96GP0368 from the NOAA Office of Global Programs.

References

Chelton, D. B., M. G. Schlax, D. L. Witter, and J. G. Richman, 1990: Geosat altimeter observations of the surface circulation of the Southern Ocean. *J. Geo. Res.*, **95**, 17 877-17 904.

Chelton, D. B., and M. G. Schlax, 2003: The accuracies of smoothed sea surface height fields constructed from tandem altimeter datasets. *J. Atmos. Oceanic Technol.*, **20**, 1276-1302.

Chelton, D. B., S. K. Esbensen, M. G. Schlax, N. Thum, M. H. Freilich, F. J. Wentz, C. L. Gentemann, M. J. McPhaden and P. S. Schopf, 2001: Observation of coupling between surface wind stress and sea surface temperature in the eastern tropical Pacific. *J. Climate*, **14**, 1479-1498.

Cornillon, P., and K.-A. Park, 2001: Warm core ring velocities inferred from NSCAT. *Geophys. Res. Lett.*, **28**, 575–578.

Deser, C., J. J. Bates, and S. Wahl, 1993: The influence of sea surface temperature on stratiform cloudiness along the equatorial front in the Pacific Ocean. *J. Climate*, **6**, 1172-1180.

Emery, W. J., S. Castro, G. A. Wick, P. Schluessel, and C. J. Donlon, 2001: Estimating sea surface temperature from infrared satellite and in situ temperature data. *Bull. Amer. Meteor. Soc.*, **82**, 2773-2784.

Freilich, M. H., D. G. Long, and M. W. Spencer, 1994: SeaWinds: A Scanning Scatterometer for ADEOS II - Science Overview. *Proc. Int. Geosci. Rem. Sens. Symposium*, Pasadena, California, August 8-12, 960-963.

Freilich, M. H., and R. S. Dunbar, 1999: The accuracy of the NSCAT-1 vector winds: Comparisons with National Data Buoy Center buoys. *J. Geophys. Res.*, **104**, 11 231-11 246.

Hahn, C. J., S. G. Warren, and J. London, 1995: The effect of moonlight on observation of cloud cover at night, and application to cloud climatology. *J. Climate*, **8**, 1429-1446.

Hashizume, H., S.-P. Xie, W. T. Liu, and K. Takeuchi, 2001: Local and remote atmospheric response to tropical instability waves: a global view from space. *J. Geophys. Res.*, **106**, 10 173-10 185.

Hashizume, H., S.-P. Xie, M. Fujiwara, M. Shiotani, T. Watanabe, Y. Tanimoto, W. T. Liu, and K. Takeuchi, 2002: Direct observations of atmospheric boundary layer response to slow SST variations over the eastern equatorial Pacific. *J. Climate*, **15**, 3379-3393.

Hayes, S. P., M. J. McPhaden, and J. M. Wallace, 1989: The influence of sea surface temperature on surface wind in the eastern equatorial Pacific: Weekly to monthly variability. *J. Climate*, **2**, 1500-1506.

Hsu, S. A., 1984: Sea-breeze-like winds across the north wall of the Gulf Stream: An analytical model. *J. Geophys. Res.*, **89**, 2025-2028.

Jury, M. R., and N. Walker, 1988: Marine boundary layer modification across the edge of the Agulhas Current. *J. Geophys. Res.*, **93**, 647-654.

Jury, M. R., 1993: A thermal front within the marine atmospheric boundary layer over the Agulhas Current south of Africa: Composite aircraft observations. *J. Geophys. Res.*, **99**, 3297-3304.

Kelly, K. A., S. Dickinson, M. J. McPhaden and G. C. Johnson, 2001: Ocean currents evident in satellite wind data. *Geophys. Res. Lett.*, **28**, 2469–2472.

Large, W. G., and S. Pond, 1981: Open ocean momentum flux measurements in moderate to strong winds. *J. Phys. Oceanogr.*, **11**, 324-336.

Levitus, S., and T. P. Boyer, 1994: *World Ocean Atlas 1994.* Vol. 4: *Temperature: NOAA Atlas NESDIS 3,* U.S. Government Printing Office, 117 pp.

Lindzen, R. S, and S. Nigam, 1987: On the role of sea surface temperature gradients in forcing low-level winds and convergence in the tropics. *J. Atmos. Sci.*, **44**, 2418-2436.

Liu, W. T., X. Xie, P. S. Polito, S.-P. Xie, and H. Hashizume, 2000: Atmospheric manifestation of tropical instability waves observed by QuikSCAT and Tropical Rain Measuring Mission. *Geophys. Res. Lett.*, **27**, 2545-2548.

Nonaka, M., S.-P. Xie, 2002: Co-variations of sea surface temperature and wind over the Kuroshio and its extension: Evidence for ocean-to-atmosphere feedback. *J. Climate*, **16**, 1404-1413.

Reynolds, R. W., 1988: A real-time global sea surface temperature analysis. *J. Climate*, **1**, 75-86.

Reynolds, R. W., and D. C. Marsico, 1993: An improved real-time global sea surface temperature analysis. *J. Climate*, **6**, 114-119.

Reynolds, R. W., and T. M. Smith, 1994: Improved global sea surface temperature analyses using optimum interpolation. *J. Climate*, **7**, 929-948.

Polito, P. S., J. P. Ryan, T. W. Liu, and F. P. Chavez, 2001: Oceanic and atmospheric anomalies of tropical instability waves. *Geophys. Res. Lett.*, **28**, 2233-2237.

Rossow, W. B., and R. A. Schiffer, 1991: ISCCP cloud data products. *Bull. Amer. Meteor. Soc.*, **72**, 2-20.

Rouault, M., and J. R. E. Lutjeharms, 2000: Air-sea exchange over an Agulhas eddy at the subtropical convergence. *Global Atm. Oc. Sys.*, **7**, 125-150.

Schlax, M. G., D. B. Chelton, and M. H. Freilich, 2001: Sampling errors in wind fields constructed from single and tandem scatterometer datasets. *J. Atmos. Oceanic Technol.*, **18**, 1014-1036.

Stammer, D., F. Wentz and C. Gentemann, 2002: Validation of microwave sea surface temperature measurements for climate purposes. *J. Climate*, **16**, 73-87.

Sweet, W. R., R. Fett, J. Kerling, and P. LaViolette, 1981: Air-sea interaction effects in the lower troposphere across the north wall of the Gulf Stream. *Mon. Wea. Rev.*, **109**, 1042-1052.

Thum, N., S. K. Esbensen, D. B. Chelton, and M. J. McPhaden, 2002: Air-sea heat exchange along the northern sea surface temperature front in the Eastern Tropical Pacific. *J. Climate*, **15**, 3361-3378.

Wai, W. M., and S. A. Stage, 1989: Dynamical analysis of marine atmospheric boundary layer structure near the Gulf Stream oceanic front. *Quart. J. Roy. Meteor. Soc.*, **115**, 29-44.

Wallace, J. M., T. P. Mitchell, and C. Deser, 1989: The influence of sea surface temperature on surface wind in the eastern equatorial Pacific: Seasonal and interannual variability. *J. Climate*, **21**, 1492-1499.

Warner, T. T., M. N. Lakhtakia, J. D. Doyle, and R. A. Pearson, 1990: Marine atmospheric boundary layer circulations forced by Gulf Stream sea surface temperature gradients. *Mon. Wea. Rev.*, **118**, 309-323.

Xie, S.-P., M. Ishiwatari, H. Hashizume, and K. Takeuchi, 1998: Coupled ocean-atmosphere waves on the equatorial front. *Geophys. Res. Lett.*, **25**, 3863-3866.

Table 2.1: The coupling coefficients computed in this analysis over the Antarctic Circumpolar Current (ACC) and the values computed by Chelton et al. (2001) over the eastern tropical Pacific (ETP) during the period 21 Jul 21–20 Oct 1999. The coupling coefficient α_D represents the linear relation between the wind stress divergence and the downwind component of the SST gradient (Fig. 2.7a). The coupling coefficient α_C represents the linear relation between the wind stress curl and the crosswind component of the SST gradient (Fig. 2.7b). The units are in N $m^{-2}\,°C^{-1}$ $\times 100$.

Location	α_D	α_C
ACC	1.24	0.68
ETP (1°S to 5°S)	2.47	1.12
ETP (3°N to 1°S)	1.35	0.75

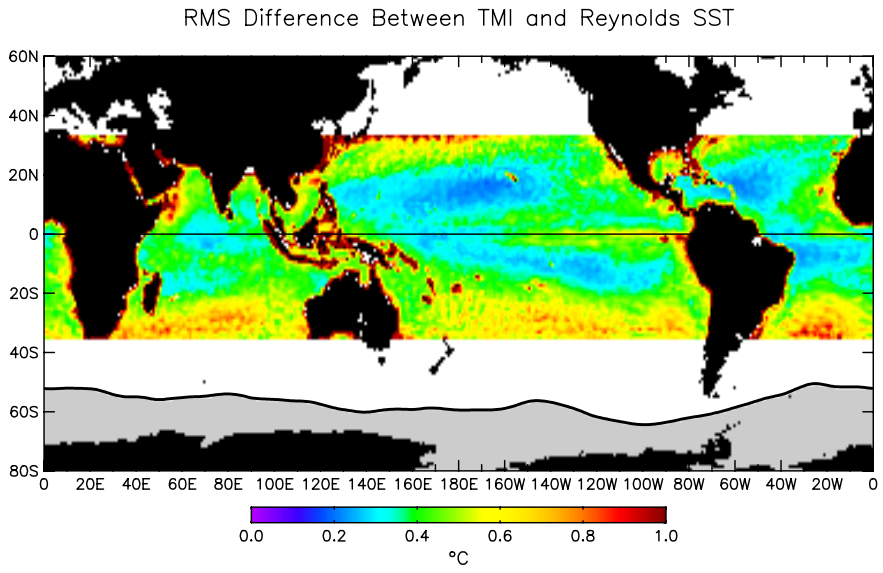

Figure 2.1: A global map of the root-mean-squared (rms) difference between the weekly averaged TMI SST and the weekly averaged Reynolds SST analyses. Also shown is the northernmost extent of the Antarctic sea ice over the analysis region for the period 1 Aug 1999–31 Jul 2001. The area masked from the analysis in shaded in gray.

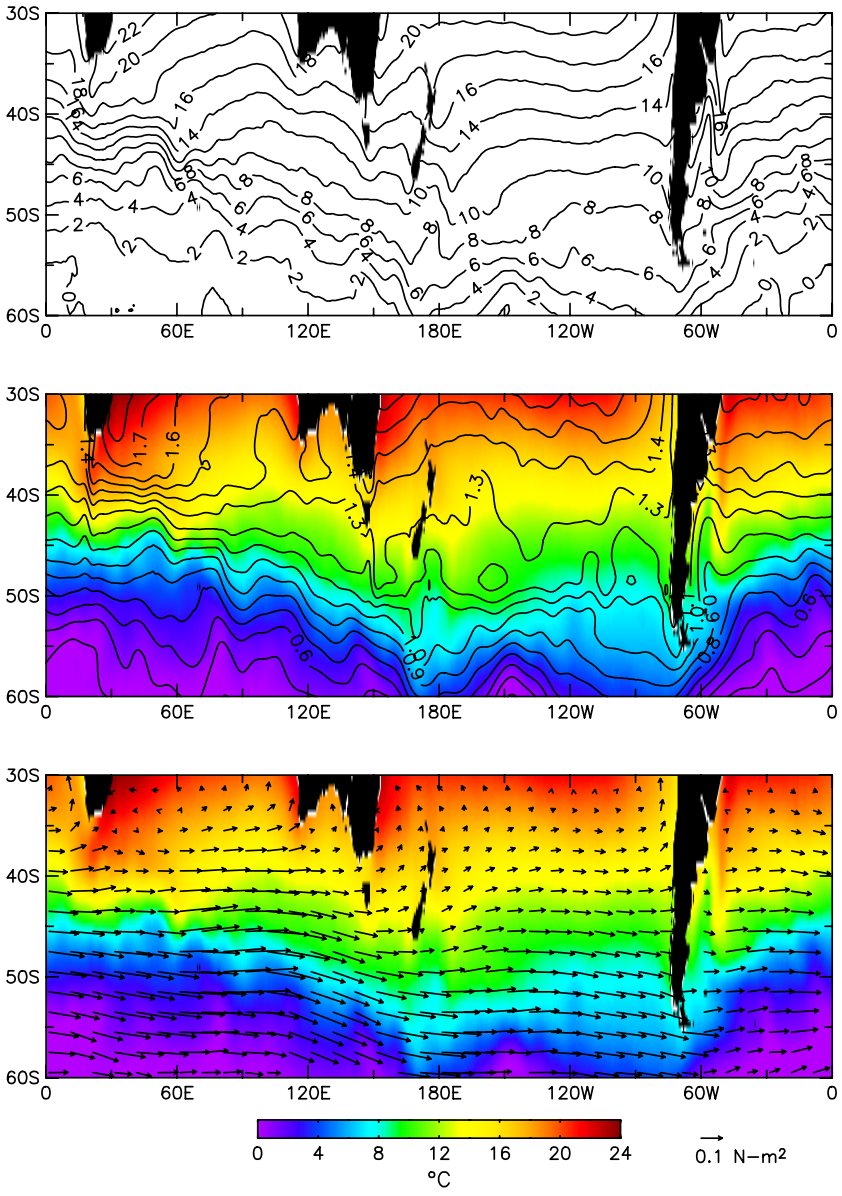

Figure 2.2: Averages over the 2-yr period 1 Aug 1999–31 Jul 2001: (top) Reynolds SST analyses; (middle) contours of the climatological average dynamic height relative to 1000-m depth from Levitus and Boyer (1994) with the 2-yr average SST shown in color according to the scale at the bottom; (bottom) vector average wind stress from QuikSCAT overlaid on the 2-yr average SST.

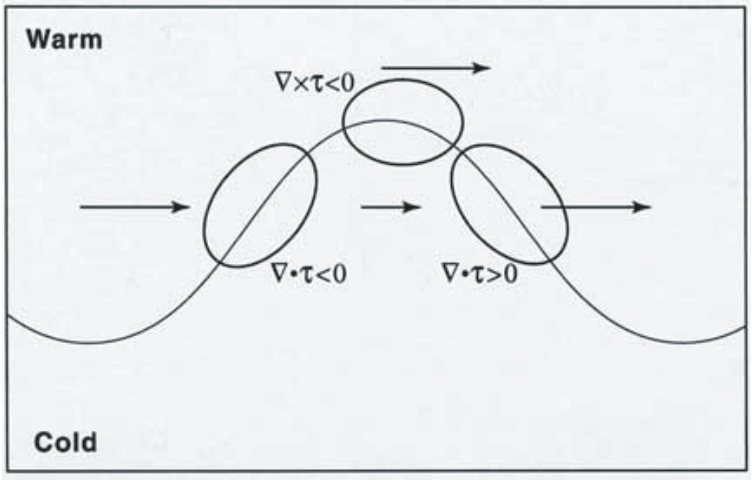

Figure 2.3: Schematic of the hypothesized interaction between wind stress and SST for wind blowing obliquely across a meandering SST front. The SST front is delineated as the black sinusoidal curve, separating warm and cold water. The lengths of the arrows schematically represent the hypothesized relative magnitudes of the surface wind stress. Regions of nonzero wind stress curl and divergence are indicated.

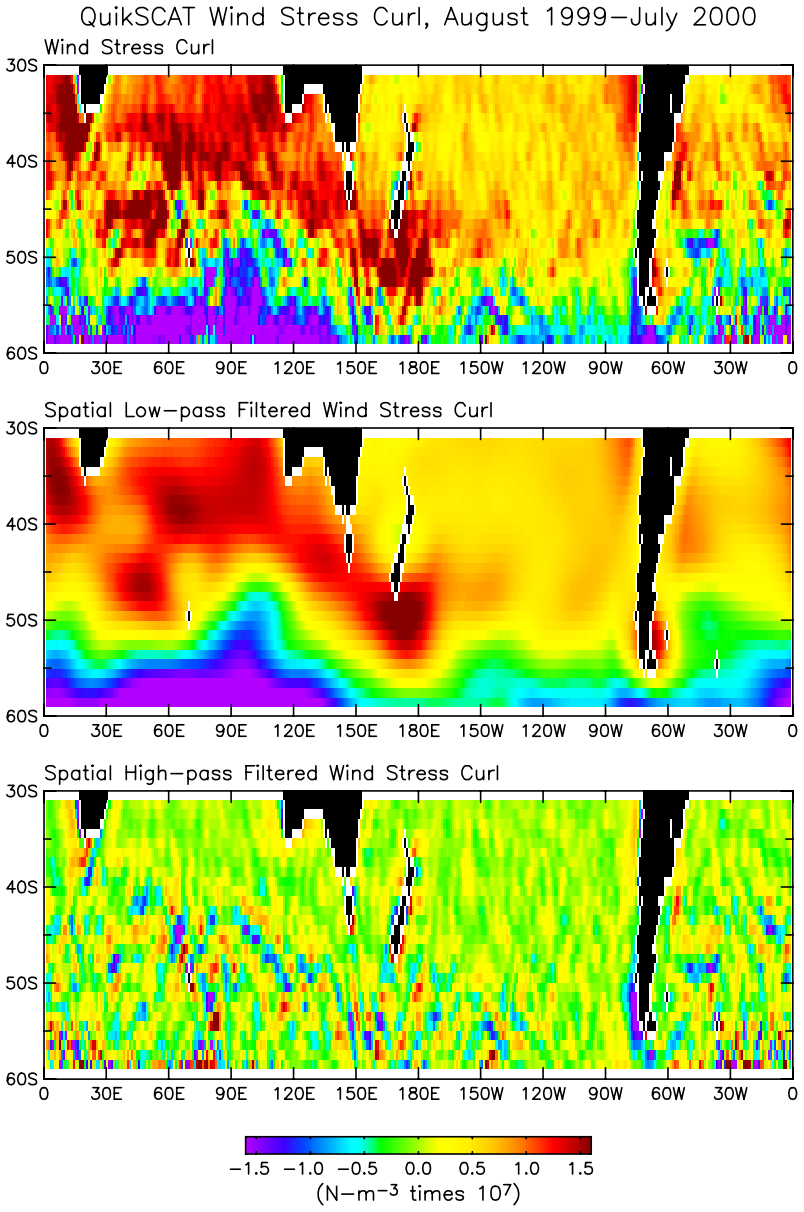

Figure 2.4: Average maps over the 2-yr period 1 Aug 1999–31 Jul 2001: (top) wind stress curl; (middle) spatially smoothed wind stress curl with wavelengths longer than 10° latitude by 30° longitude; (bottom) spatially high-pass filtered wind stress curl field with wavelengths shorter than 10° latitude by 30° longitude. The contours overlaid on the bottom panel are the 2-yr average SST from Fig. 2.2a with a contour interval 1°C.

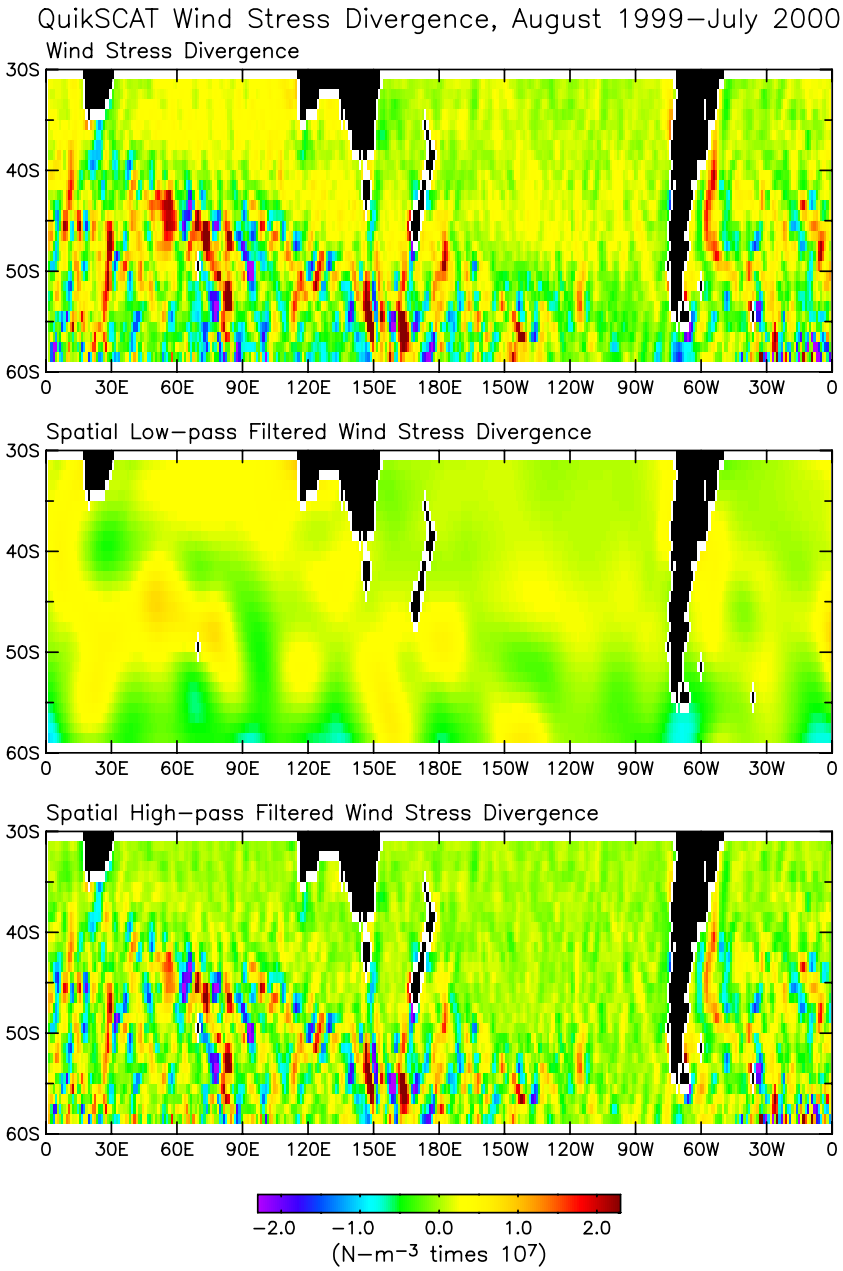

Figure 2.5: Same as Fig. 2.4 except for the wind stress divergence.

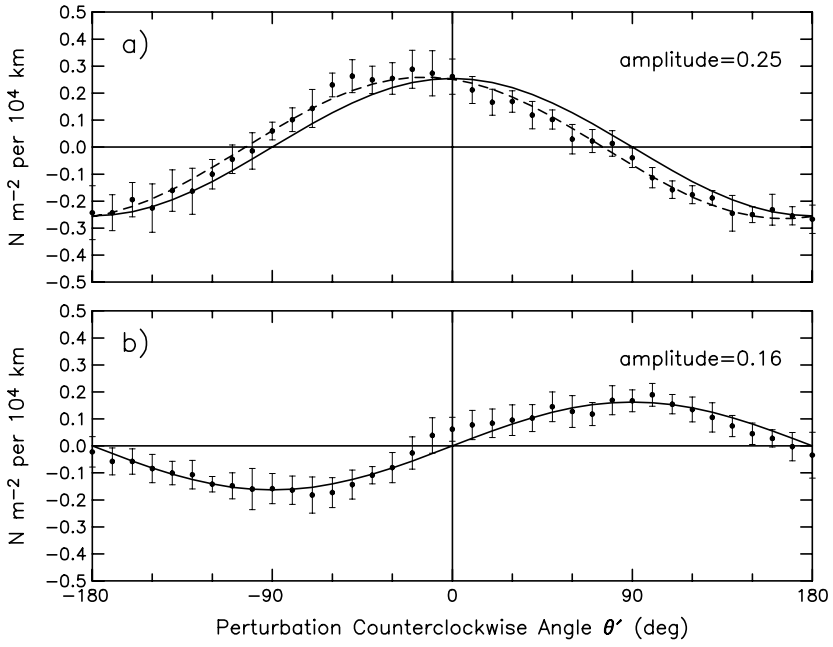

Figure 2.6: Binned scatterplots of the angular dependencies of (a) perturbation wind stress divergence, $\nabla \cdot \hat{\boldsymbol{\tau}}'$, and (b) perturbation wind stress curl, $\nabla \times \hat{\boldsymbol{\tau}}' \cdot \hat{\mathbf{k}}$ on the perturbation angle θ' defined by Eqn. 2.1. The points in (a) and (b) are the means within each bin computed from 11 overlapping 3-month averages over the 2-yr analysis period, and the error bars represent ± 1 std dev of the means within each bin. The solid lines in (a) and (b) represent least squares fits to a sine and a cosine, respectively. The dashed curve in (a) is the least squares fit to a sinusoid, which is shifted 23° clockwise relative to a cosine of zero phase.

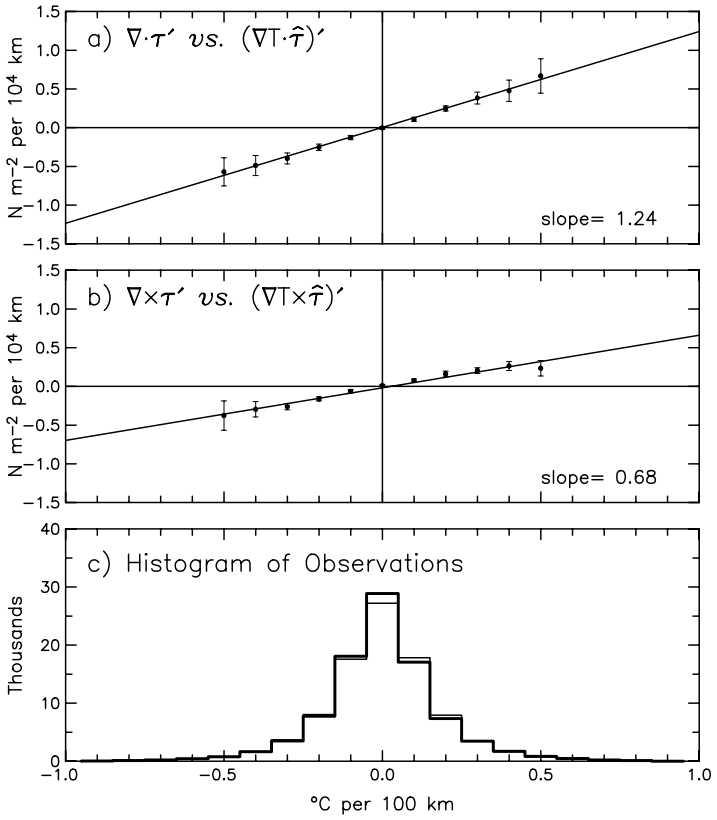

Figure 2.7: Binned scatterplots of the relationships between the spatially high-pass filtered SST and wind stress fields: (a) the perturbation wind stress divergence, $\nabla \cdot \hat{\boldsymbol{\tau}}'$, plotted as a function of the perturbation downwind SST gradient, $(\nabla T \cdot \hat{\boldsymbol{\tau}})'$; (b) the perturbation wind stress curl, $\nabla \times \hat{\boldsymbol{\tau}}' \cdot \hat{\mathbf{k}}$, plotted as a function of the perturbation crosswind SST gradient, $(\nabla T \times \hat{\boldsymbol{\tau}})' \cdot \hat{\mathbf{k}}$; and (c) histograms of the number of observations within each bin for (a) (thick line) and (b) (thin line). The points in (a) and (b) are the means within each bin computed from the 11 individual 3-month averages, and the error bars are ± 1 std devs within each bin. The lines through the points represent least squares fits of the binned overall means to straight lines.

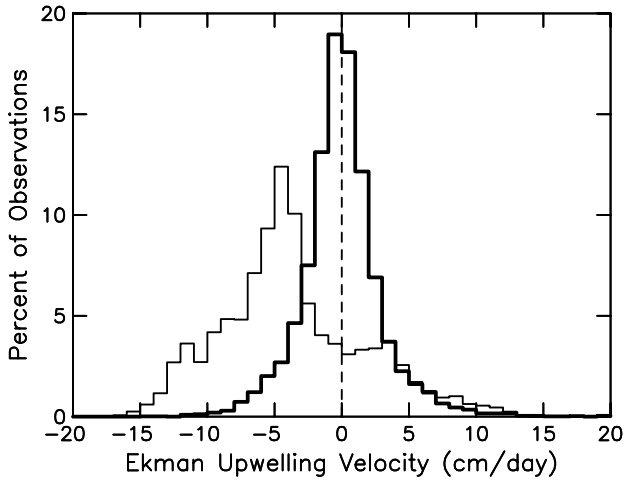

Figure 2.8: Histograms of the Ekman pumping calculated from the spatially low-pass filtered wind stress curl field (thin line), and from the spatially high-pass filtered wind stress curl field (heavy line). Units are in cm day^{-1}.

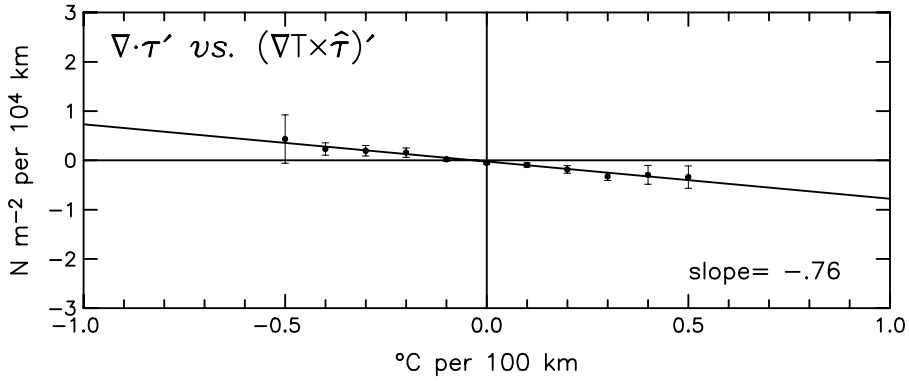

Figure 2.9: Binned scatterplot of the relationship between the spatially high-pass filtered wind stress divergence and the perturbation crosswind SST gradient. The points are the means within each bin computed from the 11 individual 3-month averages, and the error bars are ±1 std dev within each bin. The line represents a least squares fit of the binned overall means to a straight line.

HIGH-RESOLUTION SATELLITE MEASUREMENTS OF THE ATMOSPHERIC BOUNDARY LAYER RESPONSE TO SST VARIATIONS ALONG THE AGULHAS RETURN CURRENT

Larry W. O'Neill, Dudley B. Chelton, Steven K. Esbensen, and Frank J. Wentz

Journal of Climate

45 Beacon Street

Boston, MA 02108-3693

Vol. 18, 15 July 2005

Chapter 3

Abstract

The marine atmospheric boundary layer (MABL) response to sea surface temperature (SST) perturbations with wavelengths shorter than 10° latitude by 30° longitude along the Agulhas Return Current (ARC) is described from the first year of SST and cloud liquid water (CLW) measurements from the Advanced Microwave Scanning Radiometer (AMSR) on the Earth Observing System (EOS) *Aqua* satellite and surface wind stress measurements from the QuikSCAT scatterometer. AMSR measurements of SST at a resolution of 58 km considerably improves upon a previous analysis (O'Neill et al. 2003) that used the Reynolds SST analyses, which underestimate the short-scale SST gradient magnitude over the ARC region by more than a factor of 5. The AMSR SST data thus provide the first quantitatively accurate depiction of the SST-induced MABL response along the ARC. Warm (cold) SST perturbations produce positive (negative) wind stress magnitude perturbations, leading to short-scale perturbations in the wind stress curl and divergence fields that are linearly related

to the crosswind and downwind components of the SST gradient, respectively. The magnitudes of the curl and divergence responses vary seasonally and spatially with a response nearly twice as strong during the winter than during the summer along a zonal band between 40°S-50°S. These seasonal variations closely correspond to seasonal and spatial variability of large-scale MABL stability and surface sensible heat flux estimated from NCEP reanalysis fields. SST-induced deepening of the MABL over warm water is evident in AMSR measurements of CLW. Typical annual mean differences in cloud thickness between cold and warm SST perturbations are estimated to be about 300 m.

3.1 Introduction

The Agulhas Return Current (ARC) separates warm subtropical water to the north from cold subpolar water to the south and marks the location of vigorous air-sea interaction processes (e.g. Jury and Walker 1988; Jury 1994; Rouault and Lutjeharms 2000; O'Neill et al. 2003, hereafter referred to as OCE). Large, quasi-stationary meanders in the sea surface temperature (SST) front associated with the ARC coincide with the location of the Agulhas Plateau and the Mozambique Escarpment (Lutjeharms and van Ballegooyen 1984). As the winds blow across these meanders, the sharp SST front modifies the marine atmospheric boundary layer (MABL), resulting in perturbations in surface winds and cloud cover. Annually-averaged SST gradients across the ARC exceed 4°C per 100 km in some regions, which are among the strongest in the world ocean. All-weather satellite SST measurements with a resolution of about 58 km have recently become available for the first time over the ARC from the Advanced Microwave Scanning Radiometer (AMSR) on the Earth Observing System (EOS)-Aqua satellite. The objective of this study is to quantify the influence of SST on surface winds and clouds using the first 12 months of SST and cloud liquid water (CLW) measurements from the AMSR and coincident wind stress measurements from the QuikSCAT scatterometer.

The mechanisms governing the SST influence on surface winds have been identified in various areas of the world ocean from in situ observations (e.g. Sweet et al. 1981; Hsu 1984a; Jury and Walker 1988; Rogers 1989; Hayes et al. 1989; Wallace et al. 1989;

Freihe et al. 1991; Bond 1992; Jury 1994; Kwon et al. 1998; Rouault and Lutjeharms 2000; Hashizume et al. 2002; Thum et al. 2002; Cronin et al. 2003), analytical models (Hsu 1984b; Lindzen and Nigam 1987), and mesoscale atmospheric models (e.g. Wai and Stage 1989; Warner et al. 1990; Koračin and Rogers 1990; Xie et al. 1998; de Szoeke and Bretherton 2004; Small et al. 2003, 2004). SST gradients influence the MABL by modifying its stability through changes in air-sea heat flux and through the development of secondary circulations. Over colder water, decreased surface heat fluxes stabilize the MABL, inhibiting the vertical turbulent mixing of momentum from aloft to the surface, increasing the near surface wind shear, and decelerating the surface winds. Over warmer water, increased surface heat fluxes destabilize and deepen the MABL, enhancing the vertical turbulent mixing of momentum from aloft to the surface, while reducing the near surface wind shear, and accelerating the surface winds. Previous studies by Chelton et al. (2001), OCE, and Chelton et al. (2004) have shown that the decelerations and accelerations of surface winds lead to convergences and divergences in the surface wind field that are linearly related to the downwind component of the SST gradient; likewise, crosswind gradients in the SST field generate lateral variations in MABL stability, resulting in a curl of the surface wind field. A hydrostatic pressure gradient also develops across SST fronts with higher pressure and descending air over the colder water and lower pressure and ascending air over the warmer water, forming thermally-direct circulations in the MABL over the SST front that enhance the cross-frontal surface flow from colder to warmer water.

MABL clouds form preferentially over the warm, downwind side of SST fronts (e.g., Wai and Stage 1989; Rogers 1989; Deser et al. 1993; Hashizume et al. 2001; Xie et al. 2001). Over the ARC and the Agulhas Current, increases in surface fluxes and decreases in MABL stability are associated with the increased formation of stratocumulus clouds over the warmest SSTs compared to adjacent colder water (Lutjeharms et al. 1986; Lee-Thorp et al. 1998). Large surface heat fluxes over the ARC and the Agulhas Current have been observed to accompany decreases in MABL stability as the large-scale winds blow from cold to warm water (e.g., Rouault and Lee-Thorp 1996; Lee-Thorp et al. 1999; Rouault et al. 2000). These studies suggest that stability-dependent turbulent mixing regulates MABL cloud formation by deepening the MABL and by controlling the vertical mixing of moisture and heat from the surface upwards past the lifting condensation level.

Satellite measurements of surface winds, SST, surface heat fluxes, and clouds have shown that the mesoscale coupling between SST fronts and the MABL observed in regional, in situ studies occurs worldwide wherever large SST gradients exist. The eastern tropical Pacific has received the most attention (e.g., Deser et al. 1993; Xie et al. 1998; Chelton et al. 2001; Hashizume et al. 2001; Thum et al. 2002). Recent studies have focused on the North Pacific Ocean (Nonaka and Xie 2003; Chelton et al. 2004), the North Atlantic (Chelton et al. 2004) and the Southern Ocean (OCE; White and Annis 2003). These observations are consistent with the conclusions reached from in situ observations that SST fronts alter MABL stability, thereby influencing the

surface winds and the development of low-level clouds.

The accuracy of SST measurements used in air-sea interaction studies over the Southern Ocean is an important issue (e.g., OCE). At these high southern latitudes, in situ observations of SST are very sparse. Furthermore, clouds that cover more than 75% of the Southern Ocean surface in the annual mean (e.g., Rossow and Schiffer 1991; Hahn et al. 1995) introduce biases and errors in infrared measurements of SST due to errors in cloud detection algorithms. To mitigate the effects of these biases and uncertainties, Reynolds and Smith (1994) and Reynolds et al. (2002) developed an objective analysis algorithm to estimate SST by blending bias-adjusted satellite infrared SST retrievals in cloud-free regions with all available in situ measurements from ships and buoys while utilizing information on the location of the ice edge. Since few in situ observations exist over the expansive and infrequently traveled Southern Ocean, errors in the infrared satellite data generally persist into the estimated SST fields. Moreover, the advantages gained in the blending come at the expense of spatial resolution (Reynolds and Smith 1994).

Despite these shortcomings, the Reynolds SST analyses have been the best available estimate of the SST field over the Southern Ocean. Using these SST fields and surface wind stress measurements from the QuikSCAT scatterometer during the 2-yr period Aug 1999 to Jul 2001, OCE showed that surface winds were highly coupled to the underlying SST gradients over the entire Southern Ocean. Large uncertainties in the short-scale SST field estimated by the Reynolds SST analyses, however, limited

the temporal resolution of the analysis in OCE to seasonal time scales. Additionally, as will be shown in section 3.3, the coarse spatial resolution of the Reynolds SST analyses led to a substantial underestimation of the SST gradients on the spatial scales that are important to the air-sea coupling that is of interest here.

In this paper, we use the AMSR SST measurements to develop a more detailed and accurate account of the coupling between SST and both wind stress and CLW over the 1-yr period 2 Jun 2002 to 7 Jun 2003, corresponding to the first complete year of the AMSR data record. The analysis region is 0°E to 100°E and 27°S to 60°S, encompassing the Agulhas Retroflection and the Agulhas Return Current south of Africa. In the following section, the AMSR SST and CLW data, QuikSCAT wind data, and Reynolds SST analyses are described in detail. The differences between the Reynolds and AMSR SST fields are quantified in section 3.3. The coupling between SST and wind stress deduced from the AMSR and QuikSCAT observational data is summarized in section 3.4 and a brief discussion of the influence of surface-layer stability on the wind stress in presented in section 3.5. An analysis of the spatial and temporal variability of this coupling is presented in section 3.5 and an analysis and interpretation of spatial lags in the MABL response to SST forcing is presented in section 3.7. Observations of the CLW response are presented in section 3.8.

3.2 Data description

SST measurements from microwave satellite radiometers are not adversely affected by the ubiquitous cloud cover endemic to the Southern Ocean because non-precipitating clouds are essentially transparent to microwave radiation. The first calibrated and accurate satellite microwave SST sensor was the Tropical Rainfall Measuring Mission (TRMM) Microwave Imager (TMI) (Wentz et al. 2000; Chelton et al. 2000). Because of the low inclination of the TRMM orbit, TMI measurements are restricted to the latitude range 38°N to 38°S, which leaves most of the Southern Ocean unsampled. Microwave SST measurements over the high-latitude Southern Ocean have only recently become available following the launch of the EOS-Aqua satellite on 4 May 2002 and the initiation of the AMSR data record on 2 Jun 2002.

The AMSR measures horizontally and vertically polarized brightness temperatures at six microwave frequencies across a single 1445-km swath centered on the sub-satellite ground track. SST, vertically-integrated CLW, wind speed, vertically-integrated water vapor, and rain rate are estimated over most of the global oceans from these twelve microwave brightness temperatures using physically-based statistical regression (Wentz and Meissner 2000). The spatial resolution of the SST and CLW measurements utilized in this study are 58 km and 13 km, respectively. The SST and CLW measurements were averaged onto a 0.25° grid. Rain-contaminated estimates of SST and CLW were identified and excluded from further analysis based on collocated AMSR estimates of rain rate.

The accuracy of microwave SST retrievals has been evaluated through both simulation studies (Wentz and Meissner 2000) and direct comparisons with in situ observations (Wentz et al. 2000). For a single observation, the rms SST accuracy is about 0.5°C. The random errors are further reduced here from consideration of weekly averages. Due to the lack of adequate in situ observations of CLW, the accuracy of the CLW retrieval can only be assessed through simulations and theoretical error models, which indicate an uncertainty of about 0.02 mm in units of precipitable water, or 20 g m^{-2} in units of columnar-integrated liquid water density (Wentz and Meissner 2000).

In non-precipitating weather conditions, the SeaWinds scatterometer onboard the QuikSCAT satellite infers the surface wind stress at a given location from microwave backscatter measurements of sea surface roughness obtained at multiple azimuths. The microwave backscatter is calibrated to the equivalent neutral stability wind at a height of 10-m above the surface, i.e., the 10-m wind that would be associated with the observed wind stress were the atmosphere neutrally stratified (Liu and Tang 1996). The vector wind stress $\boldsymbol{\tau}$ was calculated from the 10-m neutral stability wind $\mathbf{v}_{10}^N$ from the bulk formulation $\boldsymbol{\tau} = \rho_0 C_d^N |\mathbf{v}_{10}^N| \mathbf{v}_{10}^N$, where ρ_0 is a constant surface air density and C_d^N is the neutral stability drag coefficient based on Large and Pond (1982) with a modification for low wind speeds suggested by Trenberth et al. (1990). The QuikSCAT wind stress fields were averaged onto the same 0.25° grid as the SST and CLW data. For each 0.25° grid cell, the weekly-averaged QuikSCAT wind components were not used if precipitation occurred in five or more observations as determined

from nearly coincident precipitation measurements made from a combination of four satellite microwave imagers, including the TMI and the Special Sensor Microwave Imagers (SSM/I) on the Defense Meteorological Satellite Program satellites F13, F14, and F15.

The 0.25°-gridded QuikSCAT winds and AMSR SST and CLW were averaged over weekly intervals. The QuikSCAT winds were further smoothed using a quadratic loess smoother (Cleveland and Devlin 1988; Schlax et al. 2001) with filter cutoff wavelengths of 2° latitude by 4° longitude, similar to the filtering properties of 1.2° latitude by 2.4° longitude block averages but with smaller filter sidelobes (see Fig. 1 of Chelton and Schlax 2003).

The weekly-averaged wind stress, SST, and CLW fields south of the northernmost extent of the Antarctic ice edge were masked using ice fields constructed from AMSR brightness temperatures. In the weekly-averaged data, 0.25° grid cells were flagged as ice contaminated when the AMSR measured ice 50% of the time, or when the number of times that the AMSR identified a particular cell as containing ice exceeded the number of times the cell contained valid SST and CLW data. The maximum extent of ice cover during the 1-yr period analyzed here is shaded grey in the figures presented here.

The vector-averaged QuikSCAT wind stress over the 1-yr period 2 Jun 2002 to 7 Jun 2003 (Fig. 3.1, top) is predominately westerly over the ARC region. The maximum wind stress occurred between 45°S and 50°S with a magnitude exceeding

0.25 N m^{-2}. This corresponds to a wind speed exceeding 11 m s^{-1}, which is among the largest annual mean wind speed anywhere in the world oceans. The 1-yr average SST measured by the AMSR is shown in color in the top panel of Fig. 3.1. Wind blowing across the meandering SST isotherms associated with the ARC make this an ideal region to investigate the influence of SST on the wind stress, wind stress curl and divergence, and CLW.

The 1-yr average CLW is shown in Fig. 3.1 (bottom) with SST contours overlaid. Large values of mean CLW occur between 40°S and 50°S in association with the frequent growth and passage of synoptic scale weather systems and the close proximity of the ARC to the Southern Hemisphere atmospheric polar front (Peixoto and Oort 1992). Poleward of this maximum, CLW decreases because colder atmospheric columns tend to hold less precipitable water. Equatorward of this maximum, large-scale subsidence in the subtropics is unfavorable for deep cloud formation, limiting CLW to smaller values. Spatial variability in the 1-yr average CLW is mainly attributable to variability in precipitable water and cloud forcing mechanisms that determine cloud type and thickness.

3.3 Comparison between AMSR and Reynolds SST

In our previous study of air-sea coupling over the Southern Ocean (OCE), we used the Reynolds SST analyses during the 2-yr period August 1999 to July 2001 (i.e., prior to the 2 June 2002 beginning of the AMSR data record). The Reynolds analyses of

weekly-averaged SST on a 1° spatial grid are produced by the National Oceanic and Atmospheric Administration (NOAA) using a blending of in situ and bias-adjusted satellite infrared data as described by Reynolds and Smith (1994) and Reynolds et al. (2002). The satellite infrared SST measurements are from the Advanced Very High Resolution Radiometer (AVHRR) onboard the NOAA-series of polar-orbiting satellites. Microwave SST observations from the TMI and AMSR are not presently included in the Reynolds SST analyses. The coarse resolution of the Reynolds SST fields is quantified in this section by comparisons with AMSR SST fields.

The mean Reynolds SST and SST gradient fields over the 1-yr period 2 June 2002 to 7 June 2003 (Figs. 3.3b and 3.3d) capture the main features in the ARC, but with much less detail than in the AMSR SST field (Figs. 3.3a and 3.3c). In the 1-yr average AMSR SST gradient field (Fig. 3.3c), the ARC SST front is twice as intense as in the Reynolds SST (Fig. 3.3d). The much higher spatial resolution of the AMSR SST is clearly evident from the detailed structure of the meanders in the ARC that remained essentially stationary over the 1-yr period analyzed here. Boebel et al. (2003) has previously observed that these meanders in the ARC are nearly stationary from an analysis of three years (1997-1999) of merged sea surface height data from the TOPEX/Poseidon and ERS altimeters.

Of particular interest in this study are the small-scale features in the AMSR SST field. These were obtained by first isolating the large-scale SST fields by applying a loess filter with half-power filter cutoff wavelengths of 10° latitude by 30° longitude,

roughly equivalent to 6° latitude by 18° longitude block averages. The spatially high-pass filtered fields were then obtained by subtracting the loess smoothed fields from the unsmoothed SST fields. The resulting 1-yr average high-pass filtered SST fields are shown in Fig. 3.4 (top) as contours overlaid on the spatially high-pass filtered QuikSCAT wind stress magnitude. The spatially high-pass filtered fields analyzed throughout this study are referred to hereafter as perturbation fields. The high spatial correlation of 0.83 between the 1-yr average perturbation AMSR SST field and the 1-yr average perturbation QuikSCAT wind stress magnitude (upper panel of Fig. 3.4) is consistent with the earlier observations of SST influence on surface winds summarized in section 3.1. The spatial correlation between 1-yr averages of the perturbation Reynolds SST field and the perturbation QuikSCAT wind stress magnitude (bottom panel of Fig. 3.4) is only 0.65.

In addition to the lower correlation between the Reynolds SST fields and the overlying wind fields, it is apparent from Fig. 3.4 that the intensities of the short-scale perturbations in the Reynolds SST field are significantly underestimated because of the inherently coarse spatial resolution of the Reynolds SST analyses. The weak short-scale SST gradients in the Reynolds analyses are statistically quantified in Fig. 3.5. The short-scale SST gradient magnitudes computed from the Reynolds analyses are, on average, about a factor of 5 smaller than those computed from the AMSR SST (Fig. 3.5, top). The distribution of the perturbation SST gradient magnitudes for the Reynolds SST (Fig. 3.5, bottom) has a dynamic range that is only about half

that of the AMSR. The superiority of the AMSR SST fields for investigation of SST influence on the winds and clouds in the ARC region is thus apparent.

3.4 Coupling between the wind stress and SST fields

The total SST gradient vector in Cartesian coordinates can be decomposed into local crosswind and downwind components. In vector notation, these are the cross product $\nabla T \times \hat{\boldsymbol{\tau}} = |\nabla T| \sin\theta$ and the dot product $\nabla T \cdot \hat{\boldsymbol{\tau}} = |\nabla T| \cos\theta$, respectively, where $\nabla = \hat{\imath}\partial/\partial x + \hat{\jmath}\partial/\partial y$ is the 2-dimensional gradient operator in Cartesian coordinates with unit vectors $\hat{\imath}$ and $\hat{\jmath}$ in the zonal and meridional directions, respectively, T is the SST, $\hat{\boldsymbol{\tau}}$ is a unit vector in the direction of the wind stress, and θ is the counterclockwise angle between the vectors ∇T and $\hat{\boldsymbol{\tau}}$. When the surface wind blows obliquely across an SST front, the crosswind component of the SST gradient is nonzero. A lateral (crosswind) gradient of the wind develops because the wind speed is higher over the warmer water, resulting in a curl of the wind. Similarly, a downwind component of the SST gradient is associated with a longitudinal (downwind) deceleration or acceleration of the wind across the SST front, resulting in a convergence or divergence of the low-level winds. The wind stress curl and divergence should therefore depend, respectively, on the crosswind and downwind SST gradients (see Fig. 3 of OCE).

Short-scale SST-induced perturbations of the wind stress curl field are masked somewhat by the background curl of the large-scale mean wind field. In the ARC region that is the focus of this study, the large-scale wind stress curl is, respectively, positive and negative to the north and south of the westerly wind maximum located along approximately 45°S. The wind stress curl perturbations induced by crosswind SST gradients associated with the perturbation SST field were isolated by subtracting the 10° latitude by 30° longitude loess smoothed curl field from the unsmoothed curl field (Fig. 3.6, bottom). The short-scale curl field is most intense along the ARC just south of 40°S, coincident with the largest perturbation crosswind SST gradients associated with the ARC (contours in the bottom panel of Fig. 3.6). These persistent SST-induced short-scale perturbations in the curl field from the steady meanders in the SST front have magnitudes comparable to the large-scale curl field. The associated Ekman pumping (see Fig. 8 of OCE) likely has significant regional implications for the upper ocean circulation along the ARC.

The 1-yr average wind stress divergence is shown in Fig. 3.7 (top). Like the curl, the divergence is most spatially variable over a band centered on the ARC. The spatial high-pass filtered wind stress divergence field obtained by the same filtering procedure applied to the wind stress curl is shown in the bottom panel of Fig. 3.7. The large-scale divergence field is quite small as a consequence of the tendency for the mean wind stress field to be non-divergent. The unfiltered and spatially high-pass filtered divergence fields therefore differ by relatively little when compared to the

differences between the unfiltered and spatially high-pass filtered curl fields. Positive and negative perturbations form in the divergence field over positive and negative perturbation downwind SST gradients (contours in the bottom panel of Fig. 3.7) associated with meanders in the ARC.

While the 1-yr average maps in Figs. 3.6 and 3.7 illustrate the mean properties of the wind stress curl and divergence fields over the ARC, it is desirable to average over shorter time periods for statistical analysis of the coupling between SST and the wind stress field. Energetic synoptic scale frontal disturbances in this region conceal SST-induced perturbations in the wind stress and wind stress derivative fields constructed with short temporal averaging. The effects of weather disturbances were mitigated in OCE by block averaging the wind stress and SST data over 3-month periods. The choice of a 3-month averaging period was chosen primarily to abate concerns about the accuracy of the Reynolds SST analyses in shorter time averages over the sparsely sampled Southern Ocean. The dense coverage and high spatial resolution and accuracy of the AMSR SST data obviate such concerns.

The averaging period required to reduce the effects of weather variability was investigated from the cross correlation between the QuikSCAT perturbation wind stress magnitude and the perturbation AMSR SST as a function of the block averaging period from the first 53 weeks of AMSR data. The cross correlation increases rapidly from 0.5 in weekly averages to more than 0.7 for averaging periods longer than 4 weeks, as shown by the dots in Fig. 3.8. The cross correlations with the Reynolds

SST (shown by squares in Fig. 3.8) increase more slowly with increasing averaging period and are smaller for all averaging periods, presumably because of inaccuracies in the Reynolds SST fields, due at least in part to the spatial and temporal smoothing in the Reynolds analyses (see section 3.3).

On the basis of Fig. 3.8, the data were averaged into 17 overlapping 6-week blocks at 3-week intervals for the statistical analyses in this study. The 10° latitude by 30° longitude spatial high-pass filtering was applied to each of the overlapping 6-week average wind stress magnitude, curl, divergence, SST, and the crosswind and downwind SST gradient fields. These filtered fields are denoted respectively as $|\boldsymbol{\tau}|'$, $\nabla \times \boldsymbol{\tau}'$, $\nabla \cdot \boldsymbol{\tau}'$, $(\nabla T \times \hat{\boldsymbol{\tau}})'$, and $(\nabla T \cdot \hat{\boldsymbol{\tau}})'$.

The spatially high-pass filtered crosswind and downwind components of the SST gradient can be written as

$$(\nabla T \times \hat{\boldsymbol{\tau}})' = |\nabla T'| \sin \theta' \tag{3.1}$$

$$(\nabla T \cdot \hat{\boldsymbol{\tau}})' = |\nabla T'| \cos \theta' \tag{3.2}$$

from which it is seen that the angle θ' is defined by

$$\theta' = \tan^{-1} \left[\frac{(\nabla T \times \hat{\boldsymbol{\tau}})'}{(\nabla T \cdot \hat{\boldsymbol{\tau}})'} \right]. \tag{3.3}$$

To investigate the hypothesis that the spatially high-pass filtered wind stress curl and divergence fields over the ARC are functions of $(\nabla T \times \hat{\boldsymbol{\tau}})'$ and $(\nabla T \cdot \hat{\boldsymbol{\tau}})'$, respectively,

$\nabla \times \boldsymbol{\tau}'$ and $\nabla \cdot \boldsymbol{\tau}'$ were binned as functions of θ' for each of the overlapping 6-week block averages. The overall averages within each bin are shown as points in Fig. 3.9. As previously shown for the Southern Ocean by OCE and for the eastern tropical Pacific by Chelton et al. (2001), the QuikSCAT perturbation curl and divergence fields agree remarkably well with sine and cosine dependencies on θ'. The short-scale features in the curl and divergence fields thus depend, respectively, on the perturbation crosswind and downwind components of the SST gradient.

An interesting feature in the angular dependencies of the curl and divergence is the small phase shift relative to pure sine and cosine functions, respectively. A similar phase shift for the divergence but not for the curl was noted by OCE from SST gradients computed from the Reynolds SST analyses. The lack of evidence for a phase shift in the curl fields was evidently because of the coarse resolution and perhaps inaccuracies in the Reynolds SST fields used in that study. Though small, we believe that the phase shifts in Fig. 3.9 for the ARC region are statistically significant. They may be an indication of the importance of SST-induced perturbations of the pressure gradient on the cross-frontal flow of low-level winds (Lindzen and Nigam 1987; Cronin et al. 2003; Small et al. 2004). This is a subject of ongoing analysis.

The wind stress curl and divergence responses to a given SST gradient can be determined by binning $\nabla \times \boldsymbol{\tau}'$ and $\nabla \cdot \boldsymbol{\tau}'$ as functions of $(\nabla T \times \hat{\boldsymbol{\tau}})'$ and $(\nabla T \cdot \hat{\boldsymbol{\tau}})'$, respectively. As shown in Fig. 3.10, the perturbation curl and divergence over the ARC are linearly related to the perturbation crosswind and downwind SST gradi-

ents, respectively, consistent with the mechanisms discussed in the introduction and the results obtained by OCE for the entire Southern Ocean. The magnitude of the response between the derivative wind stress fields and the SST gradient components is given by the slopes of the lines in Fig. 3.10, denoted here as α_C for the curl and α_D for the divergence.

The coupling coefficients α_C and α_D calculated here are larger than those calculated by OCE by factors of 3 and 2, respectively. Some of the stronger responses obtained from this study are due to the differences between the ARC region considered here and the entire Southern Ocean considered by OCE. An analysis of QuikSCAT and AMSR data performed over the entire Southern Ocean (not shown here) indicates that the magnitude of the coupling coefficients are about 20% larger for the ARC region. Most of the differences between the values of α_C and α_D obtained here and the values obtained in OCE are evidently due to errors in the location and magnitude of SST gradients in the Reynolds SST analyses used in OCE. It is also noteworthy that the standard deviations within each bin in Fig. 3.10 are much smaller than those obtained by OCE, evidently due to the greater accuracy of the AMSR SST fields compared with the Reynolds SST analyses.

3.5 Surface-layer stability effects on the surface wind stress

The effects of surface layer stability alone on the surface wind stress can be isolated by investigating the stability dependence of the drag coefficient C_D over warm and cool water. The change in wind stress magnitude $\Delta|\boldsymbol{\tau}|$ caused only by changes in the stability-dependent drag coefficient ΔC_D can be calculated as

$$\Delta|\boldsymbol{\tau}| = \rho_0|\boldsymbol{U}|^2\Delta C_D, \tag{3.4}$$

where $|\boldsymbol{U}|$ is the wind speed, which is considered constant for the purposes of this sensitivity analysis. C_D was calculated separately over the warm and cool water using the surface-layer similarity relation

$$C_D = \left[\frac{k}{\ln(z/z_0) - \Psi_M(\zeta)}\right]^2, \tag{3.5}$$

where k is the von Karman constant, Ψ_M is a surface-layer stability correction function for momentum (Stull 1988), $\zeta = z/L$ is the non-dimensional height, z is the measurement height of 10 meters, L is the Obukhov length scale, and z_0 is the roughness length.

To investigate the sensitivity of $\Delta|\boldsymbol{\tau}|$ to ΔC_D, we consider a large range of ζ over the ocean from -0.3 in unstable convective boundary layers over warm SST perturbations to 0.3 in stable boundary layers over cool SST perturbations, corresponding

to sensible heat fluxes of about ± 70 W m^{-2}. This range of sensible heat fluxes is generally much larger than the range contained, for example, in 1-yr averages of sensible heat fluxes in the NCEP reanalysis over the Agulhas Return Current. The effects of stability in reality are therefore smaller than those in this sensitivity analysis. For an 8 m s^{-1} incident wind over the ocean, z_0 is about 2×10^{-4} m by Charnock's relation. The resulting ΔC_D between warm and cool SST perturbations is thus about 4×10^{-4}, leading to a $\Delta|\boldsymbol{\tau}|$ of about 0.03 N m^{-2}. The cross-frontal wind stress variations caused by stability-dependent variations in C_D in this extreme case sensitivity analysis is less than a third of the typical observed differences of more than 0.1 N m^{-2} over the Agulhas Return Current as shown in the top panel of Fig. 3.4. A more realistic range of ζ from -0.3 over warm water to 0 (neutral stability) over cool water yields a wind stress difference of only about 0.01 N m^{-2}, which is an order of magnitude smaller than the observed perturbations. We therefore conclude that cross-frontal variations in C_D alone cannot explain the observed cross-frontal variations in wind stress.

3.6 Spatial and temporal variability of the ocean-atmosphere coupling

Although the 1-yr record of the AMSR data used in this study limits the investigation of temporal variability, there is strong seasonal variability in the curl and divergence response to SST (thick lines in Fig. 3.11). The coupling coefficients α_C

and α_D calculated from the AMSR SST fields increase by 100% and 75%, respectively, during the wintertime compared to the summertime. While the magnitudes of α_C and α_D computed from the Reynolds SST fields are much smaller than those computed from the AMSR SST fields as discussed in section 3.4, the 4-yr record of α_C and α_D calculated from the QuikSCAT wind stress and Reynolds SST fields reveals a well-defined seasonal cycle with maxima during July and minima during December and January (thin lines in Fig. 3.11). The surface wind stress response to SST perturbations is thus significantly stronger during the austral winter than during the summer.

The observed seasonal cycle of the coupling coefficients are likely related to large-scale seasonal variability in the depth of the MABL. In this case, one would expect the seasonal cycles of the coupling coefficients and MABL depth to be related through the effects of seasonal variations of surface heat flux and stratification of the lower troposphere. An overall decrease in ambient static stability during the wintertime because of cooler air aloft relative to the air near the sea surface would allow deeper turbulent and convective mixing of momentum and heat.

A quantitative test of the above hypothesized mechanism for the observed seasonal cycle of the coupling coefficients would require detailed information about the vertical structure of the MABL. Such information is not available from observations. The surface heat flux and atmospheric temperature fields from the National Centers for Environmental Prediction (NCEP) reanalyses (Kalnay et al. 1996) provide at least

some insight into the processes involved. Although the vertical resolution of the NCEP fields is coarse, the vertical potential temperature gradient between 700 hPa and 1000 hPa, $\partial\theta_p/dz$, where θ_p is the potential temperature, provides a rough measure of the stratification of the lower troposphere.

The first empirical orthogonal functions (EOFs) and associated amplitude time series of the monthly-averaged surface sensible heat flux and the stratification are shown in Figs. 3.12 and 3.13, respectively. The surface sensible heat flux is maximum and the stratification is minimum during the winter. Likewise, the surface sensible heat flux is minimum and the stratification is maximum during the summer. The large-scale lower troposphere over the ARC is therefore less convectively stable during the winter than during the summer.

The correspondence between the intensity of the ocean-atmosphere coupling and stratification is evident from the geographic variability of α_C and α_D. Values of α_C and α_D were calculated for 5° longitude by 3° latitude regions using the 17 overlapping 6-week averaged fields. The magnitudes of the coupling coefficients vary considerably latitudinally, with maxima located along a band centered between about 40°S-50°S latitude (Fig. 3.14). The small values of the coupling coefficients outside of this band are mainly due to a low signal-to-noise ratio; however, α_C and α_D vary geographically by about a factor of 3 within the band of significant short-scale curl and divergence variability. This relationship is statistically quantified by bin-averaging $\partial\theta_p/\partial z$ as a function α_C and α_D as shown in the top and bottom panels of Fig. 3.15, respec-

tively. It is evident from these bin-averages that the coupling coefficients increase with increasing tropospheric stability. This is consistent with the hypothesis that stratification plays an important role in determining the surface wind stress response to a given SST gradient.

Another possible mechanism for the observed seasonal variability of α_C and α_D is seasonal variability of the near-surface flow caused by ageostrophic cross-frontal pressure gradients over regions of large SST gradients. These pressure gradients owe their existence to spatial variations in MABL depth and vertical thermal structure (Lindzen and Nigam 1987; Hashizume et al. 2002; Small et al. 2003, 2004) across the SST front. Seasonal variability in the large-scale MABL depth and thermal structure could thus contribute to the seasonal cycle of the coupling coefficients. Few observations of the seasonal cycle of these variables exist to test this hypothesis over the ARC. An analysis of archived radiosonde data (not shown here) available from four island weather stations scattered within the geographical region considered here was inconclusive in determining whether seasonal variability in large-scale MABL depth and thermal structure could account for the observed seasonal variability in the coupling coefficients.

Cronin et al. (2003) found that sea level pressure perturbations associated with tropical instability waves in the eastern tropical Pacific have a magnitude of about 0.1 hPa per °C SST change. Wai and Stage (1989) found nearly the same magnitude of SST-induced pressure perturbations from a 2-dimensional mesoscale atmospheric

model of the MABL response to SST over the Gulf Stream. We are not confident that the NCEP reanalyses are sufficiently accurate to investigate the importance of such small pressure changes to the wind field in the ARC region of interest in this study.

3.7 Spatial lags in the SST-induced response

On close inspection, a consistent, but small downwind lag is visually evident in the bottom panels of Figs. 3.6 and 3.7 where local extrema of the perturbation curl and divergence consistently occur slightly downwind of local extrema of the perturbation crosswind and downwind SST gradients. A maximum correlation of 0.86 occurs when the perturbation divergence is lagged 0.25° to the east (i.e., downwind in this region of westerly winds) of the perturbation downwind SST gradient (Fig. 3.16, top). This is consistent with the notion that the surface winds do not adjust instantaneously to changes in MABL stability as the large-scale winds advect air across SST perturbations. The downwind lag depends on the MABL adjustment and advective time scales. The downwind lag of 0.25° is small in comparison with the characteristic length scale of SST and wind stress perturbations over the ARC.

The spatial-lagged cross correlation between the 1-yr average perturbation curl and crosswind SST gradient is shown in the middle panel of Fig. 3.16. A maximum cross correlation of 0.78 occurs when the perturbation curl is lagged 0.25° to the east and 0.25° to the north of the perturbation crosswind SST gradient. A similar lag

structure is observed in the spatial-lagged cross correlation between the 1-yr average perturbation wind stress magnitude and SST (bottom panel of Fig. 3.16); a maximum correlation of 0.84 occurs when the perturbation wind stress magnitude is lagged 0.25° to the east and 0.25° to the north of the perturbation SST. While the zonal lag is probably the result of the same processes that are responsible for the lag in the perturbation divergence in Fig. 3.16 (top), this cannot explain the meridional lag.

The 0.25° meridional shift in the maximum responses of the curl and wind stress magnitude to SST suggests a link to the approximately zonal surface velocity of the ARC. Strong surface ocean currents have a measurable effect on scatterometer wind stress because scatterometers measure the actual stress on the moving sea surface rather than relative to a stationary sea surface (Cornillion and Park 2001; Kelly et al. 2001; Chelton et al. 2001). Because of the quasi-geostrophic and non-divergent nature of ocean currents, the effects of the currents on the stress are manifest in the wind stress curl but not in the wind stress divergence (Chelton et al. 2004). Since the ocean surface currents are expected to be strongest along the SST front, there is a positive (negative) curl of the surface currents north (south) of the front. The true wind stress curl that is measured by QuikSCAT is thus displaced northward relative to its position if the water surface were not moving, consistent with the meridional lag observed in Fig. 3.16.

A quantitative test of this hypothesis requires knowledge of the surface ocean currents. Direct surface current observations do not exist in the ARC over the time

and space scales under consideration here and surface velocities from ocean circulation models have not been demonstrated to be quantitatively accurate enough to use as surrogate estimates of the currents. To investigate the effects of ocean currents, the geostrophic surface velocity was estimated from the AMSR SST as follows. The relationship between SST and dynamic height relative to 1000 m over the ARC was determined by regression analysis from climatological hydrographic data (Levitus and Boyer 1994). The dynamic height was found to be linearly related to SST over the Agulhas region with a correlation coefficient of 0.98 and a slope of 0.053 m $^{\circ}C^{-1}$. Weekly averages of the dynamic height fields were estimated from the weekly-averaged AMSR SST fields using this linear relation. The geostrophic surface ocean velocity was then estimated from the gradient of the dynamic height field. The typical computed geostrophic current velocity along the SST front is about 50 cm s^{-1}, which is at least qualitatively consistent with the geostrophic velocities computed by Lutjeharms and Ansorge (2001).

The wind stress and wind stress curl and divergence that would exist in the absence of surface ocean currents were estimated by adding the regression estimates of the geostrophic surface currents to the scatterometer winds. The spatial-lagged cross correlation of the resulting fields are shown in Fig. 3.17. The meridional lag vanishes in the adjusted perturbation wind stress curl and wind stress magnitude fields, suggesting a nexus between the lag and the curl of the ARC surface currents. The estimated surface currents have an otherwise inconspicuous effect on the magnitude

of the scatterometer-measured coupling between surface winds and SST.

3.8 CLW response to SST perturbations

SST-induced modification of the MABL is also evident in AMSR measurements of CLW. Positive (negative) perturbations in the CLW field are associated with warm (cool) SST perturbations (Fig. 3.18); the spatial correlation between the 1-yr average SST and CLW perturbations is 0.59. Assuming a cloud liquid water density of 0.1 g m^{-3} for low-level stratocumulus (Rogers and Yau 1996), the typical CLW perturbations of 0.015 mm observed over the ARC correspond to differences of about 300 m between cloud thickness over cold and warm SST perturbations. Although direct measurements of MABL clouds are not available over the ARC, this is of the same order as the stratocumulus thickness of ∼300-400 m observed by Wang et al. (1999) over the warm water of the mid-latitude Azores during the Atlantic Stratocumulus Transition Experiment (ASTEX). Bretherton et al. (2003) observed similar stratocumulus thicknesses over the eastern tropical Pacific Ocean during the East Pacific Investigation of Climate (EPIC) field study during September and October of 2001.

Over the geographic region considered in Fig. 3.18, the cross correlation between the 1-yr average perturbation SST and CLW is maximum when the perturbation CLW field is lagged 0.5° downwind (eastward) of perturbations in the SST field. This spatial lag, which is visually evident in Fig. 3.18, is comparable to spatial lags that have been observed from satellite studies of clouds and SST elsewhere over the

ocean. For example, Deser et al. (1993) showed from longitudinal cross-sections that anomalies in low-level cloud reflectivity were displaced about 1.25° downwind of warm cusps associated with Pacific tropical instability waves. From in situ measurements along 95°W in the tropical Pacific, Raymond et al. (2003) found that maximum CLW values occur ∼1-2° downwind of the maximum SST gradient associated with the equatorial cold tongue.

It is noteworthy that spatial correlations between the perturbation CLW and wind stress divergence over the ARC were not statistically significant. SST-induced cloud formation is evidently not due to convection from low-level convergence but from MABL deepening due to increased sensible and latent heat fluxes. This is consistent with the results obtained by Wai and Stage (1989) who concluded that the presence of clouds over warmer water is due to the increase in MABL depth through entrainment rather than to a lowering of the lifting condensation level.

3.9 Conclusions

The Agulhas Return Current is an exceptionally good region to study the MABL modification by spatially varying SST. Satellite microwave measurements of SST that have recently become available from the AMSR have allowed a quantitative reinvestigation of the coupling between wind stress and SST in a previous analysis that was based on the Reynolds SST analyses (O'Neill et al. 2003). The short-scale SST perturbations are much better resolved in the AMSR SST; SST gradients in the ARC

region computed from the AMSR SST fields are about five times stronger than those computed from the Reynolds SST analyses. SST perturbations induce nearly coincident perturbations in the surface wind stress, sensible heat flux, and cloud liquid water. The responses of the wind stress curl and divergence to SST perturbations are dominated by annual cycles, with responses nearly twice as strong during the wintertime than during the summertime. The analysis of NCEP reanalysis fields in section 3.5 suggests that this response can be explained by the annual cycle of large-scale lower tropospheric stability. Changes in the observed wind stress perturbations between warm and cool water are too large to be explained by changes in the stability-dependent surface drag coefficient alone.

It should be emphasized that the interaction described here is only part of a complex series of interactions involving the coupled ocean-atmosphere system that includes two-way interactions between the MABL and upper-ocean. The SST-induced wind perturbations cause perturbations in surface heat fluxes and upper-ocean mixing that are likely to erode SST perturbations which will feedback onto the original wind stress perturbations. Moreover, the upwelling associated with SST-induced wind stress curl perturbations will feed back on the ocean, likely altering the SST. These 2-way feedbacks are intriguing aspects of the coupled system that can significantly enhance our understanding of coupled ocean-atmosphere interactions.

Acknowledgments. We thank Ricardo Matano, Roger Samelson, Michael Schlax, Deborah Smith, and Rob Wood for helpful discussions during the course of this analysis. We also thank Holda Biskeborn for help in editing this manuscript. We thank two anonymous reviewers for their thorough reading and helpful comments on our paper that lead to improved discussion of several points in the manuscript. The research presented here was supported by NASA Grants NAS5-32965 and NAGS-12378.

References

Boebel, O., T. Rossby, J. R. E. Lutjeharms, W. Zenk, and C. Barron, 2003: Path and variability of the Agulhas Return Current. *Deep-Sea Res.*, **50**, 35-56.

Bond, N. A., 1992: Observations of planetary boundary-layer structure in the eastern equatorial Pacific. *J. Climate*, **5**, 699-706.

Chelton, D. B., F. J. Wentz, C. L. Gentemann, R. A. de Szoeke, and M. G. Schlax, 2000: Satellite microwave SST observations of transequatorial tropical instability waves. *Geophys. Res. Lett.*, **27**, 1239-1242.

Chelton, D. B., and coauthors, 2001: Observation of coupling between surface wind stress and sea surface temperature in the eastern tropical Pacific. *J. Climate*, **14**, 1479-1498.

Chelton, D. B., and M. G. Schlax, 2003: The accuracies of smoothed sea surface height fields constructed from tandem altimeter datasets. *J. Atmos. Ocean Technol.*, **20**, 1276-1302.

Chelton, D. B., M. G. Schlax, M. H. Freilich, and R. F. Milliff, 2004: Satellite measurements reveal persistent small-scale features in ocean winds. *Science*, **303**, doi:10.1126/science. 1091901.

Cleveland, W. S., and S. J. Devlin, 1988: Locally weighted regression: An approach to regression analysis by local fitting. *J. Amer. Stat. Assoc.*, **83**, 596-610.

Cornillon, P., and K.-A. Park, 2001: Warm core ring velocities inferred from NSCAT. *Geophys. Res. Lett.*, **28**, 575-578.

Cronin, M. F., S.-P. Xie, H. Hashizume, 2003: Barometric pressure variations associated with eastern Pacific tropical instability waves. *J. Climate*, **16**, 3050-3057.

de Szoeke, S. P., and C. S. Bretherton, 2004: Quasi-Lagrangian large eddy simulations of cross-equatorial flow in the east Pacific atmospheric boundary layer. *J. Atmos. Sci.*, **61**, 1837-1858.

Deser, C., J. J. Bates, and S. Wahl, 1993: The influence of sea surface temperature on stratiform cloudiness along the equatorial front in the Pacific Ocean. *J. Climate*, **6**, 1172-1180.

Freihe, C. A., and coauthors, 1991: Air-sea fluxes and surface layer turbulence around a sea surface temperature front. *J. Geophys. Res.*, **96**, 8593-8609.

Hahn, C. J., S. G. Warren, and J. London, 1995: The effect of moonlight on observation of cloud cover at night, and application to cloud climatology. *J. Climate*, **8**, 1429-1446.

Hashizume, H., S.-P. Xie, W. T. Liu, and K. Takeuchi, 2001: Local and remote atmospheric response to tropical instability waves: A global view from space. *J. Geophys. Res.*, **106**, 10,173-10,185.

Hashizume, H., S.-P. Xie, M. Fujiwara, M. Shiotani, T. Watanabe, Y. Tanimoto, W. T. Liu, and K. Takeuchi, 2002: Direct observations of atmospheric boundary layer response to slow SST variations over the eastern equatorial Pacific. *J. Climate*, **15**, 3379-3393.

Hayes, S. P., M. J. McPhaden, and J. M. Wallace, 1989: The influence of sea surface temperature on surface wind in the eastern equatorial Pacific: Weekly to monthly variability. *J. Climate*, **2**, 1500-1506.

Hsu, S. A., 1984a: Effect of cold-air advection on internal boundary layer development over warm oceanic currents. *Dyn. Atmos. Oceans*, **8**, 307-319.

Hsu, S. A., 1984b: Sea-breeze-like winds across the north wall of the Gulf Stream: An analytical model. *J. Geophys. Res.*, **89**, 2025-2028.

Jury, M. R., 1994: A thermal front within the marine atmospheric boundary layer over the Agulhas Current south of Africa: Composite aircraft observations. *J. Geophys. Res.*, **99**, 3297-3304.

Jury, M. R., and N. Walker, 1988: Marine boundary layer modification across the edge of the Agulhas Current. *J. Geophys. Res.*, **93**, 647-654.

Kalnay, E., and coauthors, 1996: The NCEP/NCAR 40-year Reanalysis Project. *Bull. Amer. Meteor. Soc.*, **77**, 437-472.

Kelly, K. A., S. Dickinson, M. J. McPhaden, and G. C. Johnson, 2001: Ocean currents evident in satellite wind data. *Geophys. Res. Lett.*, **28**, 2469-2472.

Koračin, D., and D. P. Rogers, 1990: Numerical simulations of the response of the marine atmosphere to ocean forcing. *J. Atmos. Sci.*, **47**, 592-611.

Kwon, B. H., B. Bénech, D. Lambert, P. Durand, A. Druilhet, H. Giordani, and S. Planton, 1998: Structure of the marine atmospheric boundary layer over an oceanic thermal front: SEMAPHORE experiment. *J. Geophys. Res.*, **103**, **C11**, 25 159-25 180.

Large, W. G., and S. Pond, 1982: Sensible and latent heat flux measurements over the ocean. *J. Phys. Oceanogr.*, **12**, 464-482.

Lee-Thorp, A. M., M. Rouault, and J. R. E. Lutjeharms, 1998: Cumulus cloud formation above the Agulhas Current. *S. Afr. J. Sci.*, **94**, 351-354.

Levitus, S., and T. P. Boyer, 1994: *Temperature*, Vol. 4, *World Ocean Atlas 1994*, NOAA Atlas NESDIS 4, 117pp.

Lindzen, R. S., and S. Nigam, 1987: On the role of sea surface temperature gradients in forcing low-level winds and convergence in the Tropics. *J. Atmos. Sci.*, **44**, 2418-2436.

Liu, W. T., and W. Tang, 1996: Equivalent neutral wind. JPL Pub. 96-17, Pasadena, CA, 8pp.

Liu, W. T., X. Xie, P. S. Polito, S.-P. Xie, and H. Hashizume, 2000: Atmospheric manifestation of tropical instability waves observed by QuikSCAT and Tropical Rain Measuring Mission. *Geophys. Res. Lett.*, **27**, 2545-2548.

Lutjeharms, J. R. E., and R. C. van Ballegooyen, 1984: Topographic control in the Agulhas Current system. *Deep-Sea Res.*, **31**, 1321-1337.

Lutjeharms, J. R. E., and I. J. Ansorge, 2001: The Agulhas Return Current. *J. Mar. Syst.*, **30**, 115-138.

Nonaka, M., and S.-P. Xie, 2003: Covariations of sea surface temperature and wind over the Kuroshio and its extension: Evidence for ocean-to-atmosphere feedback. *J. Climate*, **16**, 1404-1413.

O'Neill, L. W., D. B. Chelton, and S. K. Esbensen, 2003: Observations of SST-induced perturbations of the wind stress field over the Southern Ocean on seasonal time scales. *J. Climate*, **16**, 2340-2354.

Peixoto, J. P., and A. H. Oort, 1992: *Physics of Climate*. Springer-Verlag, 520pp.

Reynolds, R. W., and T. M. Smith, 1994: Improved global sea surface temperature analyses using optimum interpolation. *J. Climate*, **7**, 929-948.

Reynolds, R. W., N. A. Rayner, T. M. Smith, D. C. Stokes, and W. Wang, 2002: An improved in situ and satellite SST analysis for climate. *J. Climate*, **15**, 1609-1625.

Rogers, D. P., 1989: The marine boundary layer in the vicinity of an ocean front. *J. Atmos. Sci.*, **46**, 2044-2062.

Rossow, W. B., and R. A. Schiffer, 1991: ISCCP cloud data products. *Bull. Amer. Meteor. Soc.*, **72**, 2-20.

Rouault, M., and J. R. E. Lutjeharms, 2000: Air-sea exchange over an Agulhas eddy at the subtropical convergence. *Global Atmos. Ocean Syst.*, **7**, 125-150.

Schlax, M. G., D. B. Chelton, and M. H. Freilich, 2001: Sampling errors in wind fields constructed from single and tandem scatterometer datasets. *J. Atmos. Oceanic Technol.*, **18**, 1014-1036.

Small, J. R., S.-P. Xie, and Y. Wang, 2003: Numerical simulation of atmospheric response to Pacific tropical instability waves. *J. Climate*, **16**, 3723-3741.

Small, J. R., S.-P. Xie, Y. Wang, S. K. Esbensen, and D. Vickers, 2005: Numerical simulation of boundary layer structure and cross-equatorial flow in the eastern Pacific. *J. Atmos. Sci.*, **62**, 1812-1830.

Stull, R. B., 1988: *An Introduction to Boundary Layer Meteorology.* Kluwer Academic, 666 pp.

Sweet, W. R., R. Fett, J. Kerling, and P. LaViolette, 1981: Air-sea interaction effects in the lower troposphere across the north wall of the Gulf Stream. *Mon. Wea. Rev.*, **109**, 1042-1052.

Thum, N., S. K. Esbensen, D. B. Chelton, and M. J. McPhaden, 2002: Air-sea heat exchange along the northern sea surface temperature front in the eastern tropical Pacific. *J. Climate*, **15**, 3361-3378.

Trenberth, K. E., W. G. Large, and J. G. Olson, 1990: The mean annual cycle in global ocean wind stress. *J. Phys. Oceanogr.*, **20**, 1742-1760.

Wai, W. M., and S. A. Stage, 1989: Dynamical analysis of marine atmospheric boundary layer structure near the Gulf Stream oceanic front. *Quart. J. Roy. Meteor. Soc.*, **115**, 29-44.

Wallace, J. M., T. P. Mitchell, and C. Deser, 1989: The influence of sea surface temperature on surface wind in the eastern equatorial Pacific: Seasonal and interannual variability. *J. Climate*, **2**, 1492-1499.

Warner, T. T., M. N. Lakhtakia, J. D. Doyle, and R. A. Pearson, 1990: Marine atmospheric boundary layer circulations forced by Gulf Stream sea surface temperature gradients. *Mon. Wea. Rev.*, **118**, 309-323.

Wentz, F. J., and T. Meissner, 2000: Algorithm theoretical basis document, Version 2, AMSR Ocean Algorithm. [Available online at: www.remss.com/papers/AMSR_Ocean_ Algorithm_Version_2.doc.]

Wentz, F. J., C. L. Gentemann, D. Smith, and D. B. Chelton, 2000: Satellite measurements of sea surface temperature through clouds. *Science*, **288**, 847-850.

White, W. B., and J. L. Annis, 2003: Coupling of extratropical mesoscale eddies in the ocean to westerly winds in the atmospheric boundary layer. *J. Phys. Oceanogr.*, **33**, 1095-1107.

Xie, S.-P., M. Ishiwatari, H. Hashizume, and K. Takeuchi, 1998: Coupled ocean-atmosphere waves on the equatorial front. *Geophys. Res. Lett.*, **25**, 3863-3866.

Xie, S.-P., W. T. Liu, Q. Liu, and M. Nonaka, 2001: Far-reaching effects of the Hawaiian Islands on the Pacific ocean-atmosphere system. *Science*, **292**, 2057-2060.

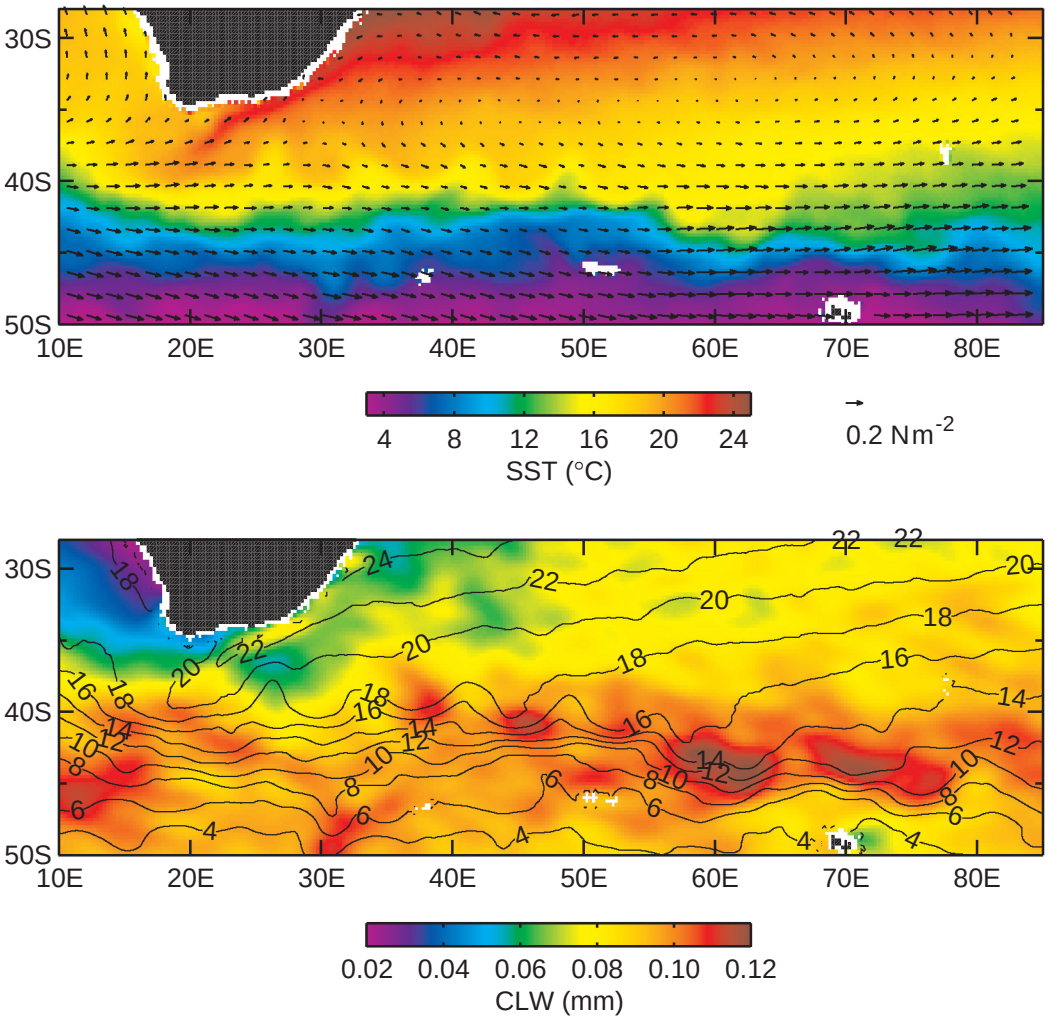

Figure 3.1: Averages over the 1-yr period 2 Jun 2002 to 7 Jun 2003: (top) vector-averaged wind stress from QuikSCAT overlaid on AMSR SST; (bottom) CLW with contours of AMSR SST.

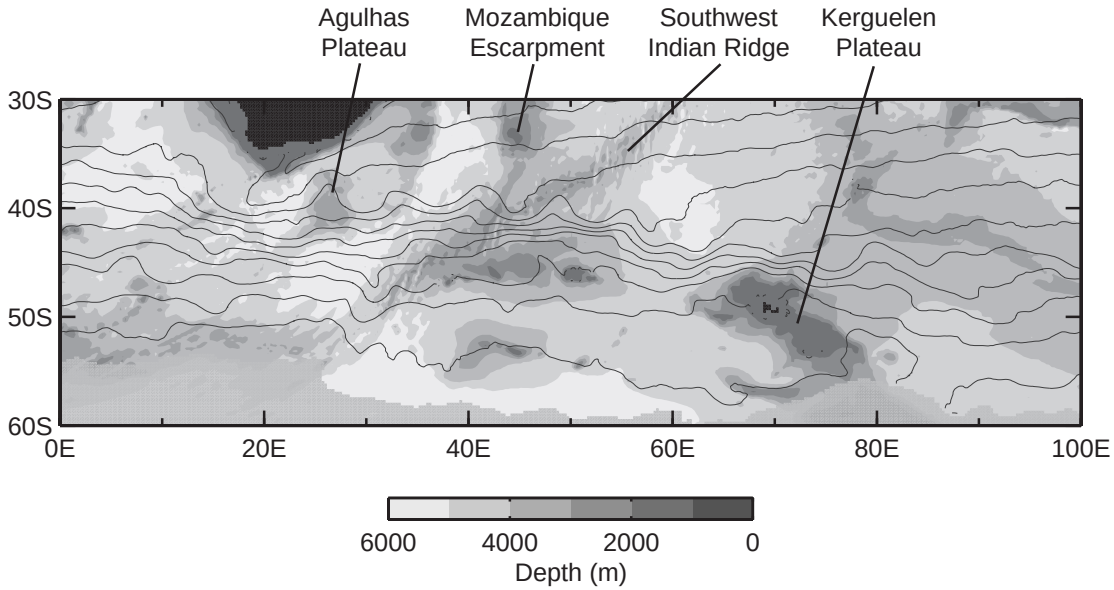

Figure 3.2: Map of the bathymetry and geographical locations of major bathymetric features in the Agulhas Return Current region (shaded) with contours of the 1-yr average AMSR SST as shown in Fig. 3.1 overlaid. The gray shade bar at the bottom of the map indicates the range of water depth.

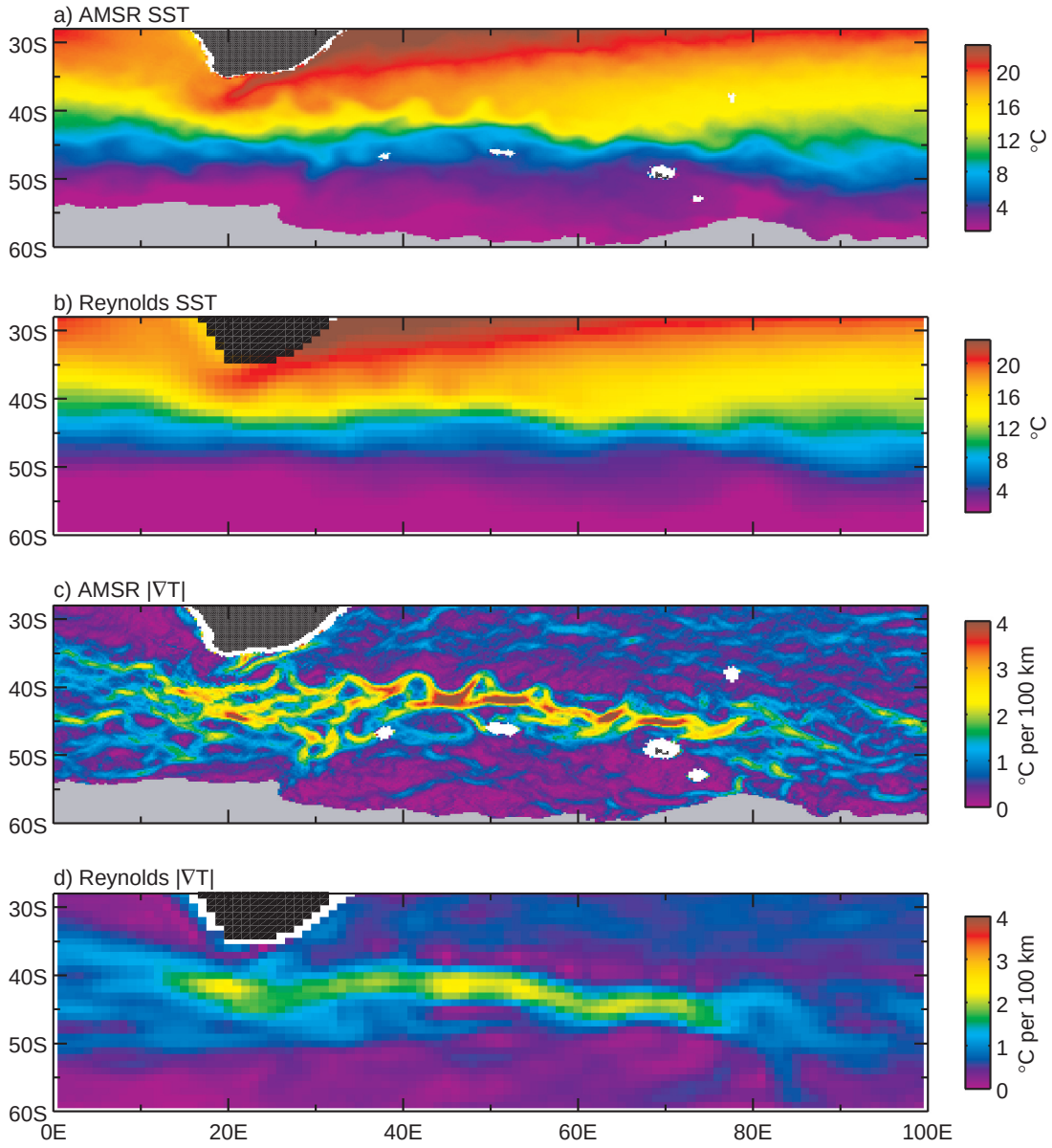

Figure 3.3: Maps of (a) AMSR SST; (b) Reynolds SST; (c) AMSR SST gradient magnitude; and (d) Reynolds SST gradient magnitude, averaged over the 1-yr period 2 Jun 2002 to 7 Jun 2003. Regions containing any sea ice during the 1-yr period are shown in gray in (a) and (c).

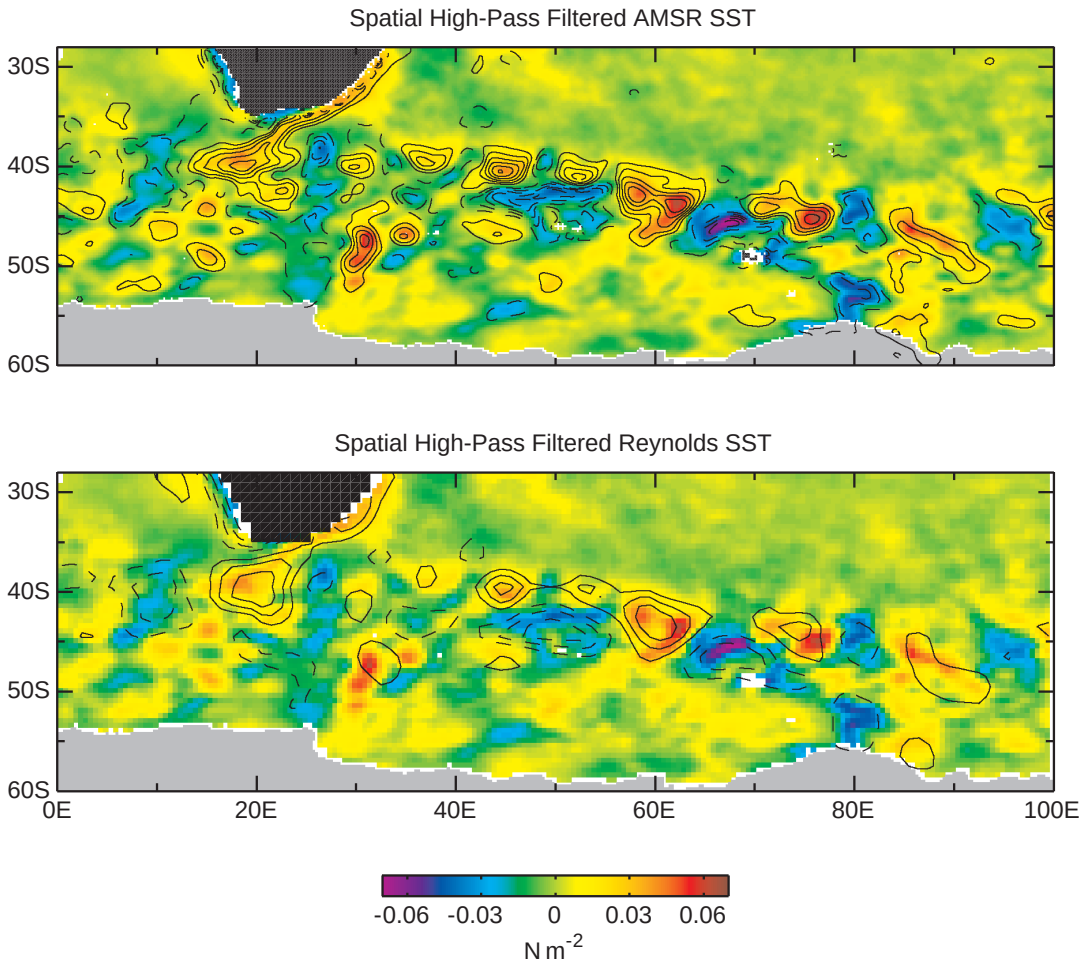

Figure 3.4: Maps of the perturbation wind stress magnitude from QuikSCAT averaged over the 1-yr period 2 Jun 2002 to 7 Jun 2003 shown in color. The overlaid contours are of the perturbation (top) AMSR SST and (bottom) Reynolds SST with a contour interval of 0.5°C. Dashed and solid contours in each panel correspond to negative and positive SST perturbations, respectively, and the zero contour has been omitted for clarity. The spatial high-pass filtering used to obtain these perturbation fields attenuates features with wavelengths longer than 10° latitude by 30° longitude.

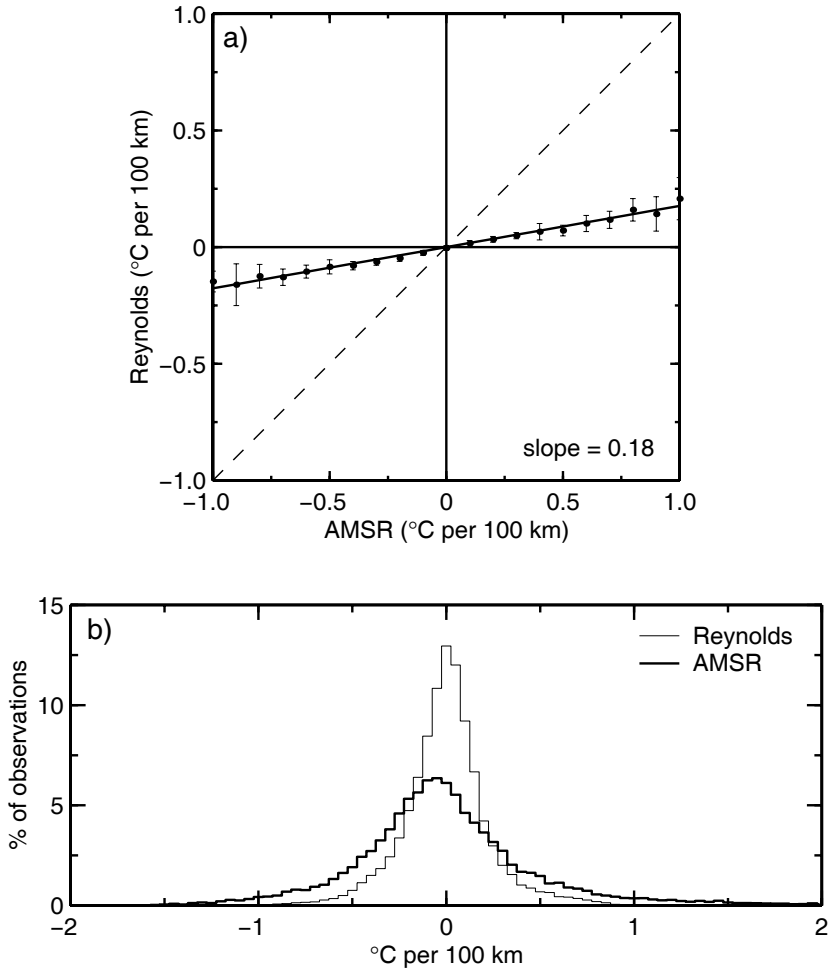

Figure 3.5: (a) Binned scatterplot of the Reynolds perturbation SST gradient magnitude as a function of the AMSR perturbation SST gradient magnitude. The points in each plot represent the means within each bin computed from 17 overlapping 6-week averages over the 1-yr period 2 Jun 2002 to 7 Jun 2003, and the error bars are ± 1 std dev of the means within each bin. The line through the points represents a least squares fit of the binned overall means to a straight line and the dashed line with unit slope is shown for reference; (b) histograms of the perturbation SST gradient magnitude computed from the Reynolds analyses (thin solid line) and AMSR (thick solid line) over the 17 individual 6-week averages. For both panels, the AMSR SST gradients were computed after block averaging the AMSR data onto the same $1^\circ \times 1^\circ$ spatial grid as the Reynolds analyses.

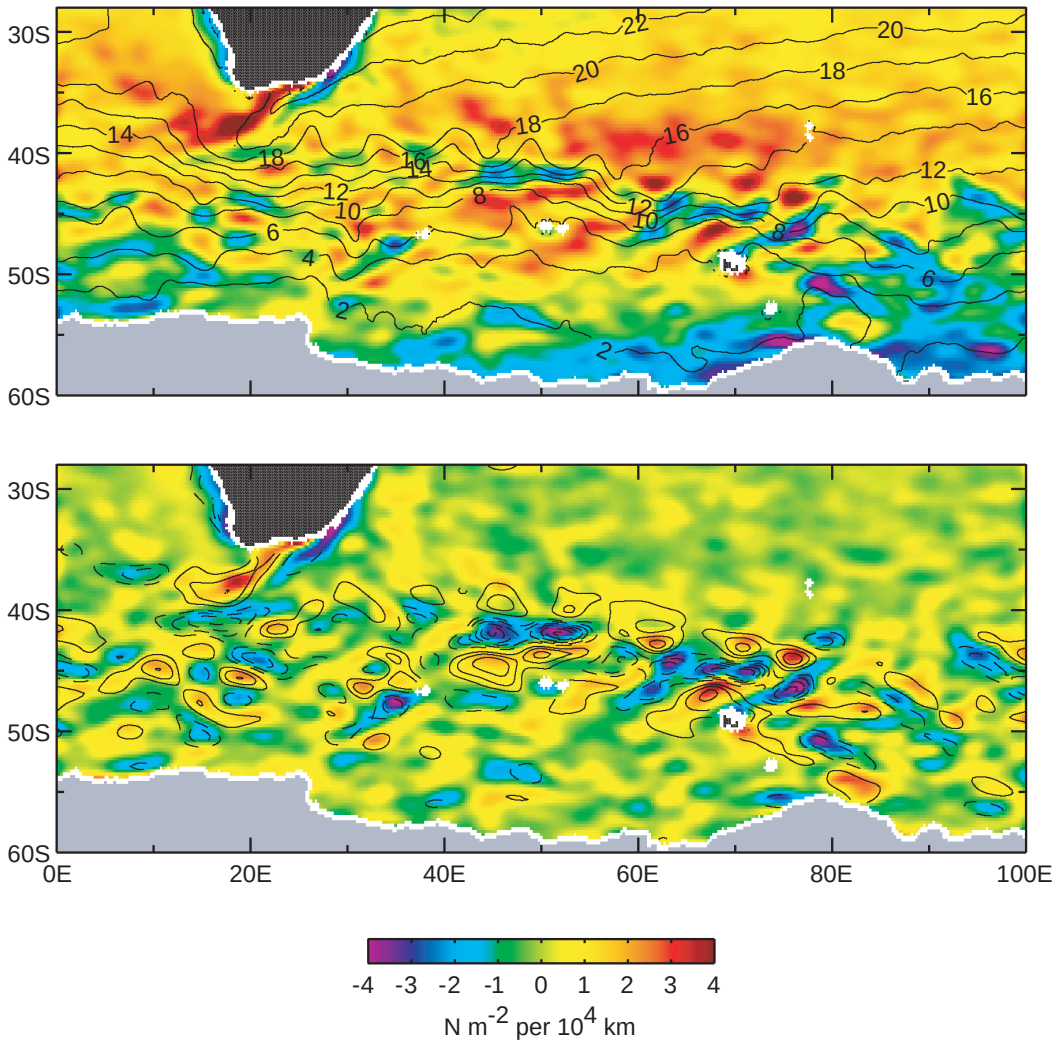

Figure 3.6: Maps of the wind stress curl averaged over the 1-yr period 2 Jun 2002 to 7 Jun 2003 from QuikSCAT of (top) 2° latitude by 4° longitude loess-smoothed fields of wind stress curl (color) and SST (contours); and (bottom) 10° latitude by 30° longitude spatially high-pass filtered fields of wind stress curl (color) and the crosswind SST gradient [contours, with a contour interval of 0.3°C per 100 km]. Dashed and solid contours in the bottom panel correspond to negative and positive crosswind SST gradients, respectively, and the zero contour has been omitted for clarity.

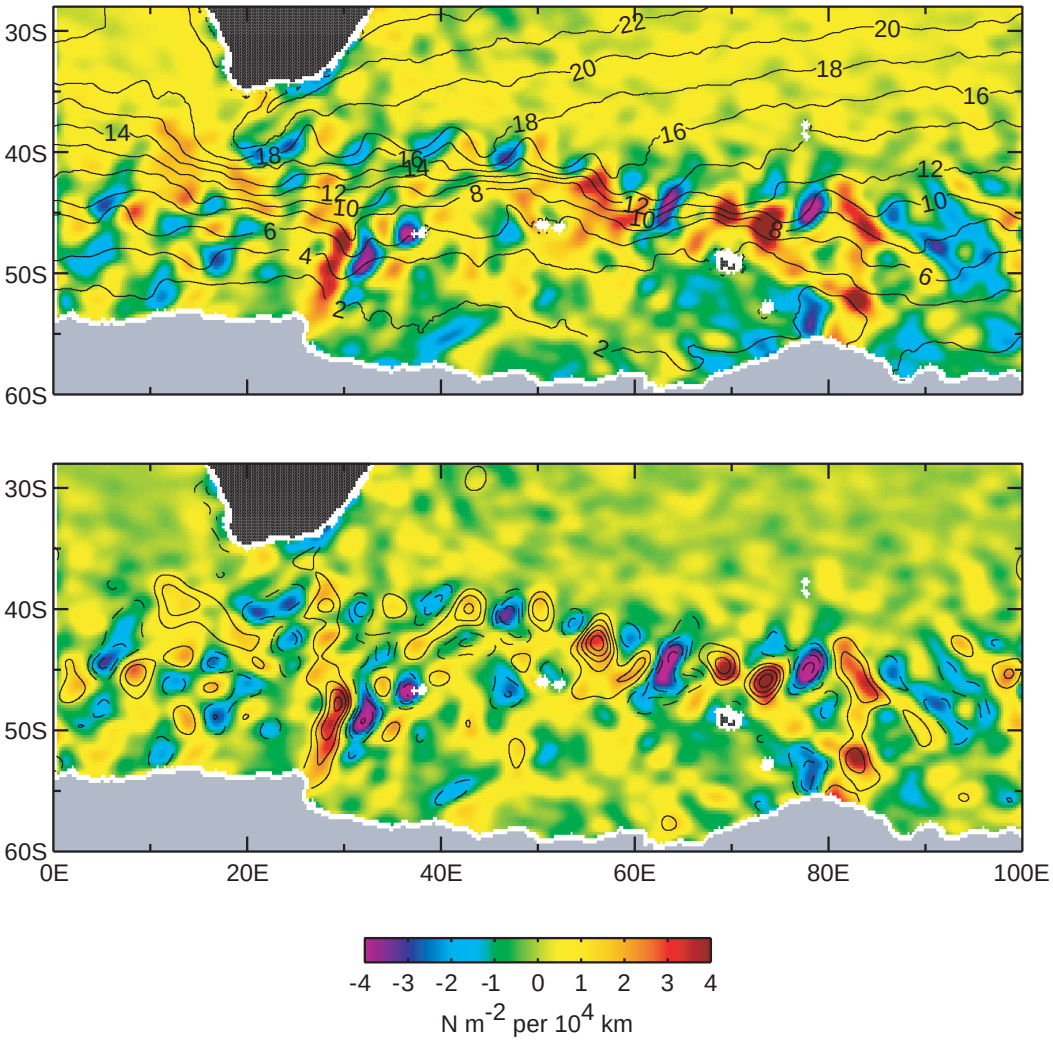

Figure 3.7: As in Fig. 3.6 except for the wind stress divergence and downwind SST gradient [contours, with a contour interval of 0.3°C per 100 km]. Dashed and solid contours in the bottom panel correspond to negative and positive downwind SST gradients, respectively, and the zero contour has been omitted for clarity.

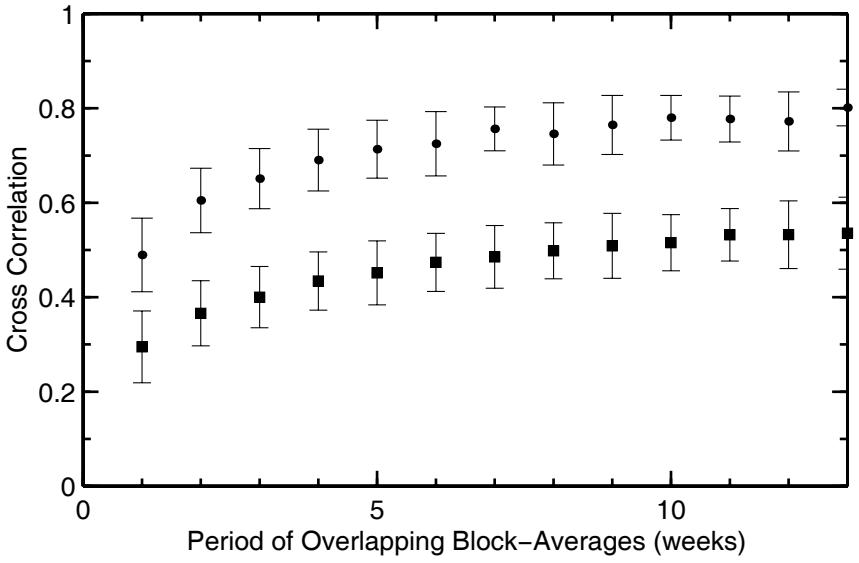

Figure 3.8: Binned scatterplot of the cross correlation between the perturbation wind stress magnitude from QuikSCAT and the perturbation SST as a function of averaging period. The round dots are for the AMSR SST and the squares are for the Reynolds SST. The points represent the mean cross correlation within each bin computed from the maximum number of overlapping block averages at weekly intervals possible within the 1-yr period 2 Jun 2002 to 7 Jun 2003. The error bars represent ± 1 std dev about the means within each bin.

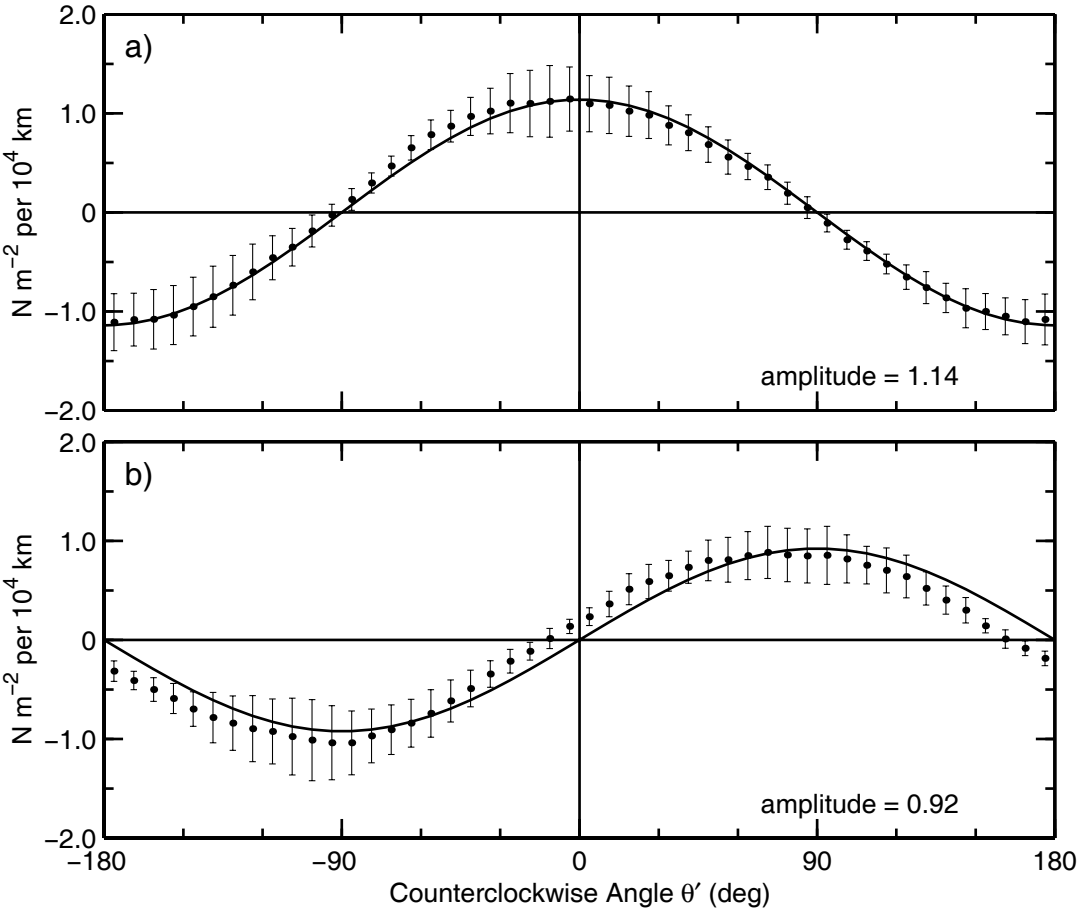

Figure 3.9: Binned scatterplots of the angular dependencies of (a) the perturbation wind stress divergence and (b) the perturbation wind stress curl on the angle θ' defined by Eq. 3.3. The points in (a) and (b) are the means within each bin computed from 17 overlapping 6-week averages over the 1-yr analysis period, and the error bars represent ± 1 std dev of the means within each bin. The solid curves in (a) and (b) represent least squares fits to a cosine and a sine, respectively.

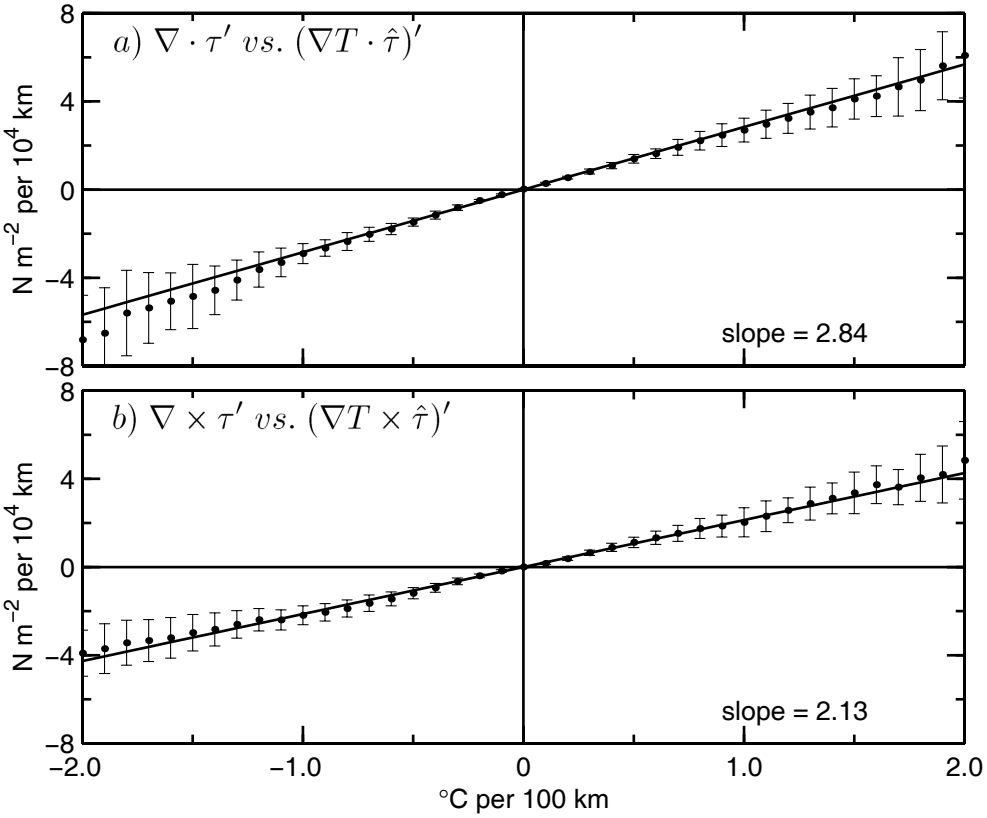

Figure 3.10: Binned scatterplots of the relationships between the perturbation SST and wind stress fields: (a) the perturbation divergence plotted as a function of the perturbation downwind SST gradient; and (b) the perturbation wind stress curl plotted as a function of the perturbation crosswind SST gradient. The points in (a) and (b) are the means within each bin computed from the 17 individual overlapping 6-week averages, and the error bars are ± 1 std dev of the means within each bin. The lines through the points represent least squares fits to straight lines.

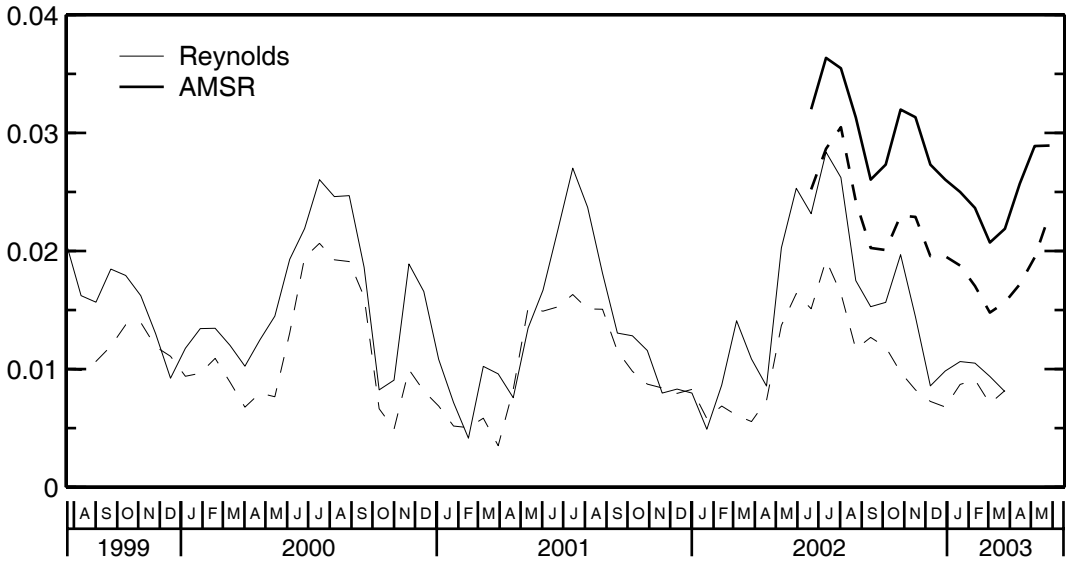

Figure 3.11: Time series of the coupling coefficients α_C (dashed lines) and α_D (solid lines) calculated from the overlapping 6-week block averages. The thick and thin lines represent the coupling coefficients calculated from the AMSR and Reynolds SST fields, respectively.

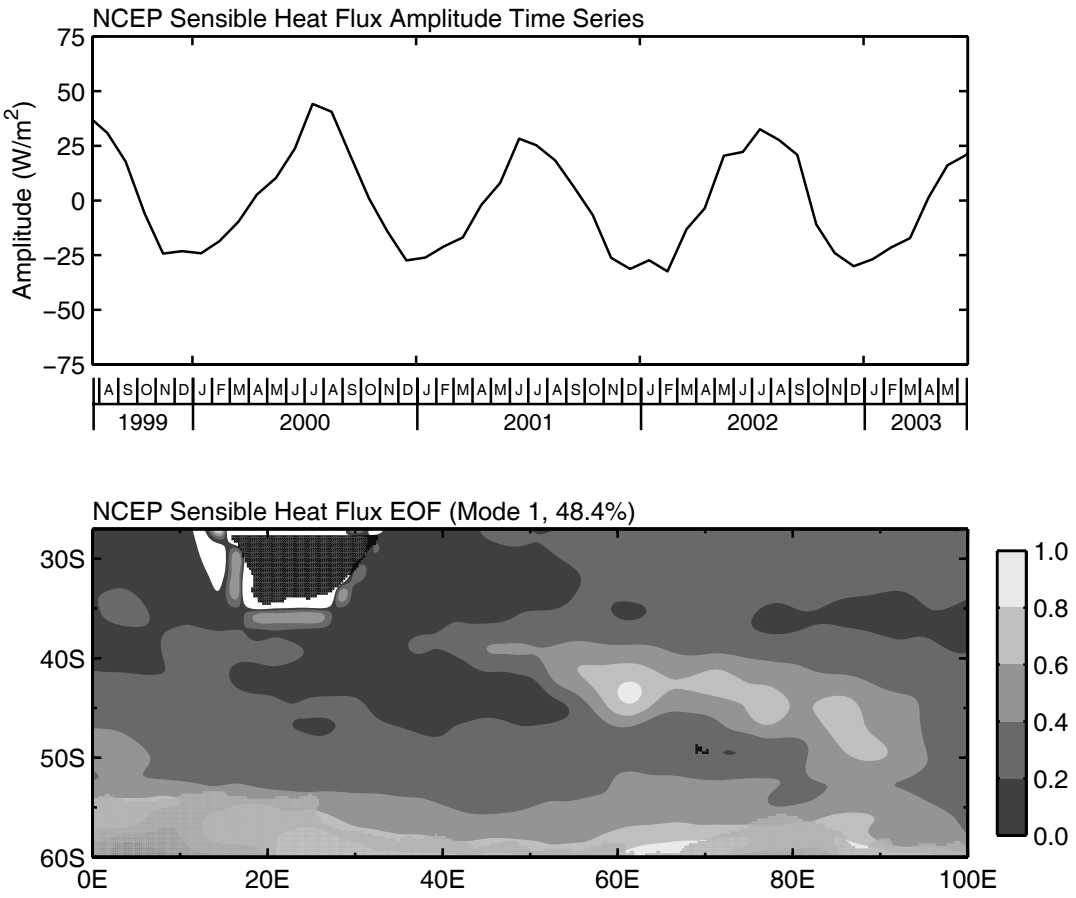

Figure 3.12: (top) First mode amplitude time series and (bottom) the corresponding empirical orthogonal function of the NCEP surface sensible heat flux over the time period from Aug 1999 to May 2003.

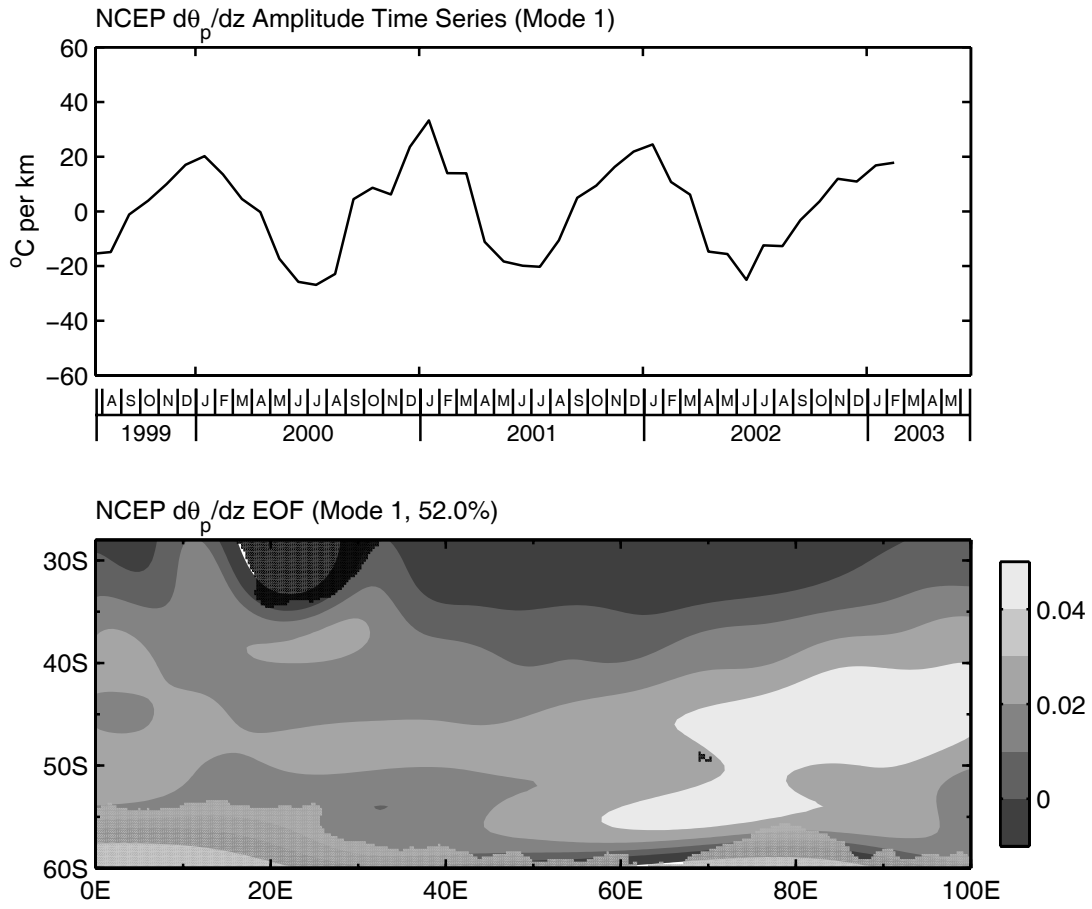

Figure 3.13: As in Fig. 3.12, except for the NCEP potential temperature lapse rate, $\partial\theta_p/\partial z$.

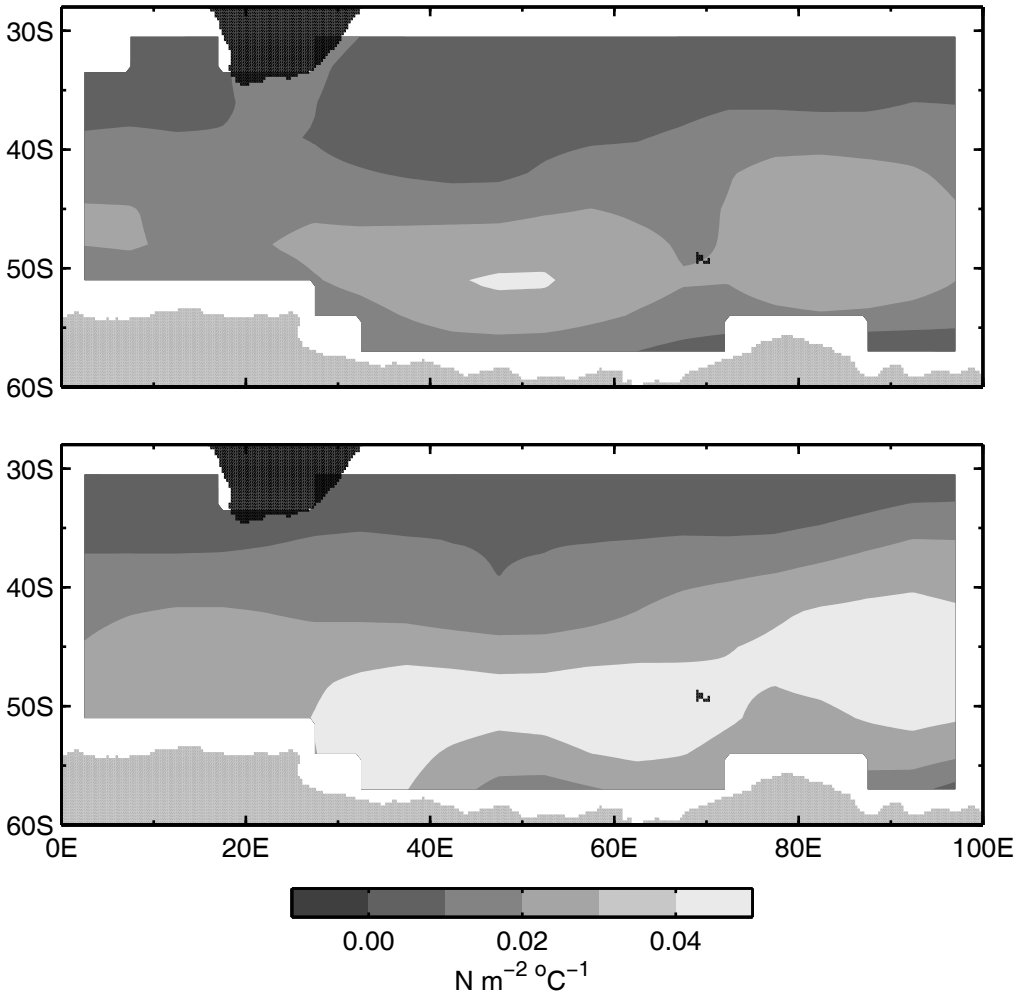

Figure 3.14: Spatial maps of the coupling coefficients α_C (top) and α_D (bottom) averaged over the 1-yr period 2 Jun 2002 to 7 Jun 2003.

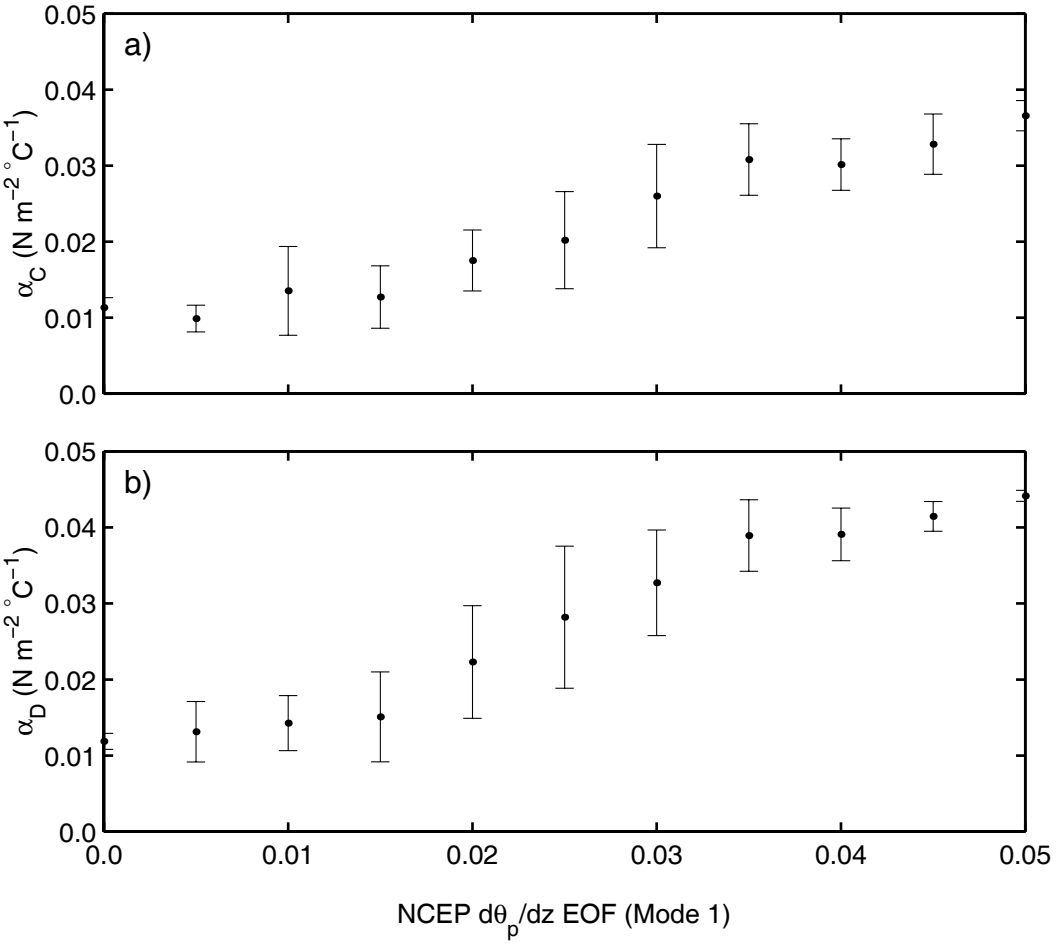

Figure 3.15: Binned scatterplots of the relationships between the NCEP potential temperature lapse rate ($\partial\theta_p/\partial z$) and the coupling coefficients α_C (top) and α_D (bottom).

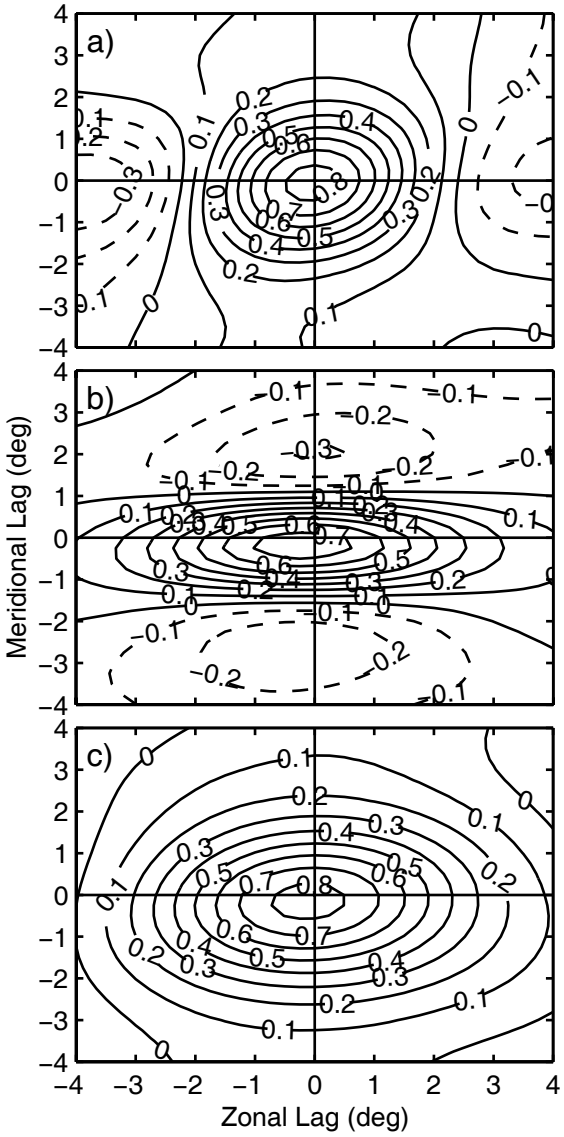

Figure 3.16: Spatial-lagged cross correlations between 1-yr average perturbations: (a) downwind SST gradient and wind stress divergence; (b) crosswind SST gradient and wind stress curl; (c) SST and wind stress magnitude. Negative meridional (zonal) lags indicate that SST perturbations are lagged to the south (west) of wind stress perturbations.

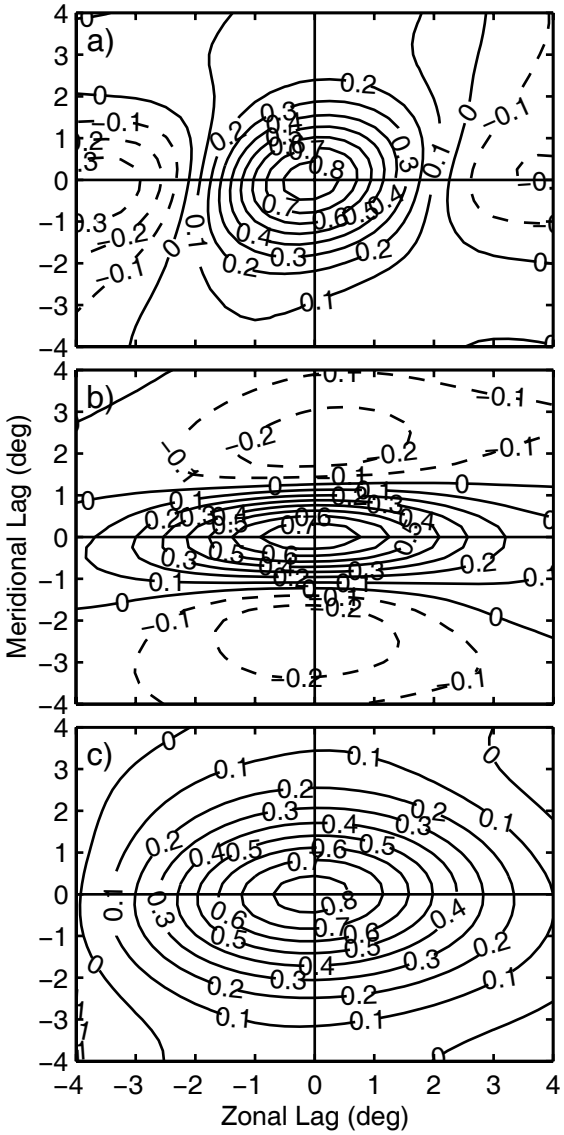

Figure 3.17: As in Fig. 3.16 except based on adjusted wind stress computed with the estimated geostrophic surface currents added to the scatterometer measured winds (see text for details).

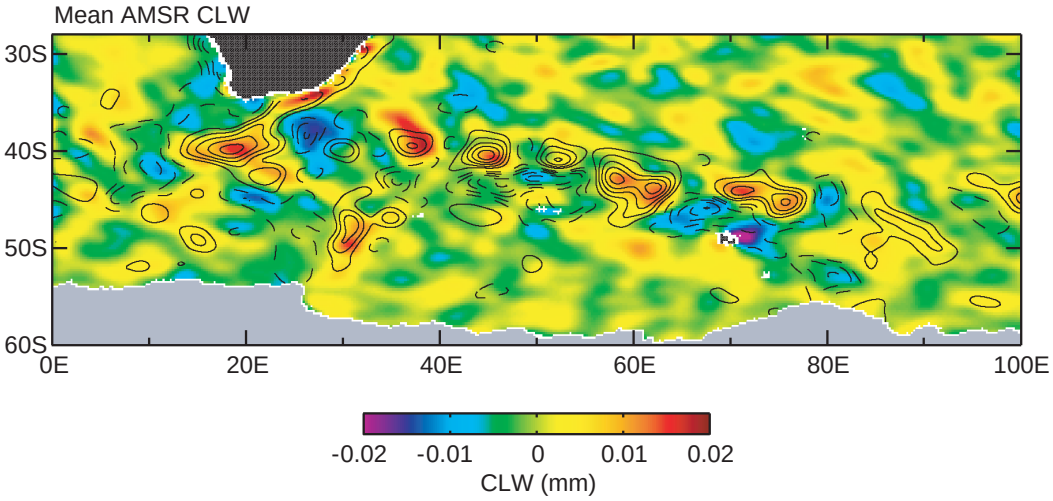

Figure 3.18: Map of AMSR measurements of CLW averaged over the 1-yr period 2 Jun 2002 to 7 Jun 2003 and spatially high-pass filtered to attenuate wavelengths longer than 10° latitude by 30° longitude; the contours overlaid are the average perturbation AMSR SST shown in color in the top panel of Fig. 3.4. The contour interval is 0.5°C and the zero contour has been omitted for clarity.

DYNAMICAL ANALYSES OF THE BOUNDARY LAYER AND SURFACE WIND RESPONSES TO SMALL-SCALE SST PERTURBATIONS: NUMERICAL SIMULATION AND COMPARISON WITH SATELLITE OBSERVATIONS

Larry W. O'Neill, Steven K. Esbensen, Nicolai Thum, and Dudley B. Chelton

To be submitted to Journal of Climate

45 Beacon Street

Boston, MA 02108-3693

Chapter 4

Abstract

The dynamical response of the atmospheric boundary layer (ABL) to meanders in SST fronts is investigated over the Agulhas Return Current using a numerical simulation from the Weather Research and Forecasting (WRF) mesoscale weather prediction model. The response is studied for the month of July 2002 using a steady time-averaged SST field derived from the Advanced Microwave Scanning Radiometer on the EOS-Aqua satellite (AMSR-E). Particular attention is focused here on the response of the vertically-integrated ABL momentum budgets, the vertical structure of the ABL momentum budgets, and the near-surface momentum budgets to small-scale perturbations in the SST field with horizontal spatial scales between 100-1000 km. The simulated surface winds from WRF are compared with satellite wind observations from the SeaWinds scatterometer on the QuikSCAT satellite to test the WRF models ability to accurately simulate the surface wind fields.

Analysis of the ABL momentum budgets indicates that the ABL, upon crossing

an SST front, responds through an advection-modified baroclinic Ekman adjustment mechanism by which vertical turbulent friction is balanced by the horizontal pressure gradient, Coriolis force, and horizontal advection. The exact role of horizontal advection in the response is made clear by consideration of the ABL momentum budgets in the local crosswind direction. In the crosswind momentum budget, the ABL response to SST perturbations is better characterized as a frictionally-modified gradient wind adjustment whereby imbalances between the crosswind pressure gradient, Coriolis force, and the crosswind component of the turbulent friction cause the ABL streamlines to develop curvature. The resulting SST-induced curvature perturbations lead to changes in the direction of the ABL flow on the order of 10°.

Horizontal air temperature gradients created by SST gradient perturbations generate significant vertical variations in the horizontal pressure gradient in lower ABL. The resulting vertical wind shear created by the vertically-varying horizontal pressure gradients are shown to modify the vertical turbulent mixing of momentum within the ABL within the context of the Ekman adjustment mechanism.

4.1 Introduction

Over spatial scales of 100 to 1000 km, satellite observations have consistently shown positive correlations between surface wind speed and sea surface temperature (SST) (see Xie et al. 2004, Chelton et al. 2004, and Small et al. 2007). Small-scale features in the surface wind field are common near large mid-latitude ocean currents and may have significant implications for underlying ocean circulations (Spall 2007a). In this study, the dynamical balances leading to the surface wind response to SST fronts are investigated over the Agulhas Return Current during July 2002 using the Weather Research and Forecasting (WRF) mesoscale numerical weather prediction model.

Observations of the surface wind speed and direction from the SeaWinds scatterometer on the QuikSCAT satellite have shown that the surface wind speed and direction are significantly modified by SST perturbations. Dynamical origins of the wind speed response have been extensively investigated through observations and numerical modeling studies. However, dynamical investigations have not specified the mechanisms leading to the separate response of the wind speed and direction. These dynamical processes are investigated in this study.

Small-scale SST perturbations have a significant effect on the vertical turbulent mixing of momentum within the ABL and enter into the ABL momentum budget through the vertical turbulent stress divergence $\partial \boldsymbol{\tau}/\partial z$, or turbulent friction, where $\boldsymbol{\tau} = (\tau^x, \tau^y)$ is the wind stress vector. To understand how turbulent friction can affect

the surface momentum balance, it is necessary first to understand the relationship between the turbulent friction and surface stress $\boldsymbol{\tau}_s$. When integrated over the depth of the boundary layer H, the turbulent friction term becomes

$$\int_0^H \frac{\partial \boldsymbol{\tau}}{\partial z} dz = \boldsymbol{\tau}_H - \boldsymbol{\tau}_s,$$

where $\boldsymbol{\tau}_H$ is the stress at the top of the boundary layer. It should be noted that H is the depth of the momentum boundary layer rather than the thermodynamic boundary layer, which can be significantly deeper. $\boldsymbol{\tau}_H$ is generally interpreted as a vertical entrainment flux of momentum into the ABL and is much smaller than the surface stress by definition. Surface stress therefore acts as a drag on the vertically-integrated boundary layer flow. The surface stress is not directly related to the vertical turbulent stress divergence term near the surface; rather, it is the vertical divergence of the surface stress over the depth of the momentum boundary layer. This distinction is pivotal for describing how turbulent mixing of momentum within the boundary layer can act both as a drag to the ABL flow while simultaneously accelerating the near-surface winds.

In section 4.2, we describe the model simulation and show the mean surface fields. The ability of the WRF model to accurately simulate the mean fields compared to satellite observations is also established. Dynamical analysis of atmospheric flow at mid-latitudes often follows along a quasi-geostrophic interpretation. In Section 4.3, we present a scale analysis of the surface momentum budget for the problem of flow

over small-scale SST perturbations applicable to the Agulhas Return Current region of interest here. We show that a quasi-geostrophic analysis is not appropriate here because it leaves out dynamics that are essential for describing the observed wind field.

One of the principle objectives of this WRF analysis is to show the distinction between the surface stress and the vertical structure of the turbulent friction term and the implications of this for the surface momentum budget. To this end, we show analysis of the vertically-integrated momentum budgets and the mechanisms responsible for the boundary layer wind response to small-scale SST perturbations in Section 4.4. In this analysis, the role of surface stress as a drag on the vertically-integrated boundary layer flow is made clear. In section 4.4, the response of the boundary layer wind structure to SST perturbations is analyzed. The role of turbulent friction in altering the near-surface winds becomes clear upon considering its role in the vertical redistribution of momentum near the surface, which is modulated by SST-induced surface heating perturbations. Implications of the results in sections 4.4 and 4.4 for the surface momentum budget are presented in section 4.6 along with a complete dynamical analysis of the surface momentum budget. The resulting SST-induced response of the boundary layer vertical structure affects both the surface wind speed and direction. A straightforward dynamical explanation is presented to account for these surface wind perturbations, consistent with the boundary layer vertically-integrated momentum budgets and the vertical structure of the terms within the

momentum budgets.

4.2 Model Simulation

4.2.1 Numerical methods

We used the Weather Research and Forecasting (WRF) numerical weather prediction model to simulate the atmospheric response to small-scale SST perturbations over the Agulhas Return Current. The WRF model is the next generation of the widely adopted PSU/NCAR MM5 model. Specific details about the options used in this model simulation are provided in Appendix A; the basic model configuration used in this analysis is briefly described. For the SST boundary condition, we used a steady, monthly-averaged SST field for July 2002 derived from SST observations made by the AMSR-E. The month of July was chosen because the surface winds have been shown to respond much stronger during the austral winter (O'Neill et al. 2005). Because the meanders in this portion of the Agulhas Return Current are quasi-stationary during this 1-month period, we kept the SST field constant throughout the 1-month simulation for simplicity.

The model simulation was performed using a 3-nested configuration. The horizontal resolution of the outer nest was 75 km, the middle nest 25 km, and the inner nest was 8.3 km. In this analysis, we consider only the model fields from the inner fine resolution nest. At the lateral boundaries of the outer nest, the model dynamic and

thermodynamic variables were updated every 6 hours using the National Centers for Environmental Prediction (NCEP) operational analyses for the period of this analysis. During this period, several large-scale transient weather disturbances propagated through the domain that were initiated outside of the domain. Using the NCEP boundary conditions thus enabled us to make a more realistic simulation for this time period to compare with the QuikSCAT wind observations.

The simulation was performed using a stretched vertical grid with 69 levels in the vertical, including 19 layers below 1000 m. The lowest model level extended from the surface to 12 m height and the highest model level was near 20 km above the surface. We chose this fine vertical resolution to accurately resolve the turbulent momentum exchange associated with the formation of convectively unstable and stable internal boundary layers as near-surface air flows across SST fronts (Thum 2006).

The boundary layer parameterization scheme implemented for this simulation was developed by Grenier and Bretherton (2001) (a detailed discussion of this boundary layer scheme is included in Appendix A). Briefly, the ABL scheme is based on a 1.5-level turbulent closure scheme which includes detailed handling of moist ABL processes. The surface momentum flux was computed using a similarity-based formulation which uses a momentum roughness length from Charnock's relation to compute the surface friction velocity over the ocean. The ocean surface was assumed stationary for this analysis. Song et al. (2006) has shown that including the 1-2 m/s surface ocean current velocities associated with the Gulf Stream in the surface friction veloc-

ity computation made small but noticeable differences in the near-surface turbulent friction. In this region of the Agulhas Return Current, however, surface ocean current velocities are only around 0.5-0.75 m/s within a small latitudinal band centered around 45°S latitude. We thus expect that inclusion of ocean current effects in the surface stress computations would only lead to minor differences from the simulation presented here.

4.2.2 Simulated surface fields

Fig. 4.1 shows the 1-month average AMSR-E SST field used as the lower boundary condition in the WRF simulation analyzed here. Removal of the large-scale SST field by spatial high-pass filtering reveals a rich array of SST perturbations corresponding to intrusions of water associated with the meandering ARC (panel b, Fig. 4.1). Spatial filtering of the wind fields is also necessary to remove large-scale spatial weather variability and the large-scale background wind field not directly influenced by the small-scale SST perturbations of interest here. Spatially high-pass filtered fields were isolated for this study by removing spatially low-pass filtered fields using a multi-dimensional loess smoothing function with half-power cutoff wavelengths of 20° longitude by 10° latitude (Schlax et al. 2001), similar to the smoothing characteristics of a 12° longitude by 6° latitude block-average smoother. Hereafter, fields spatially high-pass filtered in this manner are referred to as perturbation fields.

Perturbations in the model surface pressure field are located downstream of SST

perturbations and form as a balance between surface heating and boundary layer temperature advection (i.e., Small et al. 2003). Low pressure perturbations form about 100-200 km downwind of warm SST perturbations while high pressure perturbations form about the same distance downwind of cool SST perturbations (panel c, Fig. 4.1). Magnitudes of these SST-induced surface pressure perturbations are about ± 0.2 hPa, which are comparable to those found in other observational and modeling studies (e.g., Wai and Stage 1989; Small et al. 2003; Cronin et al. 2003; Song et al. 2006).

The model winds are well-developed during the month of July 2002 considered here, with the 1-month scalar-averaged wind speeds increasing from about 10 m/s over the western portion of the domain to nearly 16 m/s over the southeastern portion (panel d, Fig. 4.1). Westerly flow in the western portion of the domain progressively becomes more southwesterly towards the east, as evident by the southwest to northeast tilt of the surface streamlines of the 1-month vector-averaged surface wind (panel d, Fig. 4.1). Small-scale structures in the WRF surface wind speed field very closely coincide with small-scale perturbations in the SST field (panel e, Fig. 4.1).

WRF accurately simulates the perturbation surface wind field, as evident from comparisons of the 1-month scalar-averaged perturbation surface wind speed from WRF and QuikSCAT (Fig. 4.2). The relative locations of the WRF wind speed maxima compare well with the satellite observations. To quantify these qualitative comparisons, the 1-month scalar-averaged perturbation wind speed is plotted as a function of the 1-month averaged perturbation SST (Fig. 4.3) from the WRF simula-

tion and QuikSCAT observations. The perturbation wind speed V' is linearly related to the perturbation SST T' in both the WRF and QuikSCAT and can be expressed as

$$V' = \alpha_0 T'. \tag{4.1}$$

The slope α_0 computed from the WRF simulation is nearly identical to that computed from the QuikSCAT observations. The close correspondence between the perturbation wind speed response to SST perturbations from the WRF simulation with the observed response from QuikSCAT gives confidence in the WRF model's ability to accurately simulate the momentum budget associated with the SST-induced perturbation surface wind.

SST perturbations do not simply modify the surface wind speed along the direction of the streamlines of the large-scale flow; the surface winds tend to deflect equatorward over warm SST perturbations and poleward over cool SST perturbations (Fig. 4.1f). One goal of this study is to investigate the dynamics associated with these deflections from analysis of the WRF momentum budgets. In Chapter 5, we further show that these SST-induced wind deflections generate significant curvature vorticity and diffluence that are correlated with the SST gradients. Since the wind stress curl and surface vorticity are closely related quantities, correlations between the vorticity and crosswind SST gradients suggest a potentially important feedback onto the ocean from these SST-induced wind perturbations. Indeed, we showed in Fig. 2.8

that the Ekman pumping velocity computed from the SST-induced wind stress curl perturbations spanned nearly as large of a dynamic range as that computed from the large-scale curl field.

Since the winds are generally westerly throughout this region, these surface wind deflections are mostly associated with the meridional wind component. Meridional wind perturbations are, on average, positive over warm SSTs and negative over cool SSTs, as shown by histograms of the meridional wind component separated by warm and cool SST perturbations (bottom panel, Fig. 4.4). Since the dynamic range of the meridional wind is smaller than the dynamic range of the zonal wind perturbations (top panel, Fig. 4.4), we infer that the zonal wind response to SST perturbations is much different than the meridional wind response.

4.3 Scale analysis of momentum budgets

Mid-latitude atmospheric flow is often assumed to be in quasi-geostrophic (QG) balance. A scale analysis applied to the current problem of large-scale surface winds over small-scale SST perturbations, however, reveals that a QG interpretation is not appropriate. Consider the surface wind field (u, v) as the sum of large-scale $(\widetilde{U}, \widetilde{V})$ and small-scale (U', V') components, where primes denote small-scale perturbations representative of the spatially high-pass filtered wind and tildes denote the large-scale flow representative of the spatially low-pass filtered wind. The following scalings, which are appropriate over the Agulhas Return Current, are used: $\widetilde{U} \sim O(10$

m/s); $\widetilde{V} \sim O(1 \text{ m/s})$; and $(U', V') \sim O(1 \text{ m/s})$, which implies that $\frac{U'}{\widetilde{U}} << 1$ and $\frac{V'}{\widetilde{V}} \sim O(1)$. This scaling indicates that the meridional advection terms, $v\frac{\partial}{\partial y}(u, v)$, are small compared to the zonal advection terms and are therefore not retained in this scale analysis. Small wavelength perturbations in the horizontal advection terms are isolated by noting that $\frac{\partial(U', V')}{\partial x, y} >> \frac{\partial(\widetilde{U}, \widetilde{V})}{\partial x, y}$. Noting further that the local time derivative and vertical advection terms are small relative to the other terms [1], the zonal and meridional momentum equations appropriate for these scalings are

$$\widetilde{U}\frac{\partial U'}{\partial x} - fv = -fv_g - F_x$$
$$\widetilde{U}\frac{\partial V'}{\partial x} + fu = fu_g - F_y,$$

where F_x and F_y are the turbulent friction components in the zonal and meridional directions, respectively. Splitting the velocity into geostrophic and ageostrophic parts $u = u_g + u_a$ and $v = v_g + v_a$ yields

$$\widetilde{U}\frac{\partial U'}{\partial x} - fv_a = -F_x$$
$$\widetilde{U}\frac{\partial V'}{\partial x} + fu_a = -F_y$$

Define $F_x = \widetilde{F}_x + F'_x$ and $F_y = \widetilde{F}_y + F'_y$, where $(\widetilde{F}_x, \widetilde{F}_y)$ and (F'_x, F'_y) are the large-scale

[1] To formally justify neglecting the near-surface vertical advection, we scale w using the continuity equation $w \sim h\big(\partial u/\partial x + \partial v/\partial y\big)$, where h is taken to be 10 m. For a typical divergence of 10^{-5} s^{-1} associated with small-scale SST perturbations, $w \sim O(10^{-4}$ m/s). For a scale of the near-surface vertical wind shear, we use a scaling derived from similarity theory for a neutrally-stratified surface layer $u_*/(0.4h)$, where u_* is the surface friction velocity. For a typical value of $u_* = 0.3$ m/s, $\partial u/\partial z \sim O(0.1$ s$^{-1})$. This implies that the near-surface vertical advection term is $O(10^{-5}$ s$^{-1})$, which is an order of magnitude smaller than the horizontal advection.

and small-scale components of the turbulent friction, respectively. It then follows that the large-scale ageostrophic zonal wind must balance the large-scale turbulent friction such that $f\widetilde{V}_a = \widetilde{F}_x$ and $f\widetilde{U}_a = -\widetilde{F}_y$; this states that the large-scale surface flow is in Ekman balance. Further note that $\widetilde{U}_a/\widetilde{U}_g << 1$ while U'_a/U'_g and $V'_a/V'_g \sim O(1)$, which yields

$$\widetilde{U}_g \frac{\partial U'_g}{\partial x} + \widetilde{U}_g \frac{\partial U'_a}{\partial x} - fV'_a = -F'_x$$
$$\widetilde{U}_g \frac{\partial V'_g}{\partial x} + \widetilde{U}_g \frac{\partial V'_a}{\partial x} + fU'_a = -F'_y.$$

Advection of the ageostrophic wind by the geostrophic wind in both the zonal and meridional momentum balances is comparable to the other terms in the equations, thus making a QG interpretation inapplicable to describe the surface wind response to small-scale SST perturbations. Unlike the large-scale wind field, the small-scale surface winds are not in Ekman balance but are modified by zonal advection from the large-scale geostrophic winds. From this scale analysis, the response of the small-scale winds to SST perturbations is anticipated to consist of an Ekman-balanced response modified by horizontal advection.

4.4 Vertically-integrated momentum budgets

A widely held view regarding how SST perturbations affect surface winds involves the stability-dependent modification of the vertical turbulent mixing of momentum

within the ABL (e.g., Sweet et al. 1981; Wallace et al. 1989; Hayes et al. 1989). However, it has not been clear how turbulent friction near the surface can accelerate near-surface winds while simultaneously acting as a drag to the total ABL flow.

We gain insight into this question by first investigating the dynamical balances of the vertically-integrated ABL flow. The vertically-integrated momentum budgets analyzed here are

$$\int_0^H \Big(- u\frac{\partial u}{\partial x} - v\frac{\partial u}{\partial y} - w\frac{\partial u}{\partial z} + fv - \frac{1}{\rho}\frac{\partial p}{\partial x}\Big) dz - \overline{u'w'}\mid_{(z=H)} + \overline{u'w'}\mid_{(z=0)} = 0 \quad (4.2)$$

$$\int_0^H \Big(- u\frac{\partial v}{\partial x} - v\frac{\partial v}{\partial y} - w\frac{\partial v}{\partial z} - fu - \frac{1}{\rho}\frac{\partial p}{\partial y}\Big) dz - \overline{v'w'}\mid_{(z=H)} + \overline{v'w'}\mid_{(z=0)} = 0 \quad (4.3)$$

where u and v are the zonal and meridional wind components, respectively, f is the Coriolis parameter, ρ is the air density, p is the air pressure, and $\overline{u'w'}$ and $\overline{v'w'}$ are the subgrid-scale Reynolds stresses in the zonal and meridional directions, respectively. It is noted here that the local acceleration and the horizontal turbulent flux divergence are both much smaller than the other terms when averaged over the 1-month period analyzed here and are hereafter ignored. The turbulent stress at $z = H$ is mainly caused by entrainment of momentum from the free atmosphere into the boundary layer, and is relatively small compared to the other terms in the vertically-integrated momentum budget. Therefore, the vertically-integrated turbulent friction is nearly equal to the surface stress $\boldsymbol{\tau}_s = -\rho(\overline{u'w'}, \overline{v'w'})\mid_{(z=0)}$. Throughout the remaining analysis, the forces in these budgets were averaged over the 1-month simulation period July 2002.

The boundary layer depth H used for the vertical integration was chosen to be a spatially and temporally constant height of 926 m, which is the height of the 18th vertical level of the model grid above the sea surface. A constant height was chosen because, over most of the model domain, the zonal and meridional components of the turbulent friction term tended towards 0 above this level. Furthermore, SST-induced small-scale perturbations in the forcing terms in the momentum budgets tended to be small above any reasonably defined boundary layer top with little difference between warm and cool SST perturbations. Integrating some distance above $H = 926$m did not change the vertically-integrated budgets or their interpretation in any significant way. Results based on more elaborate methods that explicitly account for a spatially and temporally variable H and entrainment were not qualitatively different from those presented here using a spatially and temporally constant H.

Small-scale SST perturbations significantly impact the boundary layer wind, pressure, and thermodynamic fields (Fig. 4.5). Warm air temperature and low pressure perturbations are located $\sim$100 km downwind of warm SST perturbations while cool air temperature and high pressure perturbations are located a similar distance downwind of cool SST perturbations (Fig. 4.5b). The vertically-integrated wind speed does not show as simple a relationship with the underlying SST perturbations or with the surface wind speed, however. Evidently, the horizontal structure of the perturbation winds aloft is much different than the structure near the surface shown in the bottom panel of Fig. 4.2.

Vectors of the unfiltered vertically-integrated momentum budget are shown in the top panel of Fig. 4.6. To a large extent, the large-scale vertically-integrated boundary layer flow can be described as a geostrophic balance between the Coriolis and pressure gradient forces; therefore, only the ageostrophic components are considered. Departures from this balance arise from turbulent friction and advection of momentum. Turbulent friction acts as a drag to the vertically-integrated boundary layer flow, as evident from the blue vectors opposing the westerly flow throughout the region. Vertically-integrated advective forces are most pronounced over warm SST perturbations, where horizontal advection (green vectors) tends to accelerate the boundary layer air poleward across streamlines of the ABL flow.

We computed the perturbation components of each term in Eqns. 4.2 and 4.3 to isolate of the effects of small-scale SST perturbations on the vertically-integrated momentum budgets. The resulting perturbation force vectors are shown in the bottom panel of Fig. 4.6. Vertically-integrated pressure gradient vectors point into perturbation low pressure centers located downwind of warm SST perturbations and away from perturbation high pressure centers located downwind of cool SST perturbations. Perturbation surface stress vectors point downwind over warm SST perturbations and upwind over cool SST perturbations, consistent with increased surface stress over warm water and decreased surface stress over cool water. The perturbation Coriolis force accelerates the boundary layer flow equatorward over warm SST perturbations and poleward over cool SST perturbations and is attributable to stronger boundary

layer flow over warm SST perturbations compared to cool SST perturbations.

Information in the vertically-integrated momentum budgets is consolidated by considering the momentum budgets described in Eqns. 4.2 and 4.3 rotated into local crosswind and downwind coordinates. The vertically-integrated crosswind and downwind momentum budgets, respectively, are expressed as

$$\int_0^H \Big(- V\frac{D\psi}{Dt} - fV - \frac{1}{\rho}\frac{\partial p}{\partial n} - \boldsymbol{F}\cdot\hat{n}\Big)dz = 0 \tag{4.4}$$

$$\int_0^H \Big(- \frac{DV}{Dt} - \frac{1}{\rho}\frac{\partial p}{\partial s} - \boldsymbol{F}\cdot\hat{s}\Big)dz = 0, \tag{4.5}$$

where (s, n) are the local downwind and crosswind spatial coordinates, respectively, V is the wind speed, ψ is the counterclockwise wind direction relative to the fixed zonal direction, $D/Dt = \partial/\partial t + V\partial/\partial s + wV\partial/\partial z$ is the material time derivative, and $\boldsymbol{F}\cdot\hat{n}$ and $\boldsymbol{F}\cdot\hat{s}$ are the crosswind and downwind components of the vertical turbulent friction $\boldsymbol{F} = (F^x, F^y)$, respectively. By assuming entrainment at the ABL top is negligible, the vertically-integrated $\boldsymbol{F}\cdot\hat{n}$ and $\boldsymbol{F}\cdot\hat{s}$ are equal to the surface stress components in the crosswind and downwind directions, respectively.

Transects of the unfiltered crosswind and downwind components of the vertically-integrated momentum budgets are shown in Fig. 4.7 along 44.4°S latitude. In the downwind direction (top panel of Fig. 4.7), the downwind component of the surface stress very nearly balances the downwind component of the pressure gradient. In the crosswind direction (bottom panel of Fig. 4.7), the Coriolis force is almost exactly balanced by the crosswind component of the pressure gradient, with very little contri-

bution from the crosswind turbulent stress and advective components. The large-scale vertically-integrated boundary layer flow shown in Fig. 4.7 is therefore very nearly in Ekman balance. Note that the pressure gradient force, surface stress, and Coriolis force all increase in magnitude towards the eastern half of the domain, resulting from zonal variations in the mean large-scale forcing unrelated to the SST-induced perturbations of interest here.

Zonal transects of the perturbation components of the vertically-integrated crosswind and downwind momentum budgets defined by Eqns. 4.4 and 4.5 are shown in Fig. 4.8 along latitudes corresponding to the northern, middle, and southern edges of the SST perturbation located near 62°E, 44°S. These transects complement more complete maps of the perturbation forcing terms and SST shown later in Figs. 4.9 and 4.10. In the downwind direction (left column of panels, Fig. 4.8), the perturbation downwind component of the surface stress tends to oppose the vertically-integrated downwind pressure gradient perturbations. The downwind surface stress perturbations correlate well with the SST perturbations. Imbalances between the surface stress and the vertically-integrated downwind pressure gradient lead to non-zero values for DV/Dt.

In the crosswind direction (right column of panels, Fig. 4.8), the primary balance is between the vertically-integrated Coriolis force, pressure gradient, and horizontal advection, with the crosswind component of the surface stress of contributing very little. The crosswind component of the horizontal advection ($V^2 \partial\psi/\partial s$) is of-

ten expressed as the centrifugal force V^2/R, where $R^{-1} = \partial\psi/\partial s$ is the radius of curvature of the local streamline. The balance of forces in the crosswind direction indicate that the perturbation vertically-integrated boundary layer response to SST perturbations is in gradient wind balance (e.g., Holton 1992, Pg. 67). The streamlines of the vertically-integrated ABL flow develop curvature since the SST-induced crosswind pressure gradient does not fully balance the Coriolis force. Centrifugal force perturbations diminish as the boundary layer adjusts toward an Ekman balance downstream of SST perturbations. As will be shown in the next section, the flow curvature is mainly confined to the lowest 400 m of the ABL where the SST-induced crosswind pressure gradients are most significant. The development of curvature indicates that the direction of ABL flow changes along its trajectory while passing over SST perturbations.

Simple dynamical considerations indicate that a balance between crosswind pressure gradient and Coriolis forces is achieved within a distance on the order of the Rossby radius of deformation L. For a two-layer boundary layer, L can be estimated as

$$L = \frac{\sqrt{g'H}}{f},$$

where $g' = g\frac{\theta_2-\theta_1}{\theta_1}$ is the reduced gravity, $g = 9.8$ m/s^2 is the gravitational constant, and θ_1 and θ_2 are the potential temperatures in the bottom and top layers, respectively. For $f = 10^{-4}\ s^{-1}$, $\theta_2 = 285$ K, $\theta_1 = 280$ K, and $H = 1000$ m, L is about 150 km. The SST-induced gradient wind balance can be expected to be valid within

this distance downwind of SST perturbations. Beyond this distance, the crosswind balance between pressure gradient and Coriolis forces and the balance between downwind pressure gradients and surface stress indicate a transition from gradient wind balance to an Ekman balance. Since the spatial scales of the SST perturbations are nearly of this magnitude, the vertically-integrated boundary layer flow waxes and wanes between gradient wind and Ekman balances as the boundary layer flows over the quasi-periodic series of SST perturbations shown in Fig. 4.1b.

Dynamically, the adjustment of the vertically-integrated boundary layer flow while crossing an SST front results in a perturbation crosswind pressure gradient developing in opposition to the Coriolis force. A near balance between this crosswind pressure gradient and the Coriolis force is established within a distance comparable to the $\sim$ 150 km deformation radius. For a mean wind speed of 10 m/s, this implies an adjustment timescale of roughly 4 hours for the ABL to evolve from a gradient wind balance to an Ekman balance. There are thus multiple timescales present in the adjustment of the boundary layer to small-scale SST perturbations: one associated with the adjustment of the surface stress to the downwind pressure gradient, and one associated with the adjustment of the Coriolis force to the crosswind pressure gradient.

Maps of the 1-month averaged perturbation crosswind and downwind momentum budgets are shown in Figs. 4.9 and 4.10, respectively. In the downwind momentum budget, the surface stress is enhanced over warm SST perturbations and reduced

over cool SST perturbations and balances a large portion of the vertically-integrated downwind pressure gradient. The imbalance between them causes boundary layer air parcels to decelerate ($DV/Dt < 0$) upwind of warm SST perturbations and accelerate ($DV/Dt > 0$) upwind of cool SST perturbations (Fig. 4.10).

When taken together, the crosswind and downwind momentum budgets here show that the vertically-integrated ABL winds are in a frictionally-modified gradient wind balance. Horizontal advection modifies this state by changing the speed and direction of the vertically-integrated flow.

Vertical advection of momentum is significant in magnitude when integrated over the depth of the boundary layer (Figs. 4.9 and 4.10). The patterns of vertical advection are consistent with the patterns of vertical velocity expected from convergence and divergence of ABL flow that occur in regions of strong perturbation downwind SST gradients.

In summary, the unfiltered large-scale vertically-integrated turbulent friction term, which is equal to the surface stress, uniformly acts as a drag to the boundary layer flow. Small-scale perturbations of the surface stress, however, increase in magnitude over warm SST perturbations and decrease in magnitude over cool SST perturbations. Dynamically, the vertically-integrated ABL winds respond to SST perturbations through an Ekman adjustment mechanism modified by horizontal advection. The crosswind momentum budget indicates that horizontal advection acts in a more specific manner such that the response may also be characterized as a frictionally-

modified gradient wind adjustment. Some distance downwind from an SST front, the ABL readjusts to an Ekman balance within a distance proportional to the deformation radius.

4.5 Response of the ABL vertical structure to SST perturbations

We have shown in Section 4.2 that perturbations of the surface meridional wind tend to be equatorward over warm SST perturbations and poleward over cool SST perturbations in this simulation. Since the large-scale surface winds are westerly in this region, the changes in surface wind direction coupled to the SST perturbations are primarily associated with these meridional wind perturbations. In this section we provide a dynamical explanation for both the meridional and zonal wind perturbations based on an analysis of the momentum budgets simulated by the WRF model. The zonal and meridional momentum budgets analyzed here are expressed as

$$-u\frac{\partial u}{\partial x} - v\frac{\partial u}{\partial y} + fv - \frac{1}{\rho}\frac{\partial p}{\partial x} - F^x = 0 \tag{4.6}$$

$$-u\frac{\partial v}{\partial x} - v\frac{\partial v}{\partial y} - fu - \frac{1}{\rho}\frac{\partial p}{\partial y} - F^y = 0. \tag{4.7}$$

Height-longitude cross-sections of the simulated 1-month average zonal and meridional wind components are shown in Fig. 4.11 along 44.4°S. At the bottom of each panel, the perturbation SST boundary condition is indicated by the color bar, with

red corresponding to warm SST and blue to cool SST. The zonal and meridional wind response to these SST perturbations differs significantly from each other in the WRF simulations. At the surface, the zonal wind component has local maxima over warm water and local minima over cool water, consistent with previous observations. The zonal winds increase monotonically with height, while the meridional wind field contains a band of poleward or locally weak equatorward flow at low levels between about 100 and 200 meters. From the ageostrophic wind components shown in Fig. 4.12, it is apparent that this band of equatorward flow is related to Ekman drift; i.e., ABL turbulent friction in the zonal direction causes poleward ageostrophic flow, as evident from comparison of the meridional ageostrophic wind component in Fig. 4.12b with the zonal component of the turbulent friction force in Fig. 4.13c. In the lowest 200 m, the meridional wind shear is weaker over warm SST perturbations and stronger over cool SST perturbations (Fig. 4.12). The meridional winds become more poleward with height over cool SST perturbations compared to warm SST perturbations.

Based on the force balances in the WRF simulation shown in Figs. 4.13 and 4.14, the coupling between small-scale SST perturbations and the boundary layer wind structure can be conceptualized by dividing the lower atmosphere into 3 layers (Fig. 4.15). Above the momentum boundary layer top near 700 m, the zonal and meridional force balances in Figs. 4.13 and 4.14 show that the free atmosphere is in near geostrophic balance, with only weak effects of small-scale SST perturbations

evident in the the wind fields. In the middle layer (approximately between 400 and 700 m height), turbulent friction and the effects of SST-induced pressure gradients become significant. Advective effects are small in the zonal momentum budget and the flow is in Ekman balance. In the meridional momentum budget, the strong zonal wind acting on large zonal gradients of u and v creates significant advective effects in the middle layer, tending to shift the anomalies eastward.

The wind response to the SST perturbations in the lowest 200 m may be regarded as baroclinic Ekman flow modified by horizontal advection. Our interpretation is that the zonal turbulent friction perturbations are ultimately the cause of the meridional wind perturbations through Ekman adjustment. Advection of zonal and meridional wind perturbations by the strong zonal flow tends to shift zonal and meridional perturbations downstream; the Rossby number approaches unity. However, unlike the rapidly changing boundary layer conditions at a sharp SST front (e.g., Thum 2006), the boundary layer structures are everywhere in quasi-equilibrium with the surface conditions more than a deformation radius downstream of an SST perturbation, which was estimated to be 150 km in this region. Momentum advection may therefore be regarded as a modifying influence.

Before examining the near-surface meridional momentum budget in detail, consider the generation of the near surface zonal wind perturbations shown the Fig. 4.11a. The zonal wind anomalies are strongly ageostrophic (Fig. 4.12a) and are the result of SST-induced perturbations in the zonal pressure gradient and turbulent friction

forces (panels a and c, Fig. 4.14).

Sensible heat flux anomalies also have strong effects on turbulent kinetic energy generation and turbulent mixing of zonal momentum in the ABL. Over warm SST perturbations, there is a simultaneously strong vertical transport of westerly momentum toward the surface and a well mixed u-momentum layer (see panels a and b, Fig. 4.16). Over cold water, stable conditions weaken the turbulent momentum transport and the zonal wind shear increases.

The surprising aspect of turbulent momentum mixing and friction over the SST perturbations is that wind stress and friction anomalies are not coincident (panels b and c, Fig. 4.16). For example, local maxima of the zonal surface stress coincide with warm SSTs, but the zonal turbulent friction perturbations are anomalously high upstream and anomalously low downstream of the wind stress maximum. This can be explained by considering that much of what turbulent friction accomplishes here is simply a redistribution of zonal momentum and has little to do with the pattern of surface stress (Samelson et al. 2006). Much of the zonal acceleration in the lowest 200 m therefore simply results from this vertical redistribution of zonal momentum by turbulent friction (Fig. 4.13c).

The balance between SST-induced surface heating and ABL temperature advection determines the response of the pressure gradient to SST. Since the air temperature response responds relatively slowly to the SST forcing, the surface sensible heat flux is approximately in phase with the SST perturbations. Horizontal advection

shifts the air temperature and associated hydrostatic pressure perturbations downstream (e.g., Small et al. 2003). This effect of temperature advection on the pressure gradient can be seen in the zonal pressure gradient cross-section (Fig. 4.13a).

Fig. 4.12a shows that the zonal advection and friction perturbations generate poleward ageostrophic flow where air is moving from cold to warm water, and equatorward ageostrophic flow as air moves from warm to cold water. In addition, comparison with the zonal pressure gradient in Fig. 4.13a shows that the role of the meridional ageostrophic flow in the zonal momentum budget is to compensate for the generation of SST-induced zonal pressure gradients.

The answer to the original question of why there is equatorward flow over warm SST perturbations and poleward flow over cold anomalies in this simulation thus appears to be the Ekman adjustment of the ageostrophic zonal flow that is discussed above. Note in panels b and c in Fig. 4.13 that the meridional turbulent friction force is roughly in phase and compensates the ageostrophic zonal acceleration. Also note in Fig. 4.14a that the meridional component at the surface is in phase with the elevated meridional wind maxima. Compensation between turbulent frictional forcing and the ageostrophic effects is not perfect, however; advection of the meridional wind perturbations by the zonal wind is of similar magnitude to the other terms in the meridional momentum budget and tends to shift the meridional wind perturbations eastward.

4.6 Surface Momentum Budget

4.6.1 Surface force vectors

The SST-induced response of the surface momentum budget is investigated in this section in the context of the physical mechanisms described in the previous two sections. The perturbation surface momentum budget is strongly ageostrophic over most of the SST perturbations since the surface stress and horizontal advection responses are comparable in magnitude to the pressure gradient and Coriolis forces (Fig. 4.18). Unlike the vertically-integrated momentum budgets discussed in section 4.4, the near-surface vertical advection is negligible, which is a consequence of the very small mean vertical velocity near the surface.

Perturbation pressure gradients form downstream of the SST perturbations and play a large role in driving the surface wind response to SST perturbations in this simulation. The sign and downwind shift of the pressure gradient perturbations are consistent with the locations of pressure perturbations shown in previous observational and modeling studies (e.g., Small et al. 2003).

A puzzling aspect of the perturbation turbulent friction force vectors (blue vectors in Fig. 4.18a) is the strong cross-streamline component occurring over both warm and cool SST perturbations. SST-induced turbulent mixing perturbations therefore change not only the surface wind speed but also the surface wind direction. The turbulent friction force vectors tend to rotate poleward over warm SST perturbations

and equatorward over cool SST perturbations. The Wallace et al. (1989) hypothesis does not anticipate these cross-streamline turbulent friction accelerations. From the analysis of the ABL vertical structure in Section 4.4, it appears that these cross-streamline turbulent friction perturbations are associated with SST-induced ABL air temperature gradients and thermal wind adjustments to the vertical wind shear and the associated momentum transport by turbulent mixing. The coupling between SST-induced vertical pressure gradient structure and SST has not been previously described in the context of the small-scale wind-SST interactions of interest here.

As first noted by Thum (2006), horizontal advection is a significant component of the surface momentum balance over the Agulhas Return Current (green vectors in Fig. 4.18a). Horizontal advection evidently plays a surprisingly strong role in the SST-induced surface wind response due to the strong mean wind speed over the Agulhas Return Current, whose one-month scalar-average is between 10 and 16 m/s throughout the model domain (panel e, Fig. 4.1). The advection components are similar in magnitude to the contributions from the pressure gradients and turbulent friction, which justifies its retention in the scale analysis of the surface momentum budget above. We note that in a Reynolds averaged sense, horizontal advection caused by transient weather disturbances is generally not negligible. Thus, terms like $\partial\overline{u'v'}/\partial y$ are at times significant. The horizontal Reynolds stresses are likely to be most important in frontal disturbances where the horizontal wind shear is large in magnitude.

4.6.2 Surface crosswind and downwind momentum budgets

The effects of the forces in the surface momentum budget on the wind speed and direction can be quantitatively considered by formulating the surface momentum budgets in the local surface crosswind and downwind directions

$$-\frac{DV}{Dt} - \frac{1}{\rho}\frac{\partial p}{\partial s} - \boldsymbol{F}\cdot\hat{s} = 0 \quad (4.8)$$

$$-V\frac{D\psi}{Dt} - fV - \frac{1}{\rho}\frac{\partial p}{\partial n} - \boldsymbol{F}\cdot\hat{n} = 0. \quad (4.9)$$

The 1-month average of each term in Eqns. 4.8 and 4.9 are shown in Figs. 4.19 and 4.20, respectively. The downwind parcel acceleration DV/Dt in Fig. 4.19d is strongly tied to downwind gradients in the perturbation SST field, where parcels accelerate upwind of warm SST and downwind of cool SST and decelerate downwind of warm SST and upwind of cool SST. The downwind component of the turbulent friction (Fig. 4.19b) is highly correlated with DV/Dt perturbations, while the downwind pressure gradient perturbations tend to occur somewhat downwind of the turbulent friction perturbations. Changes in wind speed are caused by imbalances between the downwind pressure gradient and downwind component of the turbulent friction term. As air initially encounters an SST front, the downwind components of the turbulent friction and pressure gradient accelerate the flow.

Like the vertically-integrated momentum budget analyzed in Section 4.4, the surface flow in the crosswind direction can be best characterized as a frictionally-modified

gradient wind balance. Perturbations of the Coriolis force are strong and result from the modulation of surface wind speed by SST. A large crosswind turbulent friction component forms as the vertical shear of the horizontal winds is modified by the SST-induced horizontal air temperature gradients through thermal wind balance. The imbalance between the crosswind pressure gradient, Coriolis force, and crosswind component of the turbulent friction causes the surface flow to turn equatorward over warm SST perturbations and poleward over cool SST perturbation, resulting in centrifugal force perturbations correlated with the downwind SST gradients.

The surface wind responds to SST through a baroclinic Ekman adjustment in which the turbulent friction perturbations are balanced by perturbations in the Coriolis force and thermodynamically-generated horizontal pressure gradients. Horizontal advection modifies the Ekman adjustment by shifting the wind perturbations downstream. Through analysis of the momentum budgets in the crosswind and downwind directions, it becomes clear that the ABL initially responds to SST perturbations through a frictionally-modified baroclinic gradient wind adjustment.

4.6.3 SST-induced responses of the surface geostrophic and ageostrophic wind components

The surface geostrophic and ageostrophic wind vector perturbations can be analyzed to understand better the contributions of each force in the surface momentum balance to the SST-induced vector wind perturbations. The surface geostrophic wind

components (u_g, v_g) and the turbulent friction and horizontal advection components of the ageostrophic wind – (u_{turb}, v_{turb}) and (u_{adv}, v_{adv}), respectively – are computed from the zonal and meridional momentum equations as

$$u = \underbrace{-\frac{1}{\rho f}\frac{\partial p}{\partial y}}_{u_g} \underbrace{-\frac{F^y}{f}}_{u_{turb}} \underbrace{-\frac{1}{f}\frac{Dv}{Dt}}_{u_{adv}} \tag{4.10}$$

$$v = \underbrace{\frac{1}{\rho f}\frac{\partial p}{\partial x}}_{v_g} + \underbrace{\frac{F^x}{f}}_{v_{turb}} + \underbrace{\frac{1}{f}\frac{Du}{Dt}}_{v_{adv}}. \tag{4.11}$$

Note that these equations for u and v are just restatements of the meridional and zonal momentum budgets, respectively, divided by the Coriolis parameter f. Defining the wind vector (u, v) in terms of its geostrophic (u_g, v_g) and ageostrophic (u_a, v_a) components (where $u = u_g + u_a$ and $v = v_g + v_a$) means that the (u_{turb}, v_{turb}) and (u_{adv}, v_{adv}) vectors are just the components of the ageostrophic wind caused by turbulent friction and horizontal advection (*i.e.*, $u_a = u_{turb} + u_{adv}$ and $v_a = v_{turb} + v_{adv}$). The spatially high-pass filtered forms of these expressions can be written as

$$u' = u'_g + u'_{turb} + u'_{adv} \tag{4.12}$$

$$v' = v'_g + v'_{turb} + v'_{adv}. \tag{4.13}$$

Downwind of warm SST perturbations, the geostrophic flow is clockwise, while downwind of cool SST perturbations, the flow is counterclockwise (red vectors in Fig. 4.18b). Bourras et al. (2004) found a similar response of the small-scale geostro-

phic winds to SST perturbations over the northeast Atlantic, although they concluded that they were less significant than the response of the ageostrophic wind components. Over the Agulhas Return Current, we find that the geostrophic wind perturbations are at least as significant as the perturbation ageostrophic circulations.

The turbulent friction components of the ageostrophic flow (u'_{turb}, v'_{turb}) (blue vectors in Fig. 4.18b) reflect the significant cross-streamline component of the surface turbulent friction force. The modification of vertical turbulent mixing of momentum between warm and cool SST perturbations leads to surface acceleration over warm SST perturbations and deceleration over cool SST perturbations, as evident by the blue vectors pointing downstream over warm SST perturbations and upstream over cool SST perturbations, consistent with the mechanism proposed by Wallace et al. (1989). However, the (u'_{turb}, v'_{turb}) vectors do not uniformly point in the upwind and downwind directions, but rotate poleward over warm SST perturbations and equatorward over cool SST perturbations.

The contributions of the pressure gradient, turbulent friction and horizontal advection to the perturbation surface wind field from this WRF simulation are shown schematically in Fig. 4.21. The exact SST-induced surface wind vector response depends in a complex manner on the magnitudes of each of these contributions and their spatial shifts relative to the underlying SST perturbations. The summation of the forces generally leads to surface acceleration and equatorward deflection over warmer water and deceleration and poleward deflection over cooler water. The exact

phasing of the rotations depend on the magnitudes and directions of the perturbation geostrophic and ageostrophic wind components relative to each other. The close correspondence between the perturbation surface wind speed and SST is remarkably robust, despite the complicated response of the individual vector wind components.

Both the location of pressure perturbations and the magnitude of the horizontal advection term depend on the advecting wind speed. Thus, through the horizontal advection term, the surface wind speed itself plays an important role in setting the pressure and advective contributions to the SST-induced wind response. In addition to changing the surface wind speed, the forces described above often act perpendicular to the surface streamlines, deflecting the wind direction by $10 - 20^{\circ}$ as air flows over SST perturbations in the WRF simulation.

4.7 Conclusions

The dynamical response of the atmospheric boundary layer to small-scale SST perturbations over a portion of the Agulhas Return Current was investigated using the WRF mesoscale atmospheric model with a steady, 1-month averaged SST field from the AMSR-E as the surface boundary condition. Comparison of the surface winds from the WRF simulation to those observed from QuikSCAT demonstrated that the WRF model simulated the surface winds very well.

Analysis of the vertical structure of the forcing terms indicated that the SST influences on the turbulent mixing of momentum and surface stress are not coincident.

Turbulent friction acts primarily to redistribute momentum vertically within the ABL in response to SST-induced surface heating perturbations and is not in-phase with the SST-induced surface stress perturbations. Therefore, near-surface turbulent friction is shown to modulate the near surface wind speed through vertical momentum redistribution while still acting as a drag to the vertically-integrated ABL flow.

SST-induced turbulent friction perturbations are only part of the story in explaining how SST affects surface winds. From analysis of the vertical structure of the forcing terms in the zonal and meridional momentum budgets, we demostrated that SST-induced pressure gradient, horizontal advection, and Coriolis acceleration perturbations were important in the near-surface wind response. We showed that the ABL may be divided into 3 distinct layers based on the leading order force balances. Near the momentum boundary layer top at about 700 m height above the surface, the flow is in near geostrophic balance. In the middle later between about 400 m to 700 m height, turbulent friction becomes important, and the ABL response to SST perturbations can be characterized as an Ekman adjustment mechanism, whereby the separate responses of the pressure gradient, turbulent friction, and Coriolis forces balance. Below about 400 m height, horizontal advection is strong and combines with the Ekman adjustment mechanism to shift SST-induced wind perturbations downstream. SST gradients generate strong horizontal air temperature gradients that alters the baroclinic structure of the lower ABL (i.e., the vertical structure of the geostrophic winds through thermal wind balance). The SST-induced near-surface

wind response is therefore characterized as a baroclinic Ekman adjustment modified by advection. Turbulent friction and horizontal advection influence the winds mainly through spatial redistribution of momentum. Nearly all the terms in the momentum budget are important near the surface.

Meridional wind perturbations over SST perturbations have not been a well-documented phenomena. In satellite observations and in this WRF simulation, the meridional winds are equatorward over warm SST perturbations and poleward over cool SST perturbations. Through analysis of the vertical structure of the momentum budgets, meridional wind perturbations result from the baroclinic Ekman adjustment of the zonal ageostrophic flow. Since the flow is nearly zonal in this region, the meridional wind perturbations cause changes in the wind direction upon crossing SST perturbations.

Analysis of the crosswind momentum budget indicated that horizontal advection acts to change the curvature of the surface streamlines as the ABL equilibrates to an Ekman balance downstream of SST fronts. Baroclinic Ekman adjustment modified by horizontal advection appears equivalent to a baroclinic, frictionally-modified gradient wind adjustment. The distance over which horizontal advection is important is of the same order as the deformation radius.

Acknowledgments. We thank Roger Samelson, Eric Skyllingstad, Justin Small, and Qingtao Song for helpful discussions throughout the course of this analysis.

Appendix A

WRF-Model Description and Boundary Layer Parameterization

We use the Weather Research and Forecasting (WRF) modeling system Version 2 (Skamarock et al. 2005) with a state of the art moist planetary boundary layer scheme (Grenier and Bretherton 2001, hereafter GB01). The key component of the WRF-model is the Advanced Research WRF (ARW) dynamic solver (Wang et al. 2006). The solver provides the solutions to the fully compressible nonhydrostatic equations on a mass-based terrain following coordinate system. The WRF-model provides two-way nesting capabilities and full physics options for land-surface, PBL, radiation, microphysics and cumulus parameterization.

In this section we briefly describe all components of the model. The WRF software framework provides the modular infrastructure for multiple combinations of physics options. Whenever possible, we choose options that performed well in previous studies or are the defaults for fifth generation Pennsylvania State University–NCAR mesoscale model (MM5) and the NCEP Eta-model. Microphysics parameterizations include resolved water vapor, cloud, and precipitation processes. In this study the simple WRF Single-Moment 3-class (WSM3) scheme is carried out at the end of each time step. This guarantees that the final saturation balance is accurate for the updated temperature and moisture fields (Skamarock et al. 2005). Atmospheric radia-

tive heating and radiative flux divergence were calculated using the Rapid Radiative Transfer Model Longwave parameterization and the Eta Geophysical Fluid Dynamics Laboratory Shortwave parameterization. The radiation physics are only called every 4th time step (12 min.) to increase computational efficiency since radiation does not change significantly during this time. The modified version of the Kain-Fritsch scheme is used to represent sub-gridscale effects of convection and shallow clouds. In terms of cumulus physics, the grid size of 8.3 km is fine enough to resolve the largest convective eddies; however, the convective eddies are not entirely resolved and the cumulus parameterization may trigger convection at horizontal length scales between 5-10 km (Skamarock et al. 2005) to release latent heat in the column. In addition, this scheme provides the heating and moistening effects from shallow cumulus. In internally stratified boundary layers, this effect becomes important for the boundary layer parameterization because of their effects on the turbulent kinetic energy budget and hence the mixing coefficients. The surface layer scheme provides surface exchange coefficients for heat, moisture, and momentum. It does not calculate any tendencies, but only provides stability-dependent information for the land-surface and the boundary layer scheme. We chose the similarity theory-based MM5 scheme which uses a roughness length derived from Charnock's relation to compute friction velocity over the ocean. The calculation of a complex surface energy budget is not necessary because we prescribe the SST and thus we were able to use a simple thermal diffusion land-surface scheme. It provides sensible and latent heat flux to the PBL scheme.

We completed the implementation by McCaa (personal communication) of the GB01 moist PBL parameterization. The details of the GB01 PBL scheme are discussed below.

A time-splitting integration scheme is used to solve the Euler Equations, the basic set of equation is given below in their flux-forms:

$$\partial_t U + (\nabla \cdot \mathbf{V}u) - \partial_x(p\phi_\eta) + \partial_x(p\phi_x) = F_U \tag{4.14}$$

$$\partial_t V + (\nabla \cdot \mathbf{V}v) - \partial_y(p\phi_\eta) + \partial_y(p\phi_y) = F_V \tag{4.15}$$

$$\partial_t W + (\nabla \cdot \mathbf{V}w) - g(\partial_y p - \eta) = F_W \tag{4.16}$$

$$\partial_t \Theta + (\nabla \cdot \mathbf{V}\theta) = F_\Theta \tag{4.17}$$

$$\partial_t \mu + (\nabla \cdot \mathbf{V}) = 0 \tag{4.18}$$

$$\partial_t \theta + \mu^{-1}\left[(\mathbf{V} \cdot \nabla\theta) - gW\right] = 0 \tag{4.19}$$

$$\tag{4.20}$$

with the vertical coordinate μ and the flux form variables defined as

$$\mu = (p_h - p_{ht})/\mu \quad where \quad \mu = p_{hs} - p_{ht} \tag{4.21}$$

$$\mathbf{V} = \mu\mathbf{v} = (U, V, W) \quad and \quad \mathbf{v} = (u, v, w) \tag{4.22}$$

These equation form a complete set along with the diagnostic relation of the inverse density

$$\partial_\eta \phi = -\alpha\mu, \tag{4.23}$$

end the equation of state:

$$p = p_0(R_d\theta/p_0\alpha)^\gamma, \tag{4.24}$$

where $\gamma = c_p/c_v = 1.4$ is the ratio of the heat capacities and R_d is the gas constant for dry air. Further modifications are outlined below (for detailed information please refer to Skamarock et al. 2005). Moisture is included by introducing mixing ratios for hydrometeors and approximating the moist potential temperature as $\theta_m = \theta(1+1.61q_v)$. Removing the hydrostatically-balanced part of the pressure gradient yields a set of equations which are spatially discretized on an Arakawa C-grid. The temporal discretization separates low-frequency motions from high-frequency acoustic modes. The low-frequency modes are integrated with a third-order Runge-Kutta (RK3) scheme. The efficiency of the solver is increased because the high-frequency modes are calculated on shorter time steps at each RK3 integration while the low-frequency modes are held constant. The acoustic time step and the choice of the accuracy of the flux divergence (2^{nd} to 6^{th} order) determine the stable Courant number. In this study we used 5^{th} order accuracy and the theoretical Courant number is $Cr_{theory} = 1.42$. This large number comes at the expense of 3 calculations (plus acoustic mode) per time step. For a three-dimensional experiment, the time step should satisfy:

$$\Delta t_{max} < \frac{Cr_{theory}}{\sqrt{3}} \cdot \frac{\Delta x}{u_{max}} \tag{4.25}$$

The maximum time step with $\Delta x = 8333$m and $u_{max} = 100\text{ms}^{-1}$would be approximately 70 s. The acoustic step however uses a forward-backward time in-

tegration with a different Courant number. The maximum allowed time step is $Cr_{max} = c_s \Delta\tau / \Delta x < 1/\sqrt{2}$ but a more conservative estimate for the acoustic step is:

$$\Delta\tau < \frac{\Delta x}{2 \cdot c_s} \tag{4.26}$$

with the sound speed $c_s = 300\text{ms}^{-1}$and $\Delta x = 8333$m, the acoustic time step is approximately 14 s. For the WRF simulations we specified a time step of 60 s and a 1:6 ratio of RK3 time step to the acoustic time step.

To resolve the boundary layer accurately we use 69 vertical levels on a stretched vertical grid with 35 levels below 1500 m, which are listed in Tables 4.1 and 4.2. The model is either run in a 2 or 3 domain level configuration. The 2-domain (1 nest) configuration is used for the validation of the model while the 3-domain (2 nests) is used to achieve higher horizontal resolution. Time step and grid size ratios are chosen to satisfy the Courant number constraints shown above.

Special Consideration of Turbulence and Entrainment

The analysis and interpretation of the results strongly depend on the parameterization of the turbulent fluxes, namely $\frac{\partial}{\partial z}\langle u'w'\rangle$ and $\frac{\partial}{\partial z}\langle v'w'\rangle$ and on the entrainment. The boundary layer model is based on GB01 and consists of a 1.5 turbulence closure scheme. The original numerical implementation was provided by McCaa (McCaa 2001, personal communication).

$$\langle w' X'_{h,m} \rangle = K_{h,m} \rho g \frac{\delta X}{\delta p} \tag{4.27}$$

where δX is a generalized vertical difference operator. The eddy diffusivities for conserved thermodynamic variables K_h and the eddy viscosity K_m are related to the turbulent kinetic energy e, a master length scale l and stability functions $S_{h,m}$ by

$$K_{h,m} = l\sqrt{e}S_{h,m}. \tag{4.28}$$

The length scale l is based on the concept that in a turbulent environment a vertically displaced air parcel will transport its perturbation velocity u' a characteristic distance l and therefore creates a fluctuation in the turbulence. The specification of the stability function $S_{h,m}$ follow the definition of Galperin et al. (1988).

In the case of convective and stable MBLs the master length scale is specified after Blackader (1962):

$$l = kz/(1 + kz/\lambda), \tag{4.29}$$

with the asymptotic length scale $\lambda = \eta_l z_i$, $\eta_l = 0.1$. In the case of decoupled MBL where the parcel length scale l_p is more appropriate. The parcel length scale l_p consist of an upward and downward length scale l_u and l_d, and is calculated based on the buoyancy of the parcel after which it would reach zero velocity. The upward and downward length scales are limited by the distance of the parcel to the the MBL top or the surface, respectively.

$$l_p = \eta_l(l_u + l_d) \tag{4.30}$$

The parcel length scale is incorporated into the definition of the master length scale:

$$l = kz/(1 + kz/l_p) \tag{4.31}$$

and the identity with the Blackadar length scale is obvious for a single convective layer when the parcel length scale l_p becomes $l_p = \eta_l z_i = \lambda$.

The model is closed by specifying an entrainment velocity w_e at the inversion (subscript i). The Turner-Deardorff closure approach (Turner 1973) relates w_e to an eddy length scale L and a velocity scale U, the entrainment efficiency A and the buoyancy jump $\Delta_i b$ across the inversion :

$$w_e = AU^3/(L\Delta_i b) \tag{4.32}$$

With the local entrainment closure approach (GB01) the eddy and velocity scales are taken from just below the inversion and set to $L = l_i$ and $U = \sqrt{e_i}$, thus w_e becomes

$$w_e = A\frac{e_i\sqrt{e_i}}{l_i\Delta_i b} \tag{4.33}$$

In 4.33 the entrainment efficiency A is chosen following GB01. The convective MBL is assumed to be topped with an infinitely thin inversion (GB01) at some grid point i at the inversion height. The turbulent fluxes of X at this height are parameterized following (Lilly 1968):

$$\langle w'X'\rangle_i = -w_e\Delta_i X \tag{4.34}$$

The MBL model uses the the so-called 'restricted inversion' (GB01) method to calculate the inversion jump $\Delta_i X$ of variable X across the inversion. In this method the

inversion is restricted to lie on a flux level of the model. The layer which contains the inversion is therefore composed of a mix of MBL properties from below the inversion and free atmospheric properties from above. GB01 refer to this layer as the 'ambiguous layer'. This method is computationally simple and allows deepening of the boundary layer implicitly through entrainment. Entrainment acts to reduce the difference between the ambiguous layer and the well mixed PBL properties, thereby reducing the stratification until ultimately the inversion is diagnosed to lie on the grid level above the previous.

References

Blackadar, A. K., 1962: The vertical distribution of wind and turbulent exchange in a neutral atmosphere. *J. Geophys. Res.*, **67**, 3095-3102.

Bourras, D., G. Reverdin, H. Giordani, and G. Caniaux, 2004: Response of the atmospheric boundary layer to a mesoscale oceanic eddy in the northeast Atlantic. *J. Geophys. Res.*, **109**, D18114, doi:10.1029/2004JD004799.

Chelton, D. B., and coauthors, 2001: Observations of coupling between surface wind stress and sea surface temperature in the eastern tropical Pacific. *J. Climate*, **14**, 1479-1498.

Chelton, D. B., M. G. Schlax, M. H. Freilich, and R. F. Milliff, 2004: Satellite measurements reveal persistent small-scale features in ocean winds. *Science*, **303**, 978-983.

Chelton, D. B., and M. H. Freilich, 2005: Scatterometer-based assessment of 10-m wind analyses from the operational ECMWF and NCEP numerical weather prediction models. *Mon. Wea. Rev.*, **133**, 409-429.

Chelton, D. B., M. G. Schlax, and R. M. Samelson, 2007: Summertime coupling between sea surface temperature and wind stress in the California Current System. *J. Phys. Oceanogr.*, **37**, 495-517.

Cronin, M. F., S.-P. Xie, and H. Hashizume, 2003: Barometric pressure variations associated with eastern Pacific tropical instability waves. *J. Climate*, **16**, 30503057.

de Szoeke, S. P., and C. S. Bretherton, 2004: Quasi-Lagrangian large eddy simulations of cross-equatorial flow in the east Pacific atmospheric boundary layer. *J. Atmos. Sci.*, **61**, 1837-1858.

Galperin, B. L., L. H. Kantha, S. Hassid, and A. Rosati, 1988: A quasi-equilibrium turbulent energy model for geophysical flows. *J. Atmos. Sci.*, **45**, 55-62.

Grenier, H., and C. S. Bretherton, 2001: A moist PBL parameterization for large-scale model and its application to subtropical cloud-topped marine boundary layers. *Mon. Wea. Rev.*, **129**, 357-377.

Hashizume, H., S.-P. Xie, M. Fujiwara, M. Shiotani, T. Watanabe, Y. Tanimoto, W. T. Liu, and K. Takeuchi, 2002: Direct observations of atmospheric boundary layer response to slow SST variations over the eastern equatorial Pacific. *J. Climate*, **15**, 3379-3393.

Hayes, S. P., M. J. McPhaden, and J. M. Wallace, 1989: The influence of sea-surface temperature upon surface wind in the eastern equatorial Pacific. *J. Climate*, **2**, 1500-1506.

Holton, J. R., 1992: An Introduction to Dynamic Meteorology. Academic Press. 511pp.

Jury, M. R., and N. Walker, 1988: Marine boundary layer modification across the edge of the Agulhas Current. *J. Geophys. Res.*, **93**, 647654.

Jury, 1994: Thermal front within the marine atmospheric boundary layer over the Agulhas Current south of Africa: composite aircraft observations. *J. Geophys. Res.*, **99**, 3297-3304.

Lilly, D. K., 1968: Models of cloud-topped mixed layers under a strong inversion. *Quart. J. Roy. Meteor. Soc.*, **94**, 292-309.

Lindzen, R. S., and S. Nigam, 1987: On the role of sea surface temperature gradients in forcing low-level winds and convergence in the tropics. *J. Atmos. Sci.*, **44**, 2418-2436.

Mahrt, L., D. Vickers, and E. Moore, 2004: Flow adjustments across sea-surface temperature changes. *Bound. Layer Meteor.*, **111**, 553-564.

Mey, R. D., and N. D. Walker, 1990: Surface heat fluxes and marine boundary layer modification in the Agulhas Retroflection region. *J. Geophys. Res.*, **95**, 15997-16015.

O'Neill, L. W., D. B. Chelton, and S. K. Esbensen, 2003: Observations of SST-induced perturbations on the wind stress field over the Southern Ocean on seasonal timescales. *J. Climate*, **16**, 2340-2354.

O'Neill, L. W., D. B. Chelton, S. K. Esbensen, and F. J. Wentz, 2005: High-resolution satellite measurements of the atmospheric boundary layer response to SST perturbations over the Agulhas Return Current. *J. Climate*, **18**, 2706-2723.

Samelson, R. M., E. D. Skyllingstad, D. B. Chelton, S. K. Esbensen, L. W. O'Neill, and N. Thum, 2006: On the coupling of wind stress and sea surface temperature. *J. Climate*, **19**, 1557-1566.

Seo, H., A. J. Miller, and J. O. Roads, 2007: The Scripps coupled ocean-atmosphere regional (SCOAR) model, with applications in the eastern Pacific sector. *J. Climate*, **20**, 381-402.

Schlax, M. G., D. B. Chelton, and M. H. Freilich, 2001: Sampling errors in wind fields constructed from single and tandem scatterometer datasets. *J. Atmos. Oceanic Tech.*, **18**, 1014-1036.

Skamarock, W. C., J. B. Klemp, J. Dudhia, D. O. Gill, D. M. Barker, W. Wang and J. G. Powers, 2005: A description of the Advanced Research WRF Version 2, available at http://wrf-model.org/wrfadmin/docs/arw_v2.pdf.

Skyllingstad, E. D., D. Vickers, L. Mahrt, and R. Samelson, 2006: Effects of mesoscale sea-surface temperature fronts on the marine atmospheric boundary layer. *Bound.-Layer Meteorol.*, doi:10.1007/s10546-006-9127-8.

Small, R. J., S.-P. Xie, and Y. Wang, 2003: Numerical simulation of atmospheric response to Pacific tropical instability waves. *J. Climate*, **16**, 3722-3740.

Small, R. J., S.-P. Xie, Y. Wang, S. K. Esbensen, and D. Vickers, 2005: Numerical simulation of boundary layer structure and cross-equatorial flow in the eastern Pacific. *J. Atmos. Sci.*, **62**, 1812-1830.

Small, R. J., S. deSzoeke, S. P. Xie, L. O'Neill, H. Seo, Q. Song, P. Cornillon, M. Spall, and S. Minobe, 2007: Air-sea interaction over ocean fronts and eddies. *Dynam. Atmos. Ocean.*, Accepted.

Song, Q., T. Hara, P. Cornillon, and C. A. Friehe, 2004: A comparison between observations and MM5 simulations of the marine atmospheric boundary layer across a temperature front. *J. Atmos. Oceanic Technol.*, **21**, 170-178.

Song, Q., P. Cornillon, and T. Hara, 2006: Surface wind response to oceanic fronts. *J. Geophys. Res.*, **111**, doi:10.1029/2006JC003680.

Spall, M. A., 2007a: Effect of sea surface temperature-wind stress coupling on baroclinic instability in the ocean. *J. Phys. Ocean.*, **37**, 1092-1097.

Spall, M. A., 2007b: Mid-latitude wind stress-sea surface temperature coupling in the vicinity of oceanic fronts. *J. Climate*, *in press.*

Sweet, W. R., R. Fett, J. Kerling, and P. LaViolette, 1981: Air-sea interaction effects in the lower troposphere across the north wall of the Gulf Stream. *Mon. Wea. Rev.*, **109**, 1042-1052.

Thum, N., 2006: Atmospheric boundary layer coupling to midlatitude mesoscale sea surface temperature anomalies. Ph.D. Dissertation, Oregon State Univ., 142 pp.

Tokinaga, H., Y. Tanimoto, and S.-P. Xie, 2005: SST-induced surface wind variations over the Brazil-Malvinas Confluence: satellite and in situ observations. *J. Climate*, **18**, 3470-3482.

Tokinaga, H., and coauthors, 2006: Atmospheric sounding over the winter Kuroshio Extension: Effect of surface stability on atmospheric boundary layer structure. *Geophys. Res. Lett.*, **33**, doi:10.1029/2005GL025102.

Turner, J. S., 1973: *Buoyancy Effects in Fluids.* Cambridge University Press, 368 pp.

Wai, M., and S. A. Stage, 1989: Dynamical analysis of marine atmospheric boundary layer structure near the Gulf Stream oceanic front. *Q. J. R. Meteorol. Soc.*, **115**, 29-44.

White, W. B., and J. L. Annis, 2003: Coupling of extratropical mesoscale eddies in the ocean to westerly winds in the atmospheric boundary layer. *J. Climate*, **33**, 1095-1107.

Xie, S.-P., 2004: Satellite observations of cool ocean-atmosphere interaction. *Bull. Amer. Meteor. Soc.*, **85**, 195-208.

Table 4.1: WRF model η-levels used in this simulation.

1.0000	0.9967	0.9932	0.9896	0.9858	0.9820	0.9779	0.9738	0.9694
0.9649	0.9603	0.9554	0.9504	0.9452	0.9398	0.9342	0.9284	0.9224
0.9161	0.9096	0.9029	0.8959	0.8886	0.8811	0.8733	0.8652	0.8568
0.8481	0.8391	0.8297	0.8200	0.8099	0.7994	0.7886	0.7773	0.7656
0.7535	0.7409	0.7279	0.7143	0.7003	0.6857	0.6706	0.6549	0.6386
0.6217	0.6042	0.5860	0.5672	0.5476	0.5273	0.5063	0.4845	0.4618
0.4383	0.4139	0.3886	0.3624	0.3351	0.3069	0.2776	0.2472	0.2157
0.1829	0.1490	0.1138	0.0772	0.0393	0.0000			

Table 4.2: Nominal heights (m) corresponding to the η-levels in Table 4.1.

12.0	34.6	57.3	82.1	107.5	134.1	161.7	190.4	220.5
251.4	283.8	317.6	352.5	388.9	426.8	466.2	507.2	550.0
594.8	641.2	689.5	740.2	793.0	847.8	905.1	964.9	1027.2
1092.2	1160.1	1231.2	1305.4	1383.3	1464.4	1549.3	1638.5	1731.6
1829.2	1931.5	2038.8	2151.5	2269.7	2394.0	2524.5	2662.1	2806.9
2959.3	3120.1	3289.5	3468.7	3658.4	3858.9	4071.2	4297.2	4537.7
4793.8	5067.1	5359.2	5672.7	6009.7	6372.4	6765.1	7191.2	7656.7
8167.6	8731.8	9362.8	10076.8	10900.0				

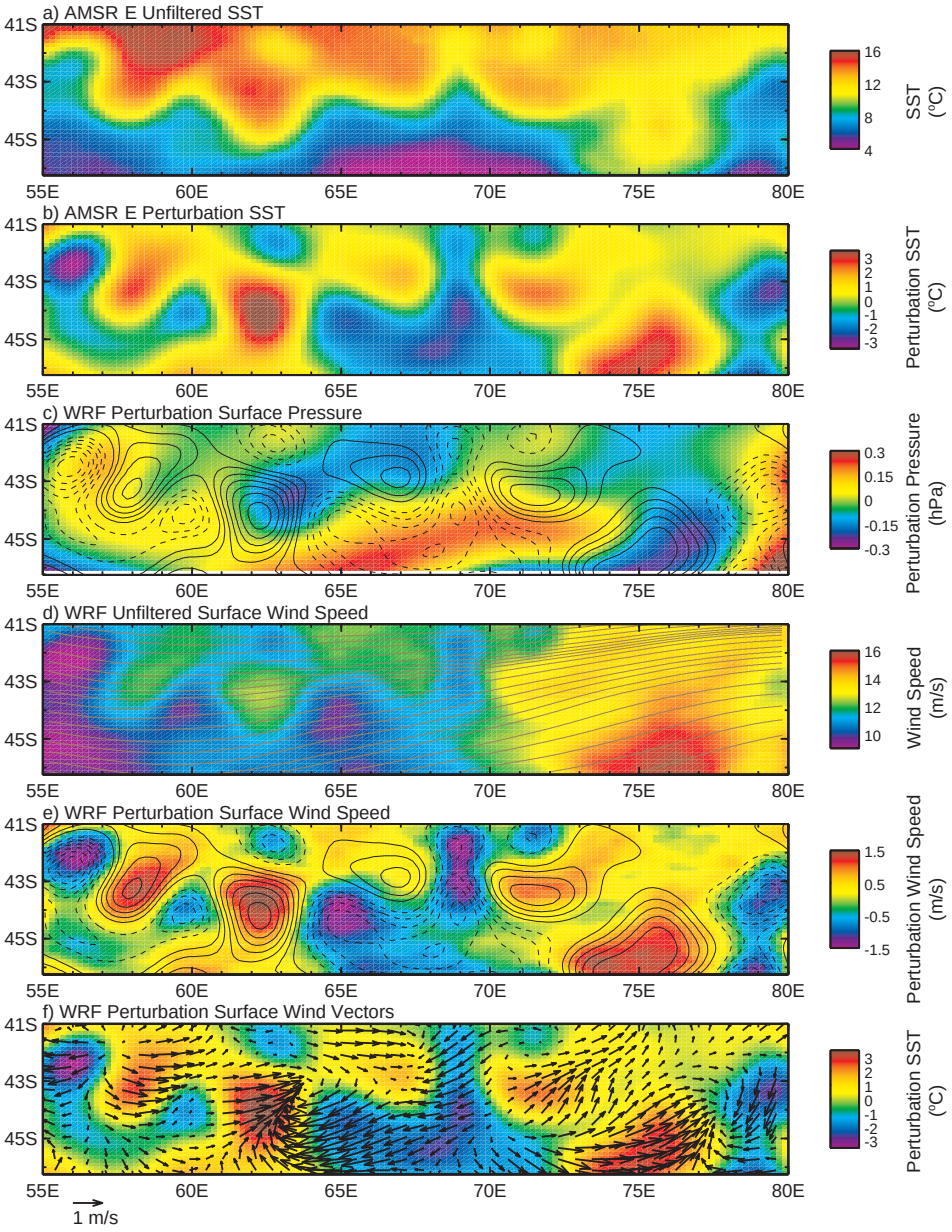

Figure 4.1: Maps of 1-month averages: (a) AMSR-E unfiltered SST; (b) AMSR-E perturbation SST; (c) WRF perturbation surface pressure (colors) with contours of the AMSR-E perturbation SST overlaid with a contour interval of 0.5°C; (d) WRF unfiltered scalar-averaged surface wind speed (colors) with contours of the streamlines of the WRF vector-averaged unfiltered surface wind; (e) WRF perturbation surface wind speed (colors) with contours of the AMSR-E perturbation SST overlaid with a contour interval of 0.5°C; (f) WRF perturbation surface wind vectors overlaid onto the AMSR-E perturbation SST (colors).

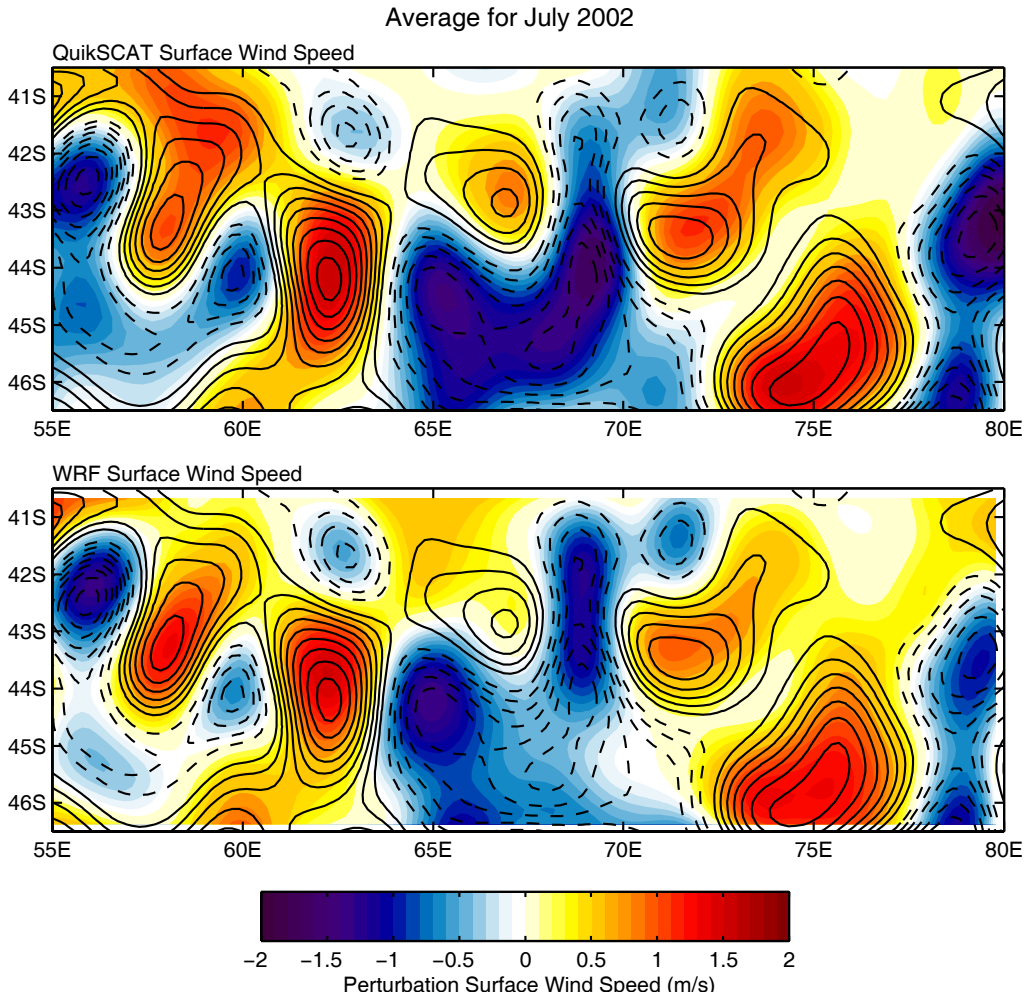

Figure 4.2: Maps of 1-month scalar-averaged perturbation surface wind speed (colors) from QuikSCAT (top) and the WRF simulation (bottom). The solid and dashed contours correspond to positive and negative AMSR-E SST perturbations, respectively, with an interval of 0.5°C and the zero contour has been omitted for clarity.

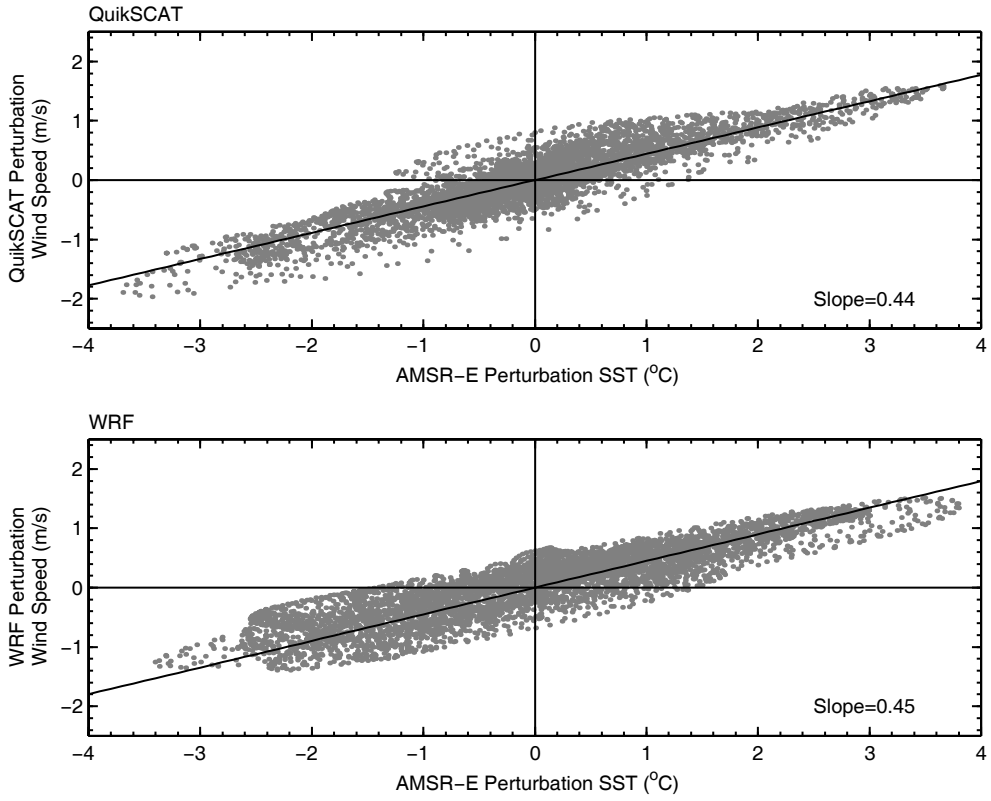

Figure 4.3: Scatterplots of the 1-month scalar-averaged perturbation surface wind speed as a function of the 1-month averaged AMSR-E perturbation SST for QuikSCAT (top) and WRF (bottom). The black line in each plot is a least-squares regression of all the points to a straight line with slope as indicated at the lower-right.

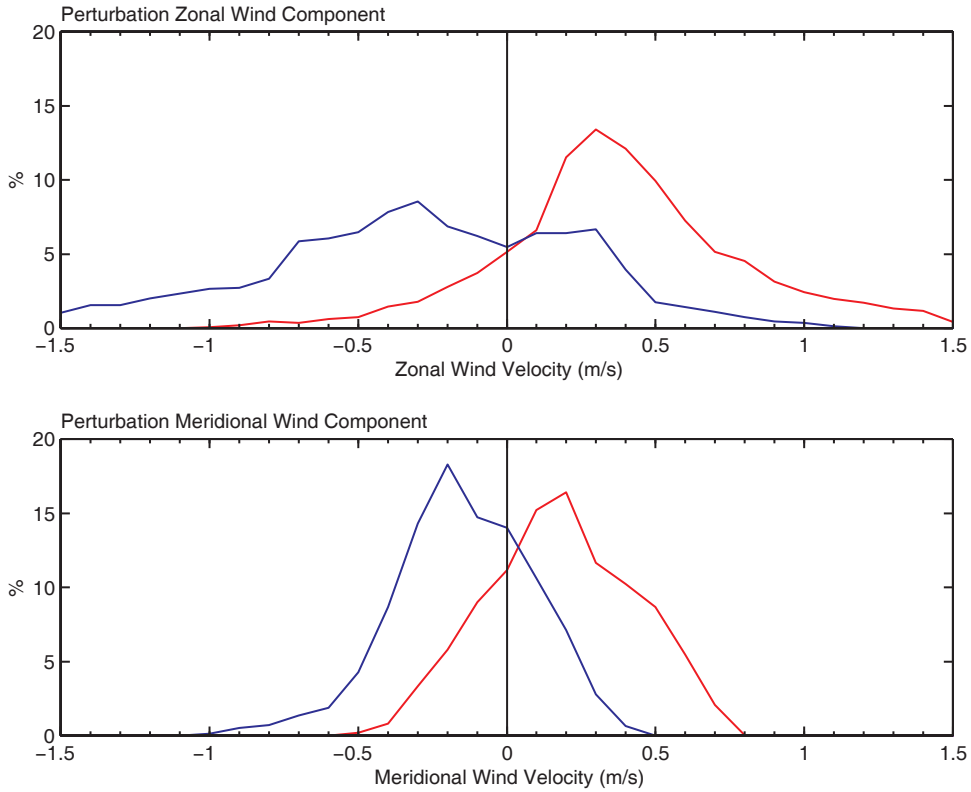

Figure 4.4: Histograms of the 1-month averaged spatially high-pass filter zonal (top) and meridional (bottom) wind components separated between positive (red) and negative (blue) perturbation SSTs.

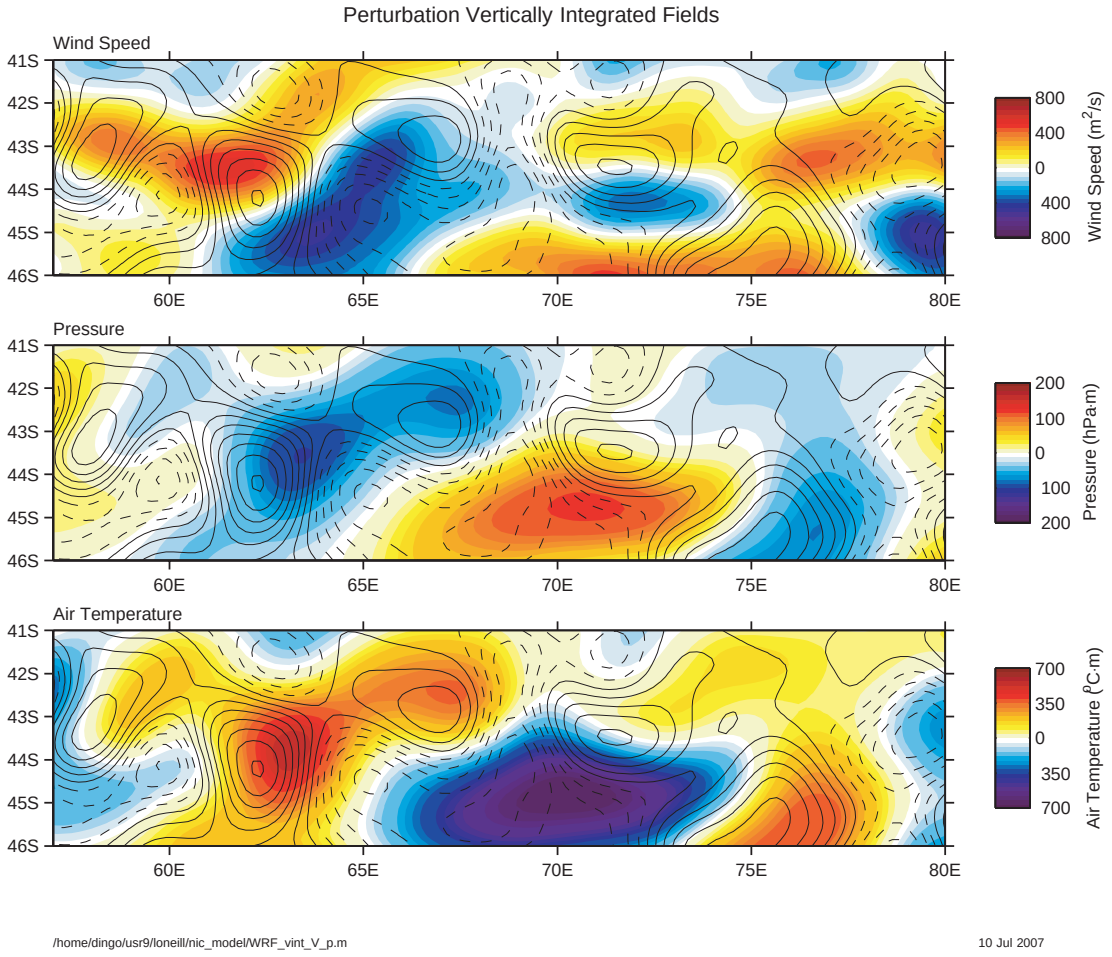

Figure 4.5: Maps of perturbation vertically-integrated boundary layer quantities averaged over the 1-month period of the WRF simulation: (top) wind speed; (middle) air pressure; and (bottom) air temperature. The contours are of the AMSR perturbation SST shown earlier.

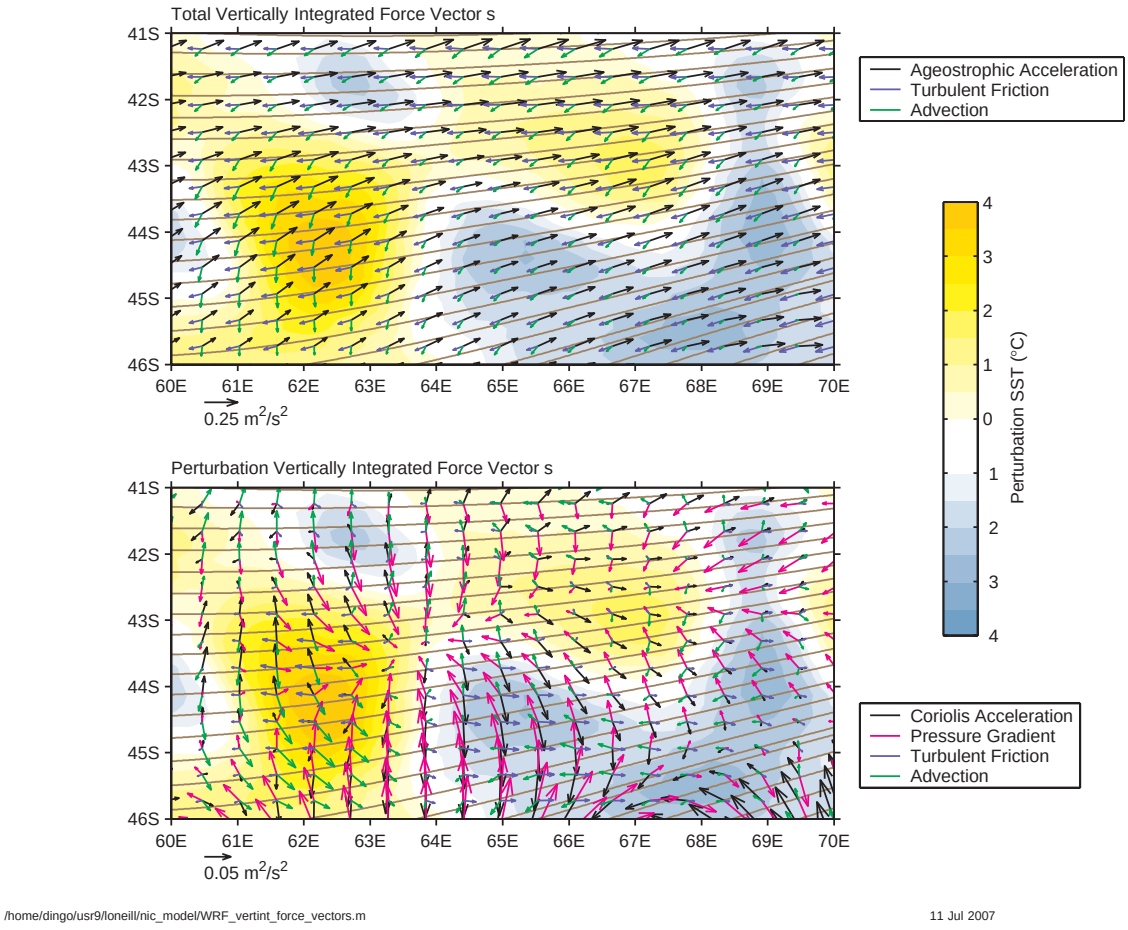

Figure 4.6: Maps of the vertically-integrated MABL momentum force vectors averaged over the 1-month period of the WRF simulation. The brown contours represent streamlines of the vertically-integrated MABL wind. The colors are the perturbation AMSR SST field. The vectors represent: (top panel) the unfiltered vertically-integrated force vectors; (bottom panel) the perturbation vertically-integrated force vectors. Note that the vector scale changes between the top and bottom panels, as indicated by the reference vectors located in the bottom left of each panel.

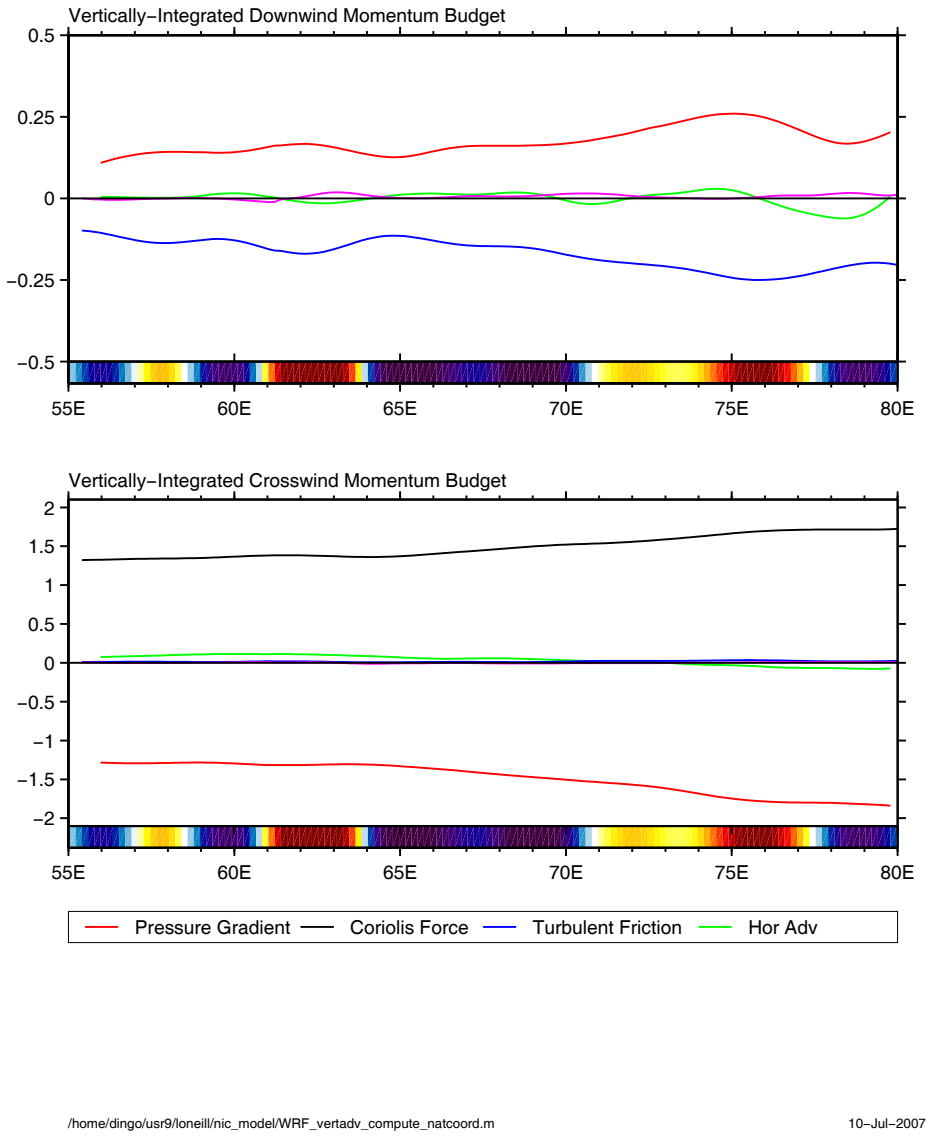

Figure 4.7: Zonal transects of the WRF vertically-integrated downwind (top) and crosswind (bottom) momentum budgets along 44.2°S latitude. The colorbar at the bottom of each panel represents the relative SST, with red representing warmer SST and blue cooler. Note that the y-axis range in the top panel is enhanced by a factor of 4 relative to the bottom panel.

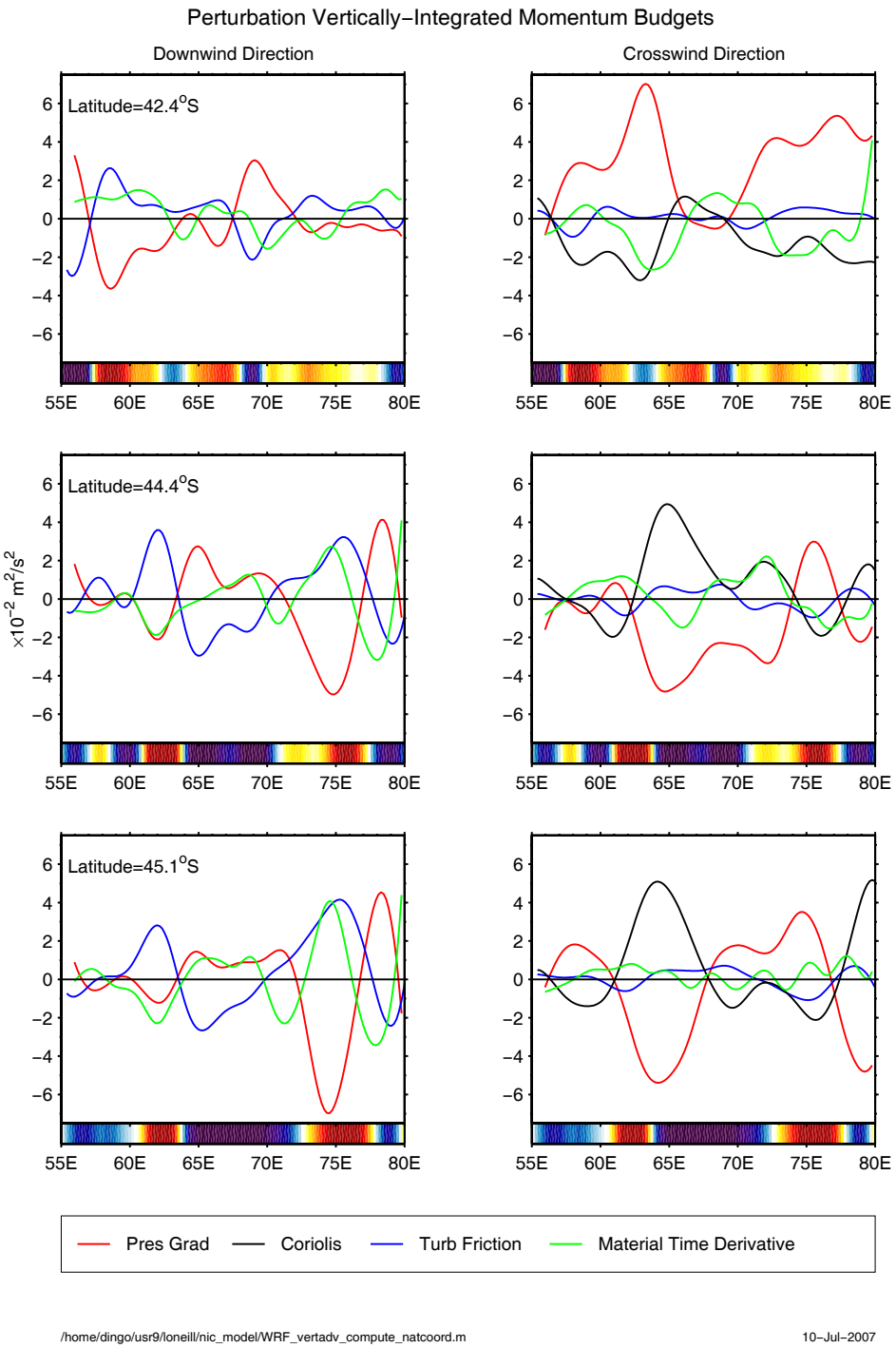

Figure 4.8: Zonal transects of the WRF perturbation vertically-integrated downwind (right column of panels) and crosswind (left column of panels) momentum budgets.

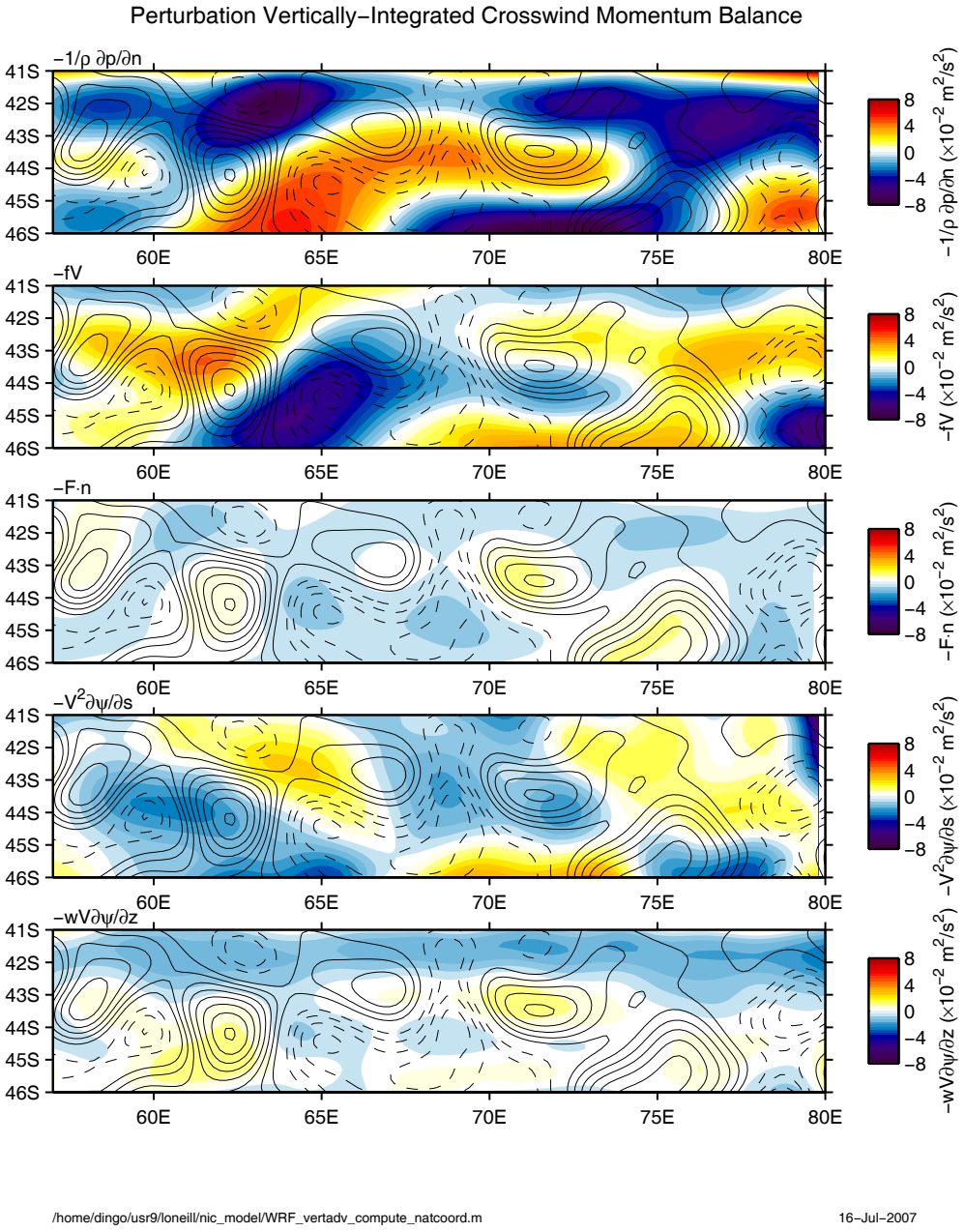

Figure 4.9: Spatial maps of the WRF perturbation vertically-integrated crosswind momentum budget as in Eqn. 4.4 averaged over the 1-month simulation period of interest here. Overlaid in each panel are contours of the perturbation AMSR-E SST as shown earlier.

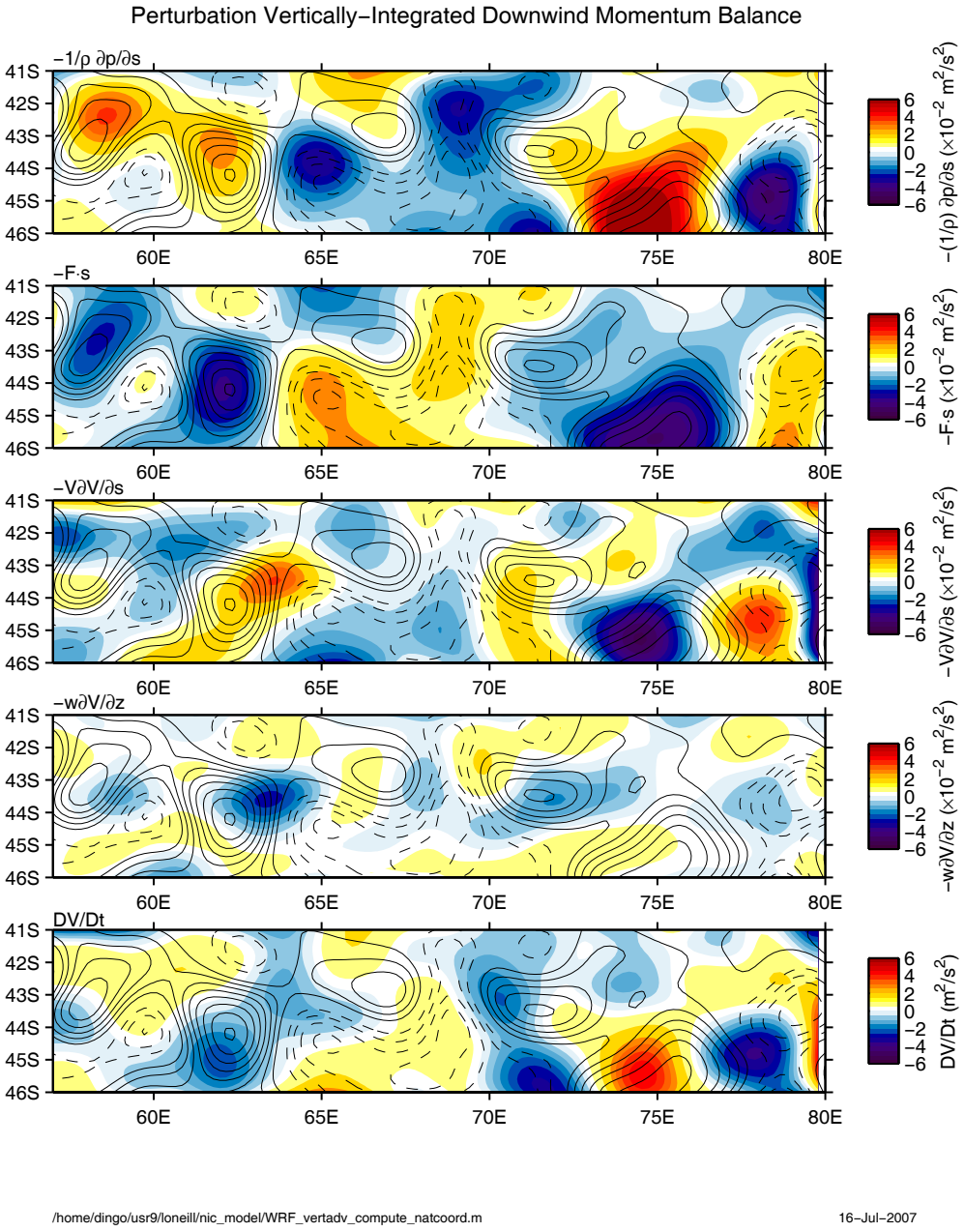

Figure 4.10: Same as Fig. 4.9, except for the perturbation vertically-integrated downwind momentum budget as in Eqn. 4.5 averaged over the 1-month simulation period of interest here. Overlaid in each panel are contours of the perturbation AMSR-E SST as shown earlier.

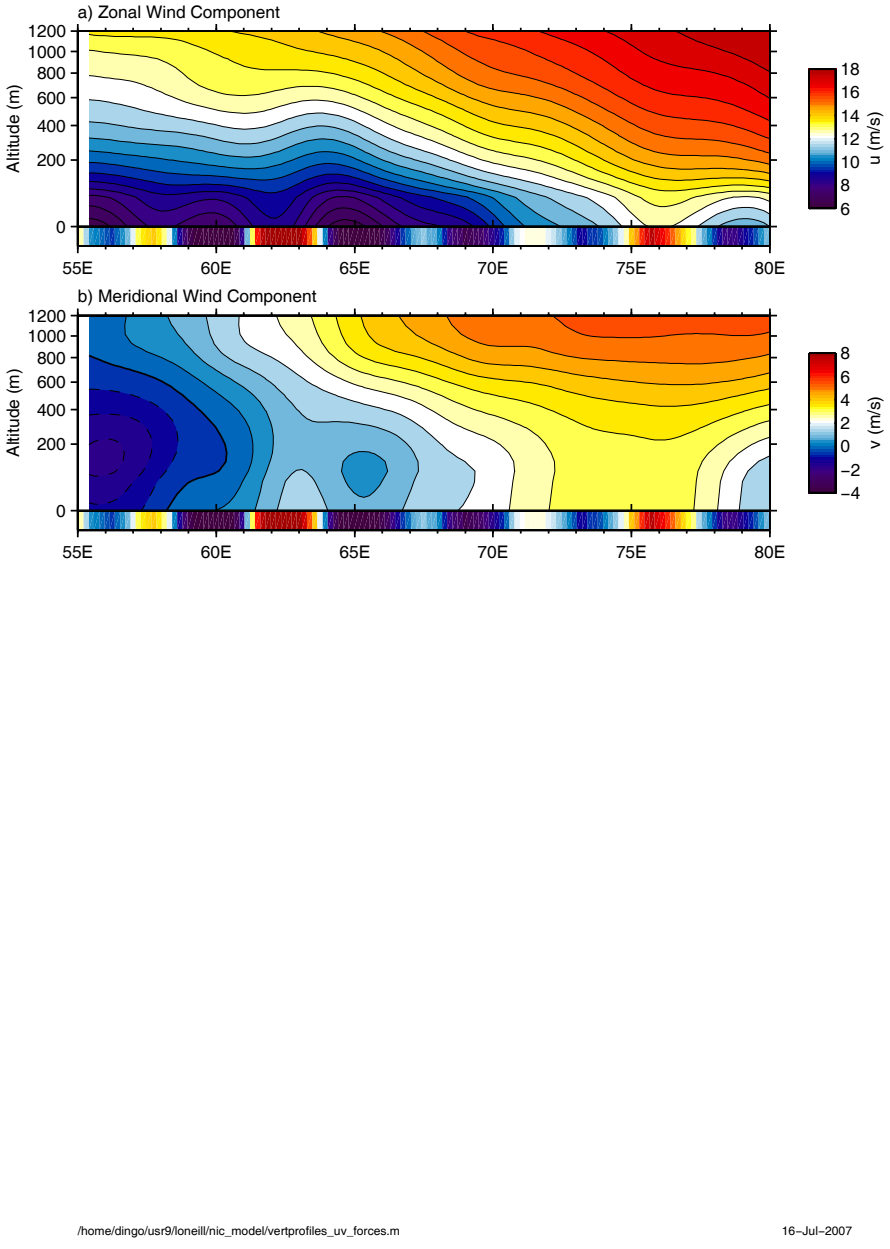

Figure 4.11: Height-longitude transects of the WRF zonal (top) and meridional (bottom) wind components at 44.4°S latitude. Note that the y-axis coordinate is stretched to emphasize the vertical structure near the surface. The colorbar attached to the bottom of each panel shows the relative magnitude of the perturbations SST along this latitude, with red corresponding to warm SST perturbations and blue to cool SST perturbations. The contour interval is 0.5 m/s.

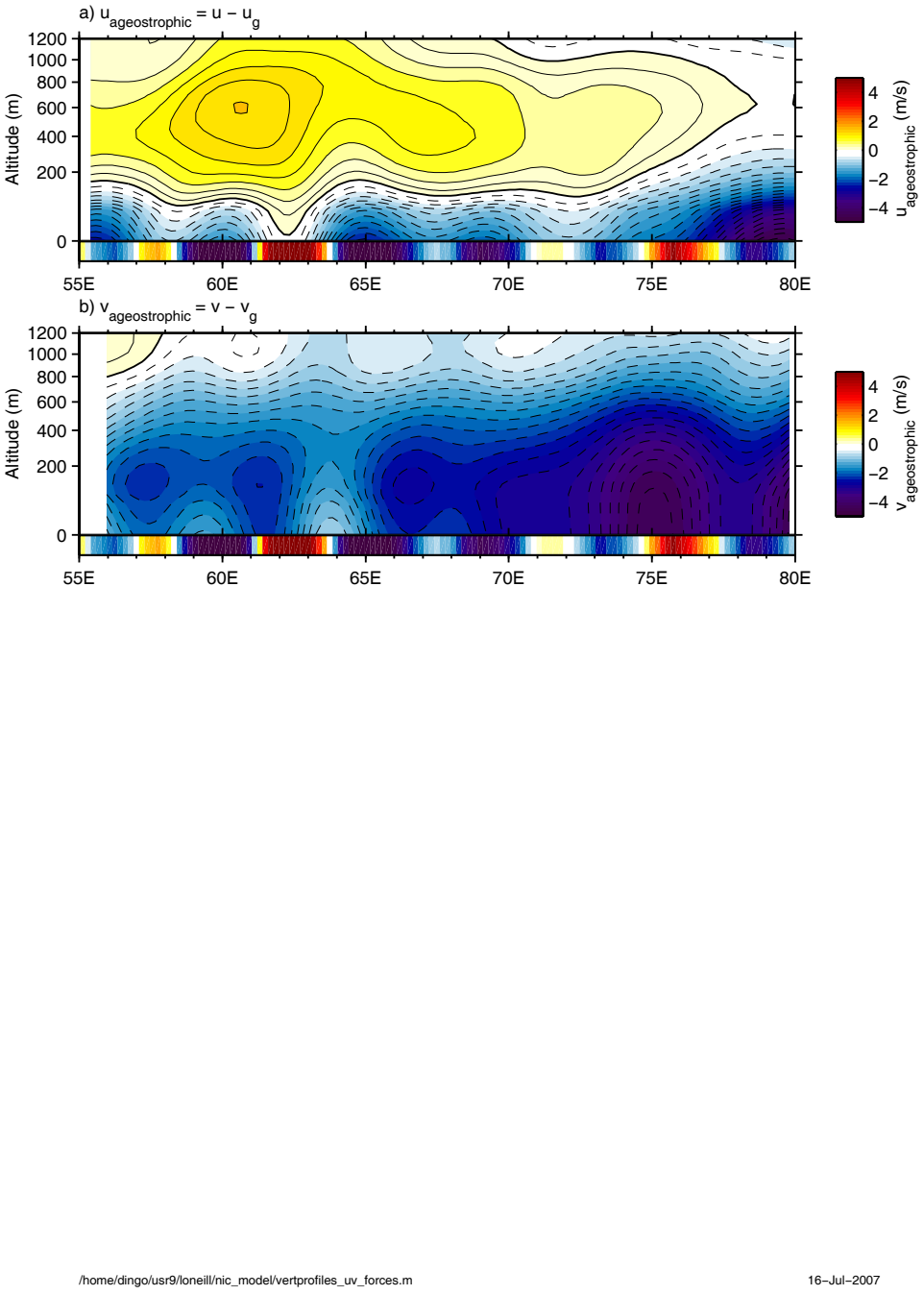

Figure 4.12: Same as Fig. 4.11, except for the WRF zonal (top) and meridional (bottom) ageostrophic wind components.

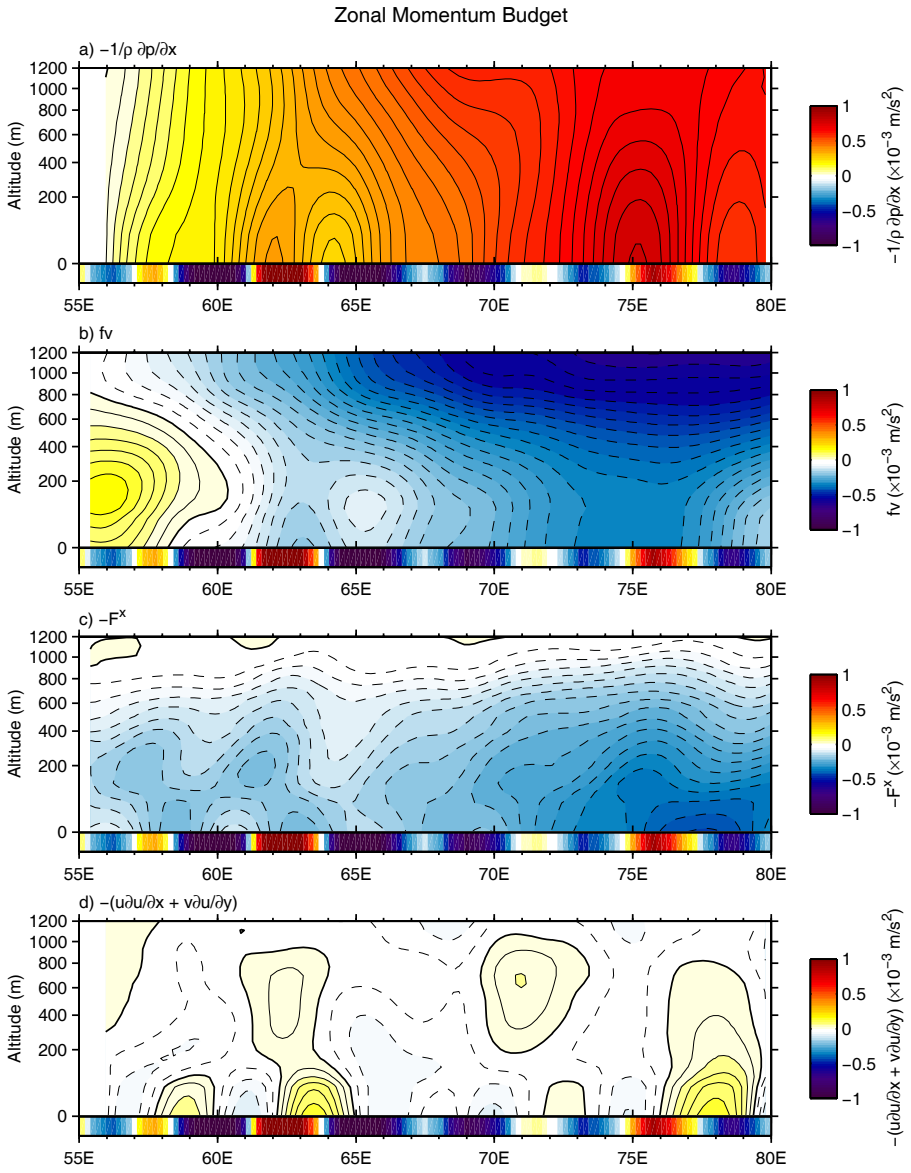

Figure 4.13: Height-longitude transects of the components of the WRF zonal momentum budget at 44.4°S latitude shown in Eqn. 4.6: (a) pressure gradient force; (b) Coriolis force; (c) turbulent friction force; and (d) horizontal advection force. The contour interval is 0.25×10^{-4}, and the solid and dashed contours correspond to positive and negative force values, respectively. The heavy solid contour is the zero contour.

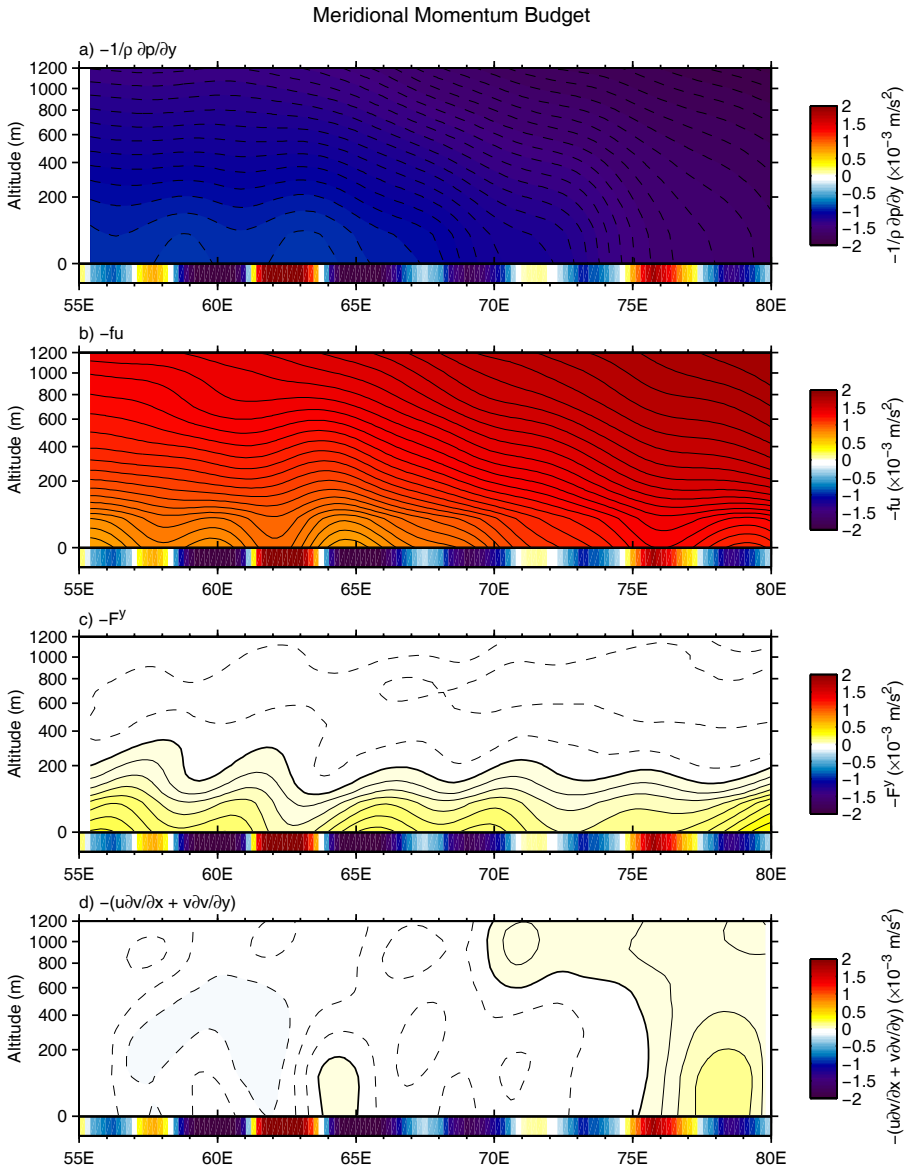

Figure 4.14: Height-longitude transects of the components of the WRF meridional momentum budget at 44.4°S latitude shown in Eqn. 4.7: (a) pressure gradient force; (b) Coriolis force; (c) turbulent friction force; and (d) horizontal advection force. The contour interval is 0.4×10^{-4}, and the solid and dashed contours correspond to positive and negative force values, respectively. The heavy solid contour is the zero contour.

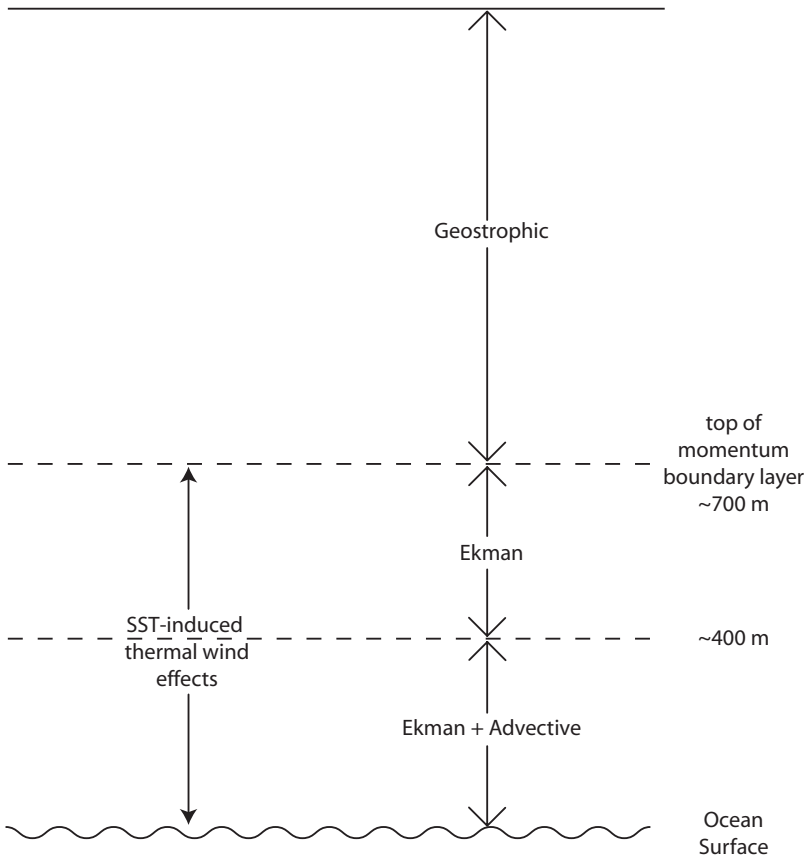

Figure 4.15: Schematic of the 3-layer structure of the lower atmosphere proposed here based on analysis of the WRF simulation.

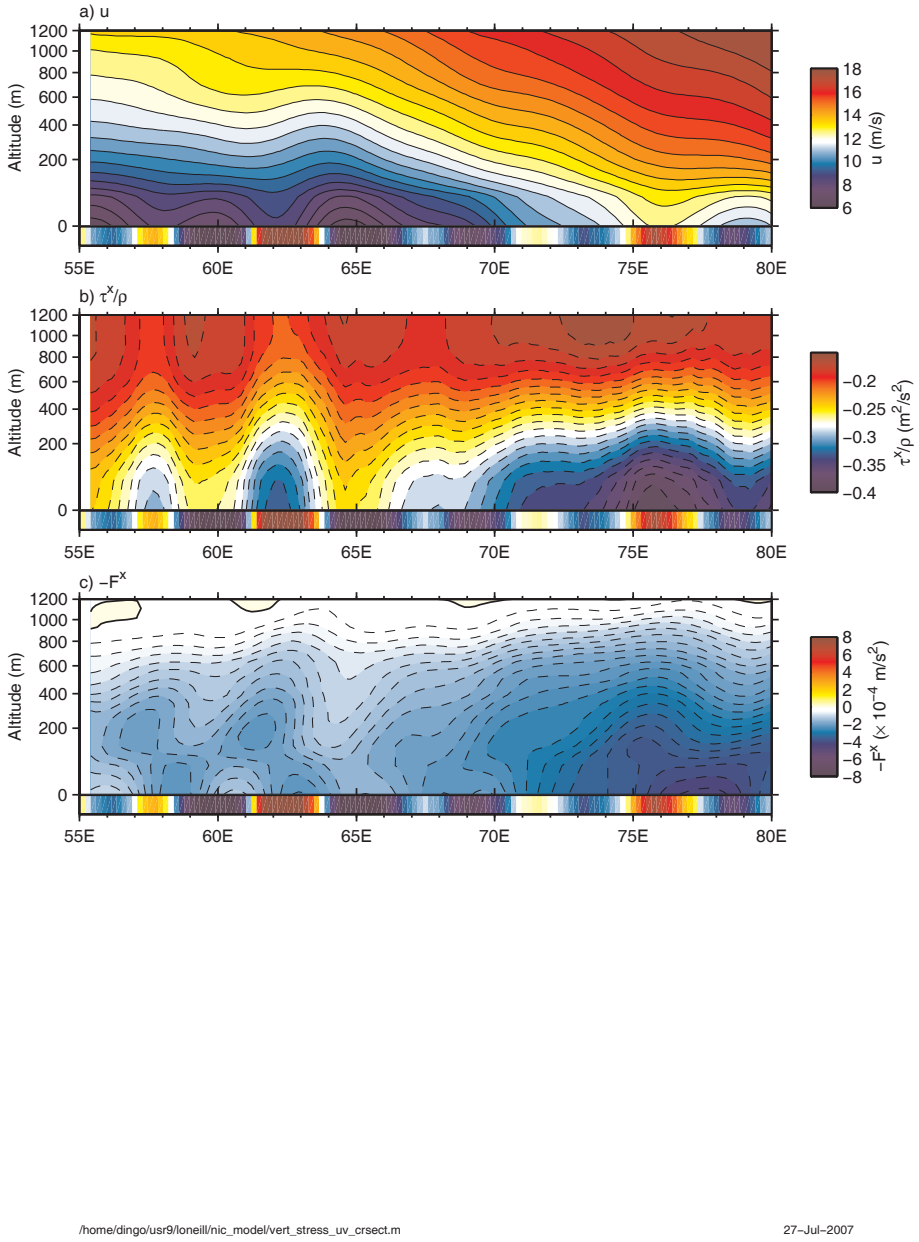

Figure 4.16: Height-longitude transects of the WRF zonal wind (top panel), zonal component of the turbulent wind stress τ^x (middle panel), and the zonal component of the vertical turbulent wind stress divergence $-F^x$ (bottom panel). Note the y-axis coordinate is stretched to emphasize the vertical structure near the surface. The colorbar attached to the bottom of each panel shows the relative magnitude of the perturbations SST along this latitude, with red corresponding to warm SST perturbations and blue to cool SST perturbations.

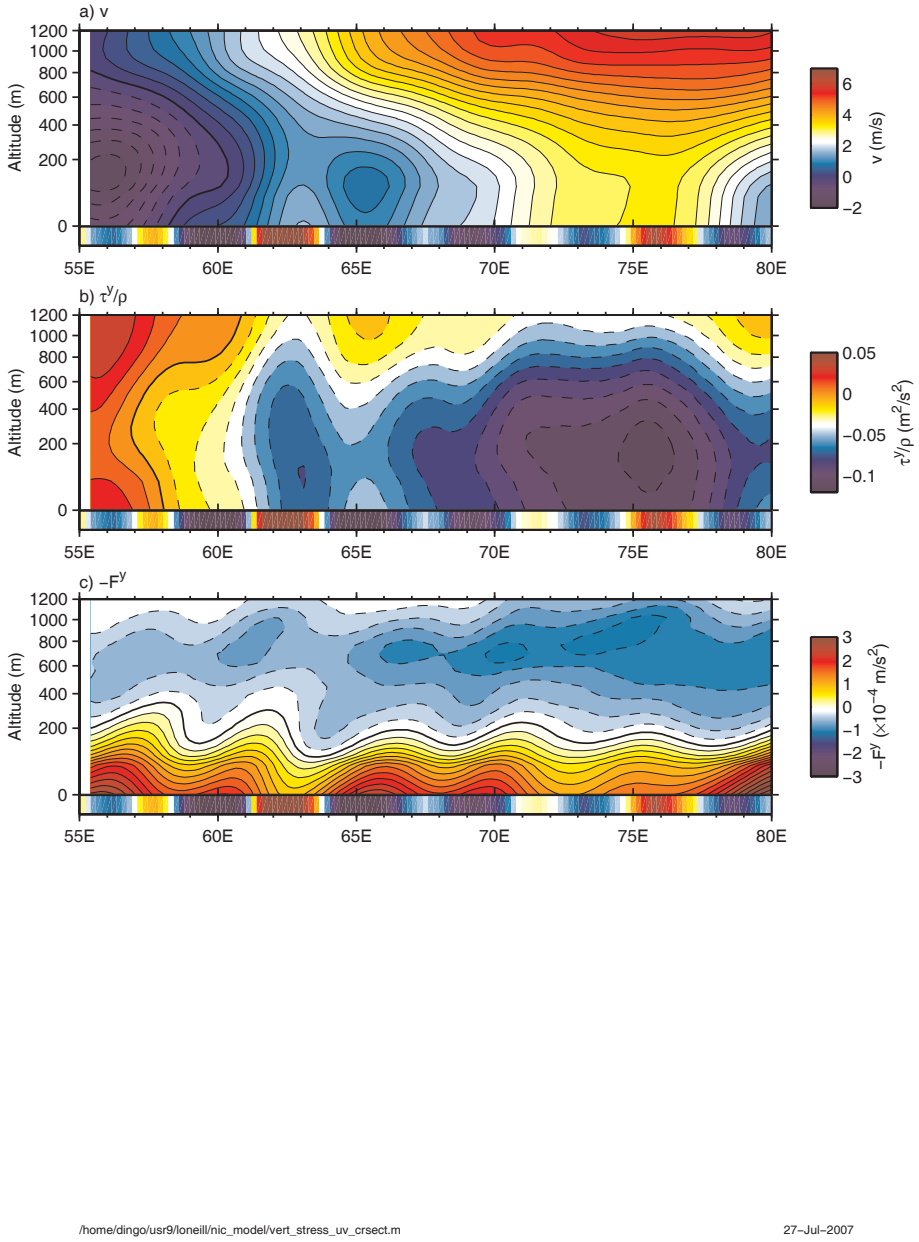

Figure 4.17: Height-longitude transects of the WRF meridional wind (top panel), meridional component of the turbulent wind stress τ^y (middle panel), and the meridional component of the vertical turbulent wind stress divergence $-F^y$ (bottom panel). Note that the y-axis coordinate is stretched to emphasize the vertical structure near the surface. The colorbar attached to the bottom of each panel shows the relative magnitude of the perturbations SST along this latitude, with red corresponding to warm SST perturbations and blue to cool SST perturbations.

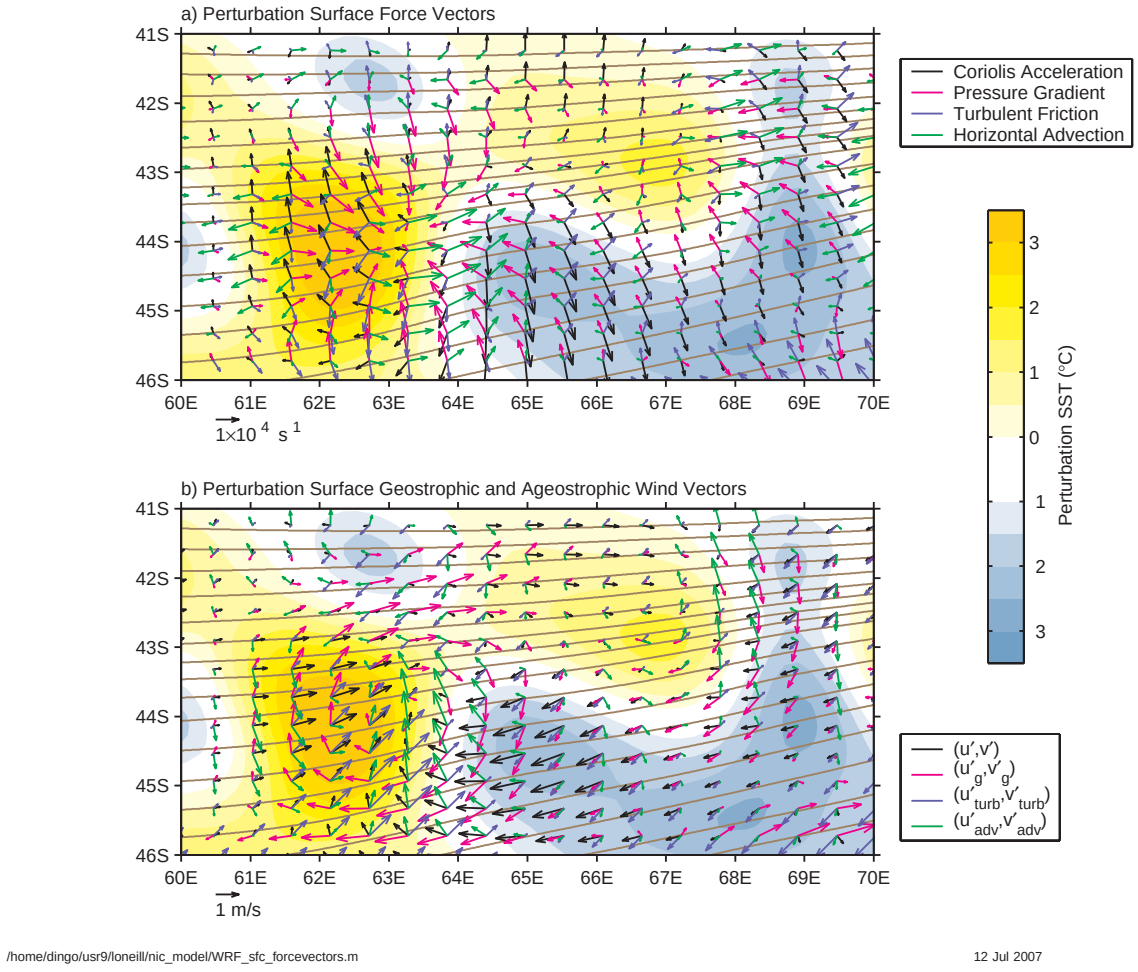

Figure 4.18: Maps of the surface ABL momentum force vectors averaged over the 1-month period of the WRF simulation. The brown contours represent streamlines of the 1-month vector-averaged surface winds. The colors are the perturbation AMSR SST field. The vectors represent: (top) the perturbation surface force vectors defined by Eqns. 4.6 and 4.7; (bottom) the geostrophic and ageostrophic force vectors defined by Eqns. 4.10 and 4.11. Vectors are only plotted at every third point in latitude and longitude for clarity. Note that the vector scale changes between the top and bottom panels, as indicated by the reference vectors located at the lower left of each panel.

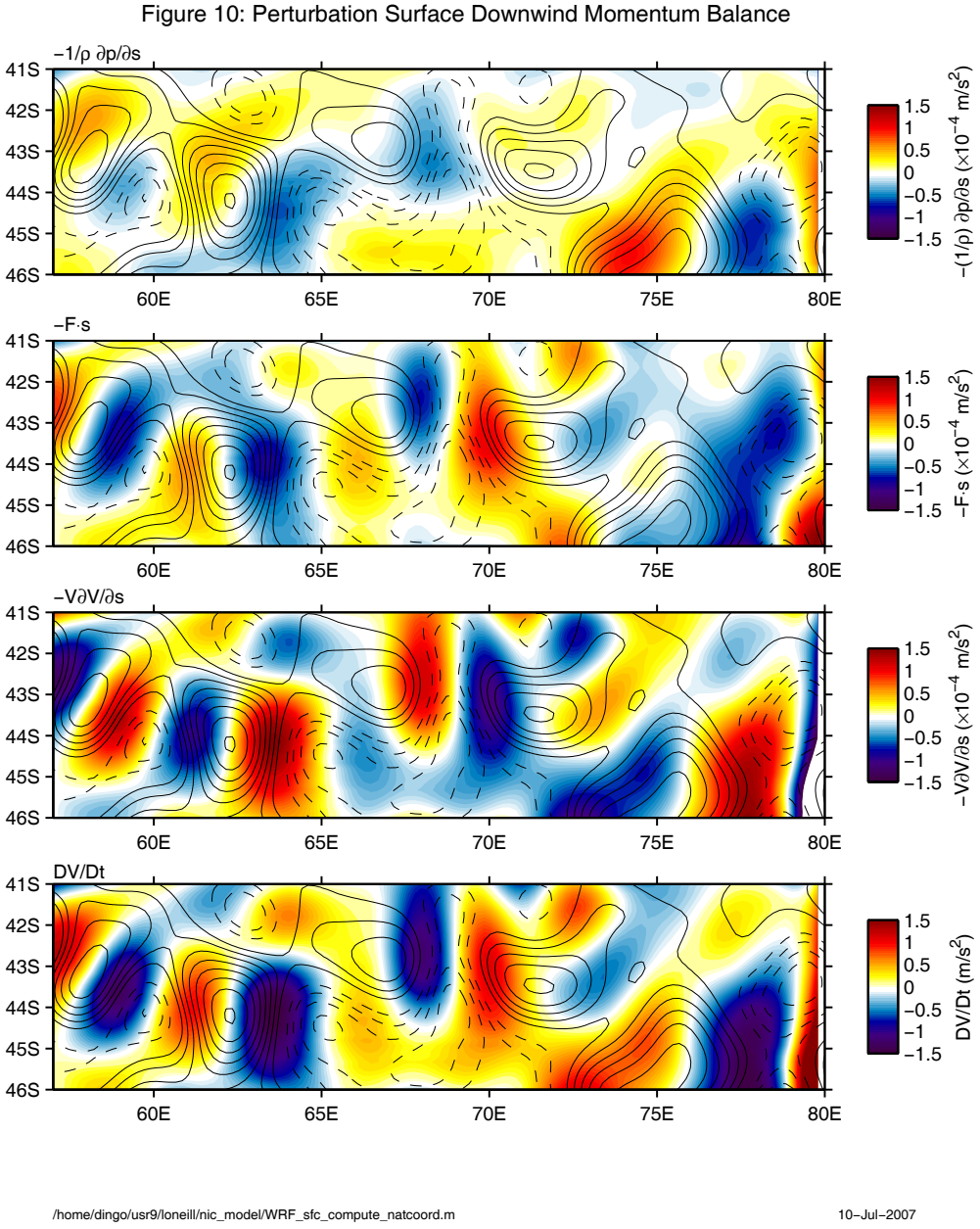

Figure 4.19: Maps of the 1-month average perturbation terms of the downwind component of the surface momentum budget: (a) downwind pressure gradient; (b) downwind component of the vertical turbulent friction; (c) downwind component of the horizontal advection; (d) material time derivative of the horizontal wind speed V. The dashed and solid contours in each panel are of the perturbation AMSR SST and correspond to negative and positive perturbations, respectively, with a contour interval of 0.5°C. The zero contour has been omitted for clarity.

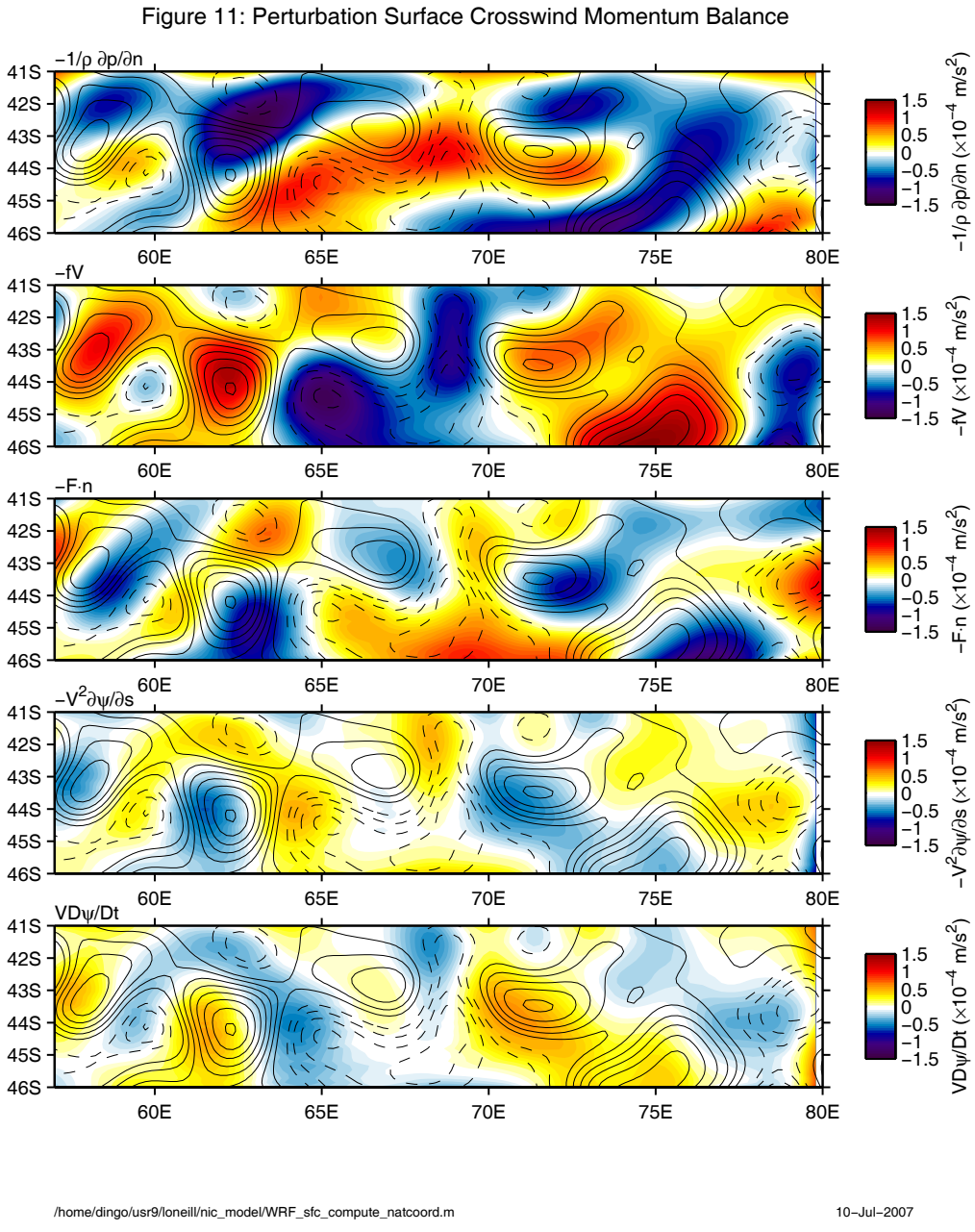

Figure 4.20: Same as Fig. 4.19, except for the surface crosswind momentum budget.

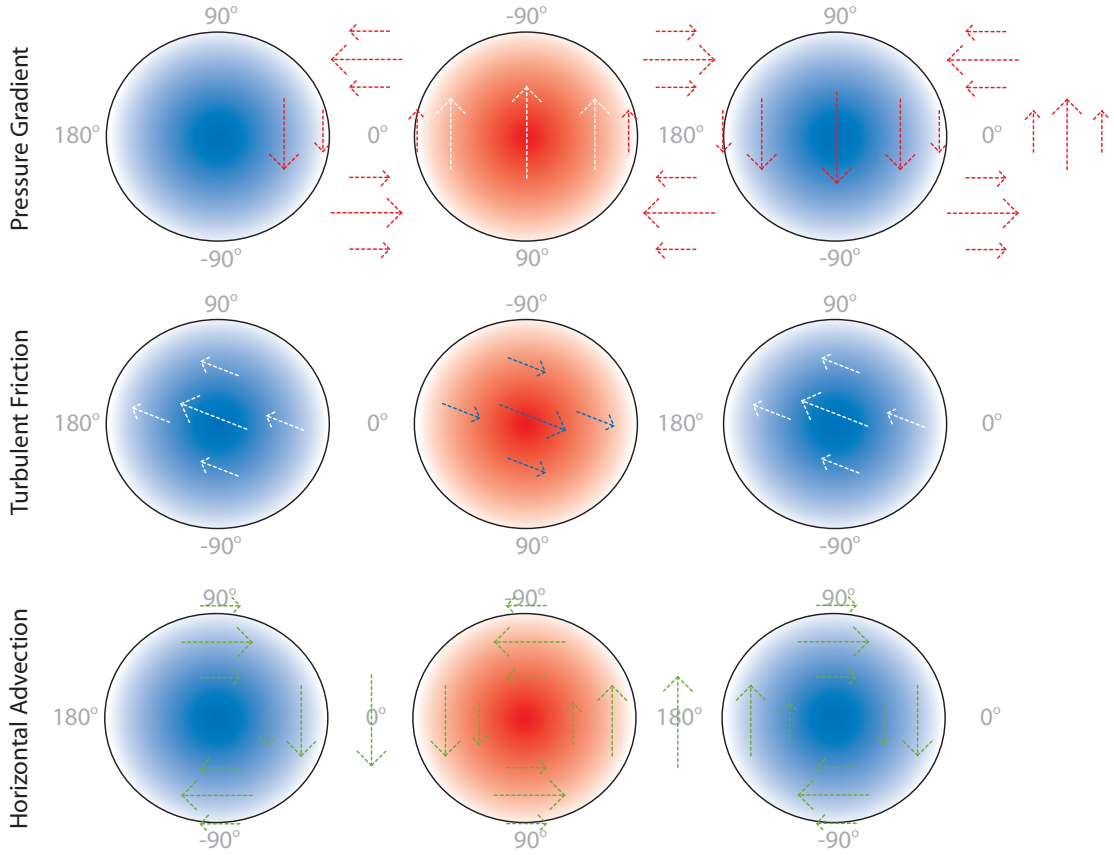

Figure 4.21: Schematic of SST-induced surface vector wind perturbations: (top row) (u'_g, v'_g); (middle row) (u'_{turb}, v'_{turb}); (bottom row) (u'_{adv}, v'_{adv}). Solid red circles indicate warm SST perturbations while solid blue circles indicate cool SST perturbations. The large-scale flow is from left to right. The angles shown in grey are the counterclockwise angles between the large-scale wind and perturbation SST gradient vectors.

THE EFFECTS OF SST-INDUCED HORIZONTAL SURFACE WIND SPEED AND DIRECTION GRADIENTS ON MID-LATITUDE VORTICITY AND DIVERGENCE FIELDS: OBSERVATIONS AND NUMERICAL SIMULATION

Larry W. O'Neill, Dudley B. Chelton, Steven K. Esbensen, and Nicolai Thum

To be submitted to Journal of Climate

45 Beacon Street

Boston, MA 02108-3693

Chapter 5

Abstract

The effects of surface wind speed and direction gradients on mid-latitude surface vorticity and divergence fields near sea surface temperature (SST) fronts are investigated using one year of vector wind observations from the SeaWinds scatterometer on the QuikSCAT satellite and SST from the Advanced Microwave Scanning Radiometer on the EOS-Aqua (AMSR-E) satellite. As shown from previous studies, strong spatial gradients in wind speed develop in response to persistent ocean mesoscale sea surface temperature (SST) fronts with spatial scales between 100-1000 km associated with the Kuroshio Extension, Gulf Stream, South Atlantic, and Agulhas Return Current regions. It is shown here that mid-latitude SST fronts also significantly modify surface wind direction; the time-averaged surface wind speed and direction responses to typical SST variations of about 4°C are on average about 2 m/s and 20°, respectively, over all four regions.

Several previous observational analyses have shown that small-scale perturbations

in the surface vorticity and divergence fields are linearly related to the crosswind and downwind components of the SST gradient field, respectively. In curvilinear natural coordinates, the vorticity and divergence fields are composed of both wind speed and direction gradients in the crosswind and downwind directions. We show that the crosswind and downwind wind speed gradients are the components of the vorticity and divergence that depend on the crosswind and downwind SST gradients, respectively. SST-induced wind direction gradients also significantly modify the surface vorticity and divergence fields, weakening the response of the vorticity to crosswind SST gradients while enhancing the divergence response to downwind SST gradients.

The physical processes giving rise to these SST-induced surface vorticity and divergence responses are investigated from a numerical simulation using the Weather Research and Forecasting (WRF) mesoscale model. We show that the direction gradient response is mainly attributable to the SST-induced response of the surface geostrophic wind; weaker vorticity and enhanced divergence responses are shown to be consequences of these surface geostrophic wind perturbations through their effects on wind direction gradients. The vertical turbulent mixing of momentum in the WRF simulation is shown to play a role in the vorticity and divergence responses, but through a baroclinic Ekman adjustment mechanism modified by horizontal advection. Wind speed gradient responses to SST gradients are shown to be a consequence of this baroclinic Ekman adjustment.

5.1 Introduction

Sea surface temperature (SST) anomalies are known to be negatively correlated with surface wind anomalies on basin scales (e. g. Mantua et al. 1997; Okumura et al. 2001). Over these large spatial scales, large-scale atmospheric circulation patterns change surface ocean temperatures through modulation of surface heat fluxes and upper ocean mixing. On smaller spatial scales between 100 and 1000 km, however, contemporaneous near-global satellite measurements of surface vector winds and SST have uncovered intense spatial variability in the surface wind field positively correlated with SST perturbations (see reviews by Xie 2004, Chelton et al. 2004, and Small et al. 2007). These small-scale features in the surface wind field are particularly prevalent near large mid-latitude ocean currents. Previous studies have investigated SST-induced changes in wind speed across these SST fronts, but changes in wind direction have not yet been examined. One of the goals of this study is to determine how small-scale SST perturbations affect both surface wind speed and direction from satellite wind and SST observations, and to determine their cumulative effects on the surface vorticity and divergence fields over four large mid-latitude ocean regions of strong currents: the Kuroshio Extension in the North Pacific, the Gulf Stream in the North Atlantic, the Brazil-Malvinas Confluence in the South Atlantic, and the Agulhas Return Current in the Southern Ocean.

Spatial variations in surface wind speed associated with small-scale SST variability develop surface vorticity and divergence with magnitudes comparable to the curl

and divergence of the large-scale wind fields over mid-latitudes (Chelton et al. 2004; O'Neill et al. 2003, 2005; Chelton et al. 2007). These SST-induced curl and divergence perturbations are well-correlated with small-scale perturbations in the crosswind and downwind components of the SST gradient, respectively (Chelton et al. 2001, 2004, 2007; Chelton 2005; O'Neill et al. 2003, 2005). Significant differences between the curl response to crosswind SST gradients and the divergence response to downwind SST gradients noted in all of these previous observational studies reveal deficiencies in the understanding of how the atmospheric boundary layer (ABL) responds to small-scale SST perturbations. In particular, the curl response is consistently much weaker than the divergence response. A goal of this study is to investigate the dynamical origins of the differences between the SST-induced vorticity and divergence responses by analyzing an atmospheric mesoscale model simulation, which is presented in Section 5.4.6. In a departure from our previous studies of the interactions between wind stress and SST, we use the 10-m winds rather than the surface wind stress throughout this analysis to facilitate comparison with analysis of the surface momentum budgets from the atmospheric mesoscale model simulation.

The methods used to compute the small-scale vorticity and divergence fields from the QuikSCAT surface wind observations are discussed in Section 5.3. In Section 5.3.4, The QuikSCAT vorticity and divergence are shown to depend on the crosswind and downwind SST gradients in a manner analogous to the dependencies of the wind stress curl and divergence considered in our previous studies. While the vorticity and

divergence responses to SST gradients have been previously explained in terms of SST effects on wind speed, we show that SST perturbations can also generate vorticity and divergence by affecting wind direction gradients. The relationship between the QuikSCAT wind speed and AMSR-E SST fields are also quantified in Section 5.3.4. In Section 5.4.6, we perform an atmospheric model simulation over a portion of the Agulhas Return Current to investigate the dynamical balances that give rise to the vorticity and divergence responses to SST perturbations. We close in Section 5.6 with a discussion of the implications of this studies results for coupled wind-SST interactions.

5.2 Background

The response of surface winds to small-scale SST perturbations is the culmination of adjustment processes extending throughout the depth of the ABL. Surface heat fluxes are enhanced or suppressed depending on whether the flow is from cold to warm water or vice versa. Regional studies have shown that ABL turbulent momentum mixing generally plays an important role in the coupling of surface winds and SST directly over SST fronts (e.g. Sweet et al. 1981; Wallace et al. 1989; Hayes et al. 1989; Mey and Walker 1990; Wai and Stage 1989; Warner et al. 1990; Jury 1994; Hashizume et al. 2001, 2002; de Szoeke and Bretherton 2004; Skyllingstad et al. 2006). Surface heating directly controls turbulent mixing of momentum from aloft to the surface immediately over SST fronts, resulting in acceleration of surface winds over warmer

water and deceleration over cooler water.

Across SST fronts, variations in surface heating also cause cross-frontal pressure gradients near the surface since cooler, shallower layers over cooler water form higher surface pressures than do warmer, deeper layers over warmer water. Pressure gradients can therefore accelerate the boundary layer flow across SST isotherms from cooler to warmer water. Lindzen and Nigam (1987) attributed acceleration of cross-equatorial surface flow north of the equatorial cold tongue in the eastern tropical Pacific to thermally-driven pressure gradients. Subsequent studies have found that, even though some of the assumptions of their model are not generally valid, SST-induced pressure gradients in the Pacific and other regions do significantly influence the surface winds (e.g., Wai and Stage 1989; Warner et al. 1990; Small et al. 2003, 2005; Cronin et al. 2003; Mahrt et al. 2004; Bourras et al. 2004; Song et al. 2004, 2006). While pressure gradients act to accelerate the flow perpendicular to SST isotherms, it has not yet been explained how they generate surface vorticity as air blows parallel to SST isotherms, a feature generally observed in scatterometer wind fields. One of the goals of this study is to resolve whether pressure gradients contribute to the generation of vorticity perturbations near SST fronts.

Wallace et al. (1989) and Hayes et al. (1989) argued that vertical turbulent mixing of momentum from aloft to the surface was more consistent with the changes in vertical wind shear and the acceleration of surface winds occurring across the northern edge of the equatorial Pacific cold tongue, which contradicted the Lindzen and Nigam

(1987) hypothesis. SST-induced surface heating modifies the static stability of the boundary layer, enhancing the vertical turbulent mixing of momentum over warmer water and reducing it over cooler water. Indeed, observations of the near-surface vertical turbulent momentum flux throughout the World's oceans have generally shown considerable variation upon crossing SST fronts (e.g., Sweet et al. 1981; Mey and Walker 1990; Freihe et al. 1991; Jury 1994; Mahrt et al. 2004). Consistent with this hypothesis, reduced vertical shear over the warmer sides of SST fronts compared to the cooler sides have commonly been observed and attributed to changes in lower atmospheric static stability (e.g., Sweet et al. 1981; Mey and Walker 1990; Freihe et al. 1991; Bond 1992; Tokinaga et al. 2006).

Modeling studies of the role of turbulent friction in the SST-induced surface wind response have been less clear. Some investigators find a significant role (Wai and Stage 1989; Koračin and Rogers 1990; de Szoeke and Bretherton 2004; Bourras et al. 2004; Song et al. 2004; Thum 2006) while others conclude less significant roles (Small et al. 2003, 2005; Song et al. 2005; Samelson et al. 2006). Thum et al. (2006) has shown that the vertical resolution of the boundary layer, particularly near the surface, is important to resolve the effects of turbulent stress divergence on the surface winds, and that this may explain some of the discrepancies between different modeling studies.

Samelson et al. (2006) argued that changes in boundary layer depth somewhat downwind of the sharpest SST gradients, rather than the vertical redistribution of

momentum, could be responsible for the changes in surface stress observed over SST perturbations. This mechanism acts through a balance of the large-scale pressure gradient and the vertical turbulent stress divergence integrated vertically over the depth of the boundary layer such that the ratio of surface stress to boundary layer height $\boldsymbol{\tau}/H$ is equal to a constant large-scale pressure gradient integrated over the depth of the boundary layer. While this balance may hold in a vertically-integrated sense, it says nothing about the vertical structure of the boundary layer winds or the role that turbulent friction plays in redistributing momentum vertically within the boundary layer. In this study, we analyze the role of surface turbulent friction in contributing to the surface vorticity and divergence fields in a mesoscale atmospheric model simulation.

At mid-latitudes, Coriolis accelerations have been shown to be important to the response of the surface winds to small-scale SST perturbations (Wai and Stage 1989; Thum 2006; Song et al. 2006; Spall 2007). Although the Coriolis force cannot contribute to a net change in kinetic energy associated with fluid flow, it does factor strongly in the analysis and interpretation of the force balances associated with the SST-induced surface wind response. As will be shown here, the Coriolis force is essential to describe how pressure gradients, turbulent friction, and momentum advection generate surface vorticity and divergence perturbations.

5.3 Satellite observational fields

5.3.1 QuikSCAT wind fields

This study utilizes high-resolution surface vector wind observations over the 1-yr period 1 January- 31 December 2003 from the SeaWinds scatterometer onboard the QuikSCAT satellite. Scatterometers infer surface vector winds over water from radar measurements of small-scale surface roughness caused by surface wind stress. For lack of abundant, direct surface stress measurements, scatterometer measurements of radar backscatter are calibrated to buoy anemometer measurements of the so-called equivalent neutral stability wind at 10 meters, which is the 10-m wind uniquely related to the surface wind stress in a neutrally stratified layer (Liu and Tang 1996). The relation between the equivalent neutral stability wind vector $\boldsymbol{u}$ and the surface wind stress vector $\boldsymbol{\tau}$ is $\boldsymbol{\tau} = \rho_0 C_D^N V \boldsymbol{u}$, where ρ_0 is the surface air density, V is the magnitude of $\boldsymbol{u}$, and C_D^N is a neutral stability drag coefficient (for instance, from Large et al. 1994).

The QuikSCAT winds correspond to the winds at 10 m above the surface that would exist for a given wind stress if the near-surface atmosphere were neutrally stable. The computations throughout this paper using QuikSCAT winds are based on 10-m equivalent neutral stability winds. On average, anemometer measurements of 10-m wind speed are about 0.2 m s^{-1} lower than the corresponding neutral-stability wind speeds at 10-m (Mears et al. 2001; see also Fig. 16 of Chelton and Freilich 2005)

because the atmospheric surface layer is usually slightly unstable over the world's oceans.

Through comparisons with high-quality buoy anemometer measurements, random QuikSCAT wind speed measurement errors have been estimated to be about 1.7 m s^{-1} (Chelton and Freilich 2005). The wind direction accuracy improves with increasing wind speed; for wind speeds greater than about 5 m s^{-1}, the direction accuracy of individual wind measurements is better than 15° (see Fig. 8 in Chelton and Freilich 2005). Additionally, there is no evidence of SST-dependent measurement biases in the QuikSCAT wind observations (Chelton et al. 2001; Ebuchi et al. 2002).

The vector wind components and spatial derivatives of wind components, wind speed, and wind direction analyzed in this study were computed within each measurement swath, which avoids complications arising from estimating spatial derivatives using wind field composites comprised of several swaths at different measurement times. For instance, large errors near swath edges generally occur where centered first-differenced derivative estimates are comprised of measurements from different swaths taken at different times. The various wind and derivative wind fields of interest in this study were constructed on a 0.25° latitude by 0.25° longitude grid by fitting swath measurements to a quadratic surface using locally weighted regression ("loess" smoothing, Cleveland and Devlin 1988) with a half span of 80 km. Based on the filter transfer function of the loess smoother (Schlax et al. 2001; Chelton and Schlax 2003), the resulting gridded fields have a spatial resolution analogous to that

of approximately 50 km block averages. The spatial derivative fields were found at each grid point directly from the regression coefficients of the quadratic surface. The wind fields were then averaged at weekly intervals from the gridded swath data.

5.3.2 AMSR-E SST fields

The results of this study would not be possible without the high-resolution microwave observations of SST over the middle and high latitude regions available following the start of the AMSR-E geophysical observational record in June 2002 (Chelton and Wentz 2005). The main advantage of microwave measurements of SST is the ability to measure SST through non-precipitating clouds, which are essentially transparent to microwave radiation. Cloud cover generally obscures the mid-latitude ocean regions of interest in this study more than 70% of the time (Chelton and Wentz 2005). Large regions of missing data often occur in SST fields constructed from infrared satellite measurements over the sharpest ocean fronts and eddies where strong ocean-atmosphere interactions are expected to occur (see, for example, Fig. 6 of Chelton and Wentz 2005). Indeed, stratocumulus and cumulus cloud bands often form over sharp SST fronts as a consequence of some of the same ABL adjustment processes affecting ABL winds of interest in this study.

The footprint size of AMSR-E measurements of SST is 56 km and the rms accuracy of individual SST measurements is about 0.4°C (Chelton and Wentz 2005). Random SST measurement errors are mitigated in this study by temporally averaging the SST

fields over weekly intervals. The SST fields were gridded onto the same 0.25° grid as the QuikSCAT surface wind fields.

5.3.3 Crosswind and downwind gradient computations

As discussed in the introduction, previous studies have shown that the wind stress curl and divergence fields are statistically found to be linearly related to the crosswind and downwind components of the SST gradient fields, respectively. Crosswind and downwind gradients in this study were computed using a curvilinear natural coordinate system (s, n), where s and n are local along and crosswind coordinates, respectively (e.g., Haltiner and Martin 1957; Holton 1992). The unit vector $\hat{s}$ is everywhere tangent to, and in the same direction as, the surface wind vector $\boldsymbol{u}$. The positive unit vector $\hat{n}$ points 90° counterclockwise relative to $\hat{s}$. The crosswind and downwind components of the SST field $T(x, y)$ in natural coordinates are computed from Cartesian derivatives by

$$\begin{aligned} \frac{\partial T}{\partial s} &= \cos\psi \frac{\partial T}{\partial x} + \sin\psi \frac{\partial T}{\partial y} \\ \frac{\partial T}{\partial n} &= -\sin\psi \frac{\partial T}{\partial x} + \cos\psi \frac{\partial T}{\partial y}, \end{aligned} \tag{5.1}$$

where (x, y) are the zonal and meridional Cartesian coordinates, respectively, and ψ is the counterclockwise surface wind direction relative to the x axis.

Because of the non-linearities inherent in the crosswind and downwind derivative operations in Eqn. 5.1, these derivatives are computed in-swath (i.e., within

individual swaths) rather than from temporally vector-averaged wind and derivative components. The crosswind and downwind components computed in-swath are significantly smaller than the analogous components computed from vector-averaged wind and SST gradient fields because the temporally-averaged crosswind and downwind gradients shown in Eqn. 5.1 are generally not equal to the crosswind and downwind gradients computed from temporally-averaged wind components[1]. Over the Agulhas Return Current, for instance, the differences were about 30%.

Since the QuikSCAT and EOS-Aqua satellites are not synchronous, measurements of surface winds and SST are not available simultaneously, making in-swath computations of the crosswind and downwind SST gradient components impractical. The crosswind and downwind SST gradients computations were performed here by combining gridded swath measurements of QuikSCAT wind direction with SST gradients computed from 0.25° gridded 3-day averaged AMSR-E SST fields centered on the day of each QuikSCAT measurement swath. Averaging the SST field in this manner is preferable to averaging the vector wind field because the SST field evolves relatively slowly compared to the wind field. Averaging the SST field over 3-day intervals further reduces random SST measurement errors and is sufficient to eliminate gaps in spatial coverage, thus eliminating difficulties associated with collocating in-swath

[1]Crosswind and downwind gradients of SST in our previous studies (Chelton et al. 2001, 2004; Chelton 2005; and O'Neill et al. 2003, 2005) were computed from gridded, vector-averaged wind stress and SST gradient components. Because of this, the SST-induced wind response in those studies is somewhat underestimated. Also note that the definition of the crosswind SST gradient used in our previous studies $\nabla T \times \hat{\boldsymbol{u}}$ is equal to $-\partial T/\partial n$ and the downwind SST gradient $\nabla T \cdot \hat{\boldsymbol{u}}$ is equal to $\partial T/\partial s$.

QuikSCAT and AMSR-E measurement in space and time.

5.3.4 Spatial high-pass filtering

Small-scale SST-induced wind perturbations are often obscured by energetic, large-scale synoptic weather variability and spatial gradients of the mean background wind field. Small-scale variability was isolated by removing spatially low-pass filtered fields using multi-dimensional loess smoothing with half-power filter cutoffs of 30° longitude by 10° latitude. Wind and SST fields spatially high-pass filtered in this way are hereafter referred to as perturbation fields. Effects of small-scale synoptic weather variability were mitigated by averaging over time periods of a week or longer (O'Neill et al. 2005). Before the spatial high-pass filtering was applied, crosswind and downwind gradient fields were first computed from unfiltered vector wind and scalar fields.

5.4 Influence of SST fronts on mid-latitude surface winds

5.4.1 Surface wind speed response to small-scale SST perturbations

Maps of the 1-yr scalar-averaged perturbation wind speed and SST fields over each of the 4 regions considered here are shown in Fig. 5.1. Characteristic of regions

near mid-latitude SST fronts, strong horizontal variations of surface wind speed occur near meandering SST fronts, with stronger wind speeds over warmer water and weaker wind speeds over cooler water. Typically, surface wind speed variations of more than 2 m s^{-1} accompany SST variations exceeding 4°C over cross-frontal distances of O(100 km). This is an appreciable fraction of the unfiltered wind speeds in these regions, which are typically 8-12 m s^{-1} in 1-yr averages (Fig. 5.2). For the 1-yr average perturbation fields, the spatial correlation between the perturbation wind speed field and the perturbation SST field varies between 0.7 over the Kuroshio to 0.85 over the South Atlantic (Table 5.1).

The small-scale response of the wind speed to SST is statistically quantified by bin-averaging the perturbation QuikSCAT wind speed as a function of the perturbation AMSR-E SST at weekly intervals over the 1-yr analysis period (Fig. 5.3). Statistically, wind speed perturbations are linearly related to and positively correlated with small-scale SST perturbations over all four regions. The relationship between the spatially high-pass filtered wind speed V' and SST T' can thus be expressed as

$$V' = \alpha_0 T', \tag{5.2}$$

where α_0 is the slope of these linear relations. Note that $\alpha_0 = \partial V'/\partial T'$ and represents the change in wind speed per unit change in SST. The sensitivity of the response, as measured by the slope α_0 of the linear relation, varies considerably between the 4 regions, from 0.28 m/s per °C over the Kuroshio to 0.44 m/s per °C over the

Agulhas Return Current (see Table 5.1). The larger std devs at large perturbation SST magnitudes in Fig. 5.3 are due to the smaller numbers of samples in these bins. The geographic variability of α_0 between the four regions is not yet understood, but is likely attributable to geographic differences in vertical structure of the boundary layer and large-scale forcing.

5.4.2 Spatial gradients of perturbation wind speed and SST

From the linear statistical relationship between V' and T', it follows that crosswind and downwind gradients of wind speed should depend, respectively, on the crosswind and downwind components of the SST gradient field so that

$$\left(\frac{\partial V}{\partial n}\right)' = \alpha_c^{spd}\left(\frac{\partial T}{\partial n}\right)' \tag{5.3}$$

$$\left(\frac{\partial V}{\partial s}\right)' = \alpha_d^{spd}\left(\frac{\partial T}{\partial s}\right)', \tag{5.4}$$

where α_c^{spd} and α_d^{spd} are the coupling coefficients for the speed gradient responses to SST gradients. The crosswind and downwind speed gradient components are indeed linearly related to the crosswind and downwind SST gradient components, respectively (Fig. 5.4). Moreover, within each region, α_c^{spd} and α_d^{spd} are nearly equal to α_0 from Fig. 5.3. The scalar wind speed and speed gradient responses to SST perturbations are therefore manifestations of the wind speed modulation by small-scale SST perturbations. These relationships between the crosswind and downwind speed gra-

dients and the underlying SST gradients has important implications for the surface vorticity and divergence fields and are discussed in the next section.

The linear relationships between the perturbation wind speed and SST fields can be further investigated by expressing the perturbation crosswind and downwind components of the SST gradient as

$$\begin{aligned} \left(\frac{\partial T}{\partial n}\right)' &= M_T \sin\theta' \\ \left(\frac{\partial T}{\partial s}\right)' &= M_T \cos\theta', \end{aligned} \tag{5.5}$$

where M_T is the magnitude of the perturbation SST gradient,

$$M_T = \sqrt{\left(\frac{\partial T}{\partial s}\right)'^2 + \left(\frac{\partial T}{\partial n}\right)'^2}, \tag{5.6}$$

and the angle θ' is defined such that

$$\theta' = \tan^{-1}\left[\frac{(\partial T/\partial n)'}{(\partial T/\partial s)'}\right]. \tag{5.7}$$

A physical interpretation of the counterclockwise angle θ' is given in Appendix 5.8. Geometrically, θ' closely approximates the angle between the surface streamlines and the perturbation SST gradient vector $\nabla T'$ to within an RMS uncertainty of 7.6°. The largest downwind speed gradients should occur as surface winds blow perpendicular to perturbation SST isotherms toward warmer water ($\theta' = 0°$ or $\pm 180°$); likewise, the largest crosswind speed gradients should occur as the surface winds blow along

perturbation SST isotherms (when $\theta' = \pm 90^\circ$).

The angular dependencies of the perturbation crosswind and downwind speed gradients on θ' are shown in Fig. 5.5. The crosswind and downwind speed gradients closely follow sine and cosine functions, respectively, of the angle θ', in agreement with the hypothesized dependencies relating the orientation of the surface streamlines to the perturbation SST isotherms. Close inspection of Fig. 5.5 reveals small but consistent phase shifts from the expected pure sine and cosine curves. From these statistical results, we may thus express the crosswind and downwind speed gradients as

$$\left(\frac{\partial V}{\partial n}\right)' = \alpha_c^{spd} M_T \sin\left(\theta' + \phi_c^{spd}\right) \tag{5.8}$$

$$\left(\frac{\partial V}{\partial s}\right)' = \alpha_d^{spd} M_T \cos\left(\theta' + \phi_d^{spd}\right), \tag{5.9}$$

where α_c^{spd} and α_d^{spd} are the amplitudes of the speed gradient responses to θ' shown in Fig. 5.5 and ϕ_c^{spd} and ϕ_d^{spd} are the phase shifts (counterclockwise for positive values). The values of the amplitudes and phase shifts are shown in Table 5.2. Within each region, α_c^{spd} and α_d^{spd} are nearly equal. Note that ϕ_c^{spd} is essentially 0° over all 4 regions while ϕ_d^{spd} is about $5 - 11^\circ$ with opposing signs between hemispheres. The dynamical mechanisms responsible for these phase shifts are investigated in Section 5.4.6.

5.4.3 SST-induced variability in the surface vorticity and divergence fields

The importance of SST-induced perturbations in the crosswind and downwind speed gradient fields becomes more readily apparent by considering the vorticity and divergence of the surface wind field. The separate effects of spatial gradients in wind speed and direction on the vorticity and divergence fields are found by expressing the vorticity and divergence in curvilinear natural coordinates (e. g., Haltiner and Martin 1957),

$$\nabla \times \boldsymbol{u}' = -\Big(\frac{\partial V}{\partial n}\Big)' + \Big(V\frac{\partial \psi}{\partial s}\Big)' \tag{5.10}$$

$$\nabla \cdot \boldsymbol{u}' = \Big(\frac{\partial V}{\partial s}\Big)' + \Big(V\frac{\partial \psi}{\partial n}\Big)', \tag{5.11}$$

where, as before, ψ is the counterclockwise wind direction, $\boldsymbol{u}$ is the surface wind vector, and V is the magnitude of $\boldsymbol{u}$. Eqn. 5.10 partitions the perturbation vorticity field into the difference between the local crosswind speed gradient and a term related to downwind gradients in flow direction. Likewise, Eqn. 5.11 partitions the perturbation divergence field into the sum of the downwind speed gradient and a term related to the crosswind gradient in flow direction. The direction gradient term in the vorticity is related to the radius of curvature of surface streamlines, while the direction gradient term in the divergence is related to spreading or contracting of streamlines in the crosswind direction, which is often referred to as the diffluent tendency (Haltiner

and Martin 1957). Decomposing the vorticity and divergence in this manner allows investigation of the separate effects of lateral shear and downwind rotation on the vorticity, and the separate effects of downwind acceleration and crosswind rotation on the divergence.

The perturbation vorticity and divergence fields binned as functions of the perturbation crosswind and downwind SST gradients, respectively, are shown in Fig. 5.6. Small-scale perturbations in the vorticity and divergence fields are highly correlated with small-scale perturbations in the underlying SST gradient field, as demonstrated in our previous studies using the wind stress curl and divergence fields (Chelton et al. 2001, 2004; O'Neill et al. 2003, 2005). Given the results of Sec. 5.4.2 and Eqns. (5.10) and (5.11), if the surface vorticity and divergence were dependent only on the crosswind and downwind speed gradients, respectively, then the slopes of the straight line fits in Fig. 5.6 should be equal in magnitude but opposite in sign. The slope of the divergence response to downwind SST gradients is, however, significantly larger than that of the vorticity response to crosswind SST gradients, in agreement with our previous studies. Additionally, the variability within each bin, as represented by the width of the std dev for each bin, is much smaller for the speed gradient components in Fig. 5.4 than for the vorticity and divergence in Fig. 5.6. Evidently, the direction gradient terms in Eqns. (5.10) and (5.11) reduce the overall vorticity responses to crosswind SST gradients and enhance the divergence responses to downwind SST gradients, a point more rigorously quantified in the next subsection.

Besides the differences in the responses noted above, there are significant differences in the vorticity and divergence responses to θ' (Fig. 5.7) from that expected from sole consideration of SST-induced wind speed perturbations. In our previous work, we hypothesized that the surface curl should depend on the sine of θ' while the divergence should depend on the cosine of θ', consistent with the crosswind and downwind SST gradients dependencies. The vorticity and divergence do not depend exactly on the sine and cosine, respectively, of θ', but are phase-shifted. In addition to the phase shifts, the amplitude of the vorticity response to θ' is less than the amplitude of the divergence response to θ'. These differences are addressed below. Before doing so, it is necessary to investigate the responses of the direction gradient terms in Eqns. 5.10 and 5.11 to θ'. It can be anticipated that the direction gradient terms are key in understanding the differences in the vorticity and divergence responses in Fig. 5.6.

The dependencies of the direction gradient terms on θ' are shown in Fig. 5.8. Both the crosswind and downwind components of the wind direction gradients vary as phase-shifted sinusoidal functions of θ'. Within each hemisphere, the phase shifts are nearly the same (see Table 5.1). However, between each hemisphere, the phase shifts are approximately 180° out of phase. In all 4 regions, the downwind direction gradient response to θ' shows that the surface winds tend to rotate equatorward as they blow across perturbation SST isotherms toward progressively warmer water and poleward over progressively cooler water. The crosswind direction gradient response

to θ' indicates a maximum surface diffluent tendency as winds blow along perturbation SST isotherms. Statistically, the direction gradient terms can be represented by

$$\left(V\frac{\partial\psi}{\partial s}\right)' = \alpha_d^{dir} M_T \cos\left(\theta' - \phi_d^{dir}\right) \tag{5.12}$$

$$\left(V\frac{\partial\psi}{\partial n}\right)' = \alpha_c^{dir} M_T \sin\left(\theta' + \phi_c^{dir}\right), \tag{5.13}$$

where ϕ_d^{dir} and ϕ_c^{dir} are phase shifts and α_d^{dir} and α_c^{dir} are coupling coefficients for the downwind and crosswind direction gradients, respectively. The statistical responses of the direction gradient terms to θ' are not orthogonal to the associated statistical speed gradient responses. This means that, on average, wind direction gradients tend to produce vorticity and divergence at the same places that the speed gradients produce vorticity and divergence.

The statistical relations in Eqns. 5.12 and 5.13, along with the statistical relations for the speed gradients in Eqns. 5.8 and 5.9, are used in Section 5.4.2 to develop a heuristic explanation for the differences in the vorticity and divergence responses to SST gradients.

5.4.4 Why is the vorticity response to crosswind SST gradients weaker than the divergence response to downwind SST gradients?

The statistical relations developed here are utilized to explain why the vorticity response to crosswind SST gradients is less than the divergence response to downwind SST gradients. Recall that the vorticity and divergence dependencies on the crosswind and downwind SST gradients were developed through consideration of the effects of SST on wind speed only (Chelton et al. 2001). As we will show here, however, generation of vorticity and divergence from the SST-induced wind direction gradient perturbations are instrumental in generating the difference in these responses.

The QuikSCAT crosswind and downwind speed gradient responses to θ' shown in Fig. 5.5 and the crosswind and downwind direction gradient responses to θ' shown in Fig. 5.8 can be combined to relate the vorticity and divergence fields to M_T and θ' as

$$\nabla \times \boldsymbol{u}' = \underbrace{-\alpha_c^{spd} M_T \sin\left(\theta' + \phi_c^{spd}\right)}_{\text{Crosswind Speed Gradient}} + \underbrace{\alpha_d^{dir} M_T \cos\left(\theta' - \phi_d^{dir}\right)}_{\text{Downwind Direction Gradient}} \tag{5.14}$$

$$\nabla \cdot \boldsymbol{u}' = \underbrace{\alpha_d^{spd} M_T \cos\left(\theta' + \phi_d^{spd}\right)}_{\text{Downwind Speed Gradient}} + \underbrace{\alpha_c^{dir} M_T \sin\left(\theta' + \phi_c^{dir}\right)}_{\text{Crosswind Direction Gradient}} . \tag{5.15}$$

The components of the vorticity and divergence that each term empirically represents are indicated by the underbraces. Using trigonometric identities and rewriting these equations in terms of the crosswind and downwind SST gradients using Eqn. 5.5 yields

$$\nabla \times \boldsymbol{u}' = \alpha_c^{vort}\left(\frac{\partial T}{\partial n}\right)' + \alpha_d^{vort}\left(\frac{\partial T}{\partial s}\right)' \tag{5.16}$$

$$\nabla \cdot \boldsymbol{u}' = \alpha_d^{div}\left(\frac{\partial T}{\partial s}\right)' + \alpha_c^{div}\left(\frac{\partial T}{\partial n}\right)', \tag{5.17}$$

where the set of coupling coefficients $(\alpha_c^{vort}, \alpha_d^{vort})$ and $(\alpha_d^{div}, \alpha_c^{div})$ are defined as

$$\alpha_c^{vort} = -\alpha_c^{spd}\cos\phi_c^{spd} + \alpha_d^{dir}\sin\phi_d^{dir} \tag{5.18}$$

$$\alpha_d^{vort} = -\alpha_c^{spd}\sin\phi_c^{spd} + \alpha_d^{dir}\cos\phi_d^{dir} \tag{5.19}$$

$$\alpha_d^{div} = \alpha_d^{spd}\cos\phi_d^{spd} + \alpha_c^{dir}\sin\phi_c^{dir} \tag{5.20}$$

$$\alpha_c^{div} = -\alpha_d^{spd}\sin\phi_d^{spd} + \alpha_c^{dir}\cos\phi_c^{dir}. \tag{5.21}$$

Each of the coupling coefficients (α's) and the phases (ϕ's) are tabulated in Table 5.2 over the 4 regions of interest here. The phase shifts in the responses of the vorticity and divergence to θ' can now be understood in terms of the separate effects of wind speed and direction responses to SST perturbations.

Consider Eqn. 5.18 for α_c^{vort}, which is the coupling coefficient for the vorticity response to crosswind SST gradients. Both α_d^{dir} and $\sin\phi_d^{dir}$ are statistically found to be positive quantities (Table 5.2) over all 4 regions. Therefore, downwind direction gradients reduce the vorticity response to crosswind SST gradients by a factor of $\alpha_d^{dir}\sin\phi_d^{dir}$. From consideration of Eqn. 5.20 for α_d^{div}, the crosswind direction gradients enhance the divergence response to downwind SST gradients by a factor of

$\alpha_c^{dir} \sin \phi_c^{dir}$ since α_c^{dir} and $\sin \phi_c^{dir}$ are both statistically found to be positive quantities (Table 5.2) over all 4 regions. Direction gradients thus enhance the divergence but reduce the vorticity. Cross-frontal changes in wind direction associated with the small-scale SST gradients thus account for the differences in the statistical responses of the surface vorticity and divergence to crosswind and downwind SST gradients.

It will be shown in Section 5.4.6 that gradients in wind speed and direction arise from a combination of changes of all the terms in the surface momentum budget in an intricate balance controlled by SST-induced surface heating perturbations.

5.4.5 Responses of spatial gradients of u and v to θ'

In Fig. 5.9, the perturbation quantities $(\partial u/\partial x)'$, $(\partial u/\partial y)'$, $(\partial v/\partial x)'$, and $(\partial v/\partial y)'$ were bin-averaged as functions of θ' over all 4 regions. On average, the amplitude of the $(\partial u/\partial x)'$ and $(\partial u/\partial y)'$ responses to θ' were several times greater than the amplitude of the $(\partial v/\partial x)'$ and $(\partial v/\partial y)'$ responses. In addition to the smaller amplitudes, the θ' response of $(\partial v/\partial x)'$ is phase-shifted relative to $(\partial u/\partial x)'$. Likewise, the responses of $(\partial u/\partial y)'$ and $(\partial v/\partial y)'$ to θ' are phase-shifted relative to each other. From these observations, it is clear that perturbation vorticity and divergence response to θ' is mainly caused by the perturbation response of spatial gradients in u.

A stronger u response compared to v along a streamline can cause the direction of the flow to change, which could explain the downwind and crosswind direction responses to θ'. To formally justify this conclusion, the crosswind and downwind direction gradients are expressed in terms of crosswind and downwind gradients of u

and v by

$$\begin{aligned} V\frac{\partial\psi}{\partial s} &= \cos\psi\frac{\partial v}{\partial s} - \sin\psi\frac{\partial u}{\partial s} \\ V\frac{\partial\psi}{\partial n} &= \cos\psi\frac{\partial v}{\partial n} - \sin\psi\frac{\partial u}{\partial n}. \end{aligned}$$

Each of the individual terms in these equations bin-averaged as functions of θ' in Fig. 5.10. Considering the expression for $V\partial\psi/\partial s$, the term $\cos\psi\ \partial v/\partial s$ represents the local gradient in v along streamlines while the term $\sin\psi\ \partial u/\partial s$ represents the local gradient of u along streamlines. For a streamline to have no curvature, $\cos\psi\ \partial v/\partial s$ would equal $\sin\psi\ \partial u/\partial s$, and there would be no downwind direction gradients for all values of θ'. The QuikSCAT observations in Fig. 5.10 show that the response of $\cos\psi\ \partial v/\partial s$ as a function of θ' is phase-shifted relative to the $\sin\psi\ \partial u/\partial s$ response, which leads to a non-zero downwind direction gradient response to θ', and hence non-zero streamline curvature. A similar argument holds for the crosswind direction gradient response to θ'. It is evident from Fig. 5.10 that the stronger u response to θ' compared with that of v gives rise to the direction gradient terms. Additionally, although the spatial gradients of v are small, they play just as significant of a role in producing crosswind and downwind direction gradients. This is evident from the similarity of the amplitudes of the $\cos\psi\ \partial v/\partial s$ and $\sin\psi\ \partial u/\partial s$ responses and the $\cos\psi\ \partial v/\partial n$ and $\sin\psi\ \partial u/\partial n$ responses shown in Fig. 5.10.

The observation that the u and v gradients respond in a different manner to θ'

is an indication that the dynamical responses of the zonal and meridional momentum budgets are also different, consistent with the dynamical analysis performed in Chapter 4.

5.4.6 Mean wind direction near SST fronts

From the discussion in Section 5.4.5, it is apparent that SST fronts significantly alter wind direction in addition to wind speed. Maps of the direction of the 1-yr vector-averaged QuikSCAT wind components are shown in Fig. 5.11. Over the strong quasi-zonal SST fronts in all four regions, there is consistent equatorward turning of the surface wind vectors, ranging from about 5-30°. SST-induced turning of the winds diminishes where the SST isotherms become diffuse away from the fronts. Among these four regions, the strongest direction changes occur over the Gulf Stream and the weakest occur over the Kuroshio. This is consistent with the results in Section 5.3.4 showing that the weakest SST-induced wind speed perturbations generally occur over the Kuroshio.

5.5 Dynamics of SST-induced vorticity and divergence responses

From the Weather Research and Forecasting (WRF) mesoscale model simulation over the Agulhas Return Current, we showed in Chapter 4 that the near-surface winds respond to SST perturbations through a baroclinic Ekman adjustment mecha-

nism modified by horizontal advection. In terms of the crosswind momentum budget, the adjustment can also be characterized as a baroclinic gradient wind adjustment, whereby unbalanced Coriolis and crosswind pressure gradient accelerations cause curvature of the surface streamlines. In this section, we further analyze this WRF simulation to determine how these force balances lead to the observed correlations between the vorticity and divergence and the crosswind and downwind components of the SST gradient. The simulation was performed for the month of July 2002 using a steady 1-month average SST surface boundary condition derived from SST observations by the AMSR-E. Further details of the simulation can be found in Chapter 4.

5.5.1 Comparison of WRF and QuikSCAT vorticity and divergence responses

The ability of WRF to accurately simulate the perturbation surface vorticity and divergence responses to SST gradients is evaluated by comparing the responses computed from the WRF simulation with those computed from the QuikSCAT wind fields. Consistent with previous analyses, small-scale vorticity and divergence perturbations are linearly related to the crosswind and downwind components of the SST gradient, respectively (black curves, Fig. 5.12). The WRF simulation reproduces the linear dependencies obtained from the QuikSCAT observations, as evidenced by the closeness of their slopes (labeled in black in Fig. 5.12). Additionally, as was observed in Section 5.3 for the full calendar year 2003, the vorticity response to crosswind SST gradients is about 35% weaker in magnitude than divergence response to downwind

SST gradients in the WRF simulation.

The WRF speed gradient dependencies also agree well with those computed from QuikSCAT (black curves in panels b and d, Fig. 5.13), which provides further evidence of WRF's ability to simulate the SST-induced surface wind response. The slopes of the WRF crosswind and downwind speed gradient responses are nearly equal (to within $\sim 10\%$) and nearly equal to the slope of the WRF perturbation wind speed response to SST perturbations shown in Fig. 3 of Chapter 4, which was 0.45 m/s per °C.

While comparing the WRF and QuikSCAT vorticity and divergence fields, differences may arise from surface layer stability effects, which cannot be corrected for in the QuikSCAT equivalent neutral stability winds used here in the comparisons. To assess the effects of surface layer stability on these relations, the WRF vorticity and divergence responses to the SST gradients shown in Fig. 5.12 were recomputed using the equivalent neutral stability winds at 10-m in place of the actual surface winds. The WRF equivalent neutral stability wind speed $\boldsymbol{V}_{10}^N$ and vector components (u_{10}^N, v_{10}^N) were computed from the surface wind stress magnitude $\boldsymbol{\tau}$ and neutral stability drag coefficient at 10-m C_d^N using the COARE bulk flux algorithm (Fairall et al. 2003) and

$$\begin{aligned} \boldsymbol{V}_{10}^N &= \left(\frac{\boldsymbol{\tau}}{\rho_0 C_d^N}\right)^{1/2} \\ u_{10}^N &= \boldsymbol{V}_{10}^N \cos\psi \end{aligned}$$

$$v_{10}^N = \boldsymbol{V}_{10}^N \sin\psi.$$

The slopes of the vorticity and divergence responses to the crosswind and downwind SST gradients based on the equivalent neutral stability winds increase in magnitude to -0.45 and 0.67, respectively, which is only about a $10-15\%$ increase over the slopes computed in Fig. 5.12. Some of this change is simply due to adjusting the wind height in the lowest level of the WRF model from 18 m down to the 10 m level of the scatterometer winds. Based on the small change in magnitude of the slopes, surface layer stability effects have only a minor influence on the responses of the vorticity and divergence fields to SST gradients. This analysis is consistent with the conclusions of the importance of surface layer stability effects on the SST-induced surface wind response from O'Neill et al. (2005) and Spall (2007b).

5.5.2 Momentum budgets

The surface momentum equations in the zonal and meridional directions are expressed here as

$$u = -\frac{1}{\rho f}\frac{\partial p}{\partial y} - \frac{F^y}{f} - \frac{1}{f}\Big(u\frac{\partial v}{\partial x} + v\frac{\partial v}{\partial y}\Big) \tag{5.22}$$

$$v = \frac{1}{\rho f}\frac{\partial p}{\partial x} + \frac{F^x}{f} + \frac{1}{f}\Big(u\frac{\partial u}{\partial x} + v\frac{\partial u}{\partial y}\Big), \tag{5.23}$$

where p is pressure, F^x and F^y are the vertical turbulent stress divergence components in the zonal and meridional directions, respectively, f is the Coriolis parameter, and

ρ is the air density. Taking the curl and divergence of the u and v vector wind components from these equations yields

$$\begin{aligned}
\nabla \times \boldsymbol{u} &= \left[\frac{\partial}{\partial x}\Big(\frac{1}{\rho f}\frac{\partial p}{\partial x}\Big) + \frac{\partial}{\partial y}\Big(\frac{1}{\rho f}\frac{\partial p}{\partial y}\Big)\right] + \left[\frac{\partial}{\partial x}\Big(\frac{F^x}{f}\Big) + \frac{\partial}{\partial y}\Big(\frac{F^y}{f}\Big)\right] + \\
&\quad \left[\frac{\partial}{\partial x}\left(\frac{1}{f}\Big(u\frac{\partial u}{\partial x} + v\frac{\partial u}{\partial y}\Big)\right) + \frac{\partial}{\partial y}\left(\frac{1}{f}\Big(u\frac{\partial v}{\partial x} + v\frac{\partial v}{\partial y}\Big)\right)\right] \qquad (5.24) \\
\nabla \cdot \boldsymbol{u} &= \left[\frac{\partial}{\partial x}\Big(-\frac{1}{\rho f}\frac{\partial p}{\partial y}\Big) + \frac{\partial}{\partial y}\Big(\frac{1}{\rho f}\frac{\partial p}{\partial x}\Big)\right] + \left[\frac{\partial}{\partial x}\Big(-\frac{F^y}{f}\Big) + \frac{\partial}{\partial y}\Big(\frac{F^x}{f}\Big)\right] + \\
&\quad \left[\frac{\partial}{\partial x}\left(-\frac{1}{f}\Big(u\frac{\partial v}{\partial x} + v\frac{\partial v}{\partial y}\Big)\right) + \frac{\partial}{\partial y}\left(\frac{1}{f}\Big(u\frac{\partial u}{\partial x} + v\frac{\partial u}{\partial y}\Big)\right)\right] \qquad (5.25)
\end{aligned}$$

Interpretation of this expression is simplified by defining a geostrophic wind vector (u_g, v_g) and ageostrophic wind vector (u_a, v_a), where $u = u_g + u_a$ and $v = v_g + v_a$. The ageostrophic wind components associated with turbulent friction (u_{turb}, v_{turb}) and horizontal advection (u_{adv}, v_{adv}) are defined such that $u_a = u_{turb} + u_{adv}$ and $v_a = v_{turb} + v_{adv}$. Eqns. 5.24 and 5.25 can then be formulated as

$$\nabla \times \boldsymbol{u} = \nabla \times \boldsymbol{u}_g + \nabla \times \boldsymbol{u}_{turb} + \nabla \times \boldsymbol{u}_{adv} \qquad (5.26)$$

$$\nabla \cdot \boldsymbol{u} = \nabla \cdot \boldsymbol{u}_g + \nabla \cdot \boldsymbol{u}_{turb} + \nabla \cdot \boldsymbol{u}_{adv}. \qquad (5.27)$$

By decomposing the vorticity and divergence fields into geostrophic and ageostrophic components, the relative influences of pressure gradients, turbulent friction, horizontal advection, and Coriolis accelerations on the vorticity and divergence fields can be investigated from WRF. The crosswind and downwind speed and direction gradient fields can be decomposed into geostrophic and ageostrophic components in a similar

manner by first formulating the speed and direction gradients in terms of crosswind and downwind gradients of u and v

$$\begin{aligned}
\frac{\partial V}{\partial s} &= \cos\psi\frac{\partial u}{\partial s} + \sin\psi\frac{\partial v}{\partial s} \\
\frac{\partial V}{\partial n} &= \cos\psi\frac{\partial u}{\partial n} + \sin\psi\frac{\partial v}{\partial n} \\
V\frac{\partial \psi}{\partial s} &= \cos\psi\frac{\partial v}{\partial s} - \sin\psi\frac{\partial u}{\partial s} \\
V\frac{\partial \psi}{\partial n} &= \cos\psi\frac{\partial v}{\partial n} - \sin\psi\frac{\partial u}{\partial n}.
\end{aligned}$$

These expressions were found by differentiation of $V = \sqrt{u^2 + v^2}$ and $\psi = \tan^{-1}(v/u)$. Substitution of Eqns. 5.22 and 5.23 for u and v into the above equations yields the following expressions for the downwind and crosswind speed and direction gradients

$$\frac{\partial V}{\partial s} = \Big(\frac{\partial V}{\partial s}\Big)_p + \Big(\frac{\partial V}{\partial s}\Big)_{turb} + \Big(\frac{\partial V}{\partial s}\Big)_{adv} \tag{5.28}$$

$$\frac{\partial V}{\partial n} = \Big(\frac{\partial V}{\partial n}\Big)_p + \Big(\frac{\partial V}{\partial n}\Big)_{turb} + \Big(\frac{\partial V}{\partial n}\Big)_{adv} \tag{5.29}$$

$$V\frac{\partial \psi}{\partial s} = \Big(V\frac{\partial \psi}{\partial s}\Big)_p + \Big(V\frac{\partial \psi}{\partial s}\Big)_{turb} + \Big(V\frac{\partial \psi}{\partial s}\Big)_{adv} \tag{5.30}$$

$$V\frac{\partial \psi}{\partial n} = \Big(V\frac{\partial \psi}{\partial n}\Big)_p + \Big(V\frac{\partial \psi}{\partial n}\Big)_{turb} + \Big(V\frac{\partial \psi}{\partial n}\Big)_{adv}, \tag{5.31}$$

where

$$\begin{aligned}
\Big(\frac{\partial V}{\partial s, n}\Big)_p &= -\cos\psi\frac{\partial}{\partial s, n}\Big(\frac{1}{\rho f}\frac{\partial p}{\partial y}\Big) + \sin\psi\frac{\partial}{\partial s, n}\Big(\frac{1}{\rho f}\frac{\partial p}{\partial x}\Big) \\
\Big(\frac{\partial V}{\partial s, n}\Big)_{turb} &= -\cos\psi\frac{\partial}{\partial s, n}\Big(\frac{F^y}{f}\Big) + \sin\psi\frac{\partial}{\partial s, n}\Big(\frac{F^x}{f}\Big)
\end{aligned}$$

$$
\begin{aligned}
\left(\frac{\partial V}{\partial s,n}\right)_{adv} &= -\cos\psi\frac{\partial}{\partial s,n}\left(\frac{1}{f}\frac{Dv}{Dt}\right)+\sin\psi\frac{\partial}{\partial s,n}\left(\frac{1}{f}\frac{Du}{Dt}\right)\\
\left(V\frac{\partial\psi}{\partial s,n}\right)_{p} &= \cos\psi\frac{\partial}{\partial s,n}\left(\frac{1}{\rho f}\frac{\partial p}{\partial x}\right)-\sin\psi\frac{\partial}{\partial s,n}\left(\frac{-1}{\rho f}\frac{\partial p}{\partial y}\right)\\
\left(V\frac{\partial\psi}{\partial s,n}\right)_{turb} &= \cos\psi\frac{\partial}{\partial s,n}\left(\frac{F^x}{f}\right)+\sin\psi\frac{\partial}{\partial s,n}\left(\frac{F^y}{f}\right)\\
\left(V\frac{\partial\psi}{\partial s,n}\right)_{adv} &= \cos\psi\frac{\partial}{\partial s,n}\left(\frac{1}{f}\left(u\frac{\partial u}{\partial x}+v\frac{\partial u}{\partial y}\right)\right)+\sin\psi\frac{\partial}{\partial s,n}\left(\frac{1}{f}\left(u\frac{\partial v}{\partial x}+v\frac{\partial v}{\partial y}\right)\right).
\end{aligned}
$$

In the following discussion, we refer only to the surface perturbation components of all these quantities.

5.5.3 Descriptive responses of the vorticity and divergence fields

Vorticity

The spatial distribution of the vorticity shows that both the geostrophic and ageostrophic components of the perturbation vorticity all have similar magnitudes (panels c, f, i, and l, Fig. 5.14). In this manner, the SST-induced vorticity response is consistent with the advection-modified Ekman adjustment mechanism discussed in Chapter 4.

Geostrophic wind perturbations form in association with the SST-induced surface pressure perturbations[2]. Geostrophic vorticity perturbations form that are cyclonic downwind of warm SST perturbations and anti-cyclonic downwind of cool SST perturbations (panel c, Fig. 5.14). Because the surface pressure perturbations are located downwind of the SST perturbations (e.g., Small et al. 2003; also note that the pertur-

[2]For reference, the mean surface geostrophic and ageostrophic wind vectors associated with this WRF simulation are shown in Fig. 18b of Chapter 4

bation pressure distribution shown in Fig. 3 of Chapter 4 from this WRF simulation), the geostrophic vorticity perturbations are apparently correlated with the downwind SST gradients (panel c, Fig. 5.14). The geostrophic vorticity response is composed of nearly equal contributions from the geostrophic components of the crosswind speed gradient and downwind direction gradient (panels a and b, Fig. 5.14, respectively).

$\nabla \times \boldsymbol{u}'_{turb}$ only partially contributes to the total SST-induced vorticity response, as evidenced by the existence of $\nabla \times \boldsymbol{u}'_{g}$ and $\nabla \times \boldsymbol{u}'_{adv}$ fields of similar magnitude as the turbulent friction forcing (panels c, f, and i, Fig. 5.14). The turbulent friction contribution to the vorticity is apparently correlated with the downwind SST gradients rather than with the crosswind SST gradients as suggested by Wallace et al. (1989) (panel f, Fig. 5.14). This can be explained by the SST-induced baroclinic modification of the near-surface vertical turbulent momentum flux discussed in Chapter 4, which, instead of simply modulating the surface wind speed, also deflects the surface winds over the SST perturbations; this generates significant vorticity through modification of the curvature of the surface streamlines (panel e, Fig. 5.14).

Perhaps coincidently, the $(V\frac{\partial \psi}{\partial s})'_{turb}$ and $(V\frac{\partial \psi}{\partial s})'_{adv}$ fields tend to nearly oppose each other (panels e and h, Fig. 5.14). Since these ageostrophic components nearly cancel, the net SST-induced downwind direction gradient response is mainly comprised of the geostrophic contribution, as evident from comparing panels b and k in Fig. 5.14. Note that the $(V\frac{\partial \psi}{\partial s})'_{turb}$ and $(V\frac{\partial \psi}{\partial s})'_{adv}$ fields are nearly collocated with the SST perturbations rather than their gradients.

Horizontal advection is more important in the downwind direction gradient term (panel h, Fig. 5.14) and less important in the crosswind speed gradient term (panel g, Fig. 5.14). $\nabla \times \boldsymbol{u}'_{adv}$ thus mainly affects the vorticity through the curvature of the streamlines rather than the crosswind shear.

Divergence

Since the geostrophic winds are essentially non-divergent, $\nabla \cdot \boldsymbol{u}'_g$ does not contribute to the SST-induced divergence response (panel c, Fig. 5.15); the geostrophic contribution to the downwind speed gradient and crosswind direction gradients therefore very nearly balance (panels a and b, Fig. 5.15). Both $\nabla \cdot \boldsymbol{u}'_{turb}$ and $\nabla \cdot \boldsymbol{u}'_{adv}$ comprise the divergence response to SST gradients (panels f and i, Fig. 5.15).

$\nabla \cdot \boldsymbol{u}'_{turb}$ is mainly affected by $(\frac{\partial V}{\partial s})'_{turb}$, with only smaller contributions through the diffluent term (panels d, e, and f, Fig. 5.15). The effect of turbulent friction on the downwind speed gradient is therefore consistent with the influence hypothesized by Wallace et al. (1989), where the vertical turbulent mixing of momentum from aloft to the surface causes downwind speed gradients in regions of significant downwind SST gradients.

Horizontal advection plays an unexpectedly large role in the generation of divergence (panel i, Fig. 5.15). In both the downwind speed gradient and the crosswind direction gradient responses, horizontal advection shifts wind perturbations downstream from where the baroclinic Ekman adjustment occurs over the sharpest SST

gradients.

5.5.4 Statistical responses of the vorticity and divergence fields

In this section, the dependencies of the WRF surface vorticity, divergence, and speed and direction gradients on the crosswind and downwind SST gradients are discussed in terms of the dynamical framework developed thus far. Instead of providing an extensive accounting of these statistical dependencies, our main objective here is to explain succinctly two statistical phenomena found in the analysis of the satellite wind and SST observations. First, can we determine the dynamics of the weaker vorticity response to crosswind SST gradients compared to the divergence response to downwind SST gradients? Second, can we determine the dynamics of the phase-shifts in the response of the vorticity, divergence, and the speed gradients to the angle θ' between the surface wind and perturbation SST gradient vector? In doing both, we also demonstrate that the turbulent mixing of momentum mechanism hypothesized by Wallace et al. (1989) cannot fully explain the statistical responses of the vorticity and divergence to SST perturbations in the WRF simulation. In place of the simpler Wallace et al. (1989) mechanism, we will show that the vorticity and divergence responses to the crosswind and downwind SST gradients result, unfortunately, from more complicated dynamics involving most of the terms in the surface momentum budget.

Dynamical responses of the surface vorticity and divergence to the crosswind and downwind SST gradients

Since $\nabla \cdot \boldsymbol{u}'_g$ is negligible (red curve in panel a, Fig. 5.12), the divergence response to downwind SST gradients is only composed of the ageostrophic turbulent friction and horizontal advection components. While $\nabla \cdot \boldsymbol{u}'_{turb}$ is linearly related to the downwind SST gradient (blue curve in panel a, Fig. 5.12), its slope is only about half that of the $\nabla \cdot \boldsymbol{u}'$ response (black curve in panel a, Fig. 5.12). The ageostrophic turbulent friction component can therefore account for only about half of the divergence response to downwind SST gradients. Like the $\nabla \cdot \boldsymbol{u}'_{turb}$ response to downwind SST gradients, $\nabla \cdot \boldsymbol{u}'_{adv}$ is nearly linearly related to the downwind SST gradients (green curve in panel a, Fig. 5.12). $\nabla \cdot \boldsymbol{u}'_{turb}$ and $\nabla \cdot \boldsymbol{u}'_{adv}$ contribute roughly equally to the divergence response to downwind SST gradients, as evident by their nearly equal slopes.

Although the vorticity depends linearly on the crosswind SST gradient, $\nabla \times \boldsymbol{u}'_g$, $\nabla \times \boldsymbol{u}'_{turb}$, and $\nabla \times \boldsymbol{u}'_{adv}$ in general do not respond individually in a linear manner (panel c, Fig. 5.12). The superposition of these forces, however, does yield a nearly linear vorticity response. A more definitive assessment of the vorticity response to SST gradients requires consideration of the angle between the surface streamlines and the perturbation SST gradient vector, which is presented below.

To further validate the ability of the WRF model to simulate the SST-induced surface wind response, the $\nabla \times \boldsymbol{u}'_{adv}$ and $\nabla \cdot \boldsymbol{u}'_{adv}$ terms can be compared with those computed from the QuikSCAT wind fields. While slightly noisier, the response of

the QuikSCAT $\nabla \times \boldsymbol{u}'_{adv}$ and $\nabla \cdot \boldsymbol{u}'_{adv}$ terms is quantitatively similar to the response computed from the WRF simulation (green curves, Fig. 5.12). The quantitative agreement between the WRF and QuikSCAT responses of $\nabla \cdot \boldsymbol{u}'$ and $\nabla \cdot \boldsymbol{u}'_{adv}$ to downwind SST gradients (black and green curves in panels a and b, respectively, Fig. 5.12) suggests that WRF simulates the ageostrophic turbulent friction response to SST perturbations reasonably well.

Dynamical responses of the surface vorticity and divergence to the angle θ'

From statistical analysis of the QuikSCAT wind fields in Section 5.3.4, we found that the phase-shifts in the responses of the vorticity and divergence to the angle θ' were caused by the direction gradient terms. In the WRF simulation, geostrophic flow perturbations most strongly contribute to both the crosswind and downwind direction gradient response to θ' (panels b and e, Fig. 5.16). Dynamically, the downwind and crosswind direction gradient responses to θ' are mainly consequences of the

SST-induced geostrophic adjustment since the ageostrophic turbulent friction and horizontal advection component responses depend only weakly on θ'.

In contrast, the geostrophic and ageostrophic turbulent friction and horizontal advection components all strongly contribute to the crosswind and downwind speed gradient responses to θ' (panels a and d, Fig. 5.16). These dynamical responses are consistent with the advection-modified baroclinic Ekman adjustment mechanism discussed in Chapter 4. The phase shifts in the turbulent friction components of the speed gradients apparently result from the rotations of the ageostrophic turbulent friction vectors (u'_{turb}, v'_{turb}) discussed in Chapter 4.

The amplitude of the $\nabla \times \boldsymbol{u}'_g$ response to θ' is approximately twice that of both the $\nabla \times \boldsymbol{u}'_{turb}$ and $\nabla \times \boldsymbol{u}'_{adv}$ responses (panels a, b, and c, Fig. 5.16), indicating that $\nabla \times \boldsymbol{u}'_g$ makes the largest contribution to the SST-induced surface vorticity response in the WRF simulation. Additionally, the $\nabla \times \boldsymbol{u}'_{turb}$ and $\nabla \times \boldsymbol{u}'_{adv}$ responses nearly oppose the $\nabla \times \boldsymbol{u}'_g$ response (panel c, Fig. 5.16). Because of the SST-induced rotations of the (u'_{turb}, v'_{turb}) vectors, $\nabla \times \boldsymbol{u}'_{turb}$ generates vorticity as winds blow across perturbation SST isotherms (i.e., when $\theta' = 0^\circ$ or $\pm 180^\circ$), as evident from the cosine dependence of $\nabla \times \boldsymbol{u}'_{turb}$ on θ'. This is unexpected based on the Wallace et al. (1989) hypothesis. Horizontal advection generates cyclonic vorticity slightly downwind of warm SST perturbations and anti-cyclonic vorticity slightly downwind of cool SST perturbations (panel i, Fig. 5.14). This distribution roughly leads to a cosine dependence of $\nabla \times \boldsymbol{u}'_{adv}$ on the angle θ' (panel c, Fig. 5.16), with an amplitude

less than half of the $\nabla \times \boldsymbol{u}'_{turb}$ response.

$\nabla \cdot \boldsymbol{u}'_{turb}$ is maximum when $\theta' = 0°$ and minimum when $\theta' = \pm 180°$ (panel f, Fig. 5.16) and has an approximate cosine dependence on the angle θ'. The ageostrophic turbulent friction perturbations therefore generate divergence as surface winds blow across perturbation SST isotherms (i.e., when $\theta' = 0°$ or $\pm 180°$), consistent with the Wallace et al. (1989) turbulent momentum mixing mechanism. The approximately 45° phase shift in the $\nabla \cdot \boldsymbol{u}'_{turb}$ dependence on θ' from a pure cosine function is caused by the rotation of the (u'_{turb}, v'_{turb}) vectors, which rotate poleward over warm water and equatorward over cool water, causing a secondary divergence pattern depending on the sine of θ' (i.e., convergence when $\theta' = 90°$ and divergence when $\theta' = -90°$) through the $(\frac{\partial V}{\partial s})'_{turb}$ response (panel d, Fig. 5.16). The rotations of the (u'_{turb}, v'_{turb}) vectors therefore generate divergence when winds blow along perturbation SST isotherms, although this effect is secondary to the main effect of SST-induced wind speed modification.

Since the geostrophic contribution to the divergence is nearly zero (red curve in panel f, Fig. 5.16), the nexus of the ageostrophic turbulent friction and horizontal advection components completely accounts for the divergence response to SST gradients. Both $\nabla \cdot \boldsymbol{u}'_{turb}$ and $\nabla \cdot \boldsymbol{u}'_{adv}$ depend approximately on the cosine of θ' and are nearly in phase (panel f, Fig. 5.16), consistent with their dependencies on the downwind SST gradients shown in Fig. 5.12.

5.5.5 Discussion and Summary

Previous to this analysis, the vorticity and divergence responses to the crosswind and downwind SST gradients were thought to be caused mainly by the modification of the vertical turbulent mixing of momentum within the ABL (i.e., Wallace et al. 1989). Analysis of the WRF momentum budgets, however, indicates that most of the terms in the surface momentum budget are important; the vorticity and divergence responses to small-scale SST perturbations are much more complicated than originally envisioned.

The Wallace et al. (1989) mechanism predicts that the ageostrophic turbulent friction components of the crosswind and downwind speed gradients should be correlated with the crosswind and downwind components of the SST gradients, i.e., that the maps in panels d, f, and l of Figs. 5.14 and 5.15, respectively, should be equivalent. This is not the case in this simulation, where the geostrophic components and ageostrophic horizontal advection components make as significant contributions to the SST-induced vorticity and divergence responses as does the ageostrophic turbulent friction component. In light of these dynamical results, the statistical correlations of the wind stress curl and divergence with the crosswind and downwind SST gradients observed in our previous studies seem somewhat fortuitous given that the vertical turbulent momentum mixing hypothesis of Wallace et al. (1989) apparently cannot explain these results.

In both the vorticity and divergence responses to θ', the ageostrophic turbulent

friction and horizontal advection components depend roughly on the cosine of θ' (panels c and f, Fig. 5.16). The actual divergence response is simply caused by the superposition of these ageostrophic components, giving the characteristic cosine response to θ' of the divergence. The vorticity response, however, has a large geostrophic component that also depends on the cosine of θ' but is roughly 180° out of phase with the ageostrophic vorticity components. The geostrophic vorticity response θ' also has an amplitude nearly double that of the individual ageostrophic components. Despite the complicated nature of the θ'-phase characteristics of the individual geostrophic and ageostrophic vorticity components, the actual vorticity response to θ' appears as a sine function with an approximately 45° phase shift. If the geostrophic vorticity response were equally as significant as the individual ageostrophic vorticity responses (i.e., reduce its amplitude by half), the phase shift would significantly diminish. Therefore, the phase shift in the vorticity response is to a large extent caused by the SST-induced geostrophic vorticity response because of its large amplitude response to θ'.

From the analysis of QuikSCAT data in Section 5.3.4, we concluded that the wind direction gradients enhance the divergence response to downwind SST gradients while reducing the vorticity response to crosswind SST gradients. From our analysis of the WRF simulation in this section, SST-induced geostrophic wind perturbations mainly influence the responses of the direction gradients, although there are some weaker ageostrophic effects. The SST-induced response of the geostrophic component of the direction gradients reduces the vorticity response to the crosswind SST gradient and

enhances the divergence response to downwind SST gradients.

The conclusion that the geostrophic flow perturbations enhance the divergence response may seem paradoxical at first. However, consider that the crosswind and downwind speed gradient responses to θ' are nearly equivalent. When added to the direction gradient terms, the geostrophic component of the crosswind direction gradient simply removes the geostrophic contribution from the downwind speed gradient and thus enhances the divergence response relative to the downwind speed gradient response. In contrast, the geostrophic component of the downwind direction gradient opposes the geostrophic contribution from the crosswind speed gradient and thus reduces the vorticity response relative to the crosswind speed gradient response.

Several distinct mechanisms contribute to the phase shifts in the vorticity and divergence responses to θ'. First, the baroclinic Ekman adjustment mechanism causes significant cross-streamline components of the ageostrophic turbulent friction force, which generates phase shifts in the speed gradient responses to θ'. Pressure gradients, however, generate phase shifts of the opposite sign. The net result is phase shifts in the speed gradient responses towards the direction of the stronger pressure gradient response. Second, the SST-induced geostrophic flow perturbations cause curvature vorticity and diffluent perturbations which have θ'-dependencies approximately 90° out of phase with the speed gradient responses.

It is noted that the observed change in sign of the phase shifts in the vorticity and divergence responses to θ' between the Southern and Northern hemispheres (i.e.,

Fig. 5.7) are consistent with those expected from the change in sign of the Coriolis parameter and its effects on the geostrophic and ageostrophic components analyzed here. We thus believe that the results from this simulation over the Agulhas Return Current can be potentially applied to the other mid-latitude regions studied in Section 5.3.4.

5.6 Conclusions

In Section 5.3, we determined from 1-year of QuikSCAT winds and AMSR-E SST observations that the surface winds are accelerated and deflected equatorward over warm SST perturbations and decelerated and deflected poleward over cool SST perturbations, with deflections of 10-20° and wind speed changes of 1-2 m/s. Statistical analysis of the satellite wind and SST fields showed that the surface wind speed perturbations were statistically shown to be linearly related to the SST perturbations.

Of particular importance for this analysis are the contributions of spatial gradients in both the wind speed and direction to vorticity and divergence perturbations. Statistically, these perturbations are found to be linearly related to the crosswind and downwind components of the SST gradient, respectively; the vorticity response to crosswind SST gradients was 30-50% weaker than the divergence response to downwind SST gradients, consistent with our previous studies based on wind stress (Chelton et al. 2001, 2004, 2006; O'Neill et al. 2003, 2005). The linear responses of the crosswind speed gradient to crosswind SST gradients were nearly identical to those

of the linear downwind speed gradient responses to downwind SST gradients. The vorticity and divergence responses to SST gradients differ because the SST-induced crosswind and downwind direction gradients reduce the vorticity response and enhance the divergence response to SST gradients.

To simulate the dynamical balances giving rise to these responses of the vorticity and divergence to the crosswind and downwind SST gradients, the atmospheric flow over a section of the Agulhas Return Current was simulated using the Weather Research and Forecasting (WRF) mesoscale model. Analysis of the WRF model's surface momentum budget indicated that SST-induced geostrophic wind perturbations were the dominant contributor to the SST-induced wind direction gradients. Geostrophic adjustment of the pressure gradients to SST therefore was found to weaken the vorticity response to crosswind SST gradients mainly through their effect on the downwind direction gradients.

The response of the wind speed gradient components of the vorticity and divergence were mainly a consequence of the advection-modified baroclinic Ekman adjustment mechanism discussed in Chapter 4, whereby SST perturbations generate geostrophic flow and ageostrophic turbulent friction perturbations. Horizontal advection modifies this balance by shifting wind perturbations downwind of the SST perturbations and modifying the curvature of the surface streamlines.

These results from our analysis have significant implications for our understanding of the small-scale wind-SST interactions. We now have a firm dynamical framework in

which to interpret the extensive statistical relations developed using the satellite wind and SST observations. Characteristics in the statistical results in Section 5.3 can be interpreted through the framework of dynamical balances rather than as hypothetical constructions.

The feedback onto the ocean of the SST-induced wind stress curl and upper ocean mixing is the focus of ongoing research. Preliminary results from ocean general circulation model (OGCM) simulations indicate that ocean circulation is significantly impacted by the presence of small-scale wind variability (i.e., Spall 2007). The statistical relations between vorticity, divergence, and SST are being used to develop a simple way to model the small-scale surface wind stress response to temporally-evolving SST fields in the OGCMs. This method may also be used to simulate small-scale wind stress variability in long time series of surface wind stress analyses from NCEP and ECMWF, which may be of interest to the ocean modelling community since scatterometer data records in the near future may not be able to provide uninterrupted time series of wind stress fields long enough to force longer-term integrations of OGCMs for climate studies.

Acknowledgments. We thank Barry Vanhoff, Mike Freilich, and Michael Schlax for guidance in computing the in-swath derivative fields from the QuikSCAT measurement swaths used in this paper. Qingtao Song provided technical assistance with the WRF model used here. We also thank Roger Samelson, Eric Skyllingstad, Justin Small, and Qingtao Song for helpful discussions throughout the course of this analysis.

5.7 Appendix A: Steps used to compute the crosswind and downwind speed gradients from individual QuikSCAT measurement swaths

1) In-swath wind speeds were gridded onto a 0.25-degree grid as described in Sec. 5.3 on a swath-by-swath basis.

2) At each grid point, zonal and meridional derivatives were computed from the coefficients of a least-squares fit of neighboring points to a quadratic surface.

3) Crosswind and downwind derivatives were found according to Eqn. 5.1 using wind directions computed from gridded vector winds using the same gridding procedure.

4) Each gridded swath was combined into weekly-averaged crosswind and downwind derivative fields by averaging together all swaths within each week.

5) Perturbation fields were found by spatially high-pass filtering the weekly-averaged fields.

5.8 Appendix B: Physical interpretation of θ'

The angle θ' is important in quantifying the response of the surface perturbation vorticity and divergence fields to SST fronts. Its physical relevance to the orientation of the surface winds to SST fronts, which conceptually control spatial gradients in

wind speed and direction across SST fronts, has been unknown. Mainly this is because both nonlinearities and spatial high-pass filtering of the crosswind and downwind SST gradient fields make exact analytical formulation of θ' in terms of wind and SST intractable. A physically meaningful definition can nonetheless be made that is supported empirically.

The unfiltered crosswind and downwind SST gradient components are conveniently expanded as the sum of spatially high-pass filtered components, represented by primes, and smoothed, spatially low-pass filtered components, represented by the subscript sm

$$\frac{\partial T}{\partial n} = \left(\frac{\partial T}{\partial n}\right)' + \left(\frac{\partial T}{\partial n}\right)_{sm} \tag{5.32}$$

$$\frac{\partial T}{\partial s} = \left(\frac{\partial T}{\partial s}\right)' + \left(\frac{\partial T}{\partial s}\right)_{sm}. \tag{5.33}$$

An empirical approximation can then be made by writing the crosswind and downwind SST gradient components into the following forms

$$\left(\frac{\partial T}{\partial n}\right) = |\nabla T| \sin\theta \tag{5.34}$$

$$\left(\frac{\partial T}{\partial s}\right) = |\nabla T| \cos\theta \tag{5.35}$$

$$\left(\frac{\partial T}{\partial n}\right)' = |\nabla T'| \sin\theta' \tag{5.36}$$

$$\left(\frac{\partial T}{\partial s}\right)' = |\nabla T'| \cos\theta' \tag{5.37}$$

$$\left(\frac{\partial T}{\partial n}\right)_{sm} = |\nabla T_{sm}| \sin\theta_{sm} \quad (5.38)$$

$$\left(\frac{\partial T}{\partial s}\right)_{sm} = |\nabla T_{sm}| \cos\theta_{sm}, \quad (5.39)$$

where θ is defined as the counterclockwise angle between the surface wind vector and ∇T, θ' is defined as in Eqn. 5.7, and θ_{sm} is defined as

$$\theta_{sm} = \tan^{-1}\left[\frac{(\partial T/\partial n)_{sm}}{(\partial T/\partial s)_{sm}}\right].$$

Eqns. 5.36-5.39 are only approximations that cannot be rigorously justified analytically because the loess smoother used to produce the spatially filtered SST fields here is not commutative with the nonlinear vector magnitude operator. However, they are shown empirically in Fig. 5.17 to be nearly exact, despite the nonlinearities, based on terms computed from the AMSR-E SST and QuikSCAT wind fields averaged over the 1-week period 29 Dec 2002-4 Jan 2003.

An interpretation of θ' can be obtained by eliminating θ_{sm} and T_{sm} from consideration and solving for θ' in terms of θ in a form that reveals that θ' is the angle between the wind vector $\boldsymbol{u}$ and perturbation SST gradient vector $\nabla T'$. With the above forms, equations 5.32 and 5.33 can be written as

$$|\nabla T| \sin\theta = |\nabla T'| \sin\theta' + |\nabla T_{sm}| \sin\theta_{sm} \quad (5.40)$$

$$|\nabla T| \cos\theta = |\nabla T'| \cos\theta' + |\nabla T_{sm}| \cos\theta_{sm}. \quad (5.41)$$

Now take the square of Eqns. 5.40 and 5.41, expand and add them together, and simplify to get

$$|\nabla T'|^2 + 2|\nabla T'||\nabla T_{sm}| \cos(\theta' - \theta_{sm}) + |\nabla T_{sm}|^2 = |\nabla T|^2.$$

Hence,

$$\theta_{sm} = \theta' - \cos^{-1} R, \tag{5.42}$$

where

$$R = \frac{|\nabla T|^2 - |\nabla T'|^2 - |\nabla T_{sm}|^2}{2|\nabla T'||\nabla T_{sm}|}. \tag{5.43}$$

Substituting Eqn. 5.42 into Eqns. 5.40 and 5.41 with the trigonometric identity $\sin(\cos^{-1} R) = \pm(1 - R^2)^{1/2}$ yields

$$\begin{aligned} |\nabla T| \sin\theta &= |\nabla T'| \sin\theta' + |\nabla T_{sm}|[R \sin\theta' \pm (1 - R^2)^{1/2} \cos\theta'] \\ |\nabla T| \cos\theta &= |\nabla T'| \cos\theta' + |\nabla T_{sm}|[R \cos\theta' \pm (1 - R^2)^{1/2} \sin\theta']. \end{aligned}$$

This can be rewritten as

$$|\nabla T| \sin\theta = A \sin\theta' \pm B \cos\theta' \tag{5.44}$$

$$|\nabla T| \cos\theta = A \cos\theta' \pm B \sin\theta', \tag{5.45}$$

where $A = (|\nabla T'| + |\nabla T_{sm}| R)$ and $B = |\nabla T_{sm}|(1 - R^2)^{1/2}$. The positive or negative root in each equation means there are four possible sets of equations. However, by

noting from these definitions of A and B that $A^2 + B^2 = |\nabla T|$, only two sets of equations are possible, namely

$$\begin{aligned} |\nabla T| \sin\theta &= A \sin\theta' + B \cos\theta' \\ |\nabla T| \cos\theta &= A \cos\theta' - B \sin\theta', \end{aligned}$$

or

$$\begin{aligned} |\nabla T| \sin\theta &= A \sin\theta' - B \cos\theta' \\ |\nabla T| \cos\theta &= A \cos\theta' + B \sin\theta'. \end{aligned}$$

To find a unique solution from these two possibilities, multiply the first equations in each pair by $\sin\theta'$ and add them to $\cos\theta'$ times the second equations. Doing so to both sets of equations gives the same result,

$$\begin{aligned} \cos(\theta - \theta') &= \frac{A}{|\nabla T|} \\ &= \frac{|\nabla T|^2 + |\nabla T'|^2 - |\nabla T_{sm}|^2}{2|\nabla T||\nabla T'|}. \end{aligned} \tag{5.46}$$

This equation can be simplified by substituting $T_{sm} = T - T'$, thus eliminating the low-pass filtered SST field from consideration, and expanding the gradient terms into component form:

$$
\begin{aligned}
|\nabla T|^2 &= \left(\frac{\partial T}{\partial x}\right)^2 + \left(\frac{\partial T}{\partial y}\right)^2 \\
|\nabla T'|^2 &= \left(\frac{\partial T'}{\partial x}\right)^2 + \left(\frac{\partial T'}{\partial y}\right)^2 \\
|\nabla T_{sm}|^2 &= \left(\frac{\partial T}{\partial x} - \frac{\partial T'}{\partial x}\right)^2 + \left(\frac{\partial T}{\partial y} - \frac{\partial T'}{\partial y}\right)^2.
\end{aligned}
$$

Using these relations, and after some manipulation and simplification, Eqn. 5.46 can be written in the compact form

$$\cos\left(\theta' - \theta\right) = \frac{\nabla T \cdot \nabla T'}{|\nabla T||\nabla T'|}. \tag{5.47}$$

From the definition of the dot product in the numerator of Eqn. 5.47, it is clear that the angle $\theta' - \theta$ is the counterclockwise angle between the vectors ∇T and $\nabla T'$. A schematic of these angles and SST gradient vectors is shown in Fig. 5.18. From this, it can be deduced that θ' is the counterclockwise angle between the surface wind vector $\boldsymbol{u}$ and the perturbation SST gradient vector $\nabla T'$. This deduction is confirmed statistically in the top panel of Fig. 5.19, where the angle between $\boldsymbol{u}$ and $\nabla T'$, denoted as $\widetilde{\theta}'$, is binned as a function of the angle θ' computed from Eqn. 5.7 using the weekly-averaged wind and SST fields. As the figure shows, the two angles agree very well. Differences between the two angles are quantified in the histogram in the bottom panel of Fig. 5.19, which shows a very narrow distribution centered at 0° and a standard deviation of 7.6°. The RMS difference between θ' and $\widetilde{\theta}'$ is also 7.6°. It is thus concluded that the angle θ' is a good representation of the angle between

the surface wind and perturbation SST gradient vectors.

References

Bond, N. A., 1992: Observations of planetary boundary-layer structure in the Eastern Equatorial Pacific. *J. Climate*, **5**, 699-706.

Bourras, D., G. Reverdin, H. Giordani, and G. Caniaux, 2004: Response of the atmospheric boundary layer to a mesoscale oceanic eddy in the northeast Atlantic. *J. Geophys. Res.*, **109**, D18114, doi:10.1029/2004JD004799.

Chelton, D. B., 2005: The impact of SST specification on ECMWF surface wind stress fields in the Eastern Tropical Pacific. *J. Climate*, **18**, 530–550.

Chelton, D. B., and coauthors, 2001: Observations of coupling between surface wind stress and sea surface temperature in the eastern tropical Pacific. *J. Climate*, **14**, 1479–1498.

Chelton, D. B., and M. G. Schlax, 2003: The accuracies of smoothed sea surface height fields constructed from tandem altimeter datasets. *J. Atmos. Oceanic Technol.*, **20**, 1276–1302.

Chelton, D. B., M. G. Schlax, M. H. Freilich, and R. F. Milliff, 2004: Satellite measurements reveal persistent small-scale features in ocean winds. *Science*, **303**, 978–983.

Chelton, D. B., and M. H. Freilich, 2005: Scatterometer-based assessment of 10-m wind analyses from the operational ECMWF and NCEP numerical weather prediction models. *Mon. Wea. Rev.*, **133**, 409–429.

Chelton, D. B., and F. J. Wentz, 2005: Global microwave satellite observations of sea surface temperature for numerical weather prediction and climate research. *Bull. Amer. Meteor. Soc.*, **86**, 1097–1115.

Chelton, D. B., M. G. Schlax, and R. M. Samelson, 2007: Summertime coupling between sea surface temperature and wind stress in the California Current System. *J. Phys. Oceanogr.*, **37**, 495–517.

Cleveland, W. S., and S. J. Devlin, 1988: Locally weighted regression: An approach to regression analysis by local fitting. *J. Amer. Stat. Assoc.*, **83**, 596–610.

Cronin, M. F., S.-P. Xie, and H. Hashizume, 2003: Barometric pressure variations associated with eastern Pacific tropical instability waves. *J. Climate*, **16**, 3050–3057.

de Szoeke, S. P., and C. S. Bretherton, 2004: Quasi-Lagrangian large eddy simulations of cross-equatorial flow in the east Pacific atmospheric boundary layer. *J. Atmos. Sci.*, **61**, 1837–1858.

Ebuchi, N., H. C. Graber, and M. J. Caruso, 2002: Evaluation of wind vectors observed by QuikSCAT/SeaWinds using ocean buoy data. *J. Oceanic Atmos. Technol.*, **19**, 2049–2062.

Fairall, C. W., E. F. Bradley, J. E. Hare, A. A. Grachev, and J. B. Edson, 2003: Bulk parameterization of air-sea fluxes: updates and verification for the COARE algorithm. *J. Climate*, **16**, 571-591.

Freihe, C. A., and coauthors, 1991: Air-sea fluxes and surface layer turbulence around a sea surface temperature front. *J. Geophys. Res.*, **96**, 8593-8609.

Haltiner, G. J., and F. L. Martin, 1957: Dynamical and Physical Meteorology. McGraw-Hill Book Company. 470pp.

Hashizume, H., S.-P. Xie, W. T. Liu, and K. Takeuchi, 2001: Local and remote atmospheric response to tropical instability waves: A global view from space. *J. Geophys. Res.*, **106**, 10173–10185.

Hashizume, H., S.-P. Xie, M. Fujiwara, M. Shiotani, T. Watanabe, Y. Tanimoto, W. T. Liu, and K. Takeuchi, 2002: Direct observations of atmospheric boundary layer response to slow SST variations over the eastern equatorial Pacific. *J. Climate*, **15**, 3379–3393.

Hayes, S. P., M. J. McPhaden, and J. M. Wallace, 1989: The influence of sea-surface temperature upon surface wind in the eastern equatorial Pacific. *J. Climate*, **2**, 1500-1506.

Holton, J. R., 1992: An Introduction to Dynamic Meteorology. Academic Press. 511pp.

Koračin, D., and D. P. Rogers, 1990: Numerical simulations of the response of the marine atmospheric boundary layer to ocean forcing. *J. Atmos. Sci.*, **47**, 592-611.

Jury, 1994: Thermal front within the marine atmospheric boundary layer over the Agulhas Current south of Africa: composite aircraft observations. *J. Geophys. Res.*, **99**, 3297-3304.

Liu, W. T., and W. Tang, 1996: Equivalent neutral wind. JPL Publication 96-17, Pasadena, CA, 8pp.

Large, W. G., J. C. McWilliams, and S. C. Doney, 1994: Oceanic vertical mixing: A review and a model with a nonlocal boundary layer parameterization. *Rev. Geophys.*, **32**, 363–403.

Lindzen, R. S., and S. Nigam, 1987: On the role of sea surface temperature gradients in forcing low-level winds and convergence in the tropics. *J. Atmos. Sci.*, **44**, 2418–2436.

Mahrt, L., D. Vickers, and E. Moore, 2004: Flow adjustments across sea-surface temperature changes. *Bound. Layer Meteor.*, **111**, 553–564.

Mantua, N. J., S. R. Hare, Y. Zhang, J. M. Wallace, and R. C. Francis, 1997: A Pacific interdecadal climate oscillation with impacts on salmon production. *Bull. Amer. Meteor. Soc.*, **78**, 1069–1079.

Mey, R. D., and N. D. Walker, 1990: Surface heat fluxes and marine boundary layer modification in the Agulhas Retroflection region. *J. Geophys. Res.*, **95**, 15997-16015.

Mears, C. A., D. K. Smith, and F. J. Wentz, 2001: Comparison of Special Sensor Microwave Imager and buoy-measured wind speeds from 1987 to 1997. *J. Geophys. Res.*, **106**, 11719–11729.

Okumura, Y., S.-P. Xie, A. Numaguti, and Y. Tanimoto, 2001: Tropical Atlantic air-sea interaction and its influence on the NAO. *Geophys. Res. Lett.*, **28**, 1507–1510.

O'Neill, L. W., D. B. Chelton, and S. K. Esbensen, 2003: Observations of SST-induced perturbations of the wind stress field over the Southern Ocean on seasonal timescales. *J. Climate*, **16**, 2340–2354.

O'Neill, L. W., D. B. Chelton, S. K. Esbensen, and F. J. Wentz, 2005: High-resolution satellite observations of SST modification of the marine atmospheric boundary layer over the Agulhas Return Current. *J. Climate*, **18**, 2706–2723.

Samelson, R. M., E. D. Skyllingstad, D. B. Chelton, S. K. Esbensen, L. W. O'Neill, and N. Thum, 2006: A note on the coupling of wind stress and sea surface temperature. *J. Climate*, **19**, 1557–1566.

Schlax, M. G., D. B. Chelton, and M. H. Freilich, 2001: Sampling errors in wind fields constructed from single and tandem scatterometer datasets. *J. Atmos. Oceanic Technol.*, **18**, 1014–1036.

Skyllingstad, E. D., D. Vickers, L. Mahrt, and R. M. Samelson, 2006: Effects of mesoscale sea-surface temperature fronts on the marine atmospheric boundary layer. *Boundary-Layer Meteorol.*, DOI:10.1007/s10546-006-9127-8.

Small, J. R., S.-P. Xie, and Y. Wang, 2003: Numerical simulation of atmospheric response to Pacific tropical instability waves. *J. Climate*, **16**, 3723–3741.

Small, J. R., S.-P. Xie, Y. Wang, S. K. Esbensen, and D. Vickers, 2005: Numerical simulation of boundary layer structure and cross-equatorial flow in the eastern Pacific. *J. Atmos. Sci.*, **62**, 1812–1830.

Small, R. J., S. deSzoeke, S. P. Xie, L. O'Neill, H. Seo, Q. Song, P. Cornillon, M. Spall, and S. Minobe, 2007: Air-sea interaction over ocean fronts and eddies. *Dynam. Atmos. Ocean.*, Accepted.

Song, Q., T. Hara, P. Cornillon, and C. A. Friehe, 2004: A comparison between observations and MM5 simulations of the marine atmospheric boundary layer across a temperature front. *J. Atmos. Oceanic Technol.*, **21**, 170–178.

Song, Q., P. Cornillon, and T. Hara, 2006: Surface wind response to oceanic fronts. *J. Geophys. Res.*, **111**, doi:10.1029/2006JC003680.

Spall, M. A., 2007a: Effect of sea surface temperature-wind stress coupling on baroclinic instability in the ocean. *J. Phys. Ocean.*, **37**, 1092-1097.

Spall, M. A., 2007b: Mid-latitude wind stress-sea surface temperature coupling in the vicinity of oceanic fronts. *J. Climate*, *in press.*

Sweet, W. R., R. Fett, J. Kerling, and P. LaViolette, 1981: Air-sea interaction effects in the lower troposphere across the north wall of the Gulf Stream. *Mon. Wea. Rev.*, **109**, 1042-1052.

Thum, N., 2006: Atmospheric boundary layer coupling to midlatitude mesoscale sea surface temperature anomalies. Ph.D. Dissertation, Oregon State Univ., 142 pp.

Tokinaga, H., and coauthors, 2006: Atmospheric sounding over the winter Kuroshio Extension: Effect of surface stability on atmospheric boundary layer structure. *Geophys. Res. Lett.*, **33**, doi:10.1029/2005GL025102.

Wai, W. M., and S. A. Stage, 1989: Dynamical analysis of marine atmospheric boundary layer structure near the Gulf Stream oceanic front. *Quart. J. Roy. Meteor. Soc.*, **115**, 29–44.

Wallace, J. M., T. P. Mitchell, and C. Deser, 1989: The influence of sea surface temperature on surface wind in the eastern tropical Pacific: seasonal and interannual variability. *J. Climate*, **2**, 1492–1499.

Warner, T. T., M. N. Lakhtakia, J. D. Doyle, and R. A. Pearson, 1990: Marine atmospheric boundary layer circulations forced by Gulf Stream sea surface temperature gradients. *Mon. Wea. Rev.*, **118**, 309–323.

Xie, S.-P., 2004: Satellite observations of cool ocean-atmosphere interaction. *Bull. Amer. Meteor. Soc.*, **85**, 195-208.

	α_0 m/s per °C	Correlation Coefficient
Kuroshio	0.28	0.70
Gulf Stream	0.31	0.84
South Atlantic	0.40	0.87
Agulhas	0.44	0.81

Table 5.1: (left) The coupling coefficient α_0 computed from the 1-yr average perturbation wind speed and SST; and (right) spatial correlation between the 1-yr average perturbation wind speed and SST.

	Kuroshio	Gulf Stream	South Atlantic	Agulhas
α_c^{spd}	0.29	0.28	0.40	0.44
α_d^{dir}	0.10	0.12	0.16	0.13
ϕ_c^{spd}	3°	0°	−3°	−1°
ϕ_d^{dir}	144°	140°	34°	37°
α_c^{vort}	−0.23	−0.20	−0.32	−0.36
α_d^{vort}	−0.083	−0.094	0.13	0.11
α_d^{spd}	0.33	0.32	0.46	0.45
α_c^{dir}	0.14	0.14	0.21	0.20
ϕ_d^{spd}	−7°	−11°	6°	11°
ϕ_c^{dir}	144°	149°	18°	23°
α_d^{div}	0.41	0.39	0.52	0.53
α_c^{div}	−0.11	−0.12	0.20	0.19

Table 5.2: Values of the coupling coefficients and phase angles appearing in Eqns. 5.14-5.21 computed from the QuikSCAT wind and AMSR-E SST fields. The units of the coupling coefficients are in m/s per °C.

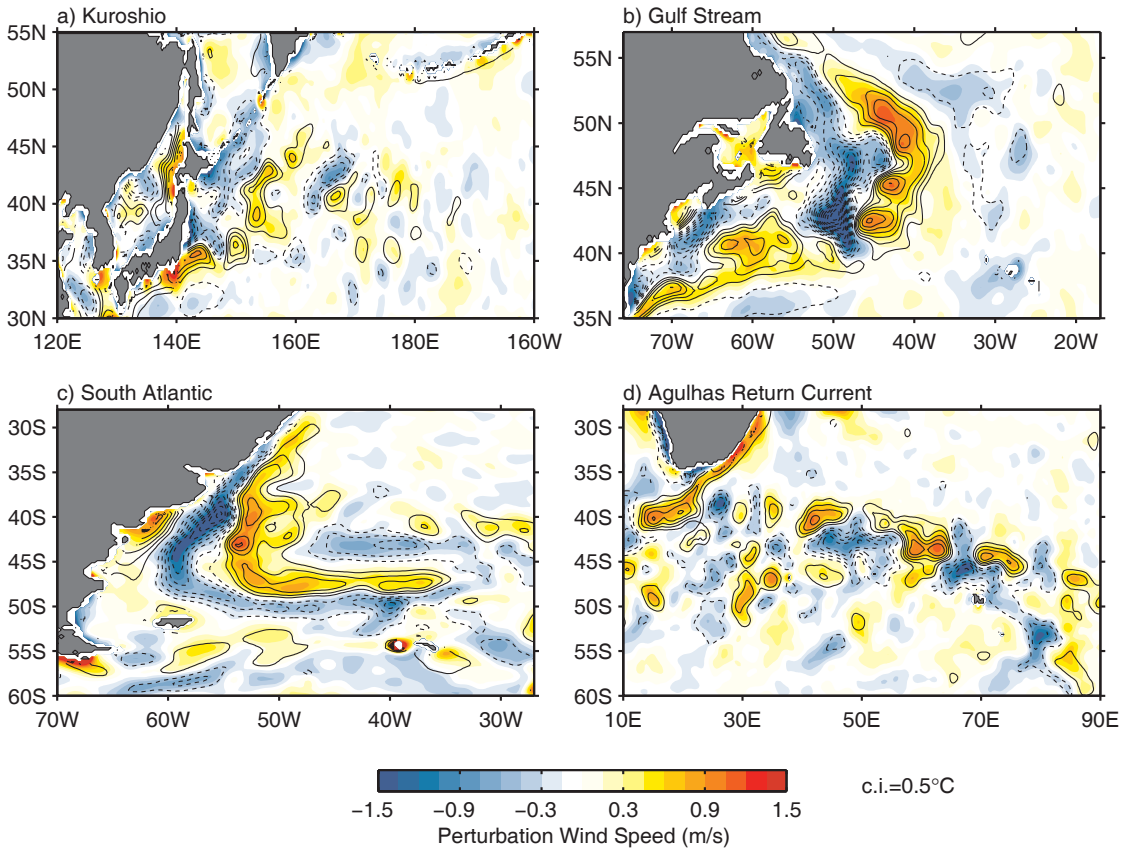

Figure 5.1: Maps of perturbation QuikSCAT wind speed (colors) and AMSR-E SST (contours) scalar-averaged over the 1-yr period 1 Jan 2003 - 31 Dec 2003 for the four regions considered in this study. The contour interval for the perturbation SST is 0.5°C and the zero contour has been omitted for clarity. The spatial high-pass filter removes spatial variability with wavelengths longer than 30° longitude by 10° latitude as discussed in the text.

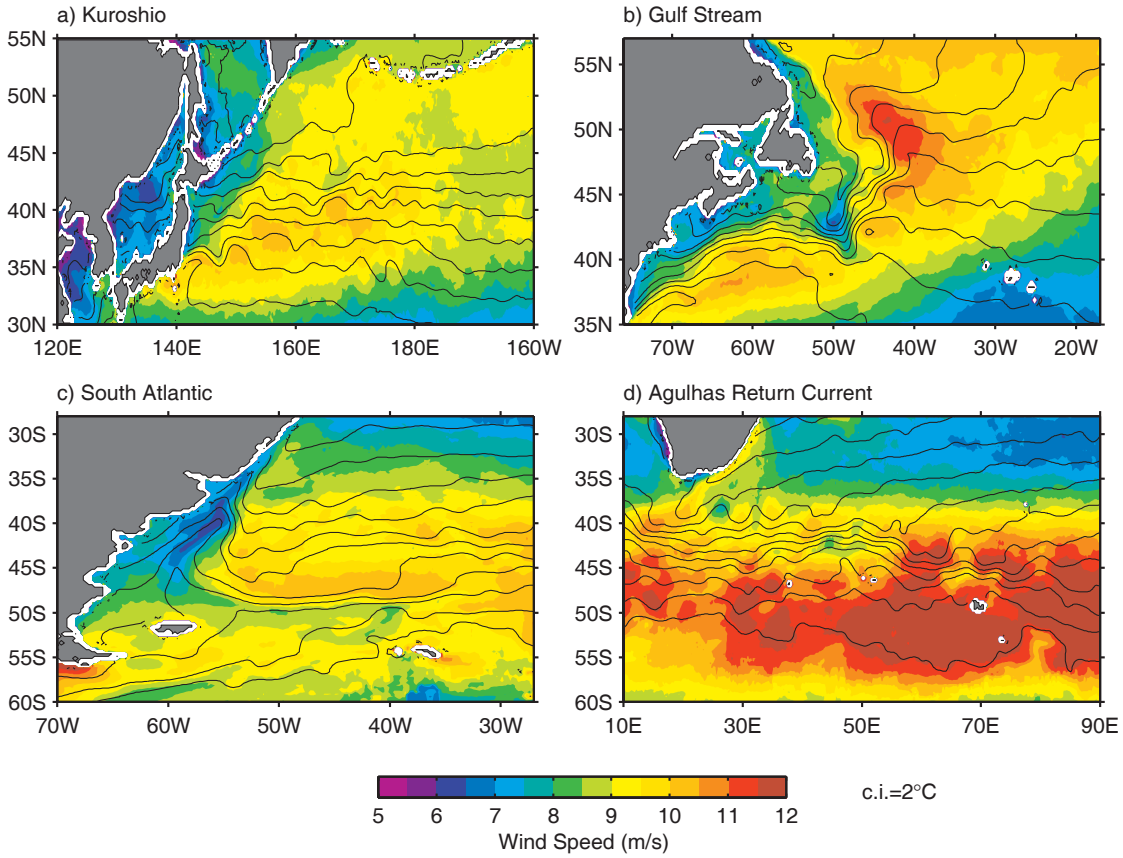

Figure 5.2: Maps of unfiltered QuikSCAT wind speed (colors) and AMSR-E SST (contours) scalar-averaged over the 1-yr period 1 Jan 2003 - 31 Dec 2003. The contour interval for the SST contours is 2°C.

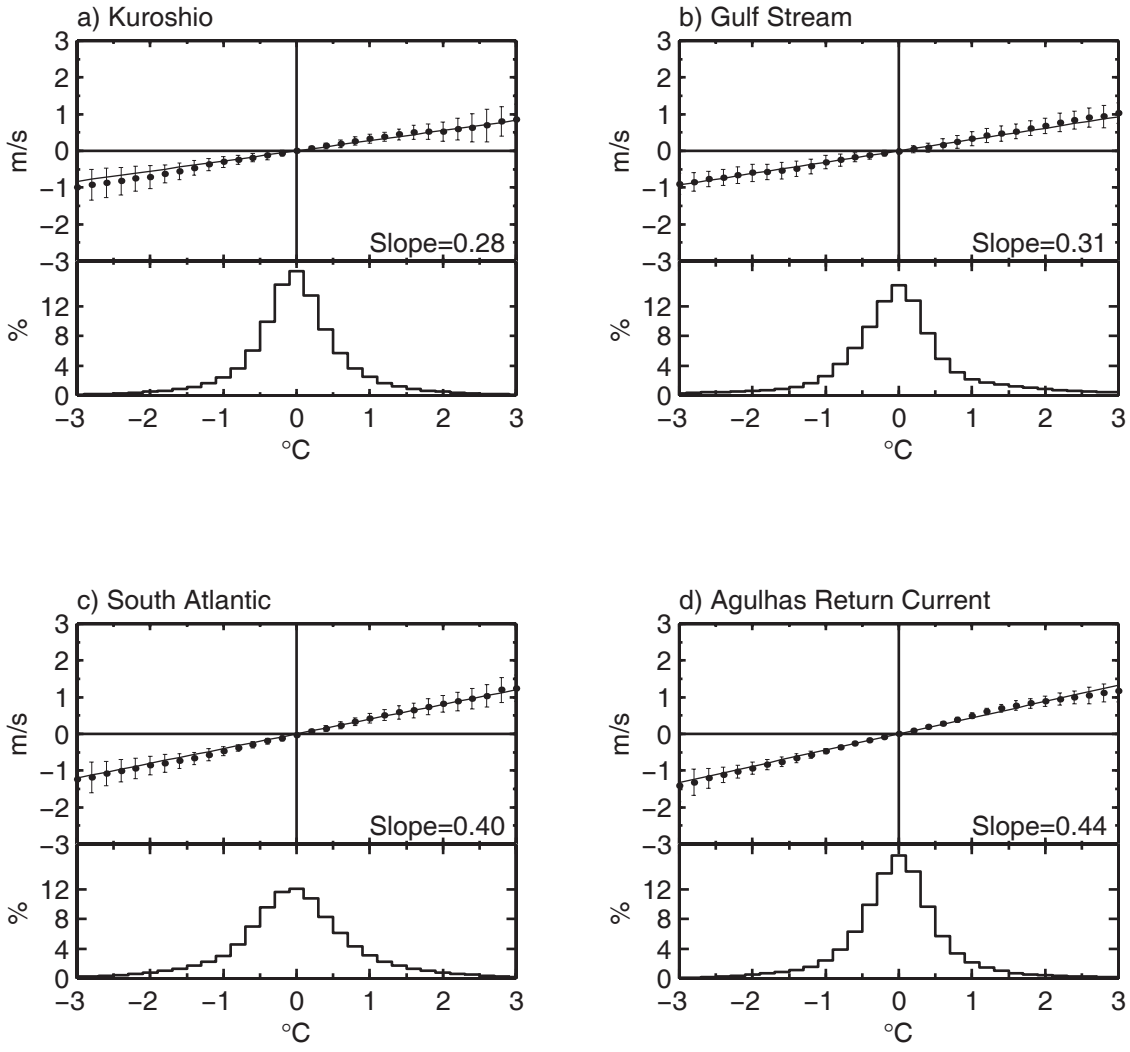

Figure 5.3: Binned scatterplots of the spatially high-pass filtered QuikSCAT wind speed (V') as a function of the spatially high-pass filtered AMSR-E SST (T'). The bin-averages were computed from weekly-averaged wind and SST fields over the 1-yr period considered here. The points and errorbars represent the means and std devs within each bin, respectively. Below each scatterplot, a histogram of the spatially high-pass filtered SST is included for reference. The dashed line is a linear least squares fit to all the points.

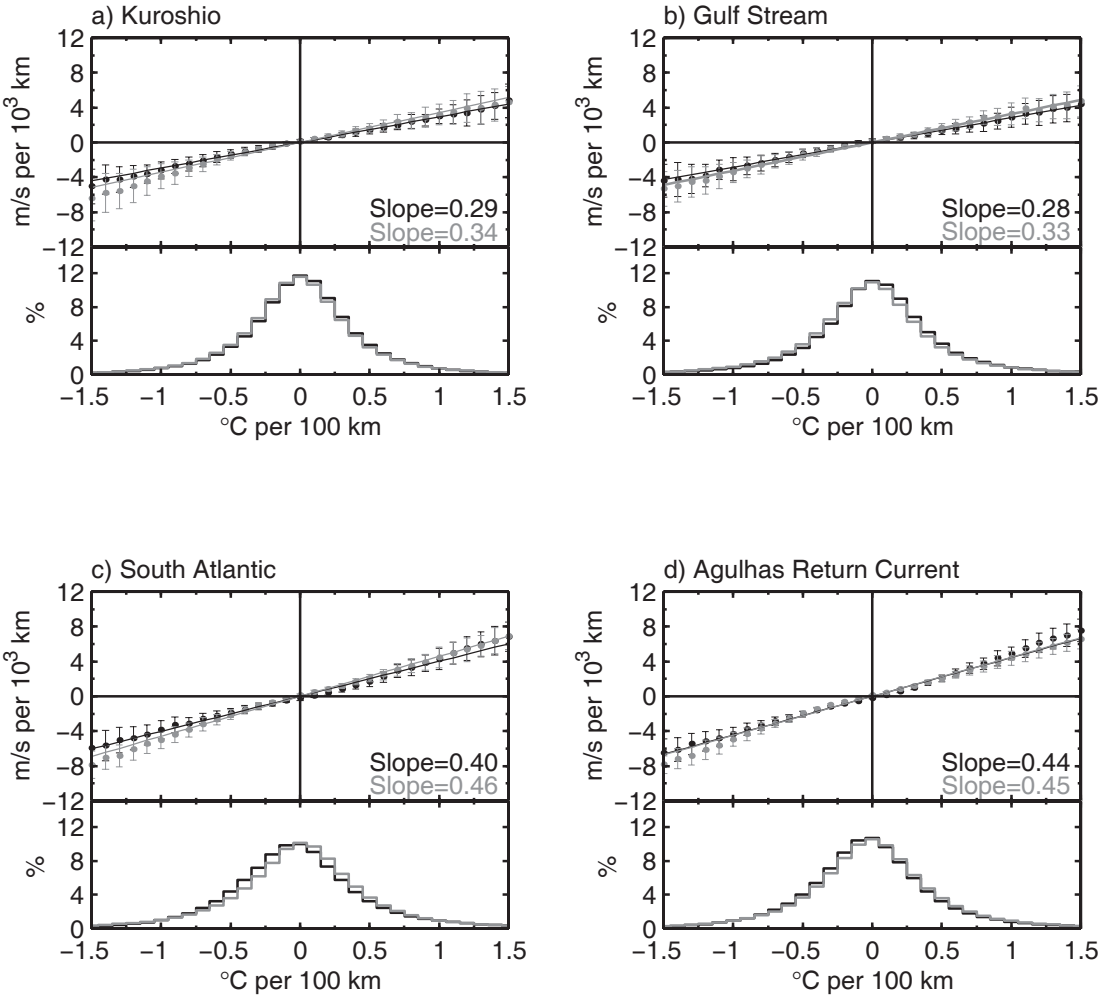

Figure 5.4: The same as Fig. 5.3, except for the QuikSCAT perturbation crosswind speed gradient $(\partial V/\partial n)'$ (black) and the QuikSCAT perturbation downwind speed gradient $(\partial V/\partial s)'$ (grey) as functions of the perturbation crosswind and downwind components of the SST gradient, respectively.

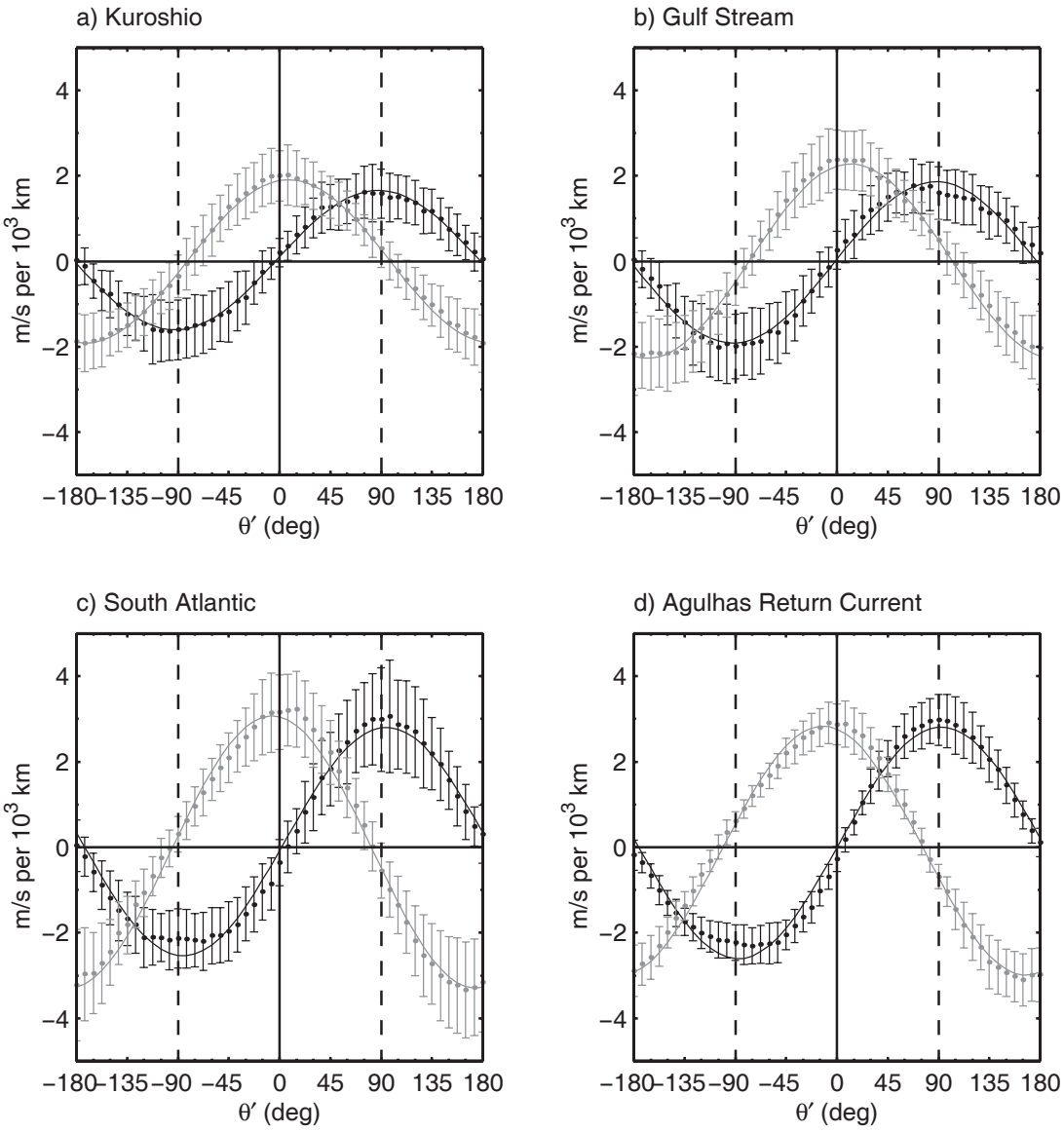

Figure 5.5: The same as Fig. 5.3, except for the QuikSCAT perturbation crosswind speed gradient $(\partial V/\partial n)'$ (black) and the QuikSCAT perturbation downwind speed gradient $(\partial V/\partial s)'$ (grey) as functions of θ'.

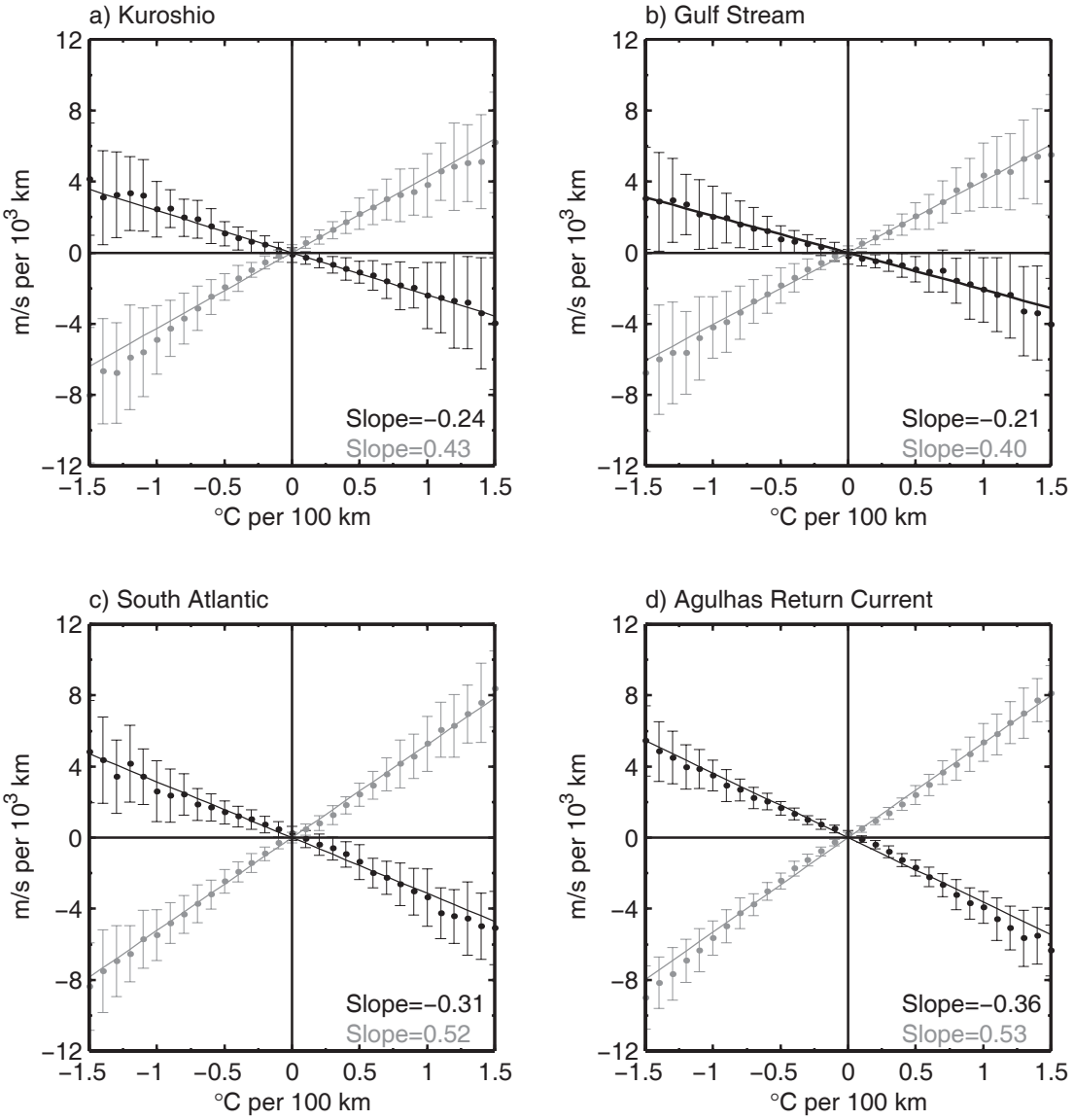

Figure 5.6: Binned scatterplots of the QuikSCAT perturbation vorticity as a function of the perturbation crosswind SST gradient (black) and the QuikSCAT perturbation divergence as a function of the perturbation downwind SST gradient (grey). The bin-averages were computed from weekly-averaged wind and SST fields over the 1-yr period considered here, and the points and errorbars represent the means and std devs within each bin, respectively. The dashed lines are least-squares fits of the binned points to straight lines.

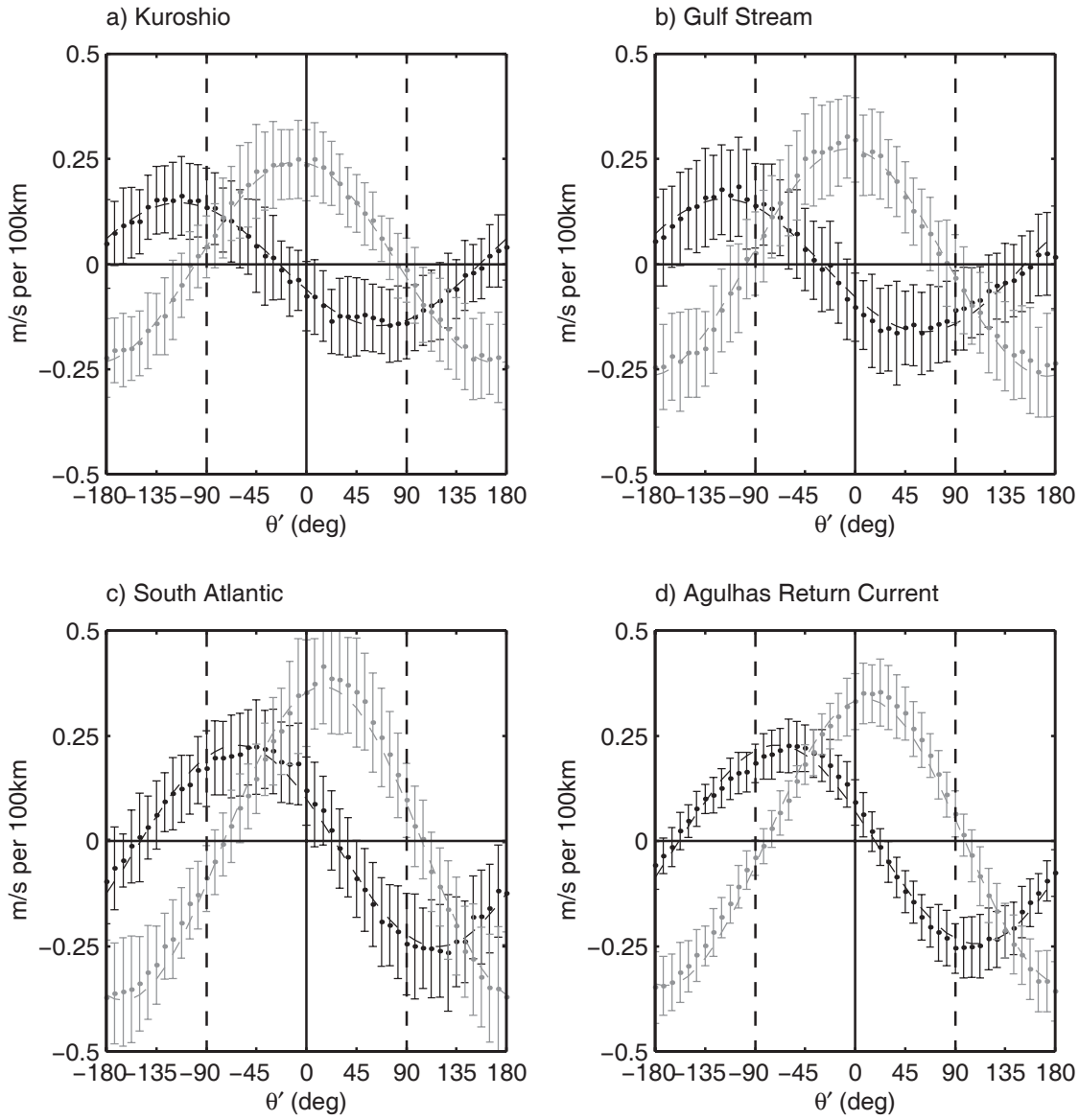

Figure 5.7: Binned scatterplots of the QuikSCAT perturbation vorticity (black) and divergence (grey) as functions of the angle θ'. The bin-averages were computed from weekly-averaged wind and SST fields over the 1-yr period considered here, and the points and errorbars represent the means and std devs within each bin, respectively. The solid curves are least-squares fits of the binned points to sinusoids.

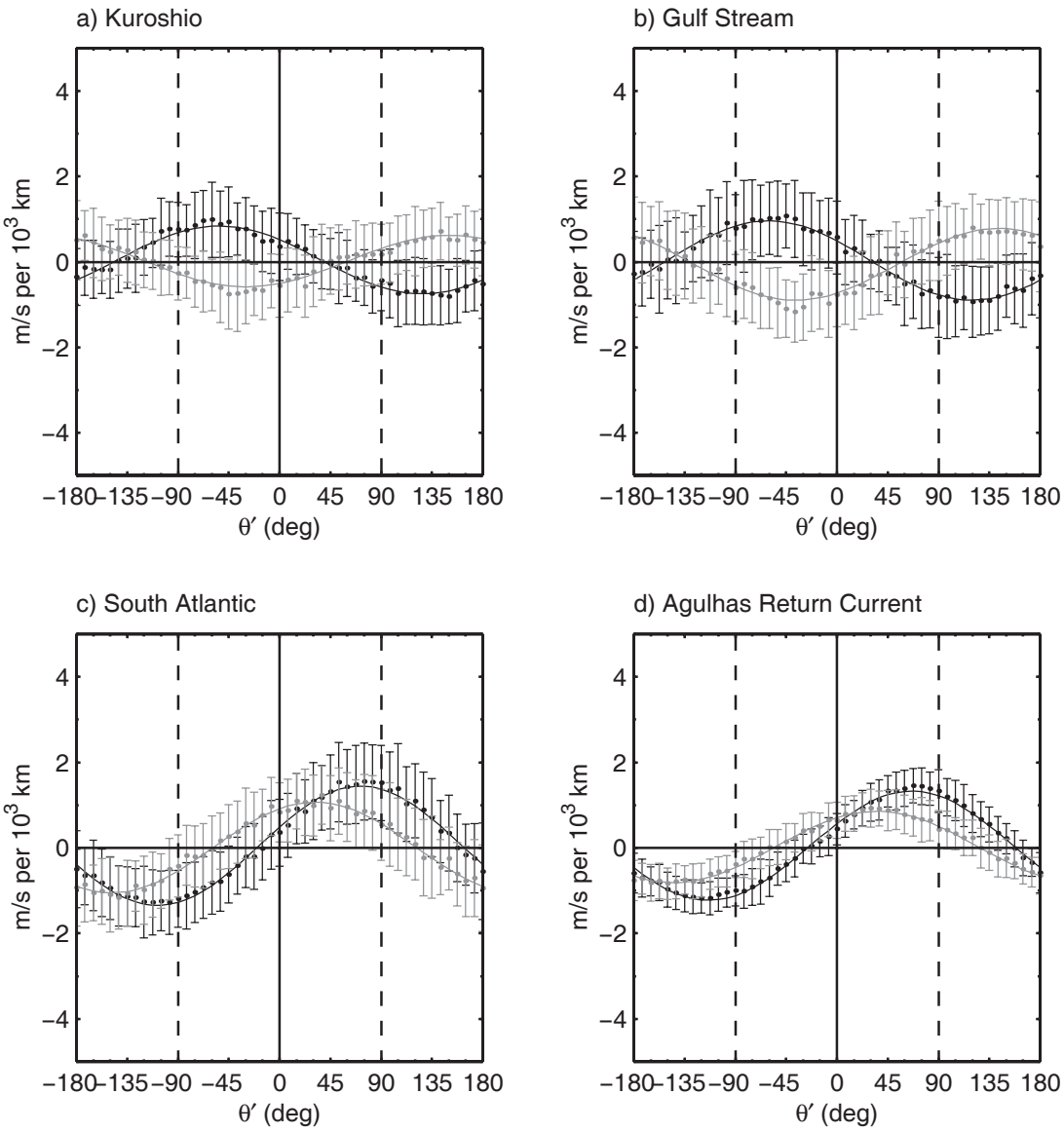

Figure 5.8: Binned scatterplots of the perturbation crosswind (black) and downwind (grey) direction gradients as functions of θ'. The bin-averages were computed from weekly-averaged wind and SST fields over the 1-yr period considered here, and the points and errorbars represent the means and std devs within each bin, respectively. The dashed lines are least-squares fits of the binned points to sinusoids.

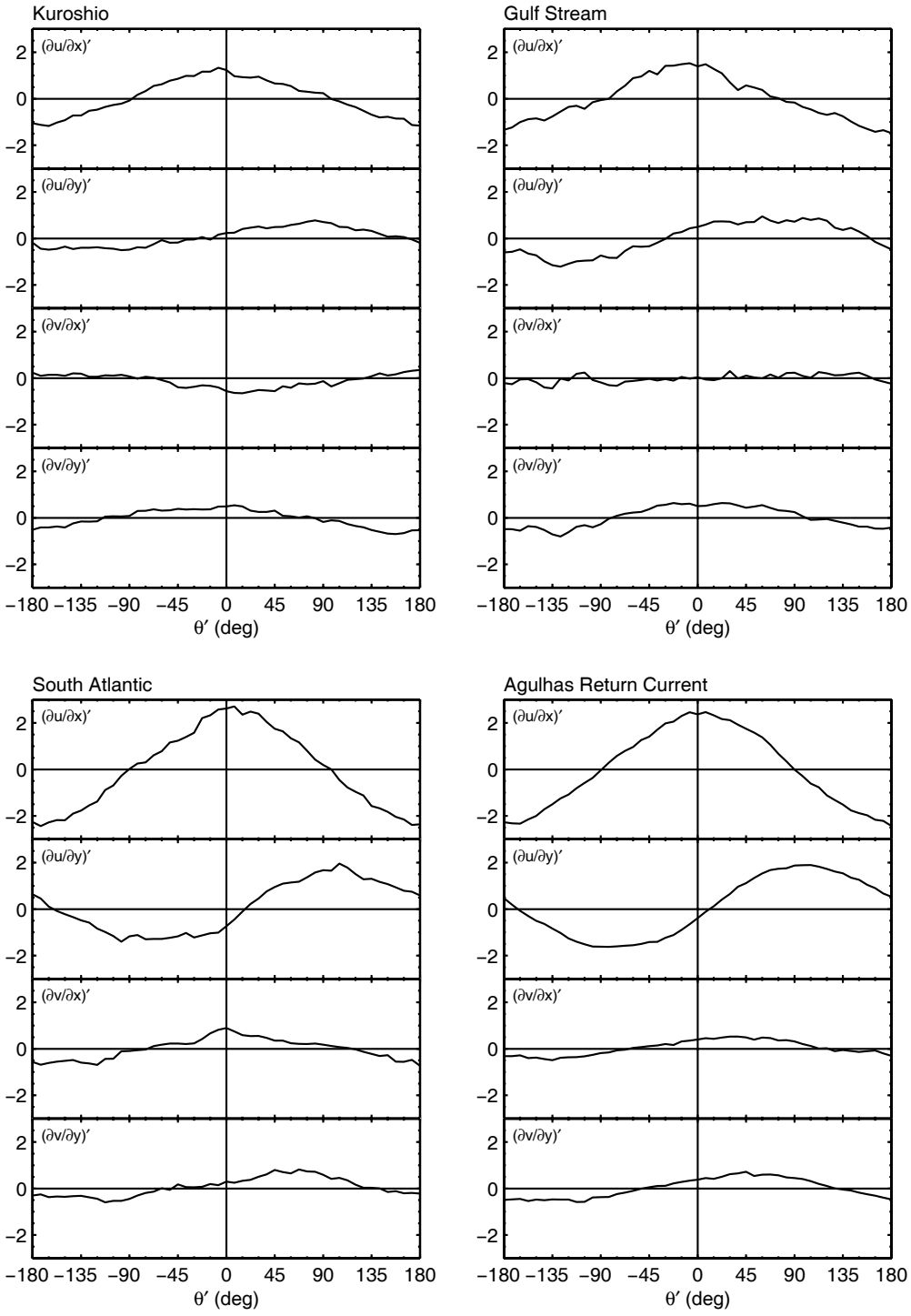

Figure 5.9: Binned scatterplots of the perturbation spatial derivatives as indicated over the 1-yr period considered here.

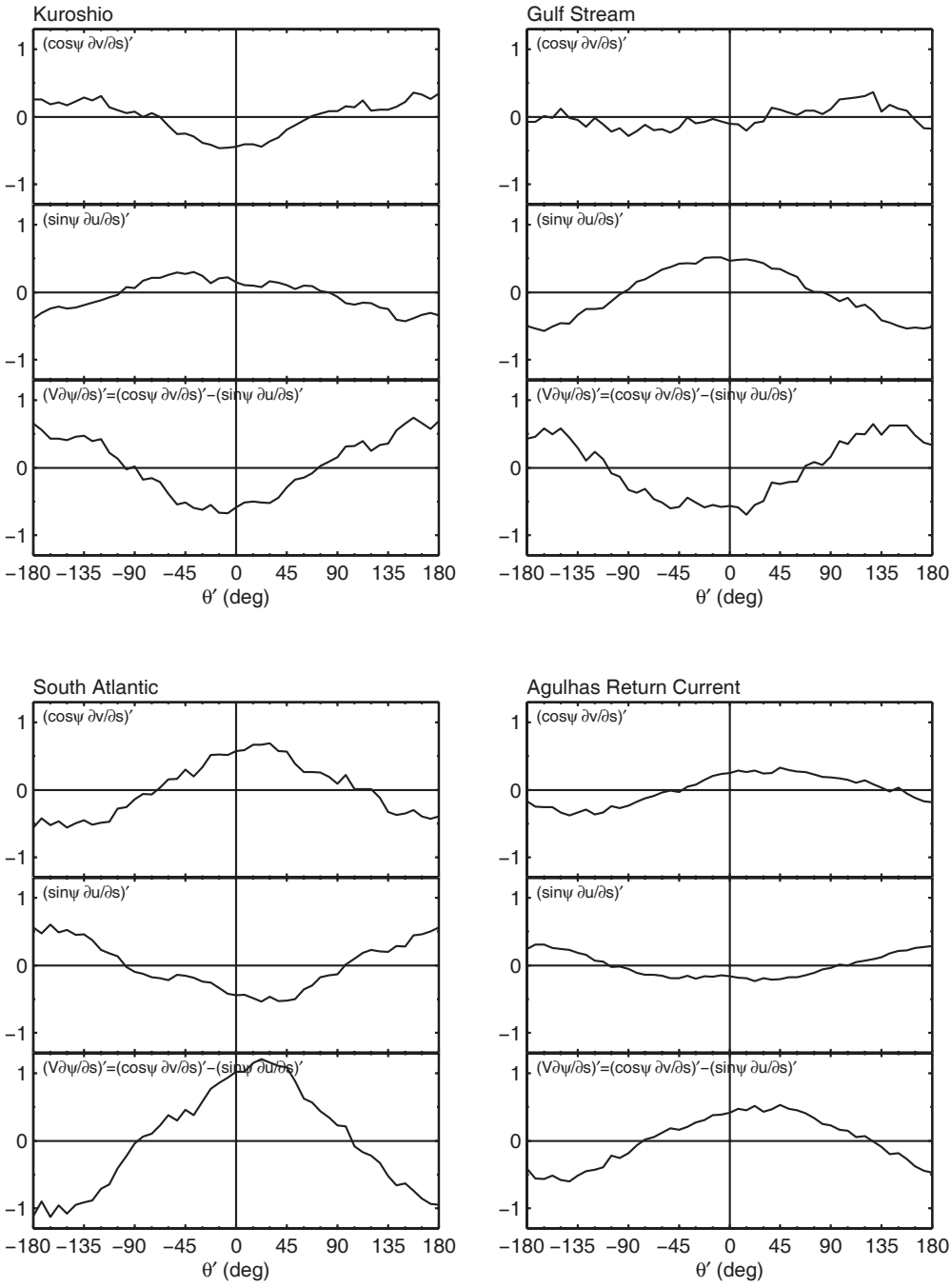

Figure 5.10: Binned scatterplots of the perturbation spatial derivatives as indicated over the 1-yr period considered here.

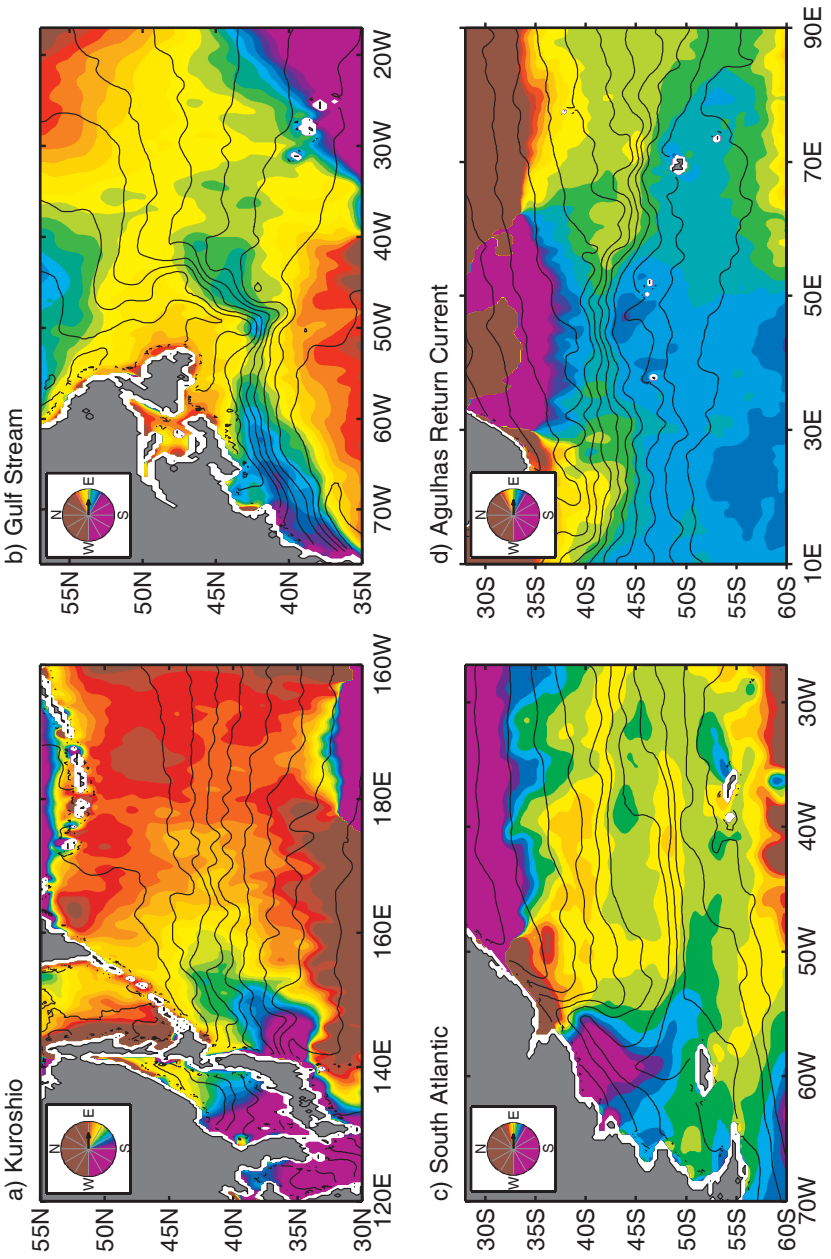

Figure 5.11: Maps of the QuikSCAT vector-averaged wind direction (colors) and AMSR-E SST (contours) averaged over the 1-yr period considered here. The circular colorbar indicates the direction the wind is blowing towards as indicated by the colors. Note that the non-saturated colors in the color palette do not correspond to the same wind direction intervals between each panel because of small regional differences in the mean wind direction.

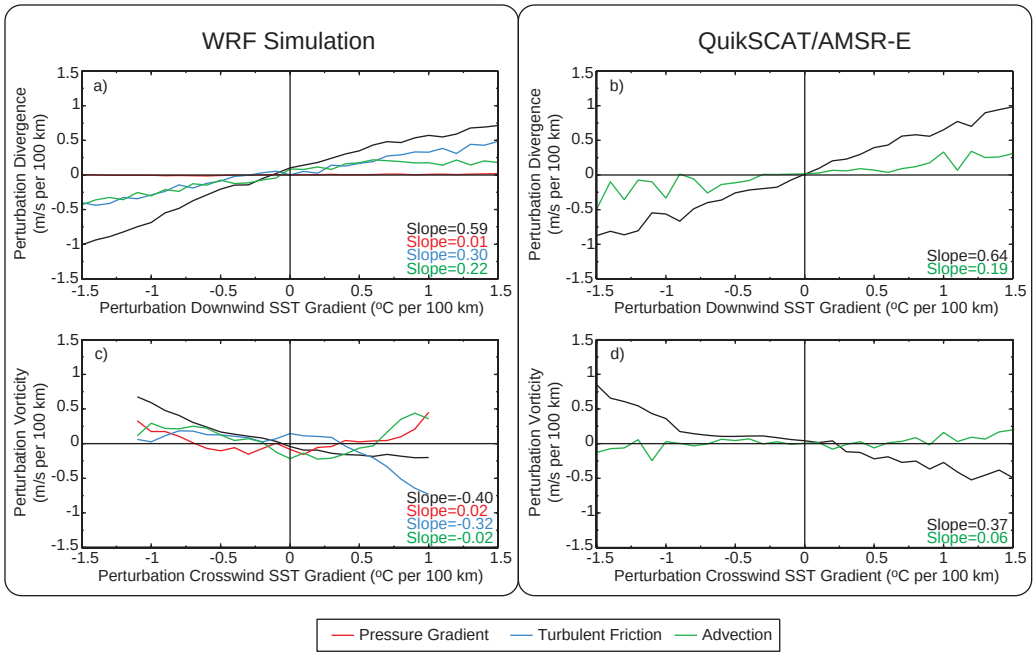

Figure 5.12: Binned scatterplots of: perturbation divergence binned as a function of the perturbation downwind SST gradient for the (a) WRF simulation and the (b) QuikSCAT/AMSR-E observations; perturbation vorticity binned as a function of the perturbation crosswind SST gradient for the (c) WRF simulation and the (d) QuikSCAT/AMSR-E observations. The slopes of the bin-averages were found by least-squares fits of the means within each bin to straight lines.

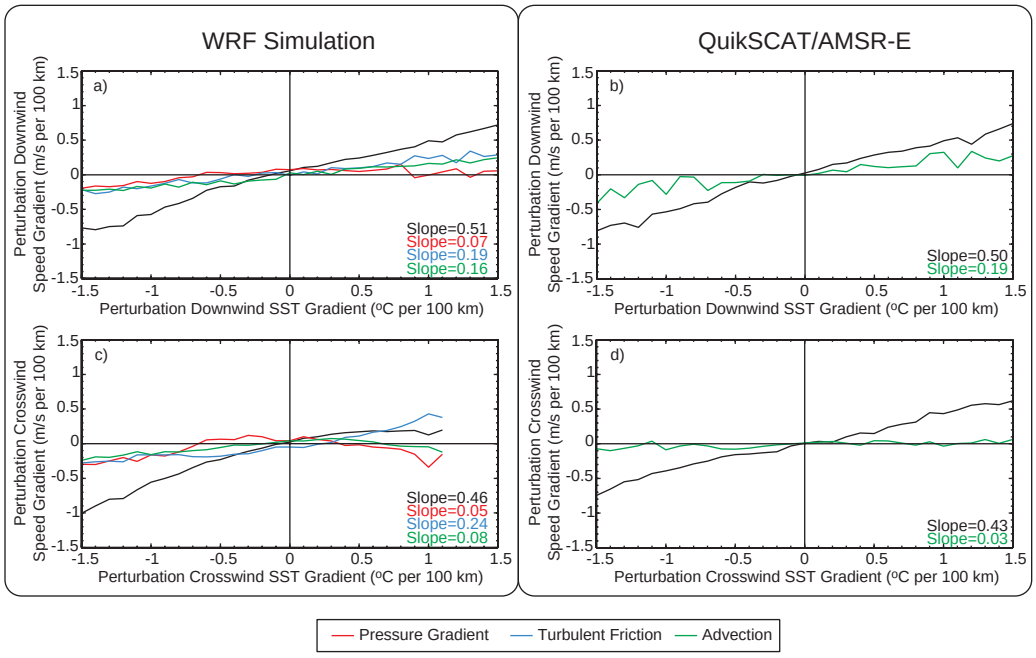

Figure 5.13: Same as Fig. 5.12, except for the crosswind and downwind speed gradients.

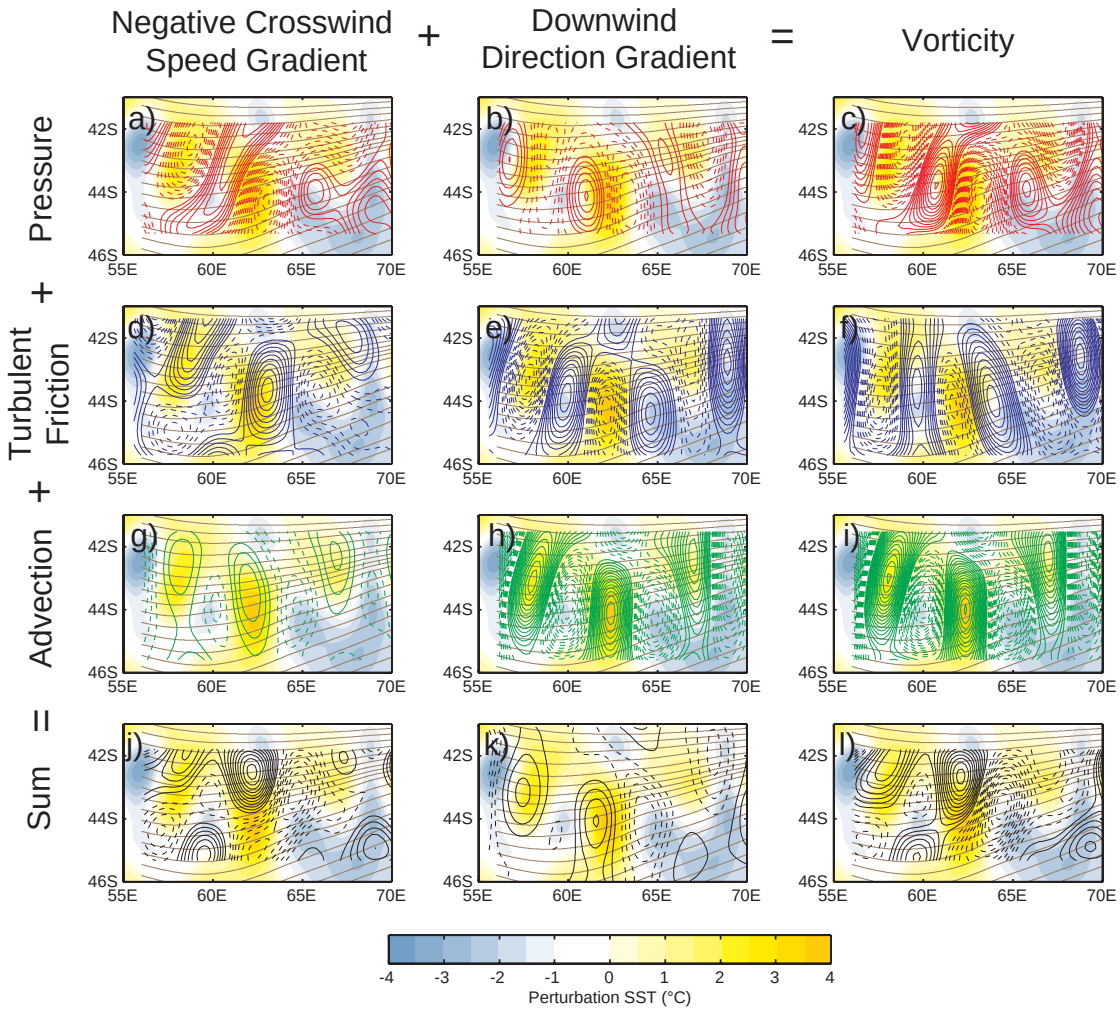

Figure 5.14: 1-month average maps of the separate forcing terms in the WRF simulation of the: negative of the perturbation crosswind speed gradient (left column); perturbation downwind direction gradient (center column); and vorticity (right column). The forcing terms were computed according to Eqn. 5.29 for the crosswind speed gradient (panels a, d, and g) and Eqn. 5.30 for the downwind direction gradient (panels b, e, and h) and include terms from pressure (red contours, panels a, b, and c); turbulent friction (blue contours, panels d, e, and f); and advection (green contours, panels g, h, and i). The brown contours in each panel show streamlines of the unfiltered surface wind field. Dashed and solid contours correspond to negative and positive perturbations, respectively, with a contour interval of 1×10^{-6} s^{-1}. The zero contour has been omitted for clarity.

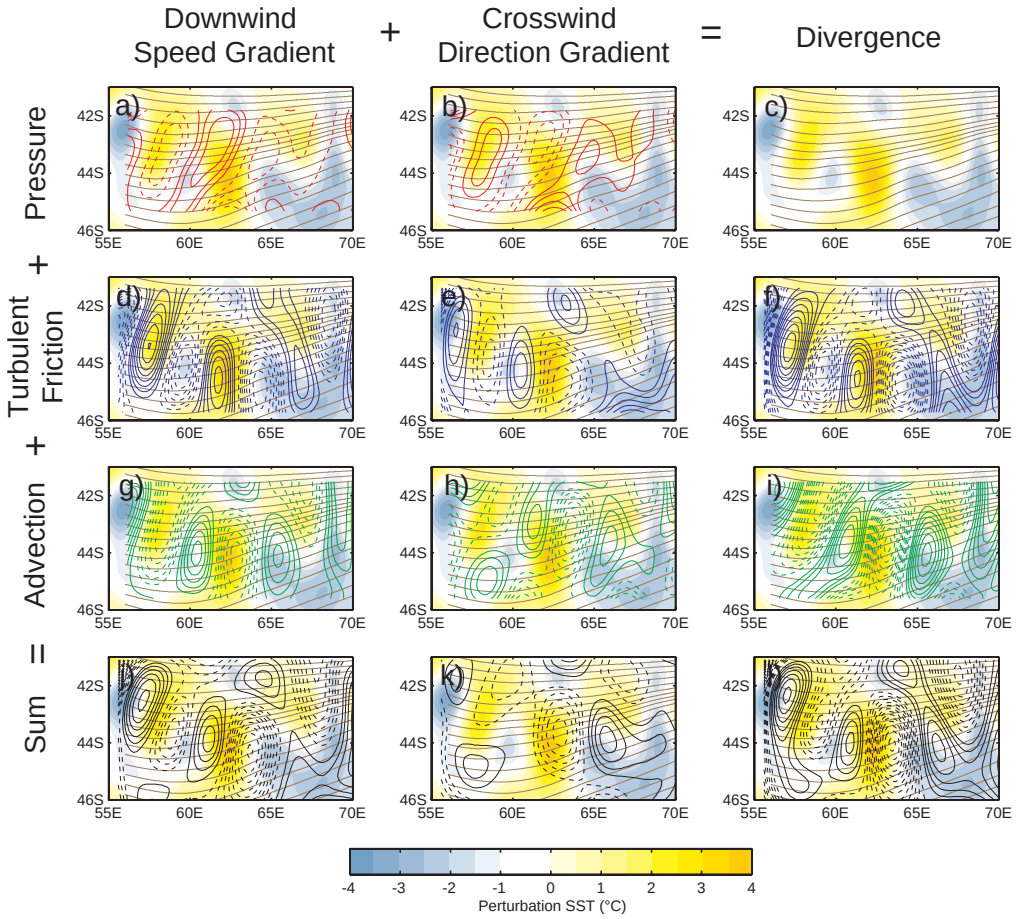

Figure 5.15: 1-month average maps of the separate forcing terms in the WRF simulation of the: perturbation downwind speed gradient (left column); perturbation crosswind direction gradient (center column); and divergence (right column). The forcing terms were computed according to Eqn. 5.28 for the downwind speed gradient (panels a, d, and g) and Eqn. 5.31 for the crosswind direction gradient (panels b, e, and h) and include terms from pressure (red contours, panels a, b, and c); turbulent friction (blue contours, panels d, e, and f); and advection (green contours, panels g, h, and i). The brown contours in each panel show streamlines of the unfiltered surface wind field. Dashed and solid contours correspond to negative and positive perturbations, respectively, with a contour interval of 1×10^{-6} s^{-1}. The zero contour has been omitted for clarity.

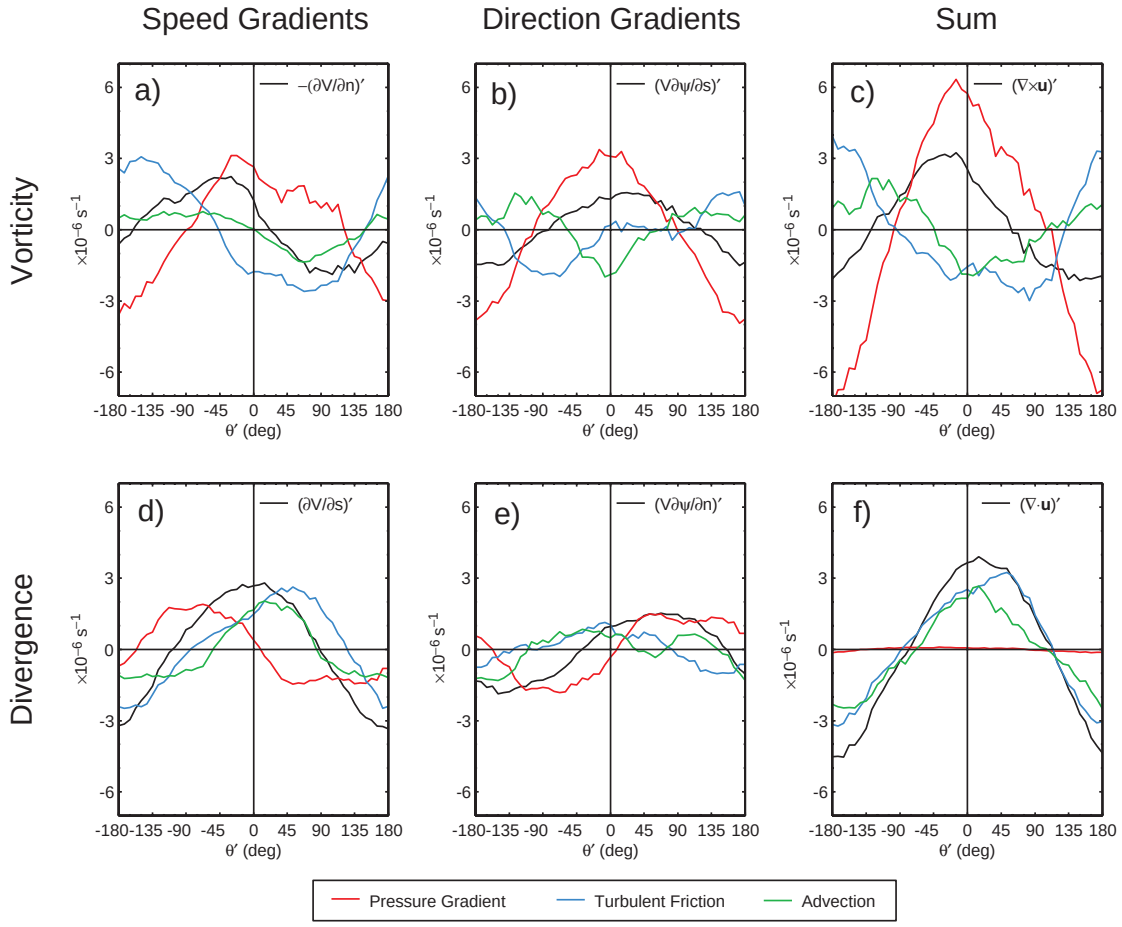

Figure 5.16: Binned scatterplots of the WRF perturbation vorticity and divergence dependencies – and their associated speed and direction gradients – on the angle θ': (a) $-(\partial V/\partial n)'$; (b) $(V\partial\psi/\partial s)'$; (c) $(\nabla \times \boldsymbol{u})'$; (d) $(\partial V/\partial s)'$; (e) $(V\partial\psi/\partial n)'$; and (f) $(\nabla\cdot\boldsymbol{u})'$. The colored lines correspond to the individual contributions in Eqns. 5.28-5.31 from the: pressure gradient (red); turbulent friction (blue); and horizontal advection (green).

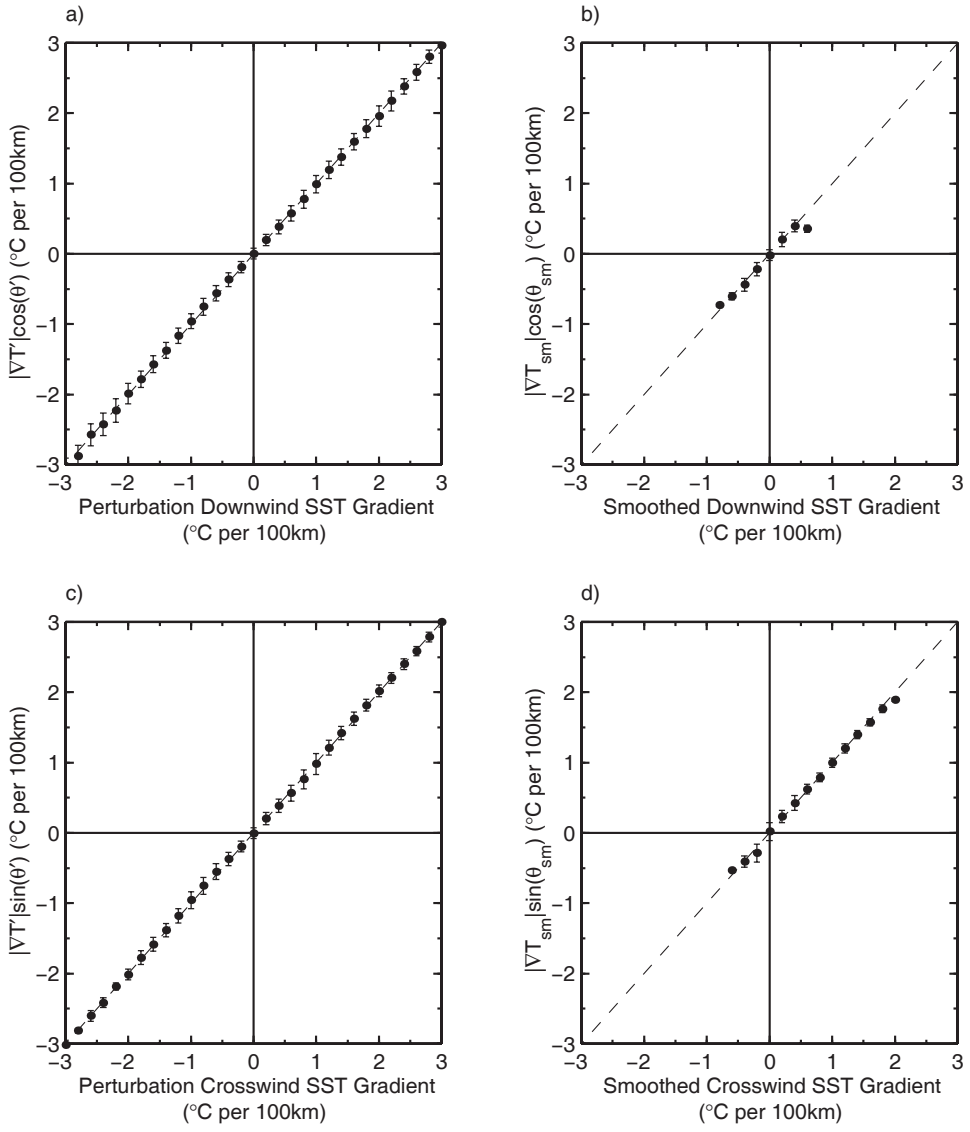

Figure 5.17: Binned scatterplots of the relations expressed by Eqns. 5.36-5.39. (a) $|\nabla T'| \cos\theta'$ vs. $(\partial T/\partial s)'$; (b) $|\nabla T_{sm}| \cos\theta_{sm}$ vs. $(\partial T/\partial s)_{sm}$; (c) $|\nabla T'| \sin\theta'$ vs. $(\partial T/\partial n)'$; (d) $|\nabla T_{sm}| \sin\theta_{sm}$ vs. $(\partial T/\partial n)_{sm}$. The points and errorbars in each panel represent the means and ± 1 std dev within each bin computed from the first weekly-averaged AMSR-E SST and QuikSCAT wind fields used in this study over the Agulhas Return Current. The dashed line in each panel has unit slope and is shown for reference.

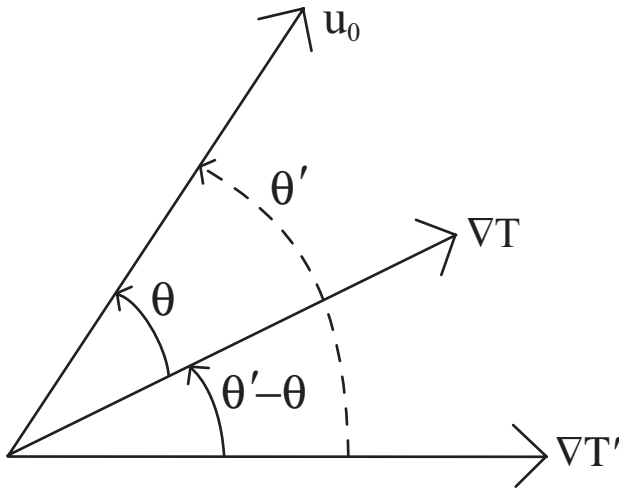

Figure 5.18: Schematic of the orientation between the surface wind vector $\boldsymbol{u}_0$, the SST gradient vector ∇T, and the perturbation SST gradient vector $\nabla T'$, and the counterclockwise angles θ and θ', as deduced from Eqn. 5.47.

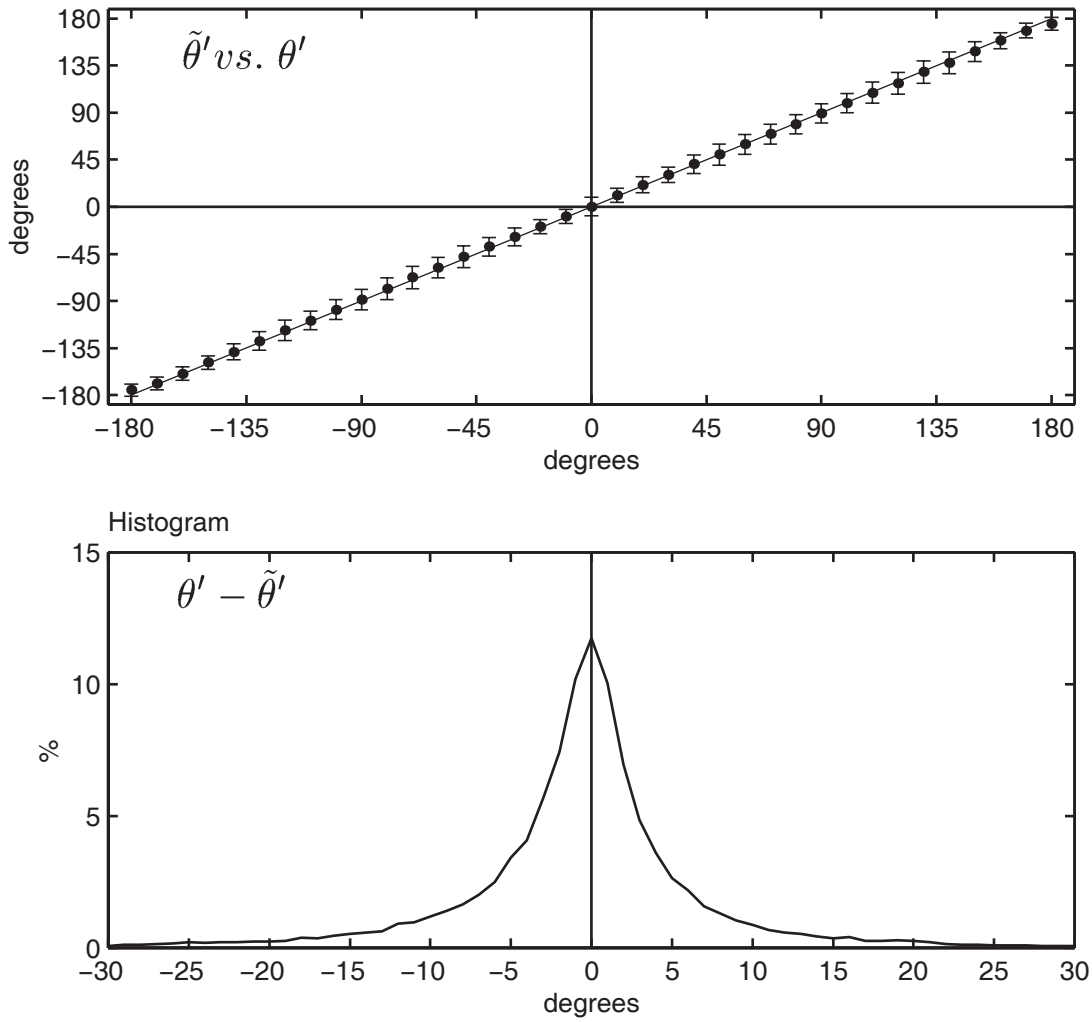

Figure 5.19: (top panel) Binned scatterplot of the angle $\widetilde{\theta'}$ between the surface wind vector and the perturbation SST gradient vector binned as a function of θ'. (bottom panel) Histogram of the differences between $\widetilde{\theta'}$ and θ'; the distribution has a std dev of 7.6°. The points and errorbars in the top panel represent the means and ± 1 std dev within each bin computed from the first weekly-averaged AMSR-E SST and QuikSCAT wind fields used in this study over the Agulhas Return Current. The dashed line in the top panel has unit slope and is shown for reference.

Appendices

Appendix A

Extension of the Samelson et al. two layer boundary layer model to include baroclinic effects

The purpose of this study is to extend a very simple analytical model of the wind structure of the boundary layer as it flows across SST fronts to better understand the more complex structure simulated by WRF. We start with the steady, incompressible, rotational, horizontally homogeneous equations of motion used by Samelson et al. (2007). For simplicity, the boundary layer is split into 2 layers, each of depth $h/2$, with a deep free atmosphere above. We assume that both layers are forced by a constant large-scale meridional pressure gradient $G^y = \frac{1}{\rho_0}\frac{\partial p}{\partial y}$, where ρ_0 is a constant reference density and p is the pressure at the boundary layer top. In the lowest layer, zonal and meridional pressure gradients $(\delta G^x, \delta G^y)$ form in response to zonal and meridional gradients in air temperature, respectively, caused here by spatial SST gradients. The zonal and meridional equations of motion for the velocity components within each layer are

$$fu_1 = -G^y - \delta G^y + \frac{2}{\rho_0 h}(\tau_i^y - \tau_s^y) \quad \text{(A.1)}$$

$$-fv_1 = -\delta G^x + \frac{2}{\rho_0 h}(\tau_i^x - \tau_s^x) \quad \text{(A.2)}$$

$$fu_2 = -G^y - \frac{2}{\rho_0 h}\tau_i^y \quad \text{(A.3)}$$

$$-fv_2 = -\frac{2}{\rho_0 h}\tau_i^x, \quad \text{(A.4)}$$

where $\boldsymbol{\tau}_i = (\tau_i^x, \tau_i^y)$ is the interfacial stress between layers 1 and 2 and $\boldsymbol{\tau}_s = (\tau_s^x, \tau_s^y)$ is the surface stress at the base of layer 1. Note that entrainment into the boundary layer, as would be represented by a stress at the top of layer 2, is assumed to be negligible. For simplicity, the surface and interfacial stresses are modeled as linearly related to the vector wind components by

$$\boldsymbol{\tau}_i = \rho_0 r_i(\boldsymbol{u}_2 - \boldsymbol{u}_1) \quad \text{(A.5)}$$

$$\boldsymbol{\tau}_s = \rho_0 r_s \boldsymbol{u}_1. \quad \text{(A.6)}$$

To facilitate solution of the layer vector components, this linear set of equations for the zonal and meridional velocities is written in matrix notation

$$\begin{bmatrix} -1 & -\frac{2r_i}{fh} - \frac{2r_s}{fh} & 0 & \frac{2r_i}{fh} \\ \frac{2r_i}{fh} + \frac{2r_s}{fh} & -1 & -\frac{2r_i}{fh} & 0 \\ 0 & \frac{2r_i}{fh} & -1 & -\frac{2r_i}{fh} \\ -\frac{2r_i}{fh} & 0 & \frac{2r_i}{fh} & -1 \end{bmatrix} \begin{bmatrix} u_1 \\ v_1 \\ u_2 \\ v_2 \end{bmatrix} = \begin{bmatrix} G^y/f + \delta G^y/f \\ -\delta G^x/f \\ G^y/f \\ 0 \end{bmatrix}.$$

The layer 1 zonal and meridional pressure gradients represented by $(\delta G^x, \delta G^y)$ are written in terms of the layer 1 air temperature T_1

$$\delta G^x = -\frac{gh}{2T_1}\frac{\partial T_1}{\partial x} \tag{A.7}$$

$$\delta G^y = -\frac{gh}{2T_1}\frac{\partial T_1}{\partial y}. \tag{A.8}$$

In this simple model, the air temperature gradients forced by SST gradients are confined to layer 1 and are not transmitted into layer 2.

Solutions for the wind components were obtained by solving the matrix equation above given values of G^y, $(\delta G^x, \delta G^y)$, and ranges of values for the internal turbulent friction parameter r_i/fh and the surface friction parameter r_s/fh. The wind components were normalized by the zonal geostrophic wind speed $U_g = -G^y/f$. Thus, we find the solutions to the following

$$\begin{bmatrix} u_1/U_g \\ v_1/U_g \\ u_2/U_g \\ v_2/U_g \end{bmatrix} = \begin{bmatrix} -1 & -\frac{2r_i}{fh} - \frac{2r_s}{fh} & 0 & \frac{2r_i}{fh} \\ \frac{2r_i}{fh} + \frac{2r_s}{fh} & -1 & -\frac{2r_i}{fh} & 0 \\ 0 & \frac{2r_i}{fh} & -1 & -\frac{2r_i}{fh} \\ -\frac{2r_i}{fh} & 0 & \frac{2r_i}{fh} & -1 \end{bmatrix}^{-1} \begin{bmatrix} -1-\kappa_y \\ -\kappa_x \\ -1 \\ 0 \end{bmatrix},$$

where $\kappa_x = \delta G^x/G^y$ and $\kappa_y = \delta G^y/G^y$ are measures of the baroclinicity of the boundary layer in this simple model, and are hereafter referred to as the zonal and meridional baroclinicity parameters, respectively. In this analysis, we seek to find the behavior of the vertical wind shear in the zonal and meridional directions as functions

of κ_x and κ_y. The model analysis is applied for the Southern Hemisphere where $f < 0$ and $G^y > 0$, which produces westerly winds. Note that the results here are directly comparable to the Northern Hemisphere case considered by Samelson et al. (2007).

The solutions for the zonal and meridional winds in both layers appropriate for the Southern Hemisphere are shown in Fig. A.1 as a function of the internal mixing parameter r_i/fh and for a fixed value of $r_s/fh = -0.5$ and for three different values each of κ_x and κ_y. $\kappa_x = 0$ and $\kappa_y = 0$ correspond to a barotropic boundary layer with no zonal and meridional pressure gradients induced by spatial air temperature gradients, equivalent to the case investigated by Samelson et al. (2007). $\kappa_x = -0.2$ and 0.2 correspond to positive and negative values of $\partial T_1/\partial x$, respectively, which is a fairly representative temperature gradient of about 1.5°C per 100 km associated with large-scale mid-latitude SST fronts. Spatial temperature gradients in layer 1 result from spatial gradients in SST as air flows perpendicular to SST fronts. For $\kappa_x = 0$, the wind profiles are identical to those computed by Samelson et al. (2007) (center panel in Fig. A.1).

As expected from Ekman dynamics, u_2 is larger than u_1 in most cases because of the effects of surface friction on the layer 1 winds. At $\kappa_x = 0.2$ and $\kappa_y = 0.2$, however, u_1 is larger than u_2. Large baroclinicity can therefore counteract the tendency of surface friction to decelerate the winds in layer 1. The zonal winds are relatively insensitive to the choice of the internal mixing parameter r_i/fh under barotropic and baroclinic conditions, as evidenced by the relatively small variation across the range

of r_i/fh considered in Fig. A.1.

When $\kappa_x = 0$, meridional flow can only result from a balance between surface friction, Coriolis force, and G^y, consistent with Ekman dynamics. This causes the v_1 wind component to be more strongly poleward than the v_2 winds aloft. In general, both v_1 and v_2 exhibit a stronger sensitivity to the internal mixing parameter in both the barotropic and baroclinic cases compared to the zonal winds, especially when $r_i/fh \gtrsim -0.5$ (Fig. A.1). Within the simple conceptual framework of this model, both baroclinicity and internal turbulent mixing are therefore expected to be important in describing the vertical structure of the meridional winds within the boundary layer.

As winds blow from cool to warm water ($\kappa_x < 0$), both $u_2 - u_1$ and $v_2 - v_1$ markedly decrease in magnitude compared to the barotropic case (top panel, Fig. A.1). Conversely, $u_2 - u_1$ and $v_2 - v_1$ markedly increase in magnitude as winds blow from warm to cool water ($\kappa_x > 0$).

The variation of the wind shear between layers 1 and 2 as a function of κ_x is shown in Fig. A.2 for fixed values of r_i/fh and r_s/fh. Consistent with Fig. A.1, the shear in the zonal and meridional winds decreases as κ_x increases from negative to positive values. For flow from warm to cool water where the temperature gradients are large in magnitude, a shear reversal can occur such that the layer 1 flow can actually exceed the upper level flow in layer 2, as evident by the change in sign of the wind shear at values of κ_x greater than 0.25 (Fig. A.2).

The shear between the 2 layers is predicted by the model to decrease until the layer 1 and layer 2 winds are equal as the internal mixing parameter is increased (Fig. A.1). Therefore, the velocity of the wind is predicted to vary as a function of κ_x. This dependency on the wind velocity and κ_x is highlighted by Fig. A.4, which shows the layer 1 winds as a function of κ_x at the fixed values of $r_i/fh = -1$ and $r_s/fh = -0.25$.

To estimate the change in wind velocity caused by a change in turbulent mixing as air flows across SST fronts, the difference in wind components between strong mixing ($r_i/fh = -1$) and weak mixing ($r_i/fh = -0.25$) is computed. The differences Δu_1 and Δv_1 are computed as

$$\begin{aligned} \Delta u_1 &= u_1(r_i/fh = -1) - u_1(r_i/fh = -0.25) \\ \Delta v_1 &= v_1(r_i/fh = -1) - v_1(r_i/fh = -0.25) \end{aligned}$$

for a fixed value of the surface friction parameter ($r_s/fh = -0.25$) (Fig. A.5). Note that the value of $r_i/fh = -1$ was chosen based on the formulation for the turbulent stress divergence used here

$$\frac{1}{\rho_0}\frac{\partial \tau^x}{\partial z} \sim \frac{r_i}{h}(u_2 - u_1),$$

which leads to an estimate of r_i/fh as

$$\frac{r_i}{fh} \sim \frac{\partial \tau^x/\partial z}{\rho_0 f(u_2 - u_1)}.$$

For typical values for $\frac{1}{\rho_0}\frac{\partial \tau^x}{\partial z}$ of 3×10^{-4} s^{-1}, $u_2 - u_1$ of 3 m/s, and f of 1×10^{-4} s^{-1}, we get an estimate of $r_i/fh \sim -1$.

$\Delta u_1/U_g$ is nearly zero in the barotropic case ($\kappa_x = 0$ and $\kappa_y = 0$). In the absence of baroclinicity, turbulent mixing therefore has relatively little effect on the zonal surface winds. $\Delta u_1/U_g$ varies significantly as a function of κ_y in this model, which controls the zonal component of the thermal wind shear. In the Southern hemisphere, $\partial T_1/\partial y > 0$ on average, which therefore makes $\kappa_y < 0$ on average. According to Fig. A.5, increased u_1 winds are expected when there is increased turbulent mixing in these conditions. This model suggests that baroclinicity is required for turbulent mixing to modulate the surface zonal winds. $\Delta u_1/U_g$ is not predicted to vary significantly as a function of κ_x.

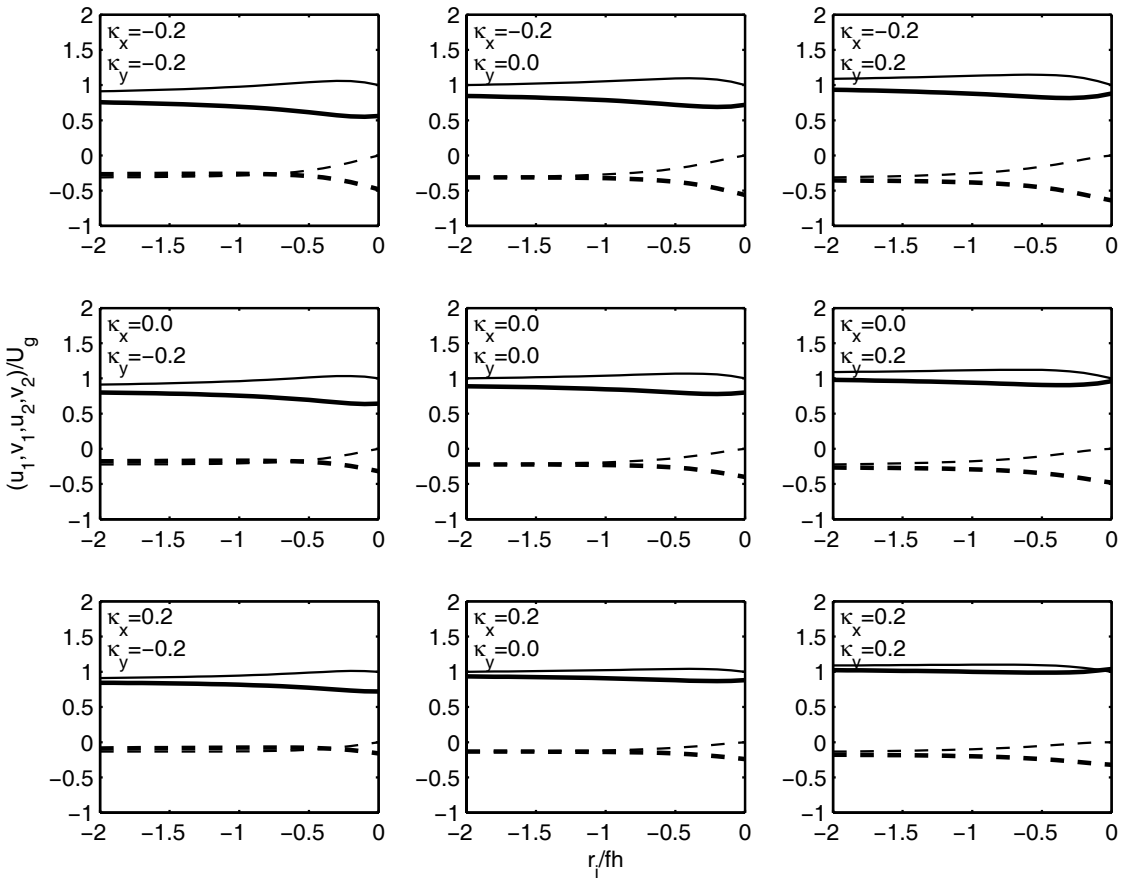

Figure A.1: Zonal (solid curves) and meridional (dashed curves) wind components in layers 1 (thick) and 2 (thin) normalized by the geostrophic wind speed U_g as a function of the internal mixing parameter r_i/fh for values of the zonal and meridional baroclinicity parameters κ_x and κ_y as indicated. The model solutions for the velocity components were performed for a fixed value of the surface friction coefficient $r_s/fh = -0.5$.

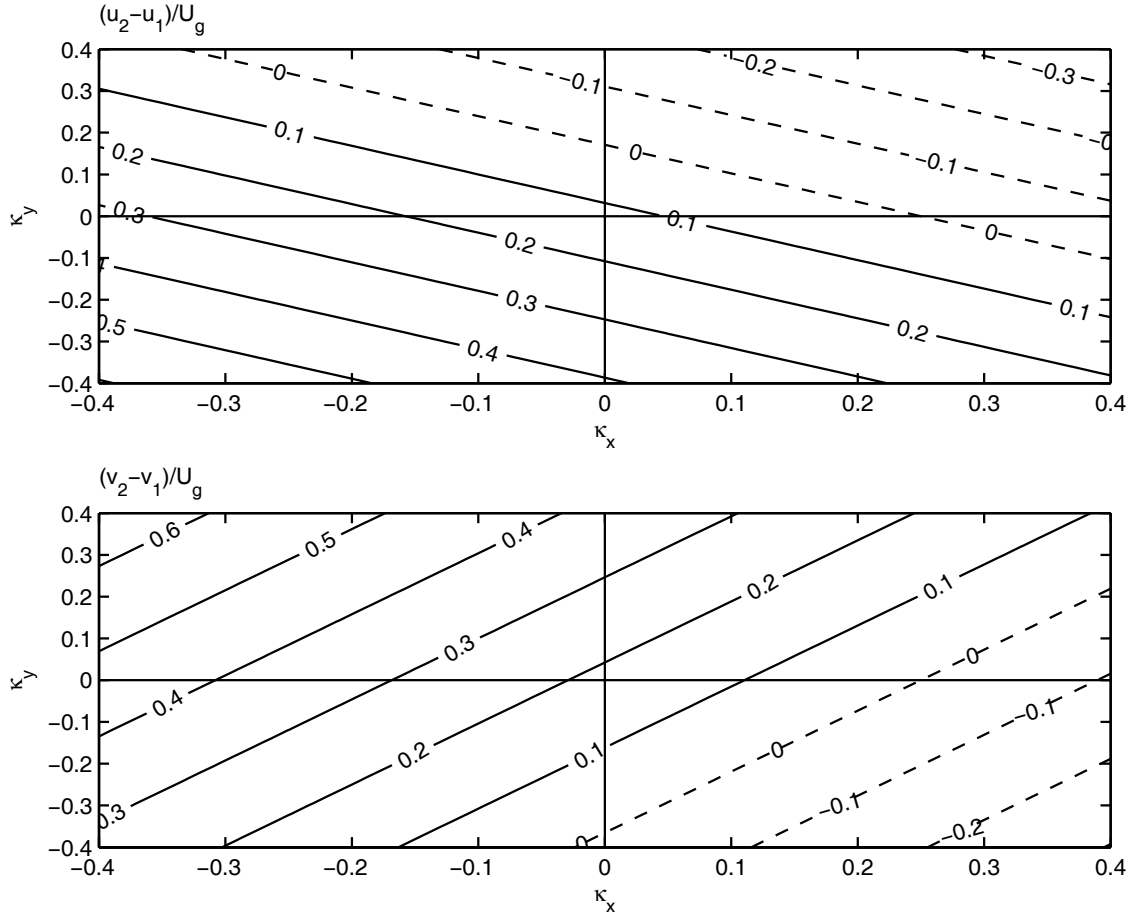

Figure A.2: Dimensionless shear as functions of the zonal and meridional baroclinicity parameters (κ_x and κ_y), respectively, for fixed values of the friction parameters $r_i/fh = -0.2$ and $r_s/fh = -0.25$.

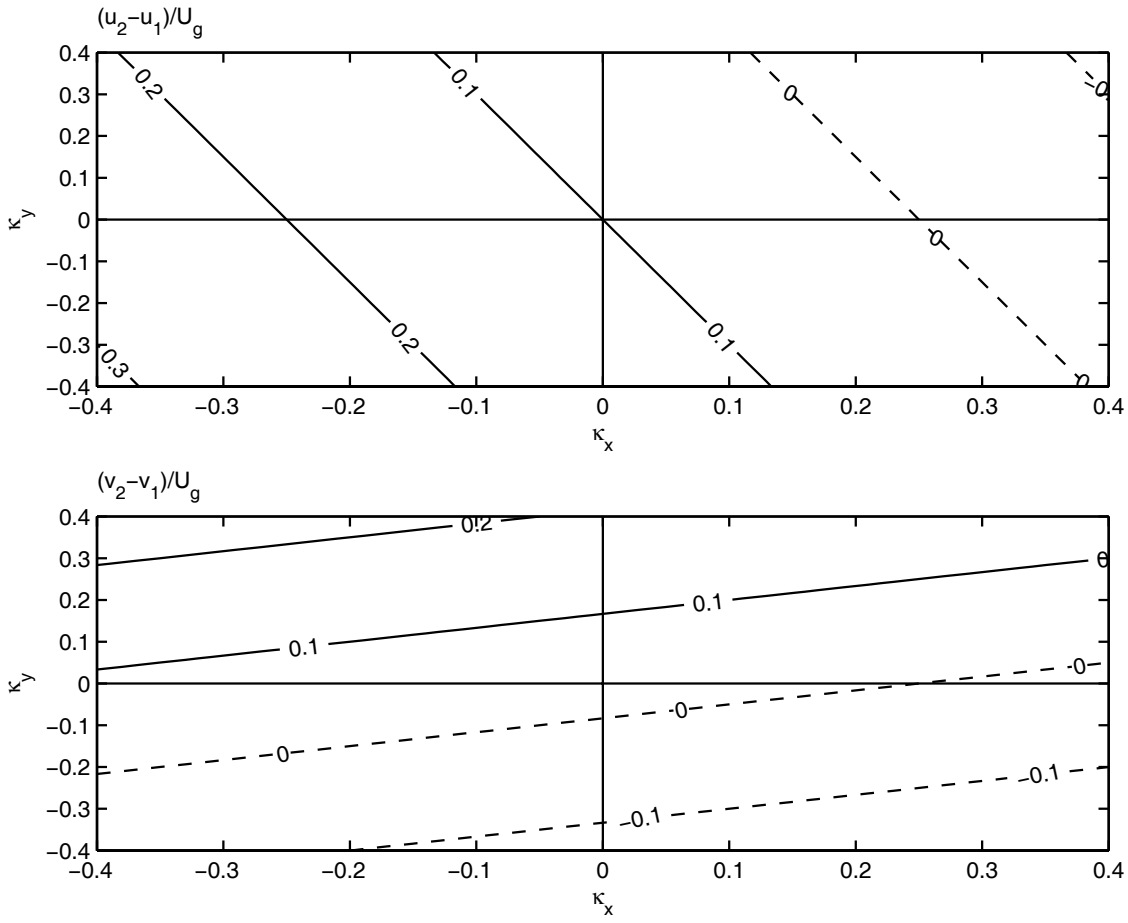

Figure A.3: Same as Fig. A.2, except for $r_i/fh = -1$ and $r_s/fh = -0.25$.

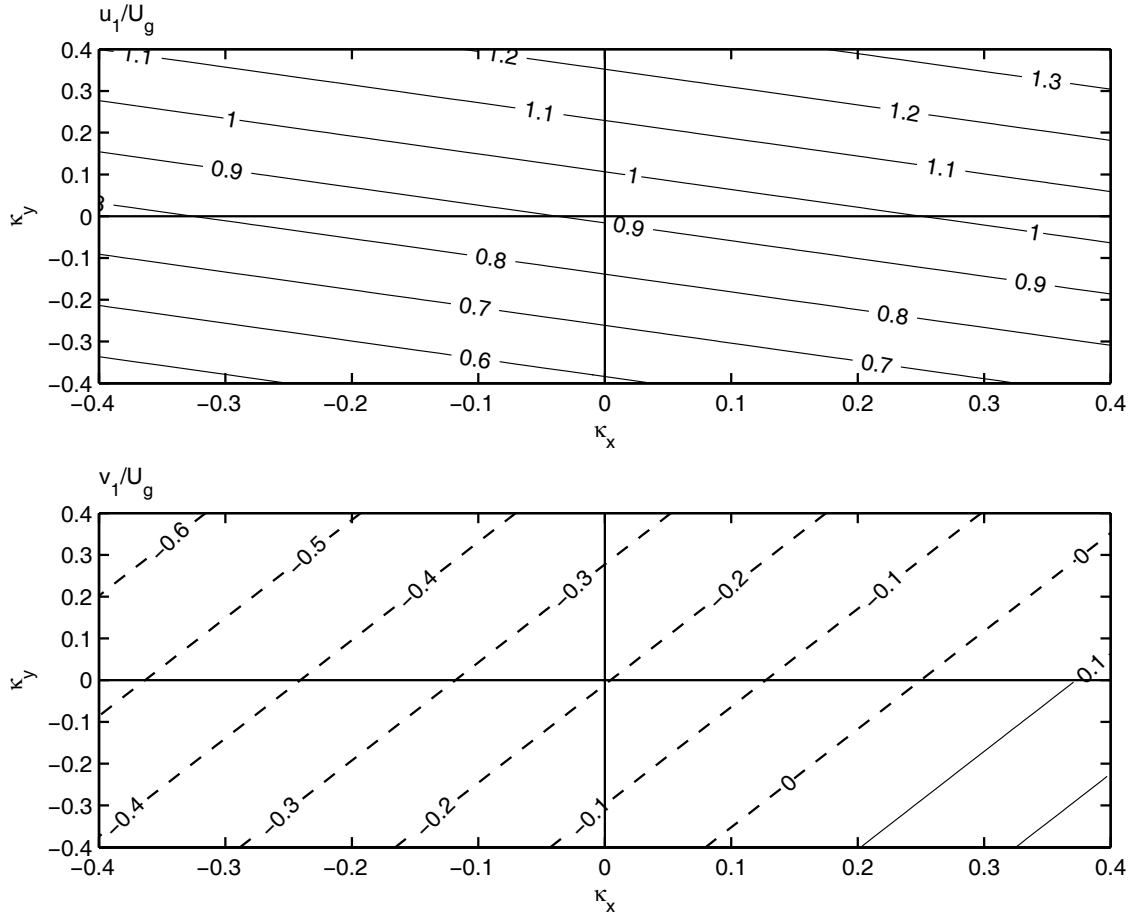

Figure A.4: Dimensionless layer 1 velocity components as functions of the zonal and meridional baroclinicity parameters (κ_x and κ_y), respectively, for fixed values of the friction parameters $r_i/fh = -0.2$ and $r_s/fh = -0.25$.

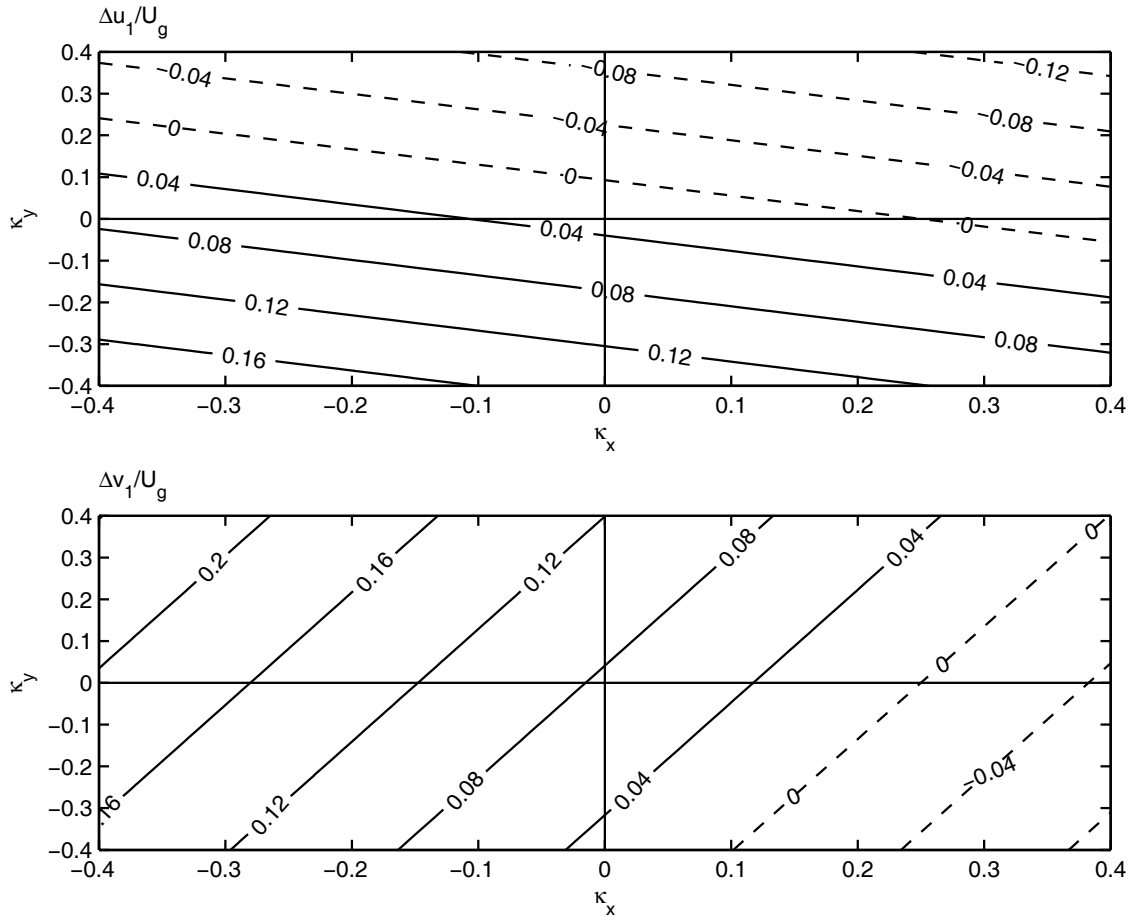

Figure A.5: The dimensionless layer 1 velocity component differences between weak and strong mixing conditions ($\Delta u_1/U_g, \Delta v_1/U_g$) as functions of the zonal and meridional baroclinicity parameters (κ_x and κ_y), respectively, for a fixed value of the friction parameters $r_s/fh = -0.25$. The mixing parameter r_i/fh used for the strong mixing case was -1.25 and for the weak mixing case was -0.2.

Appendix B

Determining Vector Wind Stress Components from SST-Induced Wind Stress Curl and Divergence

B.1 Introduction

A method for numerically determining the vector wind stress fields from given wind stress curl and divergence fields is described and evaluated. Since the small-scale wind stress curl and divergence fields are statistically related to underlying SST gradients, this method can be applied to find the SST-induced zonal and meridional components of the wind stress field. It is necessary to develop a technique to determine the SST-induced vector wind stress components since no consistent statistical relationship exists between the individual vector wind stress components and SST. This technique is suitable for determining the SST-induced small-scale wind stress structure forcing an oceanic circulation model given the models' temporally evolving SST field and a large-scale wind stress field, e.g., the surface wind analyses from op-

erational numerical prediction models or the even lower resolution surface wind fields from the NCEP-NCAR or ECMWF reanalyses.

In the next section, the mathematical relations for determining the wind stress vector given the wind stress curl and divergence fields are derived and evaluated. In Section B.3, the method is applied for determining the vector wind stress components given statistical relations between the wind stress curl and divergence fields and the underlying SST gradients.

B.2 Methods

B.2.1 Description

Define the wind stress curl and divergence fields in terms of functions $f(x, y)$ and $g(x, y)$ such that

$$\nabla \times \boldsymbol{\tau} = \frac{\partial \tau^y}{\partial x} - \frac{\partial \tau^x}{\partial y} = f \tag{B.1}$$

$$\nabla \cdot \boldsymbol{\tau} = \frac{\partial \tau^x}{\partial x} + \frac{\partial \tau^y}{\partial y} = g, \tag{B.2}$$

where $\boldsymbol{\tau} = (\tau^x, \tau^y)$ is the vector wind stress and $\nabla = (\partial/\partial x, \partial/\partial y)$ are the zonal and meridional components of the horizontal gradient field, respectively.

Separate equations for τ^x and τ^y are obtained by cross-differentation of Eqns. B.1 and B.2. An expression for τ^x can be found by subtracting $\partial/\partial y$ of (B.1) from $\partial/\partial x$

of (B.2), which cancels out terms involving τ^y. Similarly, an expression for τ^y can be found by adding $\partial/\partial x$ of (B.1) to $\partial/\partial y$ of (B.2), which removes terms involving τ^x. The resulting equations are

$$\nabla^2\tau^x = \frac{\partial^2\tau^x}{\partial x^2} + \frac{\partial^2\tau^x}{\partial y^2} = \frac{\partial g}{\partial x} - \frac{\partial f}{\partial y} = F_x \tag{B.3}$$

$$\nabla^2\tau^y = \frac{\partial^2\tau^y}{\partial x^2} + \frac{\partial^2\tau^y}{\partial y^2} = \frac{\partial f}{\partial x} + \frac{\partial g}{\partial y} = F_y. \tag{B.4}$$

where each represent a Poisson's equation for τ^x and τ^y. Numerical solutions for τ^x and τ^y are found using the successive overrelaxation (SOR) technique as described in pgs. 857-860 of Press et al. (1992), which is commonly used to solve Poisson's equations numerically.

To solve the 2-dimensional Poisson's equation for an arbitrary scalar field s with a source term S, the Laplacian operator is written in finite difference form as

$$a_{i,j}s_{i,j+1} + b_{i,j}s_{i,j-1} + c_{i,j}s_{i+1,j} + d_{i,j}s_{i-1,j} + e_{i,j}s_{i,j} = S_{i,j}, \tag{B.5}$$

where the index $i = 1, 2, \ldots, N_x$ is defined here to represent the x-direction and $j = 1, 2, \ldots, N_y$ the y-direction. For constant grid spacings, the coefficients may be expressed as

$$a_{i,j} = \frac{1}{(\Delta y)^2}$$

$$
\begin{aligned}
b_{i,j} &= \frac{1}{(\Delta y)^2} \\
c_{i,j} &= \frac{1}{(\Delta x)^2} \\
d_{i,j} &= \frac{1}{(\Delta x)^2} \\
e_{i,j} &= -2\Big[\frac{1}{(\Delta x)^2} + \frac{1}{(\Delta y)^2}\Big],
\end{aligned}
\tag{B.6}
$$

where Δx and Δy are the grid spacings in the zonal and meridional directions, respectively. For grids with non-uniform grid spacing, the coefficients are

$$
\begin{aligned}
a_{i,j} &= \frac{2}{h_2^{y2} + h_1^{y2}}\Big[1 - \frac{h_1^y(h_2^y - h_1^y)}{h_2^y h_3^y}\Big] \\
b_{i,j} &= \frac{2}{h_2^{y2} + h_1^{y2}}\Big[1 + \frac{h_2^y(h_2^y - h_1^y)}{h_1^y h_3^y}\Big] \\
c_{i,j} &= \frac{2}{h_2^{x2} + h_1^{x2}}\Big[1 - \frac{h_1^x(h_2^x - h_1^x)}{h_2^x h_3^x}\Big] \\
d_{i,j} &= \frac{2}{h_2^{x2} + h_1^{x2}}\Big[1 + \frac{h_2^x(h_2^x - h_1^x)}{h_1^x h_3^x}\Big] \\
e_{i,j} &= -2\Big[\frac{1}{h_2^{x2} + h_1^{x2}} + \frac{1}{h_2^{y2} + h_1^{y2}}\Big]
\end{aligned}
\tag{B.7}
$$

where the h's define the grid spacing as follows

$$
\begin{aligned}
h_1^x &= x_i - x_{i-1} \\
h_2^x &= x_{i+1} - x_i \\
h_3^x &= x_{i+1} - x_{i-1} \\
h_1^y &= y_j - y_{j-1} \\
h_2^y &= y_{j+1} - y_j
\end{aligned}
$$

$$h_3^y = y_{j+1} - y_{j-1}.$$

The SOR technique uses an iterative refinement algorithm to successively estimate $s_{i,j}$ until numerical convergence is attained. To start the algorithms' first iteration, the initial condition is $s_{i,j} = 0$ for all i, j. The solution is not sensitive to the choice of initial condition. Along the domain boundaries, s is set to zero. As discussed in the next subsection, the accuracy of the solution near the boundaries is sensitive to this boundary condition, as the solution tends to zero (i. e. the boundary condition) as the boundary is approached from the interior of the domain. Generally, convergence to a solution is achieved within O(100) iterations.

A layout of the algorithm used here to determine $\tau^{x\prime}$ and $\tau^{y\prime}$ is shown on Pg. 281. The primes represent spatially high-pass filtered fields, hereafter referred to as perturbation fields. Note that the spatial high-pass filtering used here is essentially a linear operator which retains wavelengths shorter than 30° longitude by 10° latitude.

Numerical weather prediction (NWP) models generally resolve the large-scale wind field adequately. They do not resolve the small-scale wind stress variability that is well-correlated with small-scale SST variability, however (e.g., Chelton and Freilich 2005). The methodology developed here is intended to reconstruct estimates of the small-scale SST-induced features in the wind field that are poorly resolved by NWP and reanalyses wind fields.

B.2.2 Evaluation of the method for determining $\tau^{x\prime}$ and $\tau^{y\prime}$

The accuracy in reconstructing $\tau^{x\prime}$ and $\tau^{y\prime}$ using the SOR algorithm to solve numerically Eqns. B.3 and B.4 is evaluated by reconstructing $\tau^{x\prime}$ and $\tau^{y\prime}$ fields from a given set of wind stress curl and divergence fields and then comparing them to the original $\tau^{x\prime}$ and $\tau^{y\prime}$ fields used in computing the wind stress curl and divergence. For a perfect method which introduces zero error, the reconstructed and original $\tau^{x\prime}$ and $\tau^{y\prime}$ fields should be identical. For this evaluation, vector-averaged QuikSCAT $\tau^{x\prime}$ and $\tau^{y\prime}$ fields at weekly-intervals over the 5-week period 3 January to 6 February 2003 are used to compute perturbation wind stress curl and divergence fields over the Agulhas Current system in the Southern Ocean encompassing the area 0°-100°E longitude by 35°-60°S latitude.

Significant errors in the reconstructed $\tau^{x\prime}$ and $\tau^{y\prime}$ fields occur in large areas surrounding missing data points associated with geographical locations of islands, as shown by Figs. B.1 and B.2, respectively. One successful technique to remove these errors involves spatially interpolating over all missing points in F_x and F_y before using the SOR algorithm. This is accomplished here by smoothing the QuikSCAT wind stress curl and divergence fields using the 2-dimensional loess smoother with half-power points of 4° longitude by 2° latitude and interpolating smoothed estimates of the curl and divergence at missing data points. The large areas of errors evident in Figs. B.1 and B.2 near missing data points then vanish in the reconstructed $\tau^{x\prime}$ and $\tau^{y\prime}$ fields (Figs. B.3 and B.4). The errors associated with missing points within the

solution domain can thus be mitigated by interpolating over all missing points before reconstruction using the SOR algorithm.

The error along the boundaries is caused by the values of the reconstructed fields tending to the boundary value as the boundary is approached from the interior. The boundary conditions for $\tau^{x\prime}$ and $\tau^{y\prime}$ used here for the SOR algorithm is zero. Setting $\tau^{x\prime}$ and $\tau^{y\prime}$ to the true values of $\tau^{x\prime}$ and $\tau^{y\prime}$ along the boundaries completely removes the boundary errors, leaving normalized errors throughout the solution domain much less than 0.1%.

In practice, boundary values for the SOR algorithm will not be known when determining $\tau^{x\prime}$ and $\tau^{y\prime}$, so setting $\tau^{x\prime}$ and $\tau^{y\prime}$ to zero at the boundaries seems the only reasonable choice. When using the zero boundary condition, reconstructed values within 20 grid points of the solution domain boundary (about 5° here with a grid spacing of 0.25°) are generally too compromised by this boundary condition to be accurate. Some influence of the errors on the boundary diffuse further into the interior of the solution domain, as evidenced by the slight elevation in error in the reconstructed $\tau^{x\prime}$ fields in the eastern half of the domain shown in Fig. B.3. Even with the errors near the boundary, the reconstructed fields on the interior of the domain appear very accurate.

Unfortunately, a method for removing the large errors along the edges of the solution domain due to the boundary condition has not yet been achieved. However, if this method is used to determine the small-scale wind stress field forcing for an

oceanic circulation model in the open ocean, it may be most desirable to have the small-scale wind stress field taper to zero towards the model domain boundaries. Along coastlines, the choice of boundary condition is less clear. It may not be critical to accurately specify the small-scale wind structure near model domain boundaries since ocean model circulation near the domain boundaries are often relaxed to a prescribed boundary condition or are within a sponge layer. Note that if cyclical boundary conditions are used in the zonal direction, then it is only necessary to specify the boundary conditions along the northern and southern boundaries.

B.3 Application to SST-induced vector wind stress perturbations

Small-scale perturbations in the wind stress curl and divergence have been found to be statistically related to the underlying crosswind and downwind components of the SST gradient field by

$$\nabla \times \boldsymbol{\tau}' = -\alpha_c^{spd}\Big(\frac{\partial T}{\partial n}\Big)' + \alpha_c^{dir}\Big(\frac{\partial T}{\partial s}\Big)' \tag{B.8}$$

$$\nabla \cdot \boldsymbol{\tau}' = \alpha_D^{spd}\Big(\frac{\partial T}{\partial s}\Big)' + \alpha_D^{dir}\Big(\frac{\partial T}{\partial n}\Big)', \tag{B.9}$$

where T is the SST and (s, n) are local downwind and crosswind coordinates, respectively, and the primes represent spatial high-pass filtering operations. The coefficients represented by α are referred to as coupling coefficients.

The downwind and crosswind gradient fields are related to their Cartesian counterparts by

$$\frac{\partial T}{\partial s} = \cos\psi\frac{\partial T}{\partial x} + \sin\psi\frac{\partial T}{\partial y} \quad \text{(B.10)}$$

$$\frac{\partial T}{\partial n} = -\sin\psi\frac{\partial T}{\partial x} + \cos\psi\frac{\partial T}{\partial y}, \quad \text{(B.11)}$$

where ψ is the wind direction. Using the RHS of Eqns. B.8 and B.9 in place of f and g, respectively, in Eqns. B.3 and B.4, we get the following expression for τ^x and τ^y

$$\nabla^2\tau^x = \alpha_D^{spd}\frac{\partial^2 T}{\partial x\partial s} + \alpha_D^{dir}\frac{\partial^2 T}{\partial x\partial n} - \alpha_C^{spd}\frac{\partial^2 T}{\partial y\partial n} - \alpha_C^{dir}\frac{\partial^2 T}{\partial y\partial s} = F_x \quad \text{(B.12)}$$

$$\nabla^2\tau^y = \alpha_C^{spd}\frac{\partial^2 T}{\partial x\partial n} + \alpha_C^{dir}\frac{\partial^2 T}{\partial x\partial s} + \alpha_D^{spd}\frac{\partial^2 T}{\partial y\partial s} + \alpha_D^{dir}\frac{\partial^2 T}{\partial y\partial n} = F_y, \quad \text{(B.13)}$$

where spatial derivatives in the coupling coefficients are neglected and the spatial derivatives of the crosswind and downwind temperature gradients are computed from Cartesian coordinates by

$$\begin{aligned}
\frac{\partial^2 T}{\partial x\partial n} &= -\cos\psi\frac{\partial\psi}{\partial x}\frac{\partial T}{\partial x} - \sin\psi\frac{\partial^2 T}{\partial x^2} - \sin\psi\frac{\partial\psi}{\partial x}\frac{\partial T}{\partial y} + \cos\psi\frac{\partial^2 T}{\partial x\partial y}\\
\frac{\partial^2 T}{\partial x\partial s} &= -\sin\psi\frac{\partial\psi}{\partial x}\frac{\partial T}{\partial x} + \cos\psi\frac{\partial^2 T}{\partial x^2} + \cos\psi\frac{\partial\psi}{\partial x}\frac{\partial T}{\partial y} + \sin\psi\frac{\partial^2 T}{\partial x\partial y}\\
\frac{\partial^2 T}{\partial y\partial n} &= -\cos\psi\frac{\partial\psi}{\partial y}\frac{\partial T}{\partial x} - \sin\psi\frac{\partial^2 T}{\partial x\partial y} - \sin\psi\frac{\partial\psi}{\partial y}\frac{\partial T}{\partial y} + \cos\psi\frac{\partial^2 T}{\partial y^2}\\
\frac{\partial^2 T}{\partial y\partial s} &= -\sin\psi\frac{\partial\psi}{\partial y}\frac{\partial T}{\partial x} + \cos\psi\frac{\partial^2 T}{\partial x\partial y} + \cos\psi\frac{\partial\psi}{\partial y}\frac{\partial T}{\partial y} + \sin\psi\frac{\partial^2 T}{\partial y^2}.
\end{aligned}$$

The spatial derivatives of the wind direction were computed from spatial gradients of the wind stress components by

$$\frac{\partial \psi}{\partial(x,y)} = \frac{1}{|\boldsymbol{\tau}|^2}\Big(\tau^x \frac{\partial \tau^y}{\partial(x,y)} - \tau^y \frac{\partial \tau^x}{\partial(x,y)}\Big). \tag{B.14}$$

The algorithm outlined on Pg. 281 was used to compute $\tau^{x\prime}$ and $\tau^{y\prime}$ using averaged QuikSCAT wind stress components and AMSR-E SST fields at weekly intervals. The coupling coefficients were computed separately, and include spatial dependencies. These terms were then spatially high-pass filtered to retain wavelengths shorter than 30° longitude by 10° latitude. Solutions for $\tau^{x\prime}$ and $\tau^{y\prime}$ were then obtained using the SOR method.

Maps of $\tau^{x\prime}$ and $\tau^{y\prime}$ computed in this way are shown in Figs. B.5 and B.6, respectively. The reconstructed $\tau^{x\prime}$ fields agree closely with the observed $\tau^{x\prime}$ fields, indicating that $\tau^{x\prime}$ is closely coupled to the SST fields. The correlation coefficient within this area between the reconstructed and observed $\tau^{x\prime}$ fields is 0.79. The reconstructed $\tau^{y\prime}$ fields do not resemble the observed $\tau^{y\prime}$ fields, indicating that the statistical model relating the curl and divergence to the SST is unable to account for the observed structure of the meridional winds. The correlation coefficient between the reconstructed and observed $\tau^{y\prime}$ fields is 0.13. The correlations between the mean perturbation wind stress curl and divergence fields and the crosswind and downwind SST gradient fields is 0.81 and 0.74, respectively. The high correlation between the reconstructed and observed $\tau^{x\prime}$ is thus nearly the same as the correlations between

the curl and divergence and the SST fields used in the statistical models.

The reconstructed perturbation wind stress components were bin-averaged as functions of the observed perturbation wind stress components and are shown in Fig. B.7. Bin-averages of the $\tau^{x\prime}$ fields show that the reconstructed $\tau^{x\prime}$ are statistically close in magnitude to the observed $\tau^{x\prime}$ fields, although they are, on average, slightly smaller in magnitude. Bin-averages of the $\tau^{y\prime}$ fields show little relationship between the reconstructed and observed $\tau^{y\prime}$ fields.

The failure to account for $\tau^{y\prime}$ is caused by a very weak statistical relationship between $\tau^{y\prime}$ and the underlying SST perturbations. While not shown here, the response of the curl and divergence to the underlying SST gradients is almost entirely attributed to the response of spatial gradients of $\tau^{x\prime}$ to SST. The lack of apparent response of $\tau^{y\prime}$ to SST perturbations in the subject of ongoing research.

References

Chelton, D. B., and M. H. Freilich, 2005: Scatterometer-based assessment of 10-m wind analyses from the operational ECMWF and NCEP numerical weather prediction models. Mon. Wea. Rev., **133**, 409-429.

Press, W. H., S. A. Teukolsky, W. T. Vetterling, and B. P. Flannery, 1992: Numerical recipes in FORTRAN: the art of scientific computing, Second Edition. Cambridge Press. 963pp.

SOR Algorithm

Algorithm to find τ^x and τ^y from the relations

$$\nabla^2 \tau^x = F_x$$

$$\nabla^2 \tau^y = F_y.$$

INPUT F_x and F_y (to use Eqns. B.12 and B.13, need the following: large-scale zonal and meridional wind stress components; coupling coefficients (constant or spatially and/or temporally varying); *unfiltered* model T); x and y grid.

OUTPUT small-scale wind stress field $\tau^{x\prime}$ and $\tau^{y\prime}$.

Step 1 If F_x and F_y already specified, go to *Step 5*, else if computing using Eqns. B.12 and B.13 go to *Step 2*.

Step 2 Compute $\frac{\partial T}{\partial x}, \frac{\partial T}{\partial y}, \frac{\partial^2 T}{\partial x^2}, \frac{\partial^2 T}{\partial y^2}, \text{and} \frac{\partial^2 T}{\partial x \partial y}$ from unfiltered SST field.

Step 3 Compute $\frac{\partial \psi}{\partial x} \text{and} \frac{\partial \psi}{\partial y}$ using Eqn. B.14 from unfiltered large-scale wind fields.

Step 4 Compute F_x and F_y from Eqns. B.12 and B.13.

Step 5 Interpolate over missing values in F_x and F_y.

Step 6 Spatially high-pass filter F_x and F_y to obtain F'_x and F'_y.

Step 7 For $i = 1, 2, \ldots, N_x$

For $j = 1, 2, \ldots, N_y$ compute $a_{i,j}, b_{i,j}, c_{i,j}, d_{i,j}, e_{i,j}$ from either Eqn. B.6 or B.7.

Step 8 Input forcing field F'_x and coefficients a, b, c, d, e to the SOR algorithm to numerically solve for $\tau^{x\prime}$.

Step 9 Input forcing field F'_y and coefficients a, b, c, d, e to the SOR algorithm to numerically solve for $\tau^{y\prime}$.

Step 10 OUTPUT ($\tau^{x\prime}$,$\tau^{y\prime}$);

STOP

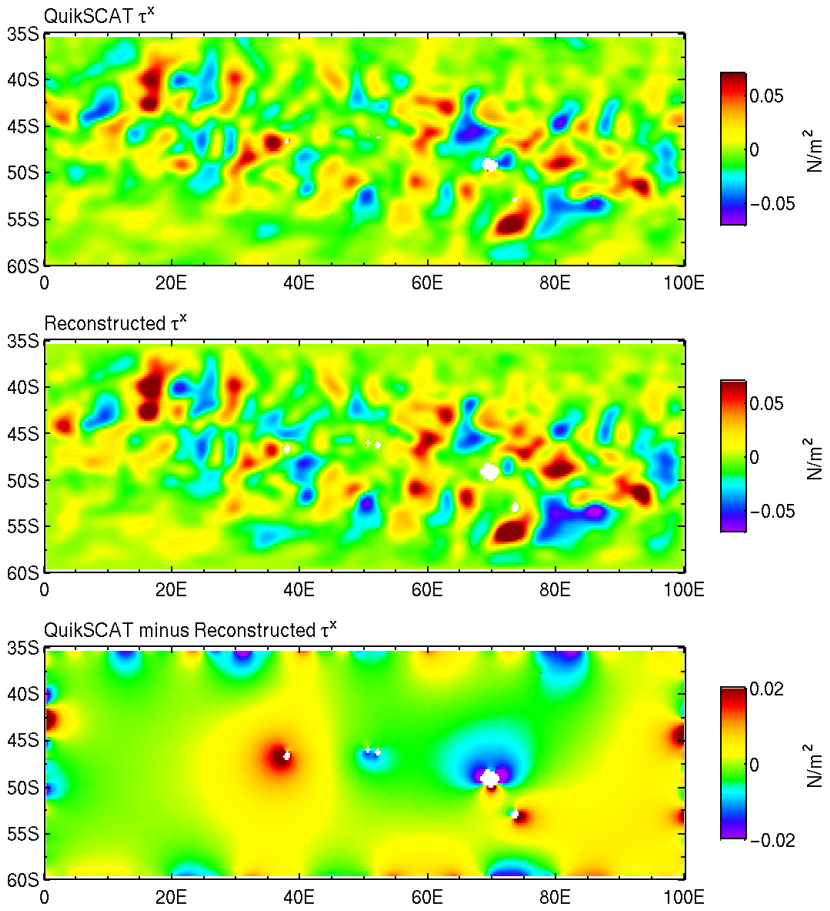

Figure B.1: Mean maps of $\tau^{x\prime}$: (top) original QuikSCAT fields; (middle) reconstructed fields; (bottom) difference between original and reconstructed fields to show amplitude and locations of error. Note the range of the colorbar is different in the bottom panel.

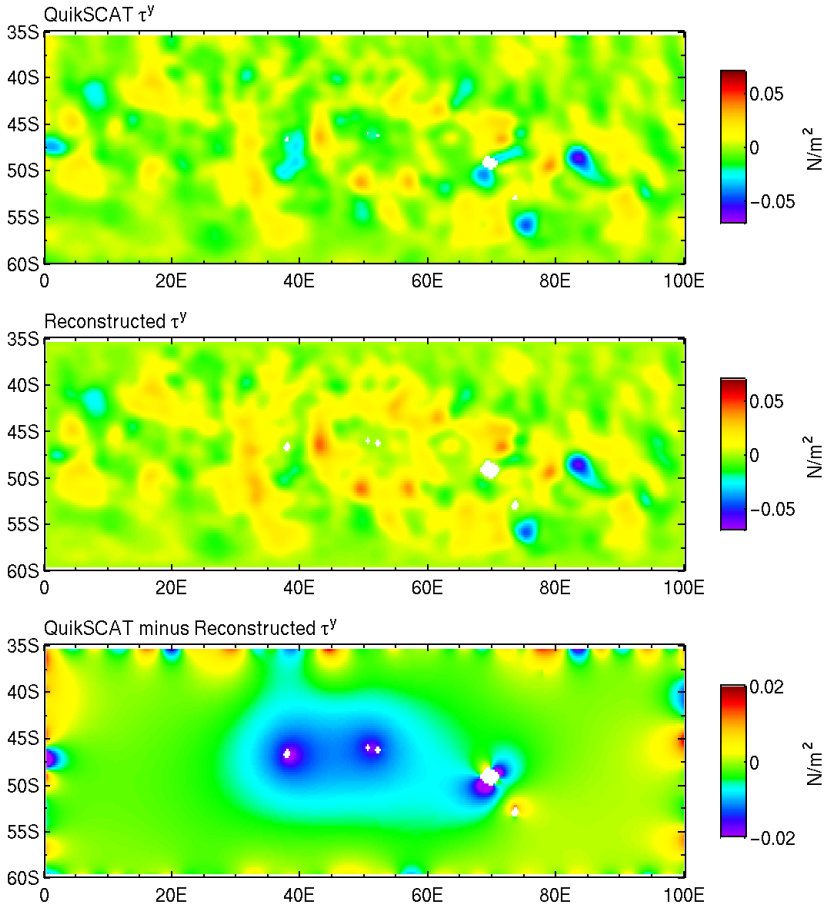

Figure B.2: Same as Fig. B.3, except for $\tau^{y\prime}$.

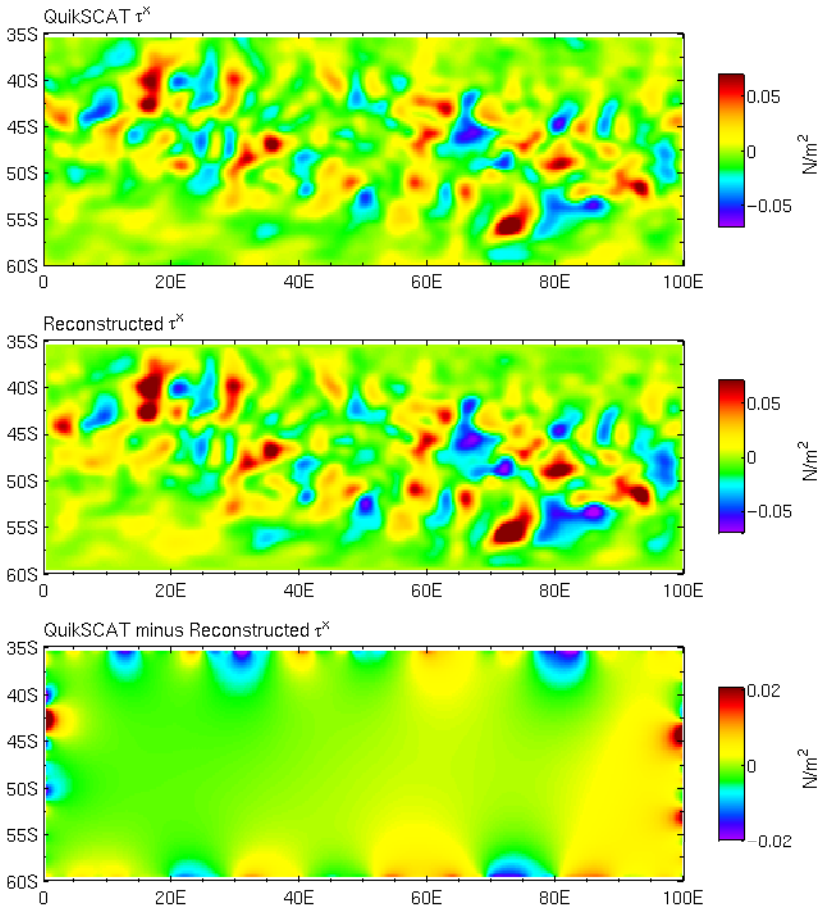

Figure B.3: Mean maps of $\tau^{x\prime}$ with missing points removed as discussed in the text: (top) original QuikSCAT fields; (middle) reconstructed fields; (bottom) difference between original and reconstructed fields to show the amplitude and locations of error. Note the range of the colorbar is different in the bottom panel.

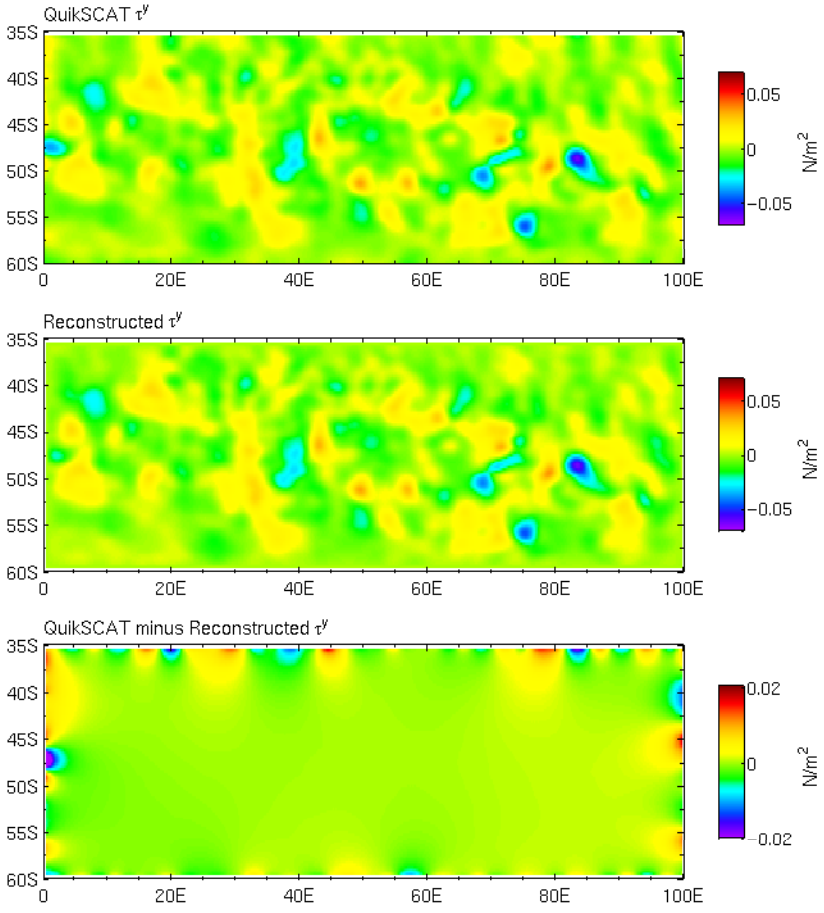

Figure B.4: Same as Fig. B.3, except for $\tau^{y\prime}$.

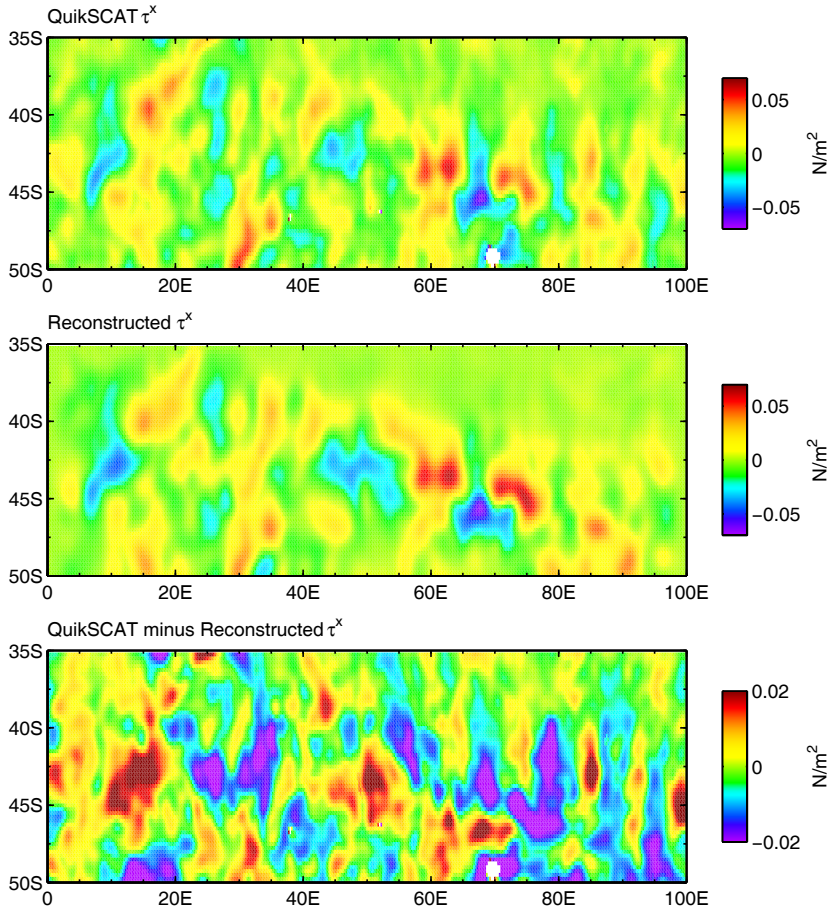

Figure B.5: Mean maps of $\tau^{x\prime}$: (top) original QuikSCAT fields; (middle) reconstructed fields computed from the AMSR-E SST fields as discussed in the text; (bottom) difference between original and reconstructed fields. Note the range of the colorbar is different in the bottom panel.

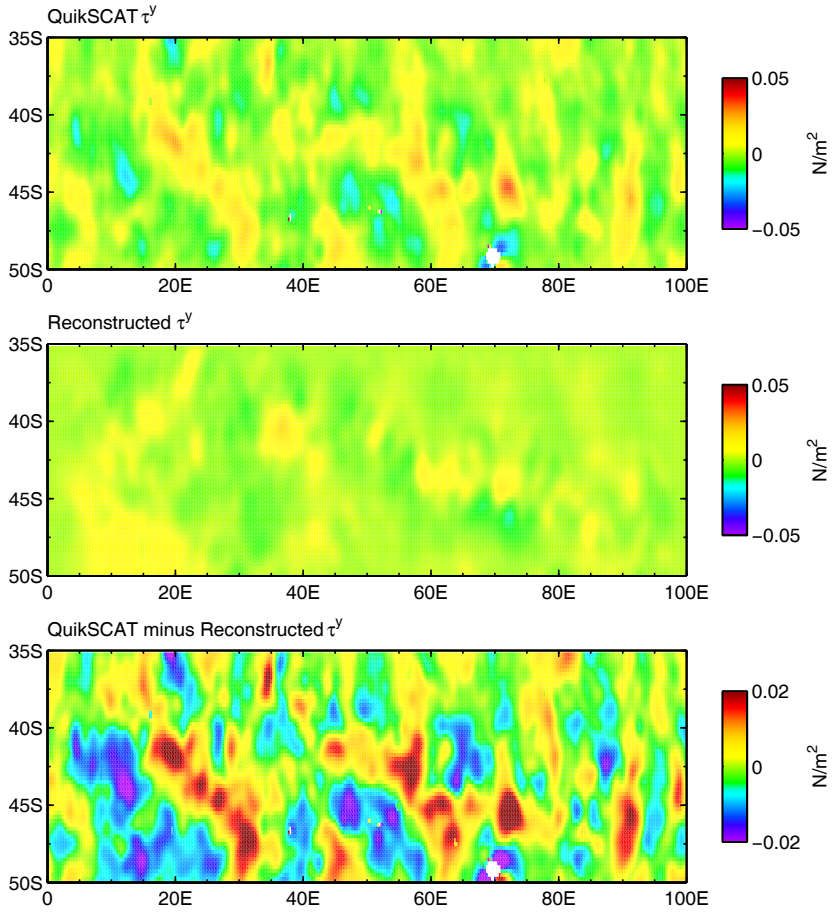

Figure B.6: Mean maps of $\tau^{y\prime}$: (top) original QuikSCAT fields; (middle) reconstructed fields computed from the AMSR-E SST fields as discussed in the text; (bottom) difference between original and reconstructed fields. Note the range of the colorbar is different in the bottom panel.

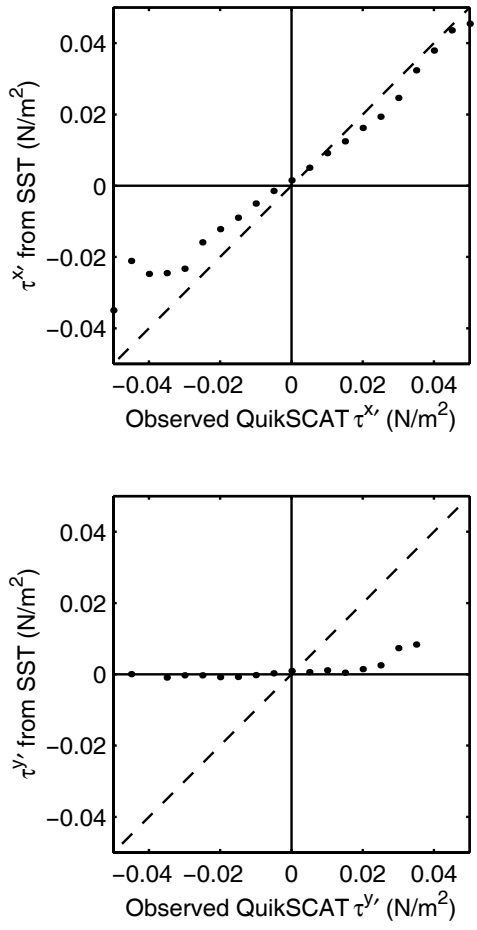

Figure B.7: Bin-averages of the mean reconstructed field binned as functions of the observed field: (top) $\tau^{x\prime}$; (bottom) $\tau^{y\prime}$.